THÈSE POUR OBTENIR LE GRADE DE DOCTEUR DE L'ÉCOLE NATIONALE SUPÉRIEURE DE CHIMIE DE MONTPELLIER

en Chimie et Physico Chimie des Matériaux

École Doctorale ED459 Chimie Balard

Unité de recherche UM5253 Institut Charles Gerhardt Montpellier

en partenariat international avec le Politecnico di Torino, ITALIE

Chimie verte sur catalyseurs pérovskites

Présentée par Quang Nguyen TRAN

Le 27 novembre 2019

Sous la direction de Francesco DI RENZO, Barbara BONELLI, Werner PAULUS et Nathalie TANCHOUX

Devant le jury composé de

Didier TICHIT, Directeur de Recherche, ENSCM	Président du jury
Stefania ALBONETTI, Professore 2a fascia, Università di Bologna	Rapporteur
Maria Elena GALVEZ, Chargé de Recherche HDR, Sorbonne Université	Rapporteur
Gabriella GARBARINO, Ricercatore RTD-B, Università di Genova	Examinateur
Marco GARAVELLI, Professore 1a fascia, Università di Bologna	Examinateur
Francesco DI RENZO, Directeur de Recherche, ENSCM	Directeur de thèse
Barbara BONELLI, Professore 2a fascia, Politecnico di Torino	Co-directeur de thèse
Werner PAULUS, Professeur, Université de Montpellier	Co-directeur de thèse
Francesco Luca BASILE, Professore 2a fascia, Università di Bologna	Membre invité
Helena KAPER, Chargé de Recherche, Saint-Gobain C.R.E.E.	Membre invité

ENSCM CHIMIE Montpellier

THESIS TO OBTAIN THE GRADE OF PHILOSOPHY DOCTOR OF THE ÉCOLE NATIONALE SUPÉRIEURE DE CHIMIE DE MONTPELLIER AND THE POLITECNICO DI TORINO

in Chimie et Physico Chimie des Matériaux - École Doctorale ED459 Chimie Balard and Scienza e Tecnologia dei Materiali – ScuDo Politecnico di Torino

Laboratories UM5253 Institut Charles Gerhardt Montpellier and DISAT

In the framework of the Erasmus Mundus Joint Doctorate SINCHEM (Sustainable Industrial Chemistry)

Green Chemistry on Perovskite Catalysts

Presented by Quang Nguyen TRAN
on 27th November 2019

under the supervision of Francesco DI RENZO, Barbara BONELLI, Werner PAULUS and Nathalie TANCHOUX

In front of the commission

Didier TICHIT, Directeur de Recherche, ENSCM	Jury President
Stefania ALBONETTI, Professore 2a fascia, Università di Bologna	Rapporteur
Maria Elena GALVEZ, Chargé de Recherche HDR, Sorbonne Université	Rapporteur
Gabriella GARBARINO, Ricercatore RTD-B, Università di Genova	Examinateur
Marco GARAVELLI, Professore 1a fascia, Università di Bologna	Examinateur
Francesco DI RENZO, Directeur de Recherche, ENSCM	Directeur de thèse
Barbara BONELLI, Professore 2a fascia, Politecnico di Torino	Co-directeur de thèse
Werner PAULUS, Professeur, Université de Montpellier	Co-directeur de thèse
Francesco Luca BASILE, Professore 2a fascia, Università di Bologna	Membre invité
Helena KAPER, Chargé de Recherche, Saint-Gobain C.R.E.E.	Membre invité

Dedicated to my little family: Ty, Khoi and Lam

This work was co-funded through a SINCHEM (Sustainable Industrial Chemistry) Grant. SINCHEM is a Joint Doctorate programme selected under the Erasmus Mundus Action 1 Programme (FPA 2013-0037)

Table of contents

Acknowledgments

Foremost, I would like to express my sincere gratitude to my supervisor Prof. Francesco Di Renzo who selected me in this project for the continuous support of my Ph.D research, for his patience, understanding of my family situation. Without his guidance and persistent help, this thesis would not have been possible.

I would like to thank my co-supervisor Prof. Werner Paulus for his introduction and guidance into the crystallography world. His insightful comments and encouragement, as well as hard questions, have incented me to widen my research from various perspectives. I am also indebted to Dr. Monica Ceretti for her instructions on doing the structure refinement and laboratory works at the University of Montpellier.

I would like to express my deep sense of gratitude to my co-supervisor at the Politecnico di Torino Prof. Barbara Bonelli who administratively supported me when was in Turin, provided me an opportunity to join her team and gave me access to the laboratory and research facilities. My sincere thanks also go to Dr. Marco Armandi, Dr. Serena Esposito and Roberto Nasi for their laboratory guidance, Prof. Fabio Deorsola and Prof. Samir Bensaid for their corrections to scientific publications.

Many thanks to my friend Ferenc Martinovic without whom the first publication would not have been accomplished; to my Vietnamese labmate Hoang-Phuoc Ho for stimulating discussions and scientific advice. I am also grateful to my MACS friends: Dr. Olinda Gimello, Kim Pla, Vasyl Veremeienko, Iqra Zubair and Sonia Aguilera for sharing time with me.

I would like to extend my gratitude to Sinchem program for funding this project, and to Prof. Stefania Albonetti for her academic comments and her organization of Sinchem schools/meetings/mobility.

Last but not least, I would like to thank to my family for supporting me spiritually throughout writing this thesis and my life in general.

ABSTRACT

The “perovskite” term is granted for any mixed metal oxides with the structural formula ABO_3. In the structure, the A is a larger cation of typically lanthanide, alkaline or alkaline-earth metals, while smaller B cation is usually a transition metal. An ideal perovskite unit cell can be described as cubic (Pm3m space group) where the A cation is 12-fold coordinated to oxygen anions, and the B cation is 6-fold coordinated to oxygen anions to assembly octahedral BO_6 (Fig.1) [1,2]. In the ideal structure, the tolerance factor *t* is of 1 ($t = (r_A + r_O)/(\sqrt{2}(r_B + r_O))$, where r_A , r_B and r_O are ionic radii of A, B, and oxygen, respectively) [3]. However, different elements can be crystallized in the perovskite structure until *t* meets the restriction of $0.75 \leq t \leq 1.0$ [3], offering a great potential to design multifunctional catalysts tailoring to specific chemical reactions.

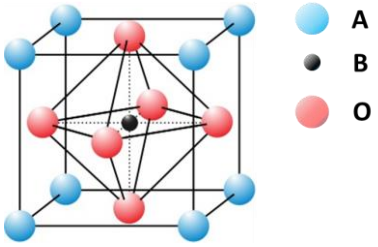

Figure 1 – A model of perovskite structure ABO_3.

One of the main advantages of the perovskite structure is its flexibility to adopt a wide range of compositions. This is possibly done by partially or fully substituting either the A or B cation, resulting in different surface and redox properties. In this regard, the first part of the thesis focuses on selecting compositions for the NO_x assisted soot oxidation for exhaust treatment of diesel vehicles. The reaction involves NO to NO_2 conversion and subsequent soot oxidation by the formed NO_2 from the gas phase, at relatively low temperature [4].

Noble metals catalysts have been commercially used for the reaction due to higher conversion at low temperatures; however, they are still limited by prohibitively expensive cost and strategic limitations of availability. Perovskite oxide $La_{0.9}Sr_{0.1}CoO_3$ appears a reasonably priced alternative since the outperformance of its noble rivals (Pt/Al_2O_3) in a recent study [5]. In this respect, the first section of the thesis developed La-Co based perovskite oxides for the soot oxidation in the presence of NO_x gases and investigated the

correlation of the catalytic activity with crystallinity, redox properties and the role of lattice oxygen.

Among the studied samples $LaAl_{1-x}Co_xO_3$, x of 0.75 exhibits superior catalytic activity for both NO to NO_2 oxidation and NO_x-assisted soot oxidation (Fig.2). The excellent performance is attributed to the synergetic interaction between Al-Co in B-site of the structure and may be linked to the high lattice surface oxygen supported by a well-crystallized perovskite structure. The study shows that this perovskite oxide is possible to be considered as a potential alternative for noble metal catalysts for diesel exhaust treatment.

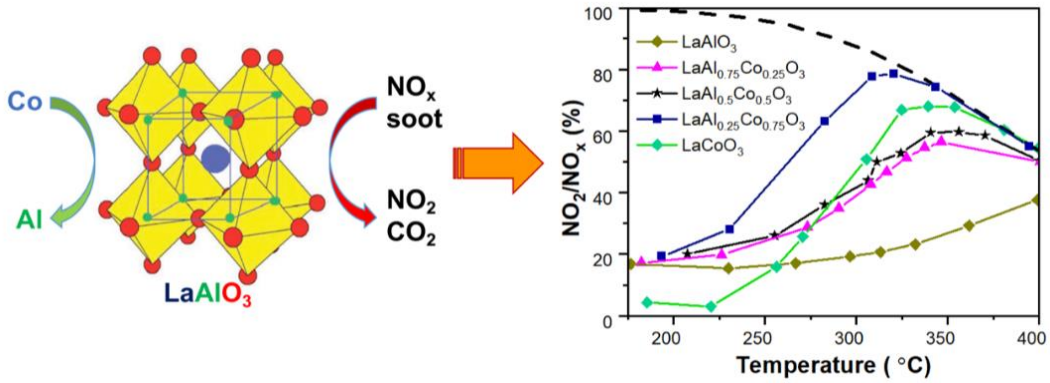

Figure 2 – Catalytic application of $LaAl_{1-x}Co_xO_3$ for NO_x – assisted soot oxidation.

While most of the research has focused on the perovskite structure/properties modifications by cation substitutions, there is a limited number of works on anion sites. Oxyhydride perovskite, $ABO_{3-x}H_x$, where hydride anions (H^-) can substitute O^{2-} in any sites of the BO_6 octahedron appears as an emerging material with intriguing characteristics: unusual low oxidation state of cobalt in $LaSrCoO_3H_{0.7}$ (+1.7) [6] or hydride mobility in $BaTiO_{3-x}H_x$ at relatively low temperature [7], promising new applications in many aspects. While only studies of structural and magnetic behaviors of oxyhydride perovskites [8,9] can be found, a limited number of literatures about catalysis of oxyhydrides have been conducted. The second part of the thesis aims to explore the possibility of using oxyhydride perovskite $BaTiO_{3-x}H_x$ and $LaSrCoO_{4-x}H_y$ for catalytic applications. The reactivity of hydride species has been tested using chemical titration of toluene at temperatures at which hydrides are expected to be mobile. The results show that $LaSrCoO_{4-x}H_y$ exhibit chemical reactivity towards toluene hydrogenation while $BaTiO_{3-x}H_x$ shows no activity under the adopted reaction conditions. The observed activity of $LaSrCoO_{4-x}H_y$ is likely linked to the metallic

sites formed by thermal decomposition and detected by the magnetic measurements, and the reactivity of oxyhydrides may be ignored.

On the other hand, this section of the thesis also investigated the stability of oxyhydride perovskite $LaSrCoO_{4-x}H_y$ in different atmospheres to understand their behaviors under reaction conditions. Under a reductive environment, the oxyhydride perovskite $LaSrCoO_{4-x}H_y$ is decomposed into metallic sites through an intermediate phase $LaSrCoO_{3.5}$ while under oxidative conditions direct conversion to $LaSrCoO_4$ is observed (Fig.3). Interestingly, under oxidative treatment, $LaSrCoO_{4-x}H_y$ exhibits rapid diffusion of hydrides to the surface to recombine into gaseous H_2 below 400 °C, while $BaTiO_{3-x}H_x$ has a slow process of hydride evolution from ~ 400 to 800 °C.

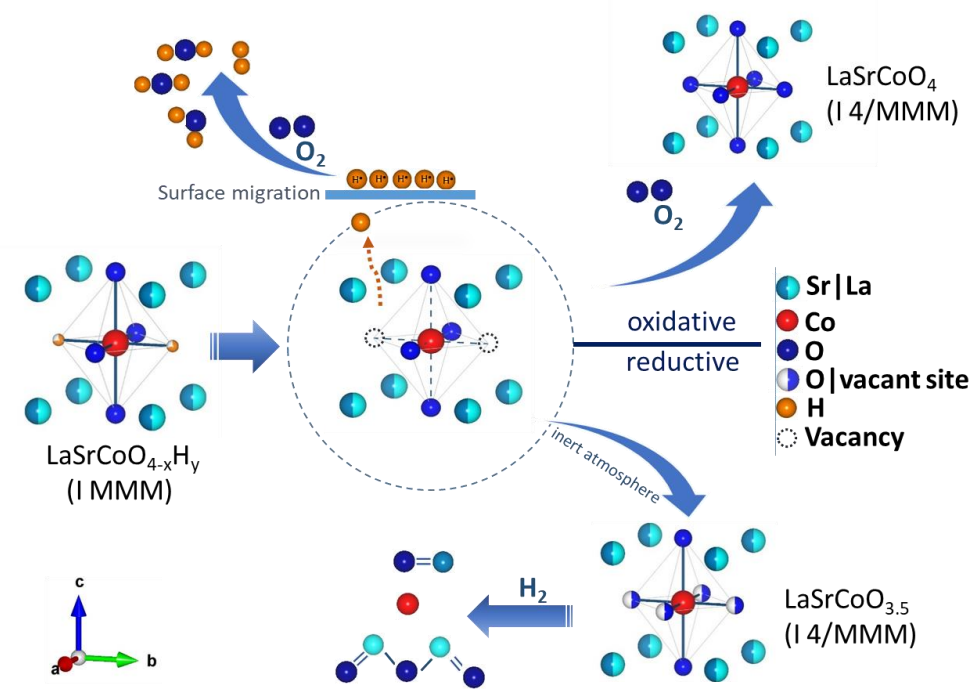

Figure 3 - A representation of hydride evolution and phase transformation under oxidative/reductive environments.

While most of the scientific works have focused on reduction and oxidation reactions over perovskites, studies on acid−base properties and reactions are limited [10]. In this respect, the final part of the thesis explores the potentiality of perovskite catalysts for chemical transformations of bio-ethanol using Co- and Ga-doped $LaAlO_3$ as examples. Substitutions result in tuning the acid-base characteristics, leading to different reaction pathways to a wide range of products (Fig.4). The catalysts were prepared by sol-gel method exhibiting

perovskite as the only crystalline phase, and Ga and Co are well introduced into the perovskite structure upon calcination at 700 °C.

The prepared perovskites are dominated by the basic sites by the nature of A-site cation. $LaAlO_3$ has the highest acidity whereas substitution of Al by Ga and Co results in a reduction in acidity. All catalysts were tested for the ethanol valorization yielding both olefins and oxygenates products with excellent conversions. The quantities of olefins may be controlled by the acidity of the catalysts whilst the formation of oxygenates depends on the nature of cation substitutions. Acetone is the major product over reducible Co-doped perovskite, and further transformed products (monoolefins>C2, pentanone-2, and C_7-oxygenates) from acetone are limited on this catalyst. On the other hand, $LaAl_{0.75}Ga_{0.25}O_3$ is an effective catalyst of aldol coupling of acetaldehyde to crotonaldehyde and further reaction to butadiene. At a high temperature of the reaction, Ga-doped perovskite becomes an effective catalyst for the formation of odd-C oxygenate products by acetone-acetaldehyde aldolization. The present study suggests the potential possibilities to tune the surface acid-base properties of perovskite catalysts by substitutions in order to tailor the production of desired products.

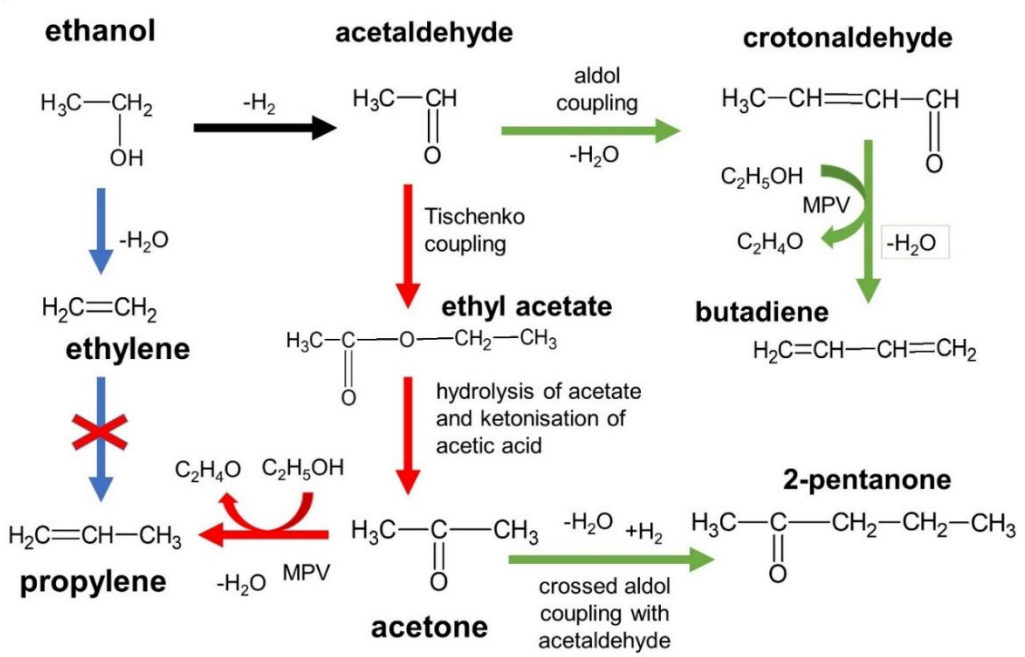

Figure 4 - Main reaction pathways in the conversion of ethanol on Ga- and Co-doped $LaAlO_3$ perovskites.

References

1 Q. N. Tran, F. Martinovic, M. Ceretti, S. Esposito, B. Bonelli, W. Paulus, F. Di Renzo, F. A. Deorsola, S. Bensaid and R. Pirone, *Appl. Catal. A Gen.*, 2020, **589**, 117304.

2 M. A. Pena and J. L. G. Fierro, *Chem. Rev.*, 2001, **101**, 1981–2017.

3 J. Zhu, H. Li, L. Zhong, P. Xiao, X. Xu, X. Yang, Z. Zhao and J. Li, *ACS Catal.*, 2014, **4**, 2917–2940.

4 T. Andana, M. Piumetti, S. Bensaid, L. Veyre, C. Thieuleux, N. Russo, D. Fino, E. Alessandra and R. Pirone, *Appl. Catal. B Environ.*, 2017, **209**, 295–310.

5 C. H. Kim, G. Qi, K. Dahlberg and W. Li, *Science (80-.).*, 2010, **327**, 1624–1627.

6 M. A. Hayward, E. J. Cussen, J. B. Claridge, M. Bieringer, M. J. Rosseinsky, C. J. Kiely, S. J. Blundell, I. M. Marshall and F. L. Pratt, *Science (80-.).*, 2002, **295**, 1882–1884.

7 Y. Kobayashi, O. J. Hernandez, T. Sakaguchi, T. Yajima, T. Roisnel, Y. Tsujimoto, M. Morita, Y. Noda, Y. Mogami, A. Kitada, M. Ohkura, S. Hosokawa, Z. Li, K. Hayashi, Y. Kusano, J. E. Kim, N. Tsuji, A. Fujiwara, Y. Matsushita, K. Yoshimura, K. Takegoshi, M. Inoue, M. Takano and H. Kageyama, *Nat. Mater.*, 2012, **11**, 507–511.

8 T. Yamamoto, R. Yoshii, G. Bouilly, Y. Kobayashi, K. Fujita, Y. Kususe, Y. Matsushita, K. Tanaka and H. Kageyama, *Inorg. Chem.*, 2015, **54**, 1501–1507.

9 C. Tassel, Y. Goto, Y. Kuno, J. Hester, M. Green, Y. Kobayashi and H. Kageyama, *Angew. Chemie - Int. Ed.*, 2014, **53**, 10377–10380.

10 F. Polo-Garzon and Z. Wu, *J. Mater. Chem. A*, 2018, **6**, 2877–2894.

RÉSUMÉ

Le terme «pérovskite» est attribué à tous les oxydes mixtes de formule développée ABO_3. Dans la structure, le A est un cation plus grand, typiquement lanthanides, alcalins ou alcalino-terreux, tandis que le cation B, plus petit, est habituellement un métal de transition. Une cellule de pérovskite idéale peut être décrite comme une unité cubique (groupe d'espace Pm3m) où le cation A est coordonné 12 fois aux anions oxygène et le cation B est coordonné 6 fois aux anions oxygène pour l'assemblage de la BO_6 octaédrique (Fig.1) [1,2]. Dans la structure idéale, le facteur de tolérance t est égal à 1, où t = $(r_A + r_O)/(\sqrt{2}(r_B + r_O))$, r_A , r_B et r_O sont les rayons ioniques de A, B, et de l'oxygène) [3]. Cependant, différents éléments peuvent être cristallisés dans la structure perovskite, pourvu que t respecte la restriction de $0{,}75 \leq t \leq 1{,}0$ [3], offrant ainsi un grand potentiel pour la conception de catalyseurs multifonctionnels adaptés à des réactions chimiques spécifiques.

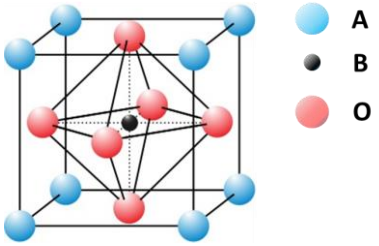

Figure 1 –structure perovskite ABO_3.

L'un des principaux avantages de la structure en pérovskite est sa souplesse, lui permettant d'adopter une large gamme de compositions. Cela est possible en substituant partiellement ou totalement les cations A ou B, ce qui entraîne des propriétés de surface et rédox différentes. À cet égard, la première partie de la thèse porte sur la sélection de compositions pour l'oxydation assistée par NOx de la suie en vue du traitement par l'échappement de véhicules diesel. La réaction implique une conversion de NO en NO_2 et une oxydation ultérieure des suies par le NO_2 formé à partir de la phase gazeuse, à une température relativement basse [3].

Des catalyseurs à base de métaux nobles ont été utilisés dans le commerce pour la réaction en raison d'une conversion plus élevée à basse température. Cependant, ils sont toujours limités par des coûts prohibitifs et par des limitations stratégiques de la disponibilité. La pérovskite $La_{0.9}Sr_{0.1}CoO_3$ apparaît comme une alternative à prix raisonnable aux compétiteurs à base de métaux noble (Pt / Al_2O_3) dans une étude récente [4]. À cet égard, la

première partie de la thèse a développé des oxydes pour l'oxydation de la suie en présence de NOx gazeux et a étudié la corrélation de l'activité catalytique avec la cristallinité, les propriétés redox et le rôle de l'oxygène du réseau.

Parmi les échantillons étudiés, $LaAl_{1-x}Co_xO_3$, avec x 0,75, présente une activité catalytique supérieure pour l'oxydation du NO en NO_2 et l'oxydation de la suie assistée par le NOx (figure 2). L'excellente performance est attribuée à l'interaction synergique entre Al-Co dans le site B de la structure et peut être liée à l'oxygène de surface supporté par une structure de pérovskite bien cristallisée. L'étude montre que cette pérovskite peut être considéré comme une alternative potentielle aux catalyseurs à base de métaux nobles pour le traitement des gaz d'échappement des moteurs diesel.

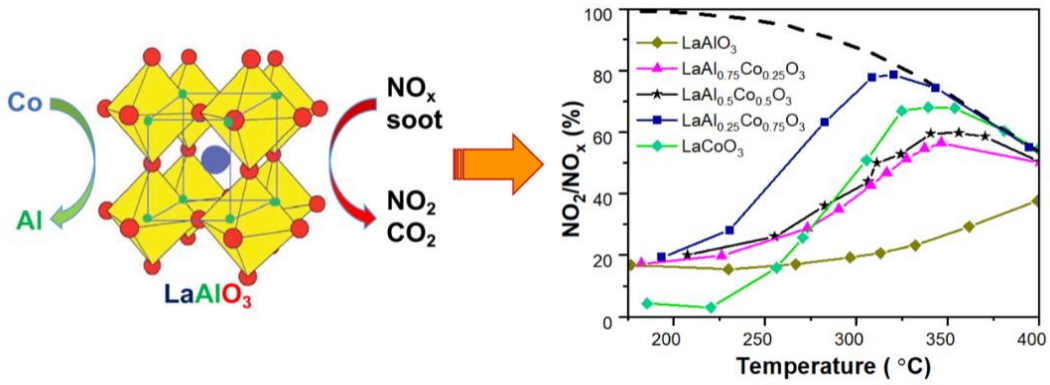

Figure 2 – Catalytic application of $LaAl_{1-x}Co_xO_3$ for NO_x – assisted soot oxidation.

Alors que la plupart des recherches ont porté sur les modifications de structure / propriétés de perovskite par substitution de cations, le nombre de travaux sur des sites anioniques est limité. Les pérovskites oxyhydrures, $ABO_{3-x}H_x$, où les anions hydrure (H^-) peuvent remplacer O^{2-} dans n'importe quel site de l'octaèdre BO_6, émergent comme un matériau présentant des caractéristiques intéressantes : inhabituel faible degré d'oxydation du cobalt (+1.7) dans $LaSrCoO_3H_{0.7}$ [5] ou mobilité des hydrures dans $BaTiO_{3-x}H_x$ à une température relativement basse [7], de nouvelles applications prometteuses à bien des égards. Alors que des études des comportements structuraux et magnétiques peuvent être trouvées en littérature pour les pérovskites oxyhydrures [8,9], un nombre très limité de publications sur la catalyse sur oxyhydrures a été réalisé. La deuxième partie de la thèse vise à explorer la possibilité d'utiliser les pérovskites $BaTiO_{3-x}H_x$ et $LaSrCoO_{4-x}H_y$ pour des applications catalytiques. La réactivité des espèces hydrures a été testée par titrage chimique du toluène à des températures auxquelles les hydrures devraient être mobiles. Les résultats montrent

que $LaSrCoO_{4-x}H_y$ présente une réactivité chimique vis-à-vis de l'hydrogénation du toluène alors que $BaTiO_{3-x}H_x$ ne présente aucune activité dans les conditions de réaction adoptées. L'activité observée de $LaSrCoO_{4-x}H_y$ est probablement liée aux sites métalliques formés par décomposition thermique et détectés par les mesures magnétiques, donc la réactivité propre des oxyhydrides peut être négligéée.

D'autre part, dans cette section de la thèse a également été étudiée la stabilité de la pérovskite oxyhydrure $LaSrCoO_{4-x}H_y$ dans différentes atmosphères afin de comprendre leurs comportements dans des conditions de réaction. Dans un environnement réducteur, la pérovskite oxyhydrure $LaSrCoO_{4-x}H_y$ est décomposée en sites métalliques par le biais d'une phase intermédiaire $LaSrCoO_{3.5}$, tandis que, dans des conditions oxydantes, une conversion directe en $LaSrCoO_4$ est observée (figure 3). Fait intéressant, sous traitement oxydant, $LaSrCoO_{4-x}H_y$ présente une diffusion rapide des hydrures à la surface pour se recombiner en H_2 gazeux en dessous de 400°C, tandis que $BaTiO_{3-x}H_x$ présente un processus lent de dégagement des hydrures d'environ 400 à 800°C.

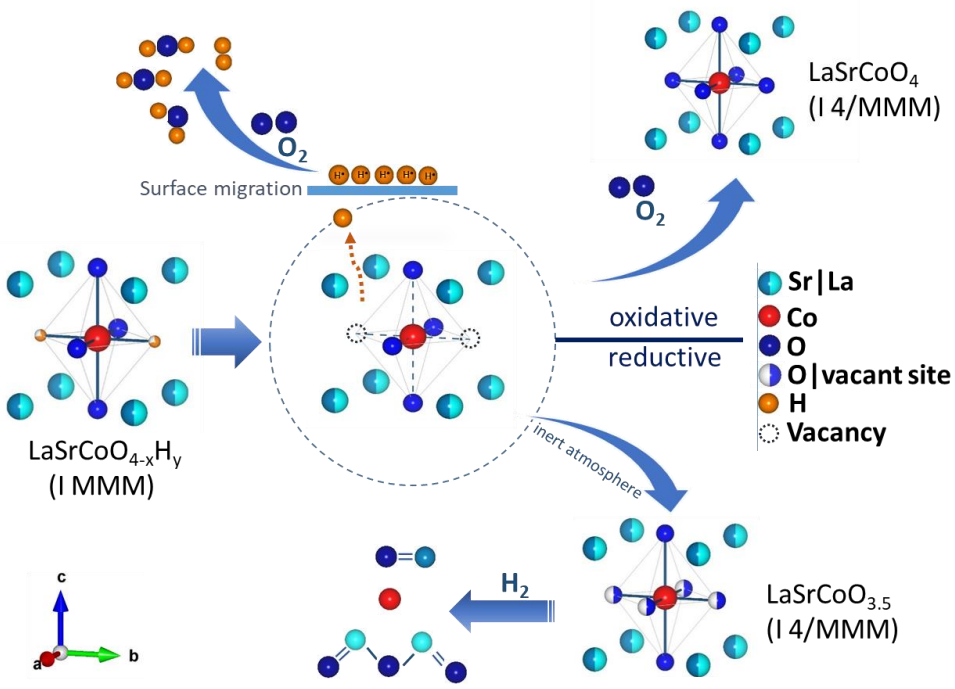

Figure 3 - Une représentation de l'évolution des hydrures et des transformations de phases en milieux oxidants/reducteurs.

Bien que la plupart des travaux scientifiques se soient concentrés sur les réactions de réduction et d'oxydation sur les pérovskites, les études sur les propriétés et les réactions

acide-base sont peu nombreux [10]. À cet égard, la dernière partie de la thèse explore le potentiel des catalyseurs pérovskite pour la conversion du bioéthanol en utilisant, comme exemples, $LaAlO_3$ dopé au Co et au Ga. Les substitutions se traduisent par un ajustement des caractéristiques acide-base, conduisant à différentes voies de réaction pour une large gamme de produits (Fig.4). Les catalyseurs ont été préparés par un procédé sol-gel présentant la pérovskite comme seule phase cristalline, et Ga et Co sont bien introduits dans la structure pérovskite obtenue par calcination à 700°C.

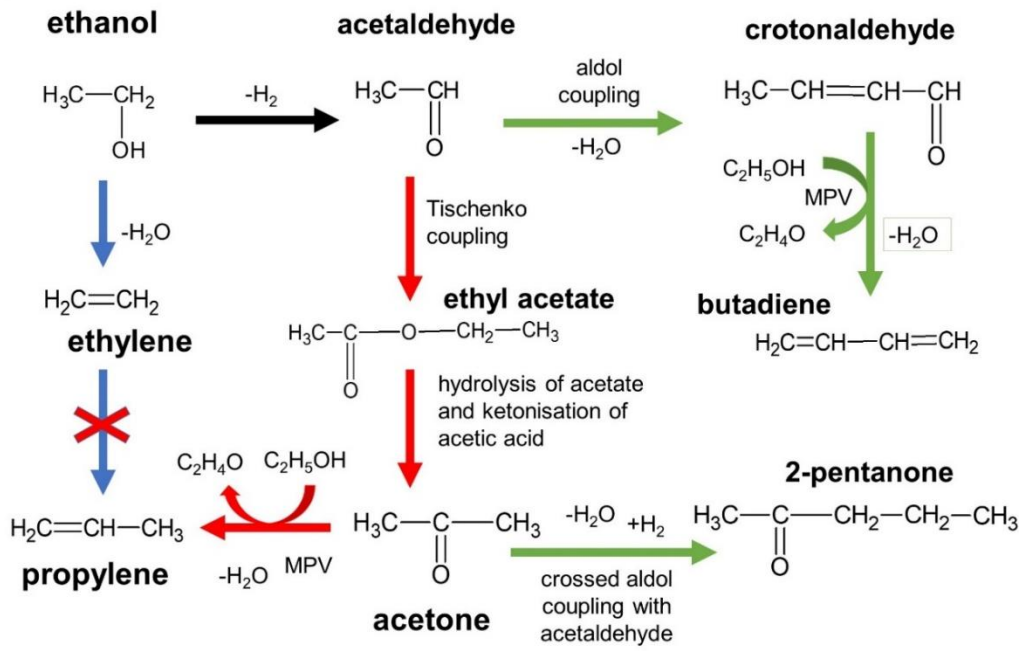

Figure 4 - Parcours de reaction principaux dans la conversion de l'éthanol sur pérovskites $LaAlO_3$ dopées au Ga et Co.

Les pérovskites préparées sont dominées par les sites basiques, en raison de la nature du cation du site A. $LaAlO_3$ a l'acidité la plus élevée, alors que la substitution de Al par Ga et Co entraîne une réduction de l'acidité. Tous les catalyseurs ont été testés pour la valorisation de l'éthanol, donnant des oléfines et des composés oxygénés avec d'excellentes conversions. Les quantités d'oléfines peuvent être contrôlées par l'acidité des catalyseurs, tandis que la formation de composés oxygénés dépend de la nature des substitutions de cations. L'acétone est le produit principal obtenu sur la pérovskite réductible dopée au Co. Les produits formés en passant par l'acétone (monooléfines = C2, pentanone-2 et oxygénés en C7) sont limités à ce catalyseur. D'autre part, $LaAl_{0.75}Ga_{0.25}O_3$ est un catalyseur efficace du couplage aldolique de l'acétaldéhyde pour former

crotonaldéhyde, ainsi que de la réaction ultérieure au butadiène. À une température élevée de réaction, la pérovskite dopée au Ga devient un catalyseur efficace pour la formation de produits oxygénés avec nombre inpair d'atome de carbone par aldolisation acétone-acétaldéhyde. La présente étude suggère les possibilités potentielles d'ajuster les propriétés de surface acide-base des catalyseurs à base de pérovskite au moyen de substitutions, afin d'adapter la production des substances désirées.

References

1 Q. N. Tran, F. Martinovic, M. Ceretti, S. Esposito, B. Bonelli, W. Paulus, F. Di Renzo, F. A. Deorsola, S. Bensaid and R. Pirone, *Appl. Catal. A Gen.*, 2020, **589**, 117304.

2 M. A. Pena and J. L. G. Fierro, *Chem. Rev.*, 2001, **101**, 1981–2017.

3 J. Zhu, H. Li, L. Zhong, P. Xiao, X. Xu, X. Yang, Z. Zhao and J. Li, *ACS Catal.*, 2014, **4**, 2917–2940.

4 T. Andana, M. Piumetti, S. Bensaid, L. Veyre, C. Thieuleux, N. Russo, D. Fino, E. Alessandra and R. Pirone, *Appl. Catal. B Environ.*, 2017, **209**, 295–310.

5 C. H. Kim, G. Qi, K. Dahlberg and W. Li, *Science (80-.).*, 2010, **327**, 1624–1627.

6 M. A. Hayward, E. J. Cussen, J. B. Claridge, M. Bieringer, M. J. Rosseinsky, C. J. Kiely, S. J. Blundell, I. M. Marshall and F. L. Pratt, *Science (80-.).*, 2002, **295**, 1882–1884.

7 Y. Kobayashi, O. J. Hernandez, T. Sakaguchi, T. Yajima, T. Roisnel, Y. Tsujimoto, M. Morita, Y. Noda, Y. Mogami, A. Kitada, M. Ohkura, S. Hosokawa, Z. Li, K. Hayashi, Y. Kusano, J. E. Kim, N. Tsuji, A. Fujiwara, Y. Matsushita, K. Yoshimura, K. Takegoshi, M. Inoue, M. Takano and H. Kageyama, *Nat. Mater.*, 2012, **11**, 507–511.

8 T. Yamamoto, R. Yoshii, G. Bouilly, Y. Kobayashi, K. Fujita, Y. Kususe, Y. Matsushita, K. Tanaka and H. Kageyama, *Inorg. Chem.*, 2015, **54**, 1501–1507.

9 C. Tassel, Y. Goto, Y. Kuno, J. Hester, M. Green, Y. Kobayashi and H. Kageyama, *Angew. Chemie - Int. Ed.*, 2014, **53**, 10377–10380.

10 F. Polo-Garzon and Z. Wu, *J. Mater. Chem. A*, 2018, **6**, 2877–2894.

SOMMARIO

Il termine "perovskite" designa qualsiasi ossido misto con formula strutturale ABO_3. Nella struttura, A è un catione più grande, tipicamente lantanide, alcalino o alcalino-terroso, mentre il catione B, più piccolo, è generalmente un metallo di transizione. Una cellula unitaria di perovskite ideale può essere descritta come cubica (gruppo spaziale Pm3m) onil catione A oordinato con 12 anioni ossigeno e il catione B coordinato con 6 anioni di ossigeno per assemblare un ottaedro BO_6 (Fig.1) [1,2]. Nella struttura ideale, il fattore di tolleranza t è 1(t = $(r_A + r_O)/(\sqrt{2}(r_B + r_O))$, dove r_A , r_B 3 r_O sono i raggi ionici di A, B e ossigeno [3]. Tuttavia, elementi diversi possono essere cristallizzati nella struttura della perovskite, fino a quando t soddisfa la restrizione $0{,}75 \leq t \leq 1{,}0$ [3], offrendo un grande potenziale per progettare catalizzatori multifunzionali su misura per specifiche reazioni chimiche.

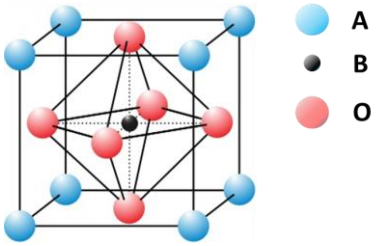

Figure 1 – Un modello della struttura perovskite ABO_3.

Uno dei principali vantaggi della struttura perovskite è la sua flessibilità nell'adottare una vasta gamma di composizioni. Questo può essere fatto sostituendo parzialmente o completamente il catione A o B, risultando in diverse proprietà di superficie e redox. A questo proposito, la prima parte della tesi si concentra sulla selezione di composizioni per l'ossidazione di particolati (soots) assistita da NOx per il trattamento dei gas di scarico dei veicoli diesel. La reazione comporta la conversione da NO a NO_2 e la successiva ossidazione dei particolati da parte dell'NO_2 formato in fase gas a temperatura relativamente bassa [4].

Catalizzatori a base di metalli nobili sono stati usati commercialmente per la reazione, a causa della maggior conversione a basse temperature. Tuttavia, tali catalizatori sono ancora limitati da costi proibitivi e limiti strategici di disponibilità. La perovskite $La_{0.9}Sr_{0.1}CoO_3$ in un recente studio è stata presentata come un'alternativa a prezzi ragionevoli alle prestazioni dei catalizzatori in competizione (Pt/Al_2O_3) [5]. A questo proposito, la prima sezione della tesi ha sviluppato perovskiti a base di La-Co per l'ossidazione di particolati

in presenza di NOx e ha studiato la correlazione dell'attività catalitica con la cristallinità, le proprietà redox e il ruolo dell'ossigeno reticolare.

Tra i campioni studiati, $LaAl_{1-x}Co_xO_3$ con x 0.75 mostra un'attività catalitica superiore sia per l'ossidazione da NO a NO_2 che per l'ossidazione di particolati assistita da NOx (Fig.2). Le eccellenti prestazioni sono attribuite all'interazione sinergica tra Al-Co nel sito B della struttura e possono essere collegate all'ossigeno superficiale supportato da una struttura perovskite ben cristallizzata. Lo studio mostra che questo ossido di perovskite può essere considerato una potenziale alternativa a i catalizzatori di metalli nobili per il trattamento dei gas di scarico dei diesel.

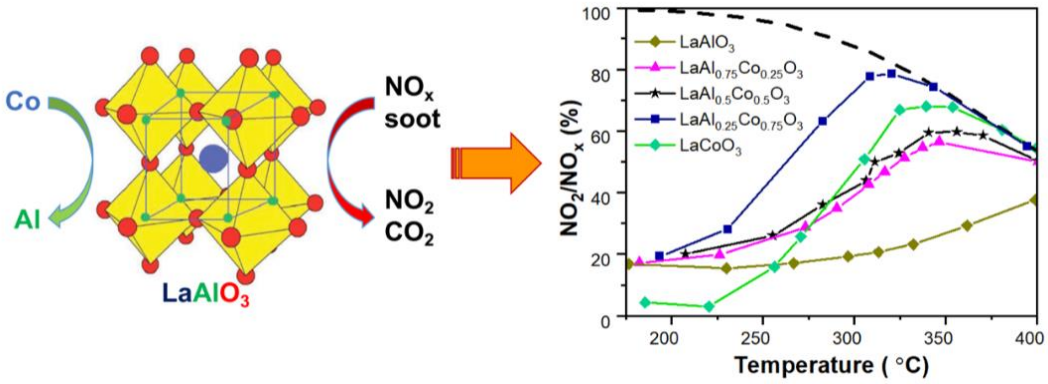

Figure 2 – Catalytic application of $LaAl_{1-x}Co_xO_3$ for NO_x – assisted soot oxidation.

Mentre la maggior parte dei lavori di ricerca si è concentrata sulla modifica di struttura e proprietà delle perovskiti mediante sostituzione di cationi, esiste un numero limitato di lavori sulle sostituzioni nei siti anionici. La perovskite idrossido, $ABO_{3-x}H_x$, in cui gli anioni idruro (H^-) possono sostituire O^{2-} in qualsiasi sito dell'ottaedro BO_6, appare come un materiale emergente con caratteristiche promettenti per nuove applicazioni: insolito basso livello di ossidazione del cobalto (+1.7) in $LaSrCoO_3H_{0.7}$ [6] o mobilità dell'idruro a temperatura relativamente bassa in $BaTiO_{3-x}H_x$ [7]. Mentre si possono trovare in letteratura abbondanti studi sulle proprietà strutturali e magnetiche delle perovskiti idrossidi [8,9], è stato condotto un numero limitato di lavori sulle loro proprietà in catalisi. La seconda parte della tesi mira a esplorare la possibilità di utilizzare lae perovskiti idrossidi $BaTiO_{3-x}H_x$ e $LaSrCoO_{4-x}H_y$ per applicazioni catalitiche. La reattività delle specie idruro è stata testata usando la titolazione chimica del toluene a temperature alle quali ci si aspetta che

gli idruri siano mobili. I risultati mostrano che $LaSrCoO_{4-x}H_y$ presenta una reattività chimica nell'idrogenazione del toluene, mentre $BaTiO_{3-x}H_x$ non mostra attività nelle condizioni di reazione adottate. L'attività osservata di $LaSrCoO_{4-x}H_y$ è probabilmente legata ai siti metallici formati dalla decomposizione termica e rilevati dalle misurazioni magnetiche, mentre la reattività propria degli idrossidi può essere ignorata.

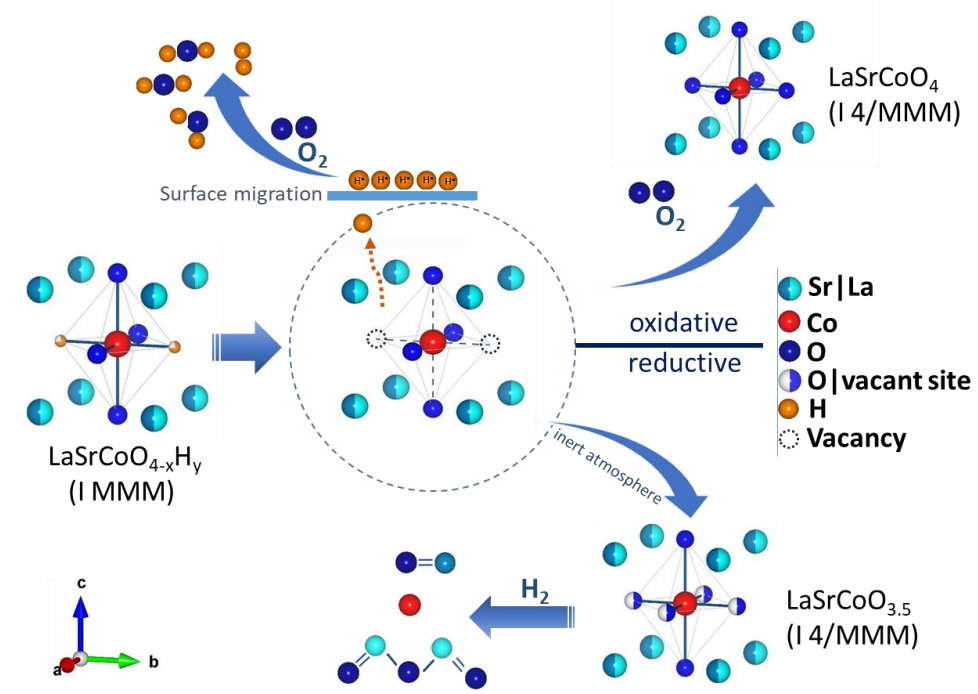

Figure 3 – Rappresentazione dell'evoluzione degli idrossidi e delle trasformazioni di fase in ambienti ossidanti-riduttivi

Mentre la maggior parte dei lavori scientifici si è concentrata sulle reazioni di riduzione e ossidazione sulle perovskiti, gli studi sulle proprietà e le reazioni acido-base sono poco numerosi [10]. A questo proposito, la parte finale della tesi esplora la potenzialità di catalizzatori perovskite per le trasformazioni chimiche del bio-etanolo, usando come esempio $LaAlO_3$ con sostituzioni Co e Ga. Le sostituzioni comportano l'ottimizzazione delle caratteristiche acido-base, portando a percorsi di reazione diversi verso una vasta gamma di prodotti (Fig.4). I catalizzatori sono stati preparati con il metodo sol-gel, prsentano la perovskite come lunica fase cristallina e hanno Ga e Co ben incorporati nella struttura della perovskite dopo calcinazione a 700 °C.

Le perovskiti preparate presentano essenzialmente siti basici, a causa della natura del catione in sito A. $LaAlO_3$ ha la più alta acidità, mentre la sostituzione di Al con Ga e Co determina una riduzione dell'acidità. Tutti i catalizzatori sono stati testati per la valorizzazione dell'etanolo producendo sia olefine che prodotti ossigenati con conversioni eccellenti. Le quantità di olefine possono essere controllate dall'acidità dei catalizzatori mentre la formazione di ossigenati dipende dalla natura delle sostituzioni cationiche. L'acetone è il principale prodotto rispetto alla perovskite riducibile sostituita al Co. I prodotti formati attraverso un intermedio acetone (monoolefine-C2, pentanone-2 e ossigenati-C7) sono limitati su questo catalizzatore. D'altra parte, $LaAl_{0.75}Ga_{0.25}O_3$ è un catalizzatore efficace di accoppiamento aldolico di acetaldeide a crotonaldeide e ulteriore reazione al butadiene. A una temperatura di reazione elevata, la perovskite drogata con Ga diventa un catalizzatore efficace per la formazione di prodotti ossigenati con numero dispari di atomi di carbonio mediante aldolizzazione di acetone e acetaldeide. Il presente studio suggerisce la possibilità di ottimizzare le proprietà acido-base superficiali dei catalizzatori perovskite mediante sostituzioni al fine di personalizzare la produzione dei prodotti desiderati.

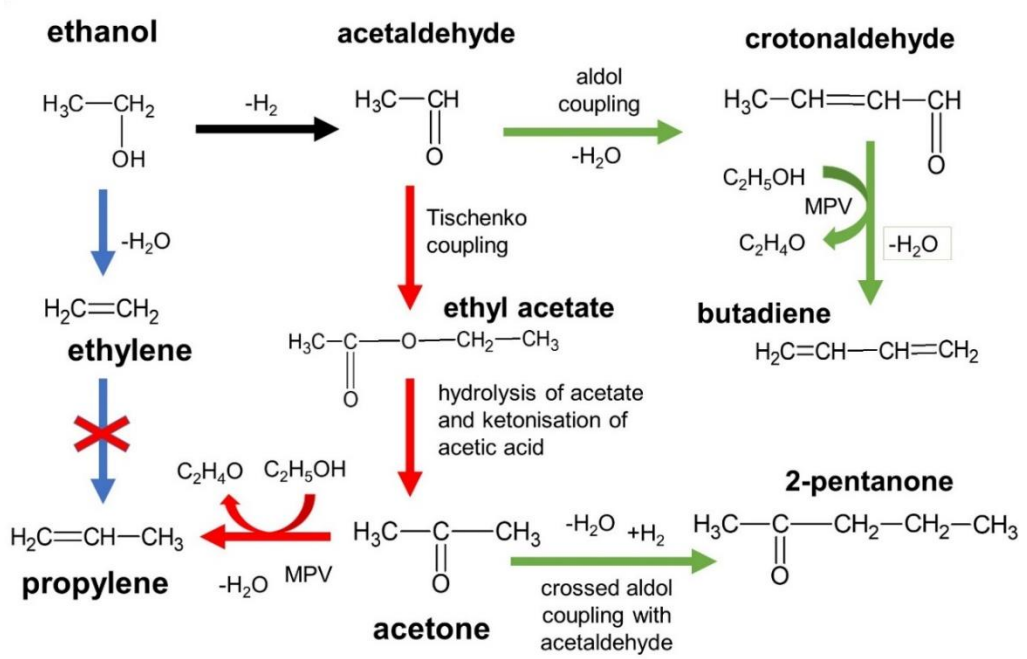

Figure 4 - Principali percorsi di reazione nella conversion dell'etanolo su perovskiti $LaAlO_3$ sostituite Ga e Co.

References

1 Q. N. Tran, F. Martinovic, M. Ceretti, S. Esposito, B. Bonelli, W. Paulus, F. Di Renzo, F. A. Deorsola, S. Bensaid and R. Pirone, *Appl. Catal. A Gen.*, 2020, **589**, 117304.

2 M. A. Pena and J. L. G. Fierro, *Chem. Rev.*, 2001, **101**, 1981–2017.

3 J. Zhu, H. Li, L. Zhong, P. Xiao, X. Xu, X. Yang, Z. Zhao and J. Li, *ACS Catal.*, 2014, **4**, 2917–2940.

4 T. Andana, M. Piumetti, S. Bensaid, L. Veyre, C. Thieuleux, N. Russo, D. Fino, E. Alessandra and R. Pirone, *Appl. Catal. B Environ.*, 2017, **209**, 295–310.

5 C. H. Kim, G. Qi, K. Dahlberg and W. Li, *Science (80-.).*, 2010, **327**, 1624–1627.

6 M. A. Hayward, E. J. Cussen, J. B. Claridge, M. Bieringer, M. J. Rosseinsky, C. J. Kiely, S. J. Blundell, I. M. Marshall and F. L. Pratt, *Science (80-.).*, 2002, **295**, 1882–1884.

7 Y. Kobayashi, O. J. Hernandez, T. Sakaguchi, T. Yajima, T. Roisnel, Y. Tsujimoto, M. Morita, Y. Noda, Y. Mogami, A. Kitada, M. Ohkura, S. Hosokawa, Z. Li, K. Hayashi, Y. Kusano, J. E. Kim, N. Tsuji, A. Fujiwara, Y. Matsushita, K. Yoshimura, K. Takegoshi, M. Inoue, M. Takano and H. Kageyama, *Nat. Mater.*, 2012, **11**, 507–511.

8 T. Yamamoto, R. Yoshii, G. Bouilly, Y. Kobayashi, K. Fujita, Y. Kususe, Y. Matsushita, K. Tanaka and H. Kageyama, *Inorg. Chem.*, 2015, **54**, 1501–1507.

9 C. Tassel, Y. Goto, Y. Kuno, J. Hester, M. Green, Y. Kobayashi and H. Kageyama, *Angew. Chemie - Int. Ed.*, 2014, **53**, 10377–10380.

10 F. Polo-Garzon and Z. Wu, *J. Mater. Chem. A*, 2018, **6**, 2877–2894.

CHAPTER I – Perovskite oxides: Preparation, properties and applications in heterogeneous catalysis

1.1 INTRODUCTION

"Perovskite" is usually referred to structures with the formula of ABO_3 where A is rare or alkaline earth cations, and B is transition metals. Oxygen anion can be partially substituted by other anions such as hydrides [1], halides [2] and oxide nitrides [34]. The ideal structure of perovskite is cubic with a space group Pm3m-O_h [5]. In the perovskite framework, A, a larger cation, has 12-fold coordination locating at the edges of the unit cell whereas B in octahedral sites bond with six surrounding oxygen anions [6]. The A_2BO_4 oxides consist of a layer of perovskite ABO_3 which is sandwiched by two AO layers (Fig.1.1). the lowest limits for r_A and r_B are 0.9 and 0.51 Å respectively [5]. These structures exhibit the versatility of compositions and tunability to physicochemical properties thanks to the possibilities of cations and anions' substitutions. These properties of perovskite oxides can be controlled by introducing desired elements into the structures, offering a feasible way of tuning physicochemical properties with catalytic performances of the materials.

Almost 90% of metallic elements in the periodic table can assembly the perovskite structures [6]. According to the Goldschmidt rule, metal ions satisfying $0.75 < t < 1.00$, with tolerance factor t determined as $t = (r_A + r_X)/(\sqrt{2}(r_B + r_X))$ and r_A , r_B and r_X are ionic radii of A, B and X respectively, are able to build up perovskite structures. Thanks to a wide range of metals adopting in the perovskite structures, together with strong redox properties and oxygen mobility, the solids have found enormous applications in catalysis: steam reforming of toluene [7–9], ethanol [10,11], CH_4 [12–14], bioglycerol [15]; valorization of bio-oil [16–19], biomass [20], HMF [21]; lignin partial oxidation [22 23]; and environmental treatment [24–28].

From the composition point of view, perovskite compounds are considered as mixed oxides which are crystallized in one framework at high temperature. Perovskite synthesis normally requires annealing at high temperature with a long calcination period, which leads to the reduction in specific surface area. Thus, preparation methods result in the low efficiency in surface catalyzed reactions in which high contact between catalyst surface and substrates is tremendous. Many efforts into preparation methods have been paid to improve textural

properties for further catalytic applications. For instance, adding organic complexing agents such as acid citric, ethylene glycol [9,29,30] shows an improvement in textural properties. Preparing nano-size or porous perovskite oxides with different surface morphologies is another approach to enhance textural properties and morphologies. These include forming perovskite nanocrystals by micro-assisted hydrothermal synthesis [31,32], macro/mesoporous perovskite nanotubes [33], and three-dimensional nano-fibrous webs [34]. Moreover, tuning compositions during preparation step is able to optimize the physicochemical properties which is of paramount importance in designing and tailoring of efficient catalysts. Correlation of synthesis pathways with properties and applications will be discussed.

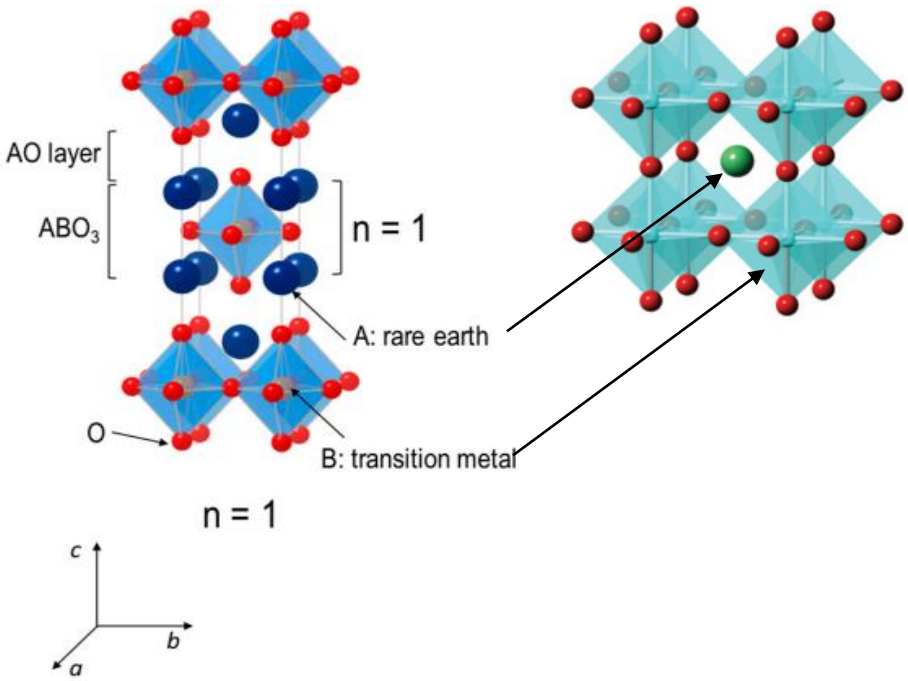

Figure 1.1 - Perovskite oxides ABO_3 and A_2BO_4 structures

1.2 SYNTHESIS OF PEROVSKITE COMPOUNDS

Perovskite oxides were initially synthesized by ceramic method, also called the solid-solid method since the 1970s when scientists started studying oxidation/reduction reactions on oxygen stoichiometric perovskites [35]. One of the advantages of the method is of simplicity, and perovskite structures can be obtained directly annealing mixture of metal oxides. With no requirements for using solvents, it is considered as an environmentally friendly approach without releasing any toxic gases. However, diffusion in the solid-state is normally slow, thus the synthesis has to be carried out at high temperature (usually above

1000 °C) and in long calcination time. These conditions result in grain growth and a decrease in surface area which are not suitable for catalytic applications. Many efforts have been paid to improve contact between metal oxides such as reactive grinding or enhance the homogeneity of starting materials by conducting in liquid phase such as co-precipitation, sol-gel.

1.2.1 Mechanochemical synthesis

Mechanochemical synthesis is also referred to the reactive grinding method using mechanical milling energy to induce chemical reactions. It has been attracted attention of researchers for preparing high surface area perovskites. Briefly, a mixture of solid precursors could be treated by ball milling, during which mechanical energy is transferred to the precursors inducing chemical reactions to take place at low temperature. This route allows particle size reduction and low surface area, and a wide range of perovskite oxides with a crystallite size down to 10 nm and a surface area up to 60 $m^2 g^{-1}$ have been reported [36–39].

The grinding method is typically performed using a high energy ball mill. Balls are normally made of hard materials such as stabilized zirconia [40] or tungsten carbide [36] in order to increase the energy of impact and reduce the ball's wear and sample contamination. The starting materials are typically powders of carbonate salts or mixed oxides, charged into reactors and milled at high speed. Preparation conditions such as milling speed, time, ball-to-powder weight ratio are remarkably important, which may result in different textural properties (Tab.1.1). The formation of the perovskite phase and milling time are strongly correlated. It is reported that perovskite phase $K_{0.5}Na_{0.5}NbO_3$ can appear after a very short period of milling and the crystallinity is improved with milling time [36] . Additives also help to enhance textural properties, it is reported that adding alkaline salts such as LiCl, NaCl, KCl, RbCl, and CsCl into mill reactors can raise the surface area of $LaCo_{0.7}Cu_{0.3}O_{3-\delta}$ up to 46.8 $m^2 g^{-1}$ [41]. However, the addition of alkaline salts requires extra washing process to avoid contamination of catalysts which may deteriorate catalytic performances.

$LaCoO_3$ was among the first perovskite synthesized by ball milling technique. It could be formed by solid-state reaction at least at 800 °C as described in a report of Crestin *et al.* [42]. Sol-gel synthesis with complexing agents such as acid citric reduces calcination temperature to 700 °C; however, the surface area is still not satisfactory for most catalytic

applications [43]. A group of Kaliaguine *et al.* [44] showed that the reactive grinding synthesis of $LaCoO_3$ with additives can enhance the surface area of the perovskite up to 100 m^2 g^{-1}. The authors also examined different grinding parameters: ball materials and size, vial

Table 1.1 – Reactive grinding synthesis of perovskites,

Perovskites	**Ball Material**	**Milling speed (rpm)**	**Ball-to-powder ratio**	**Additive**	**Milling time (h)**	**Surface area (m^2 g^{-1})**	**Crystal size (nm)**
$LaCo_{0.7}Cu_{0.3}O_{3-\delta}$ [41]	hardened steel	1000	-	Alkaline chloride	12	-	7.9-10.5
$0.7BiFeO_3$–$0.3PbTiO_3$ [40]	stabilized zirconia	800	10:1-20:1	-	≤ 8	-	20-30
$K_{0.5}Na_{0.5}NbO_3$ [36]	tungsten carbide	1000	36:1	-	0.66	-	16.4-17.6
$LaCo_{1-x}Fe_xO_3$ [47]	Tempered steel	700	-	-	28.0	37.8	9.5-16.5
$LaCo_{1-x}Fe_xO_3$ [44]	Tungsten carbide	400	72:1	ZnO	27.0	105.1	-

volume, grinding speed and additives, showing that adding ZnO has positive effects in the surface area of the catalyst. They also reported that a minimum of milling time of 16 h could fully convert oxide precursors to perovskites. Similarly, different perovskite oxides such as $LaFeO_3$ [45] and $LaCrO_3$ [46] can be prepared by the reactive grinding in other studies. This technique became a practical route for preparing perovskite catalysts with high surface area and small particle size. Although the method can synthesize samples with large surface area and small grain size, the preparation conditions are extremely vigorous, for instance, extremely high milling speed. Thus, the requirements for the equipment are critical and the synthesis conditions should be carefully considered. To lower the demand for equipment, some researchers proposed that the synthesis of bulk perovskites was first approached, which was followed by ball milling to shorten milling time and to have better textural properties. This approach was proved to be able to produce effective perovskite catalysts for the reduction of NO by propene [48], higher-alcohol synthesis [41] and stearic acid oxidation [49].

1.2.2 Microwave-assisted synthesis

Perovskite synthesis with microwave irradiation has drawn attention of researchers and industrialists since this route is fast and energy-efficient. This technique can replace convention ways of perovskite preparation due to some featured properties: (i) short synthesis time, in the scale of minutes instead of hours; (ii) a green method with limited use of solvents; (iii) high energy efficiency [50]. The synthesis is characterized by an extremely short reaction time such as 1 min for the preparation of $GdAlO_3$ instead of several hours by solid-state method [51]. In general, the microwave-assisted synthesis can be conducted by putting stoichiometric mixtures of precursors under irradiation of microwaves for a certain period of time (Fig.1.2). Starting materials can be metal oxides such as La_2O_3 and CuO for the synthesis of La_2CuO_4 [52] or carbonate/nitrate salts even though they are not microwave susceptors. In these cases, the precursor salts can mix with a microwave susceptor to assist the initial heating without reacting with other reactants. For the preparation of $BaTiO_3$ [53], the mixture of TiO_2 and $BaCO_3$ can be ground and embedded in graphite powder as a susceptor in a silica or alumnina container and then irradiated by microwave. Carbon has very high microwave susceptibility, and it can catch fire and heat the powder, initiating the decomposition of carbonates to oxides. The obtained oxide mixture can be further irradiated to form the perovskite phase. To improve the

homogeneity, the nitrate precursors can initially be dissolved in water, microwave irradiation helps to evaporate at the first step and later cause the crystallization [54,55].

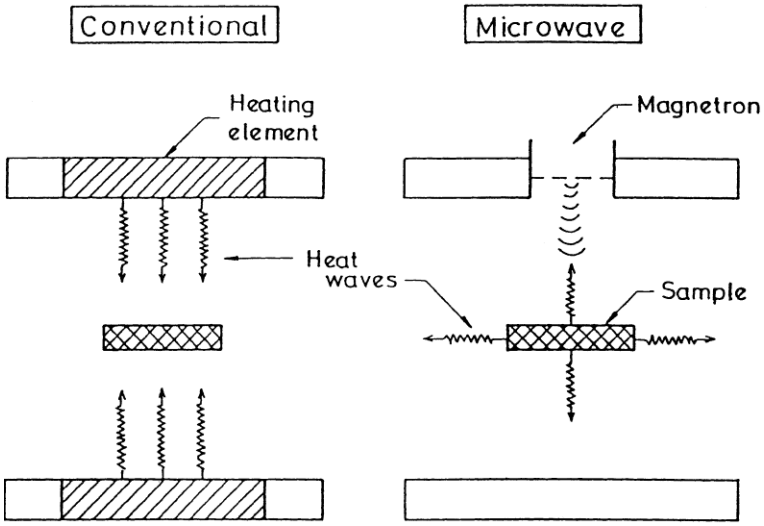

Figure 1.2 – Principle of microwave heating vs conventional heating [52].

1.2.3 Sol-gel method

Perovskite synthesis in solid-phase allows to form pure perovskite structures but simultaneously sacrifices the surface area and increases particle size. Thus it has been mostly applied for the fields of ceramics which require pure structure and high mechanical strength [56]. Because several perovskite materials possess superior optoelectronic properties, this method is still dominant in synthesis perovskite photovoltaic devices [57]. Furthermore, the pure structure exhibits high electrochemical properties, the solid-state route can be used for preparing electronic conducting material with perovskite structures [58]. However, heterogeneous catalysis where high contact between substrates and active sites drives reaction pathways requires high surface area and/or smaller particle size. Solid-state seems to be an unintelligent approach.

One efficient way is to prepare the mixture in solution instead of solid phase by using dissolved nitrate salts with organic complexes to coordinate, combust and disperse metal ions. In 1967, Pechini [59] introduced a new method to prepare lead and the alkaline earth titanates and niobates using citric acid/ethylene glycol to form resin intermediates, which are later decomposed to mixed oxides, then sintered at high temperature to form perovskite structures. This method is also referred to the Pechini or citrate sol-gel route. The process is based on the ability of hydrocarboxylic acids to chelate with metal ions, resulting in the formation of gel by polyesterification under heating. This preparation method allows

forming perovskite oxides at lower temperatures, shorter calcination period, and with higher surface area as well as lower particle size. Although the surface area of perovskite oxides obtained by sol-gel method is still not highly satisfactory, this preparation way is widely adopted for catalytic studies on perovskite materials due to the simplicity. In order to improve textural properties, various organic agents ethylenediaminetetraacetic acid (EDTA) [60,61] , ethylene glycol [62] have been tried (Tab.1.2). Besides, varying preparation parameters such as pH, the quantity of acid citric, calcination temperature and nature of transition metals yields different textural properties in a study of Onrubia *et al.* [24] however, it is difficult to optimize sol-gel synthesis conditions for each perovskite oxide.

Table 1.2 – Experimental parameters of sol-gel synthesis of perovskite oxides using acid citric,

Compounds	**Additives**	**CA/metal**	**Calcination temperature (°C)**	**Calcination time (h)**	**Surface area ($m^2 g^{-1}$)**
$La_{1-x}Sr_xCoO_3$ [60]	EDTA	1.0	700	8	8.4-12.6
$La_{1-x}K_xCo_{1-y}Ni_yO_{3-\delta}$ [63]	-	-	750	4	6.6-11
$LaCoO_3$ [62]	Ethylene Glycol	1.0	750	4	3.9
$LaMnO_3$ [24]	-	1.1	600	4	31.3
$LaFeO_3$ [21]	polyethylene glycol	1.0	750	5	4.9
$LaAlO_3$ [64]	-	-	950	5	3.0
$LaNiO_3$ [65]	-	2.5	700	2	12.7
$LaFe_{1-x}Cu_xO_3$ [66]		1.0	600	8	13.8-18.4
$LaCo_{1-x}Cu_xO_3$ [16]	-		850	5	2.1-4.3
$LaFe_{1-x}Mg_xO_3$ [67]	-	1.0	800	5	4.3-7.9
$LaNi_xFe_{1-x}O_3$ [7]		1.0	850	7	-
$La_{1-x}Ce_xNiO_3$ [68]	-	1.0	800	4	-
$La_{0.7}Sr_{0.3}Co_{1-x}Fe_xO_3$ [61]	EDTA	1.5	800	2	13.9-16.6
$La_{0.5}Sr_{0.5}CoO_3$ [69]	-	-	750	10	3.9
$LaMO_3$ (Co, Fe, Mn) [70]	-	1.1	700	5	9.7-21.8
$La_{0.8}Ce_{0.2}MnO_3$ [71]	-	1.5	700	5	17.0
$BaFe_{1-x}Cu_xO_3$ [72]	-	0.5	850	5	1.0-4.0

Alternatively, some studies have used other gel-forming agents instead of citric acid such as poly(acrylic acid) [73], poly(vinyl alcohol) [74], malic acid [75,76], and stearic acid [77]. Using malic acid to support the chelating process, $La_{0.8}Sr_{0.2}MnO_3$ is obtained with the surface area greater than those synthesized with acid citric, forwarding to higher methane combustion activity [78]. However, citric acid complexes seem to be the best stability in

comparison with other chelating agents [50]. A study of Hernandez *et al.* [79] reported that $La_{0.6}Sr_{0.4}BO_3$ (B=Mn, Fe) using malic acid their preparation exhibits much lower surface area than that of $La_{0.6}Sr_{0.4}TiO_3$ by citric acid, about 16 m^2 g^{-1} compared to 30 m^2 g^{-179}. In another work, sol-gel helps to synthesize $SrTiO_3$ nanoparticles, leading to a better catalytic performance than commercial catalysts [80]. In other research [81], sol-gel method is proved to be a potential way for nano-perovskite preparation. Nano-crystallite $LaFeO_3$ synthesized by sol-gel method exhibits crystallite size of around 40 nm, BET surface area of 9.5 m^2 g^{-1} [81].

1.2.4 Hydrothermal synthesis

1.2.4.1 Conventional hydrothermal route

Hydrothermal processing is usually referred to any heterogeneous chemical reactions in aqueous media under pressurized vessels or autoclaves at temperature above 100 °C and 1 bar [82]. Teflon makes an ideal autoclave under these conditions since it is inert to both hydrofluoric acid and alkaline media. This method draws attention for perovskite oxide synthesis due to simplicity and mostly unnecessity of high temperature calcination which may lead to deterioration of surface area and the grain growth. The crystallization process of solid-phases under hydrothermal conditions is achieved by the saturated vapor pressure of hydrothermal solution at the specified temperature and composition [83].

In the conventional hydrothermal synthesis of perovskite oxides, precursors, normally nitrate salts, are dissolved in deionized water. The solution is added with precipitating reagents (for example, KOH, NaOH) and placed in an inert autoclave heated in a few hours. Teflon-lined stainless steel autoclaves are usually used and hydrothermally treated at a temperature (240–270 °C) and designed time (24–50 h). The effects of preparation parameters in textural properties of prepared samples are normally considered: an increase in KOH amount deteriorates the surface area; shorter hydrothermal time yields higher surface area [84]. In a study on $La_{0.6}Sr_{0.4}MnO_{3+\lambda}$ [84], although, pure perovskite phase can be obtained without high-temperature calcination, the surface area is not impressive, below 16 m^2 g^{-1}. The effects of precipitant (KOH) on the morphology of $KNbO_3$ was studied by Wang *et al.*[85]. In the synthesis, the authors used undissolved precursors of oxide Nb_2O_5 and KOH which is both precipitating agent and reactant. A mixture of oxide Nb_2O_5 and KOH solution is heated at 200 °C in a Teflon autoclave, no further calcination is required. No pure and regular shaped perovskite particles could be obtained below 10 M KOH solution.

However, further increase of KOH concentration (16 M) leads to the formation of microcubes of $KNbO_3$. When the KOH concentration is increased to 30 M, well-defined nanocubes are observed [85] . On the other hand, Ta_2O_5 is used for synthesis of $ATaO_3$ (A=K, Na) [87]. Although the perovskite phase is obtained without the requirement for calcination, the surface area is unexpectedly low, between 2-7 m^2 g^{-1} which is attributed by long hydrothermal time.

Microwave irradiation can effectively reduce hydrothermal period, leading to a decrease in preparation cost and an improvement in textural properties. In this approach (so-called microwave-assisted hydrothermal synthesis), filled autoclaves are irradiated by microwave power. In order to synthesis $MSnO_3$ (M= Ca, Sr, Ba) [88], precursors solution is microwave irradiated in 4 h at 180 °C instead of 12 h of the conventional hydrothermal treatment. Morphologies of samples synthesized with and without microwave irradiation are similar, but higher activity in photocatalytic degradation in terephthalic acid is observed for the microwave-assisted sample. The authors suggested that microwave effects may reduce the surface defects on the catalysts [88]. In other work [89], $SrTiO_3$ synthesized by microwave-assisted hydrothermal route, precursors are dissolved with KOH and the solution is put in a Teflon autoclave under microwave irradiation at 140 °C in less than 160 min. Surprisingly, perovskite structures can be obtained after a very short time of around 10 min. The photodegradation activity of rhodamine B dye (RhB) under UV light and BET surface area of the microwave-assisted sample is much higher than the conventional one.

An effort to improve the textural properties of perovskite oxides is to integrate gel formation with hydrothermal treatment. In the synthesis of Cr-doped $SrTiO_3$, nitrate precursors are dissolved in ethylene glycol to form a gel, which is later added NaOH solution. The mixture is put in a Teflon stainless autoclave and heated between 20-200 °C in 24 h. The precipitate is the washed and calcined to form perovskite structures. This approach helps to prepare perovskite oxides with BET surface area in 20-65 m^2 g^{-1} and 20-30 nm particles size [90].

1.2.4.2 Modified hydrothermal for mesoporous perovskite oxides synthesis

The porous materials usually possess high surface area and allow reactants' access into both external surface and inside pores, accelerating chemical reactions. In the synthesis of porous titanate perovskites [91], porous precursor TiO_2 is initially prepared. The textural properties of TiO_2 are decisive for catalytic activity since they can be transferred to

perovskite oxides upon calcination. Porous TiO_2 can be obtained by the hydrolysis of $Ti(OC_3H_7)_4$ (TTIP) in a solution of ethanol and KCl. The resulted TiO_2 is in forms of spheres of 300- 500 nm in diameter. The perovskite $Ba(Sr)TiO_3$ are synthesized by hydrothermal treatment of mixture of obtained TiO_2 and Ba(Sr)OH at 180 °C in 12 h. Spheres of $Ba(Sr)TiO_3$ as large as parent TiO_2 are obtained, but consist of several hundreds of interconnected nanospheres with around 20 nm, assembling a mesoporous structure. However, this approach reduced the BET surface areas from 254 $m^2 g^{-1}$ of parent TiO_2 to around 10 $m^2 g^{-1}$ of $BaTiO_3$ while increased the pore diameter from 3 nm to 30 nm. In another approach [92] , flower-like layered protonated TiO_2 hierarchical spheres (Fig.1.3) is synthesized from $Ti(OC_4H_{9)4}$, dimethylformamide (DMF) and isopropyl alcohol. Protonated TiO_2 precursor is hydrothermally prepared at 200 °C in 25 h, the flower-like protonated TiO_2 is constructed spheres of 600-800 nm diameter built from many interconnected nanosheets (Fig.1.3). In the second step, the flower-like precursors TiO_2 is hydrothermally treated with Sr^{2+} in the presence of NaOH to form 3D porous $SrTiO_3$. The SEM images show that porous $SrTiO_3$ spheres of 600− 800 nm are made of hundreds of nanocubes of around 60-80 nm in size, and they are interconnected together to form pores of 10-20 nm in size. This form of assembly enhances the BET surface area to 20.83 $m^2 g^{-1}$ and support the formation of mesoporous structure [92].

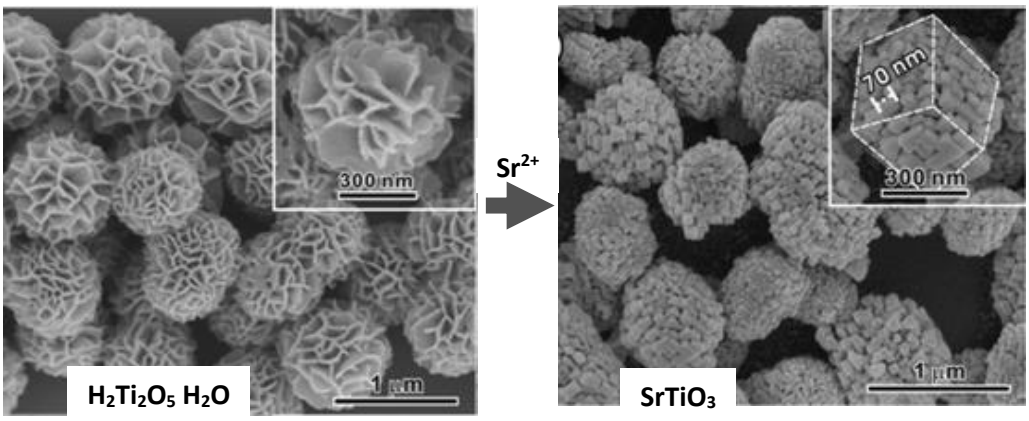

Figure 1.3 – Flower-like protonated TiO_2 precursor and its conversion to porous $SrTiO_3$ by hydrothermal treatment with Sr^{2+} [92].

An alternative route for the synthesis of porous perovskites is to generate perovskite compounds in forms of nanofibers or wires. In this case, mesopores are able to be formed by inter-aggregation of nanosheets in one direction. Mesoporous $SrTiO_3$ nanowires with the surface area up to 145 $m^2 g^{-1}$ and the pore volume of 0.43 $cm^3 g^{-1}$ are prepared through

a template-free hydrothermal treatment (Fig.1.4) [93]. The nanowires are synthesized by dropping $Ti(OC_4H_9)_4$ into $Sr(NO_3)_2$ solution in propanol. The mixed solution is then heated in a Teflon-lined autoclave at 160 °C in 48 h, following calcination at 500 °C to obtain the final nanowires $SrTiO_3$. The nanowires have a uniform cylindrical structure with a length of several micrometers and an average diameter of 20-50 nm [93], which assembly to form a mesoporous structure. Moreover, other researchers have proposed electrospinning technique to form porous perovskite $La_{0.6}Sr_{0.4}Co_{0.8}Mn_{0.2}O_3$ with similar morphology [94]. In this technique, an initial solution of precursors is prepared mixing nitrate and acetate salts with DMF and polyvinylpyrrolodone at room temperature. The obtained solution is then treated by an electrospinning process and subsequent calcination at 650 °C in 3 h. The result shows that perovskite fibers with a diameter of 200 – 300 nm are obtained with some small pores on the wall of nanofibers due to the release of decomposed gases during the calcination process. The technique provides perovskite oxide with the surface area of 17.5 $m^2\ g^{-1}$ and pore size of 22.6 nm [94].

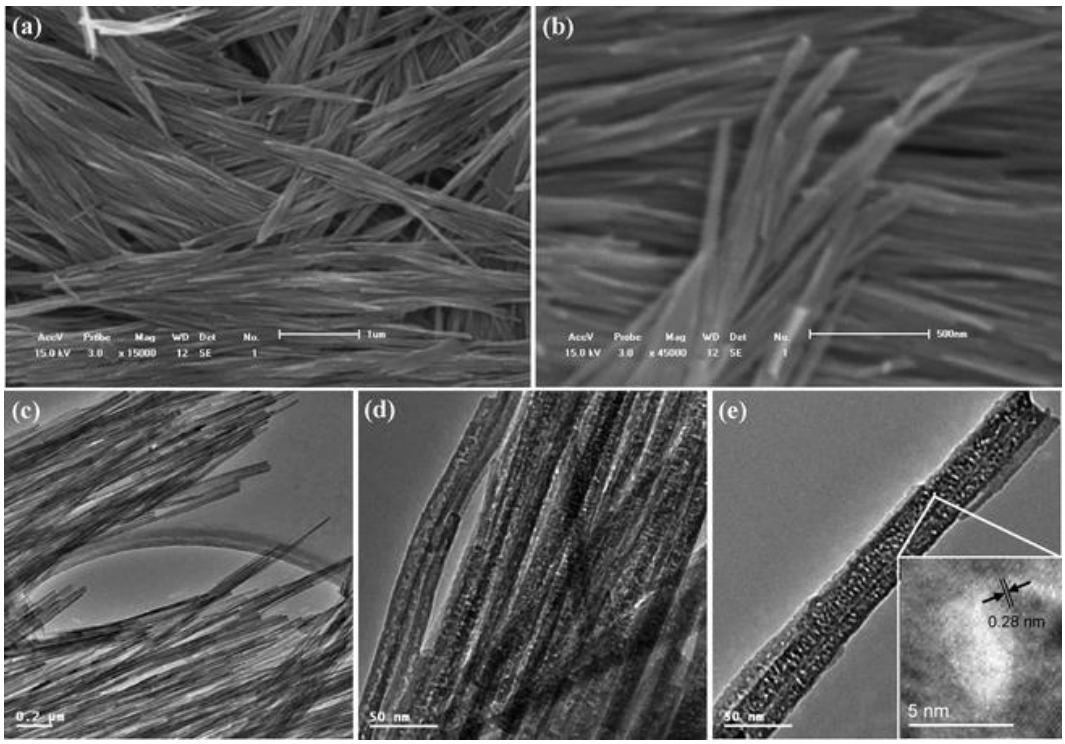

Figure 1.4 – SEM (a,b) and TEM (c,d,e) images of mesoporous $SrTiO_3$ nanowires [93].

To prepare nanoporous $LaCoO_3$, nitrate precursors are dissolved in water with glycine and polyvinylpyrrolidone, the solution is hydrothermally treated in Teflon liner with NH_4OH. The obtained solid is calcined at 600 °C to form porous $LaCoO_3$. The TEM images indicate

that the pores of nanospheres $LaCoO_3$ are produced through interconnected small nanoparticles. Further thermal treatment at 650 °C turns the nanospheres $LaCoO_3$ to be a hollowed nanosphere structure [95]. Furthermore, porous $LaNiO_3$ nanocubes is synthesized by a similar approach. The BET specific surface area of the annealed products is 35.8 $m^2 g^{-1}$, it is ten times higher than sample synthesized without glycine. The average pore diameter of the porous $LaNiO_3$ nanocubes is 30 nm [96] . Obviously, perovskites in porous structure have enhanced surface area and smaller particle size, promoting catalytic applications. In most cases with extremely high surface area, the porous morphology is made from interconnected nano-particles in a form of big spheres, tubes or wires. These porous materials seem to have weaker mechanical strength than the bulk oxides, and the pores could be collapsed in severe conditions. An alternative approach is to synthesis porous perovskites with support of templates which fix the obtained structures and resist and mechanical impacts.

1.2.5 Templating approaches

Templating is a powerful method to synthesize perovskite oxides with an organized porosity in meso-macrostructured, extremely high surface area and large pore size. In this technique, the templates, which can be commercial or home-made products with known textural properties, are first prepared. Precursors solutions can be impregnated or infiltrated in templates, subsequent calcination at high temperature to form perovskite phases. The templates can be removed using alkaline solution, allowing opening new porosity. Textural properties of porous perovskites remarkably rely on the properties of templates, and various types of templates have been discussed recently including carbonized [97], vinyl silica [98], silica xerogel [99] and polymethyl methacrylate (PMMA) [100] (Tab.1.3).

Mesoporous vinyl silica hard template is prepared from pluronic P123, NaCl, tetraethoxysilane, triethoxyvinylsilane. The synthesis is followed by dipping the template into nitrate-citrate solution of precursors. The infiltrated template is then calcined at 700 °C in 4 h, and the silica framework is removed by NaOH solution. The prepared mesoporous $LaCoO_3$ exhibits relatively high BET surface area (96.7 $m^2 g^{-1}$) with mesoporous structures. The authors also reported that the precursor solution without citric acid does not support the formation of the perovskite phase. The mesoporous $LaCoO_3$ shows much higher activity in methane combustion than the conventional $LaCoO_3$ [98]. Another common hard template is silica xerogel, which is prepared by sodium silicate and

HCl. The gel has mesoporous characteristics with a pore size of 2 – 15 nm range and BET surface area of 510 m^2 g^{-1}. By impregnation nitrate solution into xerogel, $LaFeO_3$ perovskite has the surface area 15 times higher than conventional citrate method [99]. In most cases, the silica framework has to be removed by NaOH solution and washed several times by water. The advantage of silica template is to avoid shrinking channels during heat treatment thus able to control crystalline growth inside, but extra removal step is required.

Active carbon is a cheap and readily available material for use as a template. The porous carbon can be synthesized from aggregated silica spheres, which is used as a hard template. Silica powder is mixed with a concentrated aqueous solution of sucrose, containing 0.1 g H_2SO_4 g^{-1} of sucrose [97]. The sucrose is carbonized under N_2 atmosphere at 800 °C in 5 h. The silica template is removed by HF solution, washed and dried, forming a mesoporous carbon template with a surface area of 369 m^2 g^{-1} and a pore size of 2 – 8 nm. Porous perovskite $LaFeO_3$ is then prepared based on templating technique. Typically, solution of metal nitrates is infiltrated to porous carbon template, and calcined at 800 °C under air. Further thermal treatment is required to completely remove the carbon mould [97]. The results show that the obtained sample exhibits a surface area of up to 49 m^2 g^{-1}, leading to excellent catalytic performances in NO reduction. Nano-$NaTaO_3$ can also be obtained by using 3D-mesoporous carbon as a template during its synthesis [101]. The prepared $NaTaO_3$ has particles of 20 nm and a surface area of around 34 $m^2.g^{-1}$, showing a good photoreactivity for the water splitting reaction [101].

Compared to mesoporous compounds, ordered macroporous (3DOM) perovskites reveal unique advantages since these materials allow easy mass transfer and less diffusion resistance to active sites, which is of paramount importance in catalysis. The most used templates to synthesize macroporous perovskites are colloidal crystals such as PMMA or polystyrene (PS) [102] because of their facile control in terms of array and size [103] . The process of synthesis of 3DOM perovskite from PMMA template can be described in Fig.1.5, including infiltration or soaking templates into precursor solution, drying, and calcination at different environments. PMMAs are commercially available with different pore size [104], helping to produce 3DOM $SrTiO_3$ at a wide range of pore size between 120 - 245 nm [104]. Otherwise, PMMA templates can be synthesized by mixing solutions of methyl methacrylate with $K_2S_2O_8$ as an initiator in de-ionized water under N_2 environment at 70 °C to form PMMA microsphere suspension [100]. The suspension is then centrifuged and

washed to remove K and S. Under gravity, well-ordered colloidal crystal templates PMMA are formed. 3DOM-$La_{0.6}Sr_{0.4}MnO_3$ is prepared by impregnation nitrate solutions of,

Table 1.3 – Several porous perovskite oxides and textural properties,

Compounds	**Templates**	**Pore volume ($cm^3\ g^{-1}$)**	**Surface area ($m^2\ g^{-1}$)**	**Catalytic applications**
$LaFe_{1-x}Co_xO_3$ [97]	micro-mesoporous carbon	0.07-0.09	30 - 50	Reduction of NO with CO
$LaCoO_3$ [98]	Vinyl silica	-	96.7	Methane Combustion
$LaFeO_3$ [99]	Silica xerogel	-	110	-
$SrTiO_3$ [104]	PMMA	-	-	Photocatalytic-water splitting
$La_{0.6}Sr_{0.4}MnO_3$ [100]	PMMA	0.15	48.9	-
$Eu_{0.6}Sr_{0.4}FeO_3$ [106]	PMMA	0.063	31.3	Toluene combustion
$La_{0.7}Ca_{0.3}MnO_3$ [107]	PMMA	-	24.2	-
$La_{1-x}Sr_xFeO_3$ [102]	Polystyrene	0.83	35-49	Soot combustion
$La_{0.6}Sr_{0.4}MnO_3$ [108]	PMMA	0.159	42.6	CH_4 combustion
$La_{0.6}Sr_{0.4}CoO_3$ [109]	PMMA	0.161	28	Oxidation of CO and
$La_{0.6}Sr_{0.4}MnO_3$ [110]	PMMA	0.159-0.165	42.7	CH_4 combustion
$SrFeO_{3-\delta}$ [111]	PMMA	0.111	34.0	Toluene combustion
$LaMn_{1-x}Fe_xO_3$ [105]	PMMA	-	21.0	Diesel soot oxidation
$LaFeO_3$ [112]	-	-	-	Soot oxidation
$LaFe_{1-x}Co_xO_3$ [97]	Mesoporous carbon mold	0.070	49.3	Reduction of NO with CO

precursors with ethylene glycol and ethanol in PMMA templates, and calcined at 750 °C [100]. After calcination, 3DOM $La_{0.6}Sr_{0.4}MnO_3$ exhibits high surface area of 33.5 m^2 g^{-1}. The authors also suggested that fragmentation of the porous perovskite by sonication can increase the surface area to 48.9 m^2 g^{-1} [100]. In another study on 3DOM $LaMn_{1-x}Fe_xO_3$ [105]. PMMA template is synthesized by emulsifier-free emulsion polymerization technique using water–oil phase double initiators. $K_2S_2O_8$ (water-phase initiator), azodiisobutyronitrile (AIBN, oil-phase initiator) and the acetone as co-solvent are used. By varying amounts of initiator, monomer and stirring speed, PMMA with different diameters can be obtained. Obviously, the smallest PMMA microspheres leads to the lowest pore size and the largest BET surface area. However, the catalytic activity for soot combustion increases with pore diameters and decreases with BET surface area. Soot oxidation is solid-solid contact, not depending on the surface area, but high pores size allows the reduction in the diffusional resistance. Thus the soot can easily contact with the active site and the catalytic activity is enhanced [105].

The effects of surfactants added during the gel formation process have been widely investigated. The influence of ethylene glycol on texture properties of 3DOM $SrFeO_{3-\delta}$ was studied. Different quantities of ethylene glycol added in the precursors' solution during preparation result in various pore size of prepared products [111]. In another study, citric acid is also used during the preparation of precursors' solution. Metal nitrates are homogeneously dissolved in a solution of citric acid, methanol and ethylene glycol before soaking into PMMA templates [106,113]. This approach provides the formation of macroporous perovskite $Eu_{0.6}Sr_{0.4}FeO_3$ with a BET surface area of 31.3 m^2 g^{-1}. Compared to the bulk $Eu_{0.6}Sr_{0.4}FeO_3$, the 3DOM sample has better catalytic performance in the combustion of toluene [106,113].

In order to improve infiltration of precursors solution into PMMA voids, Chi *et al.* [107] used metal acetates as starting reagents instead of nitrate salts to synthesize 3DOM $La_{0.7}Ca_{0.3}MnO_3$. Moreover, 2-methoxy- ethanol is used with HNO_3 in the process of forming gel rather than citric acid. The gel of metal acetates is dropped into PMMA templates, which are removed by calcination at 800 °C. This preparation method provides a porous network which is composed of nanometer-sized $La_{0.7}Ca_{0.3}MnO_3$ wires with highly ordered spherical voids and the pore size of 340 nm[107]. In the preparation of 3DOM $LaCoO_3$, other authors [109] suggested that using a surfactant mixture of methanol, ethylene glycol, and acid citric assists formation of perovskite phase at low calcination temperature

compared to conventional sol-gel acid citric method, 650 °C compared to 850 °C with surface areas of 28 and 4.4 $m^2 g^{-1}$, respectively [109].

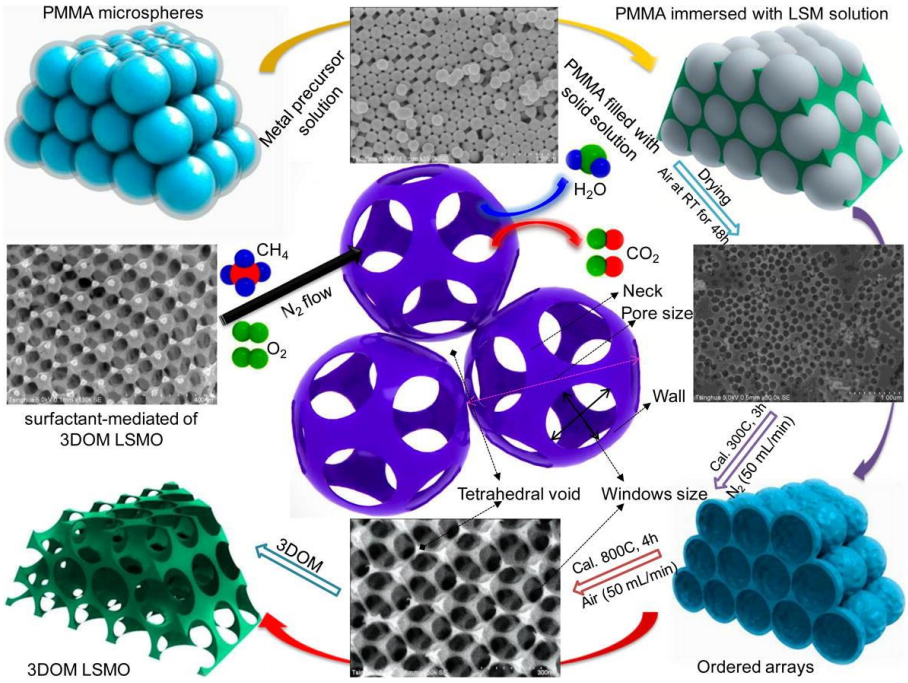

Figure 1.5 - 3DOM $La_{0.6}Sr_{0.4}MnO_3$ perovskite prepared by the PMMA-templating method and its application for methane combustion [108].

In a comprehensive study, the role of surfactants added the during gel formation process were deeply investigated including dimethoxytetraethylene glycol (DMOTEG), ethylene glycol, polyethylene glycol (PEG400), l-lysine, or triblock copolymer (Pluronic P123) in the sysnthesis of macroporous $La_{0.6}Sr_{0.4}MnO_3$ (Fig.1.5) [108]. The macropore sizes and surface areas of the 3DOM- $La_{0.6}Sr_{0.4}MnO_3$ materials are in range of 165–214 nm and 32–40 $m^2 g^{-1}$, respectively. Addition of appropriate amounts of DMOTEG and PEG400 is beneficial for the generation of high-quality 3DOM-structured $La_{0.6}Sr_{0.4}MnO_3$ and hence exhibits a good catalytic activity. 3DOM $La_{0.6}Sr_{0.4}MnO_3$ without nanovoids or mesoporous skeletons is formed without DMOTEG, whereas the high-quality 3DOM $La_{0.6}Sr_{0.4}MnO_3$ samples with nanovoids or mesoporous walls and higher surface areas (32–40 $m^2 g^{-1}$) and pore volumes (0.110 - 0.134 $cm^3 g^{-1}$) are obtained in the presence of DMOTEG [108]. Increase DMOTEG results in an rise in BET surface area to 42.1 $m^2 g^{-1}$ and pore volume to 0.159 $cm^3 g^{-1}$ [108].

1.3 PROPERTIES OF PEROVSKITE OXIDES

1.3.1 Crystal Structure

In the ideal perovskite structure, B is located in the center of cubic cell touching O at the faced centers and A at the corners. The B-O distance should be a/2 and A-O of a/√2, thus the Goldschmidt tolerance factor t is unity. Although the condition for the ideal structure is t equal to 1, it can also be found in a few cases with t closed to 1 and at high temperature. In most cases, perovskite structures exhibit different distortions, leading to deviated structures with orthorhombic, rhombohedral, tetragonal, monoclinic and triclinic symmetries. The distorted structure can be transformed into the ideal framework at high temperature through several intermediate phases [6].

The perovskite structure can be easily modified by substituting A, B sites by other ions with different size and charge or even O-site by other anions. If the charge of B changes by incorporation of foreign B, the oxygen anions are slightly shifted toward the more positive charged one, distorting the structures. Due to electroneutrality, the sum of charges of A and B-sites should equal to the total charge of oxygen. However, incorporation of elements which have oxidation states differ from substituted sites results in unbalance in charge, and generation of deficiencies of cations or anions is a way to compensate. This phenomenon leads to defective perovskites or the non-stoichiometry in perovskites which have been widely discussed [114–116].

Oxygen-deficient perovskites are more common than other types of non-stoichiometric perovskites such as cationic vacancies or oxygen hyperstoichiometry (overstoichiometric). One of the examples for oxygen-deficient perovskite is $La_2Ni_2O_5$ (or $LaNiO_{2.5}$) , which is also known as having browmillerite compounds consisting of one octahedral layer alternating with one tetrahedral layer along b-axis, in which Ni exhibits +2 oxidation state [117]. Later, Moriga *et al.* [118] reduced $LaNiO_3$ to $LaNiO_{3-\lambda}$ using controlled amounts of Al^0 under vacuum environment. By analyzing magnetic susceptibility of $LaNiO_{3-\lambda}$ with temperature, they suggested that $LaNiO_{2.5}$ structure is comprised of $Ni^{3+}O_6$ octahedral and $Ni^{+}O_4$ square planar without the existence of Ni^{2+}.

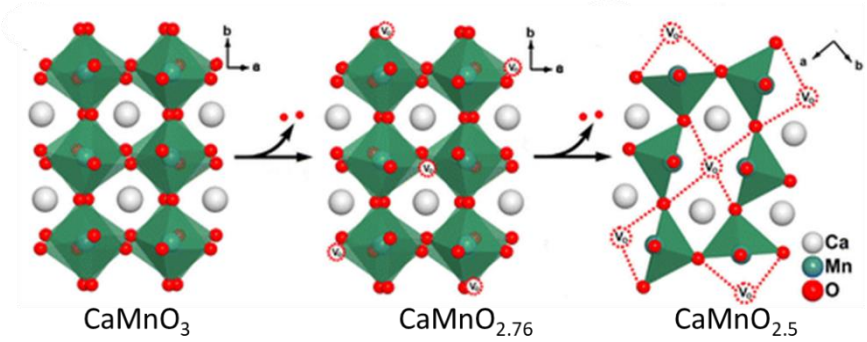

Figure 1.6 - Structural transition from $CaMnO_3$ to non-stoichiometric phases [119].

In another research, oxygen-deficient $Ca_2Mn_2O_5$ (or $CaMnO_{2.5}$) [120] can be obtained by reducing $CaMnO_3$ with hydrogen, this process occurs with the transformation Mn^{4+} to Mn^{3+}. Missing one oxygen at apex site causes some inner cell distortions, converting MnO_6 octahedral to square pyramids MnO_5 connected each other in a zigzag structure. The phase transformation of $CaMnO_3$ to $CaMnO_{2.5}$ was discussed in a study of J. Du *et al.* [119] (Fig.1.6), suggesting that cell expansion goes with increasing oxygen nonstoichiometry due to the more presence of larger Mn^{3+}. In the $CaMnO_{3-\lambda}$ the framework of the perovskite structure is essentially preserved for oxides with $\lambda < 0.5$ regardless of the elimination of some oxygen atoms.

Oxygen excess nonstoichiometric (or hyperstoichiometric) perovskite oxides are less common probably because the introduction of interstitial oxygen in perovskite structure is thermodynamically unfavorable [6]. In a study of Tofield and colleagues [121], $LaMnO_{3+\delta}$ is investigated for oxidative non-stoichiometry. $LaMnO_{3.12}$ was synthesized by annealing oxides at high temperature under air, and neutron diffraction study reveals that oxygen hyperstoichiometry is accommodated with cation vacancies, and the non-stoichiometry can also be achieved by partial substitution at A site as in case of $Ba_{0.8}La_{0.2}TiO_{3.1}$ [121]. In the $LaMnO_{3+\delta}$ the oxygen content δ increases with the synthesis temperature, and crystal structure is transformed from orthorhombic to hexagonal with δ [73]. Regarding excess oxygen quantification in $La_{2-x}Sr_xNiO_{4+\delta}$ [122], the quantity can be determined by iodometric titration assuming that oxygen excess is compensated by the presence Ni^{3+} in the perovskite structure, which is reduced to Ni^{2+} by I^{2-}. An alternative approach is a thermogravimetric analysis under reducing environment (H_2/Ar), taking into account the conversion of excess oxygen to water by H_2. The results of the two methods are considerably consistent and the Ni^{3+} is maintained.

1.3.2 Redox properties

Perovskite solids largely find applications in catalytic processes due to their intrinsic redox properties. It has been found that the catalytic activities of $LnBO_3$ (Ln = rare-earth metals) mainly depend on B elements properties and the role of trivalent A-site is not tremendous [50]. In a study on the stability of $LaBO_3$ (B = V, Cr, Mn, Fe, Co, and Ni) in reducing atmosphere in an isothermal mode, the order of the stability of theses perovskite oxides is $LaCrO_3$, $LaVO_3$ > $LaFeO_3$ > $LaMnO_3$ > $LaCoO_3$ > $LaNiO_3$ [123]. The reducibility of perovskite oxides is normally investigated by H_2 temperature program reduction (H_2-TPR). For example, the reduction of Co^{3+} in $LaCoO_3$ by H_2-TPR was generally proposed by two different pathways. In the former route, Co^{3+} is converted to Co^0 via Co^{2+} at two distinguished temperature regions at around 420 °C for Co^{3+} to Co^{2+} and 550 °C for Co^{2+} to Co^0 with the formation of intermediate brownmillerite $LaCoO_{2.5}$ [20,124–128]. This mechanism regarded as two-process mechanism should be confirmed by the area ratio of the first peak to the second one of 1:2 [123]. However, the H_2 consumption at high-temperature reduction region is usually found lower than expected [70,126,129], suggesting that Co^0 might be formed at low temperature in the first stage [126,130]. Alternatively, the Co^{3+} reduction was also proposed as one-step mechanism, in which Co^0 can be produced directly from Co^{3+} with the formation of oxygen-deficient compound $LaCoO_{3-y}$, bypassing the Co^{2+} species [130], and the splitting figure of H_2-TPR profile can be attributed to differently structural Co^{3+} species related to the distortion of perovskite structure and the oxygen defect [131]. In addition, Irusta *et al.* studied reducibility of $LaCoO_3$ calcined at different temperatures [28]. $LaCoO_3$ exhibits three reduction peaks, and peak at the lowest temperature, 242 °C can be assigned to the reduction of perovskite microcrystals. The middle peak at 395 °C is associated to reduction of Co^{3+} to both intermediate phase $LaCoO_{3-x}$ and Co^0. Finally, the peak at 550 °C for complete reduction to Co^0. The reduction peaks consistently are shifted towards higher temperatures as the calcination temperature is increased. This is because of sintering process at high calcination temperature, which decreases the surface area and increases mean crystal size. The increasing diffusional resistance displaces the reduction peaks towards higher temperatures [28].

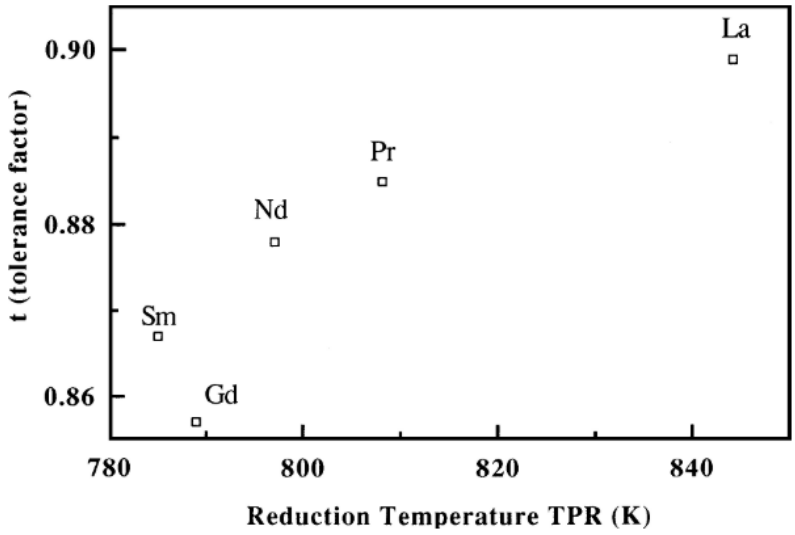

Figure 1. 7 - Goldschmidt's tolerance factor t and reduction temperature obtained from temperature-programmed reduction experiments for the $LnCoO_3$ perovskites [132].

Redox properties of perovskite oxides can be modified by A-site substitutions. Different lanthanides have been used in order to study the effect of the rare earth support on the reducibility of $LnCoO_3$ [132]. Lago *et al.* [132] suggested the larger rare-earth cations (La^{3+} >Pr^{3+}>Nd^{3+}>Sm^{3+}>Gd^{3+}) form more stable perovskite structure due to the Goldsmith tolerance factor closer to unity, resulting in the harder reducibility (Fig. 1.7). The partial replacement of La^{3+} by smaller Sr^{2+} in $LaCoO_3$ to give gives a less crystalline structure which is easier to be reduced [28]. Moreover, the incorporation of Sr^{2+} in $LaCoO_3$ favors the formation of unstable Co^{4+}, together with oxygen vacancies for charge compensation, causing the structure less stable [50,128].

According to a work of Resende *et al.* [19], $LaNiO_3$ perovskite oxide has two reduction peaks at around 420 °C and 600 °C, the first peak can be assigned to Ni^{3+} to Ni^{2+} with the formation of $LaNiO_{2.5}$, and the second peak is associated to Ni^{2+} to Ni^0 . However, in another study [15], $LaNiO_3$ is able to be reduced at lower temperatures, at 375 and 560 °C, and the lower temperature peak with the shoulder at 300 °C is assigned to the reduction of $LaNiO_3$ to $La_4Ni_3O_{10}$. The peak at 375 °C corresponds to the formation of Ni^{2+} in La_2NiO_4, while the latter peak is associated to the reduction La_2NiO_4 to Ni^0 [15,133]. The effect of A-site substitution on the reducibility of Ni-based perovskite was studied on Sr-doped $LnNiO_3$ (Ln = Pr, Sm, Eu) [134]. Small Sr^{2+} doping shifts the reduction peaks towards lower temperature as it can be seen for Co-based perovskites. Similarly, the additions of Pr and Sm to $LaNiO_3$ have the same effects [19]. However, substitution by Sr and Sm increases

the presence of dispersed NiO, leading to more H_2 consumption at high-temperature reduction zone.

For the $LaFeO_3$ perovskite, it is generally accepted that there are two reduction peaks through the whole temperature range. Below 400 °C, it is the reduction of Fe^{4+} to Fe^{3+} and the reduction peak above 700 °C is attributed to Fe^{3+} to Fe^0 [135]. However, according to Barbero *et al.* [136], the reduction of Fe in $LaFeO_3$ is followed by the sequence: $Fe^{4+} \rightarrow Fe^{4+/3+} \rightarrow Fe^{3+}$, where peak at 255 °C is assigned for Fe^{4+} reduction and peak at 385 °C for the latter. Doping divalent Ca^{2+} at A-site increases the amount of Fe^{4+} due to electroneutrality, leading to intensifying the first peak. In a study of Fang and colleagues [33], $LaFeO_3$ exhibits no clear reduction peak, doping K in $La_{1-x}K_xFeO_3$ results in appearance multiple peaks at low-temperature zone 290 – 525 °C, suggesting the formation of Fe^{4+} upon doping, which can be reduced to lower oxidation states. Nevertheless, H_2-TPR profiles of $LaFeO_3$ show extremely weak reduction peaks or no peaks in many articles [7,33,70,136 137] , suggesting that Fe forms strong interaction with La_2O_3 in perovskite structures or the presence of Fe^{4+} in the structure is minor. Similarly, Izadkhah *et al.* [138] observed a reduction region 400 – 700 °C corresponding to $Fe^{4+} \rightarrow Fe^{3+}$ in $LaFeO_3$, and there is no reduction at higher temperature up to about 1000 °C.

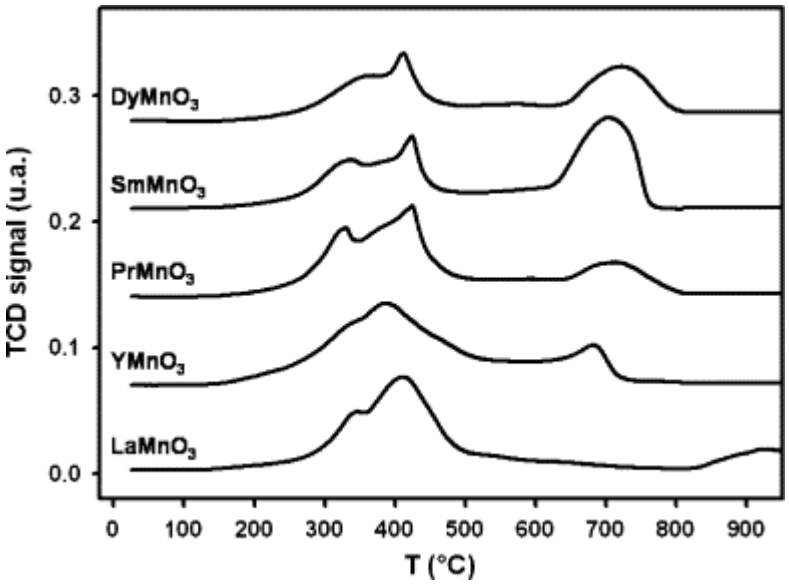

Figure 1.8 – H_2 – TPR profiles of $AMnO_3$ perovskites [139].

Mn-based perovskite oxides have two-step reduction mechanism which has been reported elsewhere [50,70]. The first low-temperature reduction peak (200 – 600 °C) can be related to the reduction $Mn^{4+} \rightarrow Mn^{3+}$, and the second peak (600 – 950 °C) can be assigned to Mn^{3+}

to Mn^{2+} [138] (Fig.1.8). It is well-known that the total reduction of Mn^{4+} into Mn^{0} over $LaMnO_3$ does not occur [140]. The shoulder at a low-temperature reduction peak can be observed in many reports, which can be assigned to the oxidation of overstoichiometric oxygen, accommodated within perovskite frameworks [50,141,142]. Sr^{2+} doping in manganese-based perovskites can result in significant differences in redox properties since doping promotes the presence of Mn^{4+} to compensate the charge imbalance [24]. As expected, an increase in Sr^{2+} in $LaMnO_3$ causes a rise in H_2 consumption of the low-temperature peak which is associated with Mn^{4+} [24]. The peak (or shoulder) placed at slightly lower temperatures, which is intense unsubstituted $LaMnO_3$ sample [143]. The partial replacement of La by Sr ($La_{0.8}Sr_{0.2}CoO_{3-\delta}$) gives a less crystalline structure which is easier to reduced [28]. The influence of A-site of $AMnO_3$ (A=Y, La, Pr, Sm, Dy) on redox properties is studied by Kaliaguine and Levasseur [139]. It can be seen in Fig.1.8, the TPR profiles of $AMnO_3$ reveals the reduction in two steps both at low and high temperature related to $Mn^{4+} \rightarrow Mn^{3+}$ and $Mn^{3+} \rightarrow Mn^{2+}$ except the case of $LaMnO_3$ with incomplete reduction. The temperatures for Mn^{4+} to Mn^{3+} were in order Pr > Sm > La > Dy > Y, and for Mn^{3+} to Mn^{2+} were La > Dy > Pr > Sm > Y which similar to $ACoO_3$ system [132]. In other research on $AMnO_3$ (A = La, Sm, Nd), the two-step reduction is also recorded and the reduction temperature decreases in order: Sm > La > Nd [144].

1.3.3 Oxygen mobility

The oxygen mobility of perovskite oxides is mainly characterized by O_2 temperature desorption (O_2-TPD) experiments and isotopic oxygen exchange analysis [50]. It is generally accepted that perovskite $LaCoO_3$ exhibits two types of desorbed oxygen. The α-oxygen which is desorbed below 750 °C usually ascribed to oxygen weakly bound to perovskite surface. β-oxygen desorbed above 750 °C is designated to lattice oxygen diffused from bulk, which is considered as an indicator of O_2 mobility in the structure [125,129,145,146]. The latter species can come from the inner bulk oxygen vacancies or can be directly associated with the B-site cation reduction in the perovskite oxide frameworks [127], and the evolution of which is a result of Co^{3+} to Co^{2+} reduction and anion vacancy generation in case of $LaCo_{1-x}Cu_xO_3$ [145]. Moreover, it should be noticed that Royer *et al.* [37] suggested that β-oxygen is likely to originate from grain boundaries between two neighbor crystal domains due to higher oxygen diffusibility within boundaries than the bulk, and the feature is significantly enhanced by substituting 20 % of Co by Fe to form $LaCo_{0.8}Fe_{0.2}O_3$ [37].

Partial substitution of La^{3+} by Sr^{2+} in $LaCoO_3$ also results in an increase of the amount of desorbed oxygen [147] . For the $La_{1-x}Sr_xCoO_3$, three main desorption peaks can be observed: physical adsorption oxygen (below 450 °C), chemical adsorbed oxygen (450−700 °C), and lattice oxygen (above 700 °C). It is reported that an increase in Sr^{2+} amounts results in a rise of the quantity of chemical adsorbed oxygen, which is explained that substitution of La^{3+} by Sr^{2+} may generate oxygen vacancies, supporting the mobility of oxygen within the perovskite structure. Previously, Nitadori *et al.* [148] studied $La_{1-x}Ce_xCoO_3$, showing that Ce^{4+} substitution enhances the O_2 desorption at about 300 °C which may be related to excess oxygen in nonstoichiometric perovskite, similar to the H_2-TPR figure. Influence of divalent A-site on $ACoO_{3-\delta}$ (A = Ba, Sr, Ca, Mg) on oxygen mobility is investigated by Shen *et al.* [149]. The quantities of desorbed oxygen at 850 °C is in order: Ba > Sr > Ca > Mg, which is in accordance with ionic radii: Ba (1.75 Å) > Sr (1.58 Å) > Ca (1.48 Å) > Mg (1.03 Å). It is believed that larger A-ions results in more stability of perovskite structure, an increase in lattice volume leading to a contribution of the mobility of oxygen ions in the crystal. The effect of B site is also studied over $BaBO_{3-\delta}$ (B = Co, Cr, Cu, Fe, Mn, Ni, Zn, Zr) by the same group [149]. Among the transition metals, $BaCoO_{3-\delta}$ has the best oxygen desorption performance.

On a study on $La_{1-x}Ca_xFeO_3$ perovskite oxide [136], $LaFeO_3$ shows a broad desorption O_2 peak between 150 and 350 °C (max at 219 °C) which is generally assigned to oxygen adsorbed on surface vacancies, and the peak shifts towards higher temperatures with more Ca^{2+}. The quantity of desorption increases with Ca amount and the formation of Fe^{4+} [136]. This observation suggests that α-O_2 cannot be ascribed only to the surface oxygen species which can be similarly obtained by Ferri *et al.* [150] and Nitadori *et al.* [148] over $LaFeO_3$ but also associated with the nature of A sites. In another study [151], $LaFeO_3$ also exhibits β-O_2 desorption above 700 °C which is attributed to oxygen liberated from the lattice with Fe reduction. Doping divalent Pd^{2+} and Cu^{2+} at B site promotes the formation of Fe^{4+} in perovskite lattice, resulting in more β-O_2 evolution at high temperature [151].

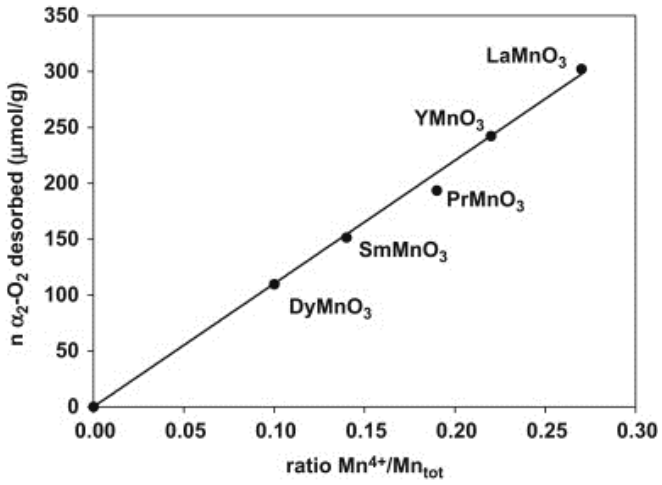

Figure 1.9 – Correlation between α_2 -oxygen desorbed and the amount of Mn^{4+} in the $AMnO_4$ perovskite structure [139].

On the other hand, the increasing presence of Mn^{4+} in Mn-based perovskite oxides enhance the O_2 desorption at low temperature. According to a study on $AMnO_3$ (A = Y, La, Pr, Sm, Dy) [139], the α-O_2 can be divided into two subgroups: low temperature desorbing (α_1 under 500 °C) is associated with surface oxygen and higher temperature desorbed species (α_2 between 630-680 °C) can be attributed to the amount of overstoichiometric oxygen induced by the presence of Mn^{4+} (Fig.1.9) . The quantities of desorbed α_2-O_2 and β-O_2 oxygen are in order: La > Y > Pr > Sm > Dy, which is in accordance with the effects of these elements on reducibility (Fig.1.7). The quantities increase with the size of ionic radii, showing that larger A-site cations enhance the stability of perovskite structure and thus more oxygen mobility. The authors also showed that the evolved α_2-O_2 is directly related to the Mn^{4+} presence which is evidence by H_2 consumption at low temperature (333-367 °C), and the temperature desorption of the α_2-O_2 seems to be closely related to the nature of the A-site cation sand particularly to its electronegativity but also to its density.

In a study on $La_{1-x}Sr_xNiO_3$, García de la Cruz *et al.* [152] showed that there is no O_2-desorprtion until about 600 °C over Ni-based perovskite probably due to low surface area, and O_2-desorption peak with a maximum around 787 °C and a low-temperature shoulder at ca. 627 °C is observed. The partial replacement of La^{3+} by Sr^{2+} up to x = 0.1 alters the oxide stoichiometry and oxygen vacancies. In addition, this substitution also intensifies the O_2-desorption peaks and shifts the desorption towards higher temperature. The influence of B-site substitution on $LaNi_{0.5}B_{0.5}O_3$ oxygen mobility has been investigated [153]. Doping Cu^{2+} induces more defects, thus increases surface chemisorbed oxygen

concentration, and then it follows the order: $Cu^{2+} > Ni^{3+} > Co^{3+} > Mn^{3+}$. By O_2 – TPD, doping Co and Cu facilities to the desorption of chemisorbed oxygen species on the surface of the catalysts; while the temperature of desorption peaks increases after doping by Mn and their areas decrease, which may be due to the strong interaction between Mn-O bonds making it more difficult for oxygen species to be desorbed.

The oxygen isotopic exchange $^{16}O/^{18}O$ reaction has also used to study the oxygen mobility of perovskite oxides. Briefly, the isotopic exchange between $^{18}O_2$ in the gas phase and ^{16}O in the solids follows steps: (i) dissociative adsorption of oxygen with a formation of adsorbed atom or ions, (ii) exchange with the adsorbed species with ^{16}O from solids, and (iii) desorption of the exchanged molecules [50]. Nakamura *et al.* [154] early investigated the effects of Sr-substituting $La_{1-x}Sr_xCoO_3$ (x=0, 0.2, 0.4) perovskite oxides on oxygen mobility by $^{16}O/^{18}O$ isotopic exchange at different temperatures [154]. At 150 °C, the isotopic exchange rates, which are determined based on ^{18}O concentration in the gas phase, are not affected for low Sr substitution (for x =0, 0.2), but with x =0.6 the rate increases by almost 30 times. At high temperature (300 °C), even low Sr-substitution can lead to a significant difference in the isotopic exchange rate which increases 9 times from x=0 to x =0.2. Moreover, the equilibration ($^{16}O/^{18}O$ exchange in the gas phase) is much more rapid at samples with Sr doping. The equilibration is supported by surface oxygen defect, and more surface vacancy is created with Sr substitution. The authors concluded that the acceleration of the isotopic exchange reaction by the Sr^{2+} may be due to the increase in oxygen diffusion rate from the bulk. This is due to the formation of unstable Co^{4+} when Sr^{2+} doping, and Co^{4+} changes Co^{3+} when oxygen is desorbed and oxygen vacancy is formed. As vacancy increases the diffusion of lattice oxygen from bulk to surface easier. Similar findings have been reported recently by Sang Ok Choi *et al.* [155]. The $LaCoO_3$ has desorption peaks at about 194, 355 and 558 °C (Fig.1.10). The low-temperature peak is attributed by oxygen exchanged with surface oxygen, and the higher peaks are from subsurface or grain boundary species. With Sr-substitution, the peaks shifted to lower temperatures indicating that oxygen exchange is enhanced by Sr-substitution. Given that the oxygen exchange rates are proportional to the slope, exchange rates for x= 0.1 and 0.3 were higher than that for the $LaCoO_3$ catalyst.

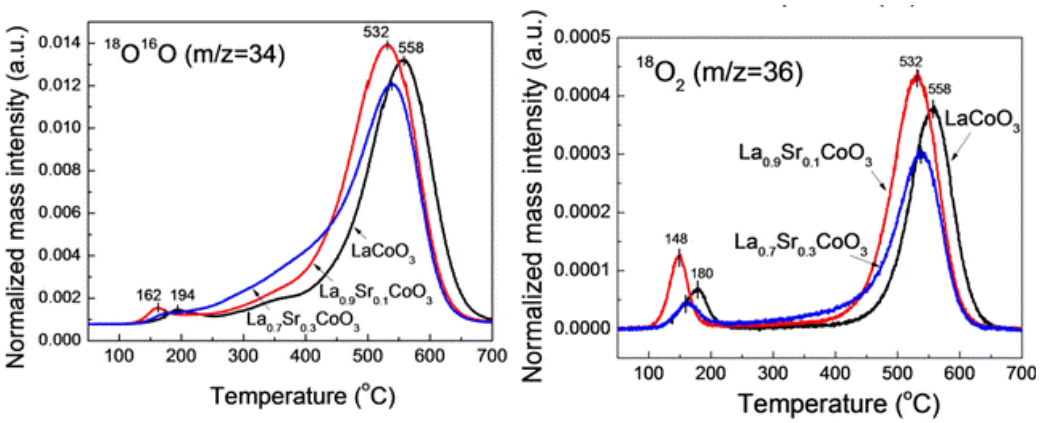

Figure 1.10 - Changes in the (left) ($^{18}O^{16}O$) and (right) ($^{18}O2$) signals for $La_{1-x}Sr_xCoO_3$ catalysts pretreated with 1% $^{18}O_2$ at 500 °C for 1 h as a function of temperature [155].

Similar results were reported for Sr-doping $La_{1-x}A_xFeO_3$ (x = 0 – 0.6) by Nitadori *et al.* [148]. The isotopic equilibrium and exchange are significantly more rapid when x increases from 0 to 0.2 indicating that the formation of oxygen vacancies and desorption of lattice oxygen is promoted with low Sr-substitution. The author supposed that the partial replacement of La^{3+} by Sr^{2+} generates unstable Fe^{4+} which is reduced to Fe^{3+} when the oxygen leaves. However, $x \geq 0.4$, although the oxygen desorption in TPD increases remarkably with x, the isotopic equilibration proceeds very slowly probably due to the dissociation of oxygen molecules, limiting the isotopic exchange. Moreover, the substitution of La^{3+} by Ce^{4+} induces the partial reduction of Fe^{3+} to Fe^{2+} and thus lowers the equilibration and the exchange over $La_{0.9}Ce_{0.1}FeO_3$.

For the $La_{1-x}Sr_xMnO_3$ (x = 0, 0.2, 0.6, 1) [156], the rate of isotopic equilibration is maximum for x = 0.6, and the isotopic exchange at 300 °C is proceeded slowly for all samples. The exchange seems to be limited to oxygen monolayer at the surface. The effects of Sr-substitution of $LaMnO_3$ varies in the study. However, in the case of $La_{1-x}Ce_xMnO_3$, the exchange rates remarkable increase with x, which results in 3 and 16 layers of oxygen exchanged after 1 h for x = 1 and 4 respectively. This effect is supposed to originate from the formation of cation vacancies at A-site upon substitution. The superior lattice oxygen diffusion and surface exchange of Ce^{4+} over Sr^{2+} substitution of $La_{1-x}A_xMnO_3$ were also reported by Kuritsyna *et al.* [157]. The authors also suggested that this behavior may be affected by metal-oxygen bonding in the perovskite structure.

1.3.4 Acido-basic Properties

Because of well-known redox properties, perovskites have been widely used to catalyze the electron-transfer reactions such as oxidation and reduction, and the knowledge on their acid−base properties is limited. For the characterization of acido-basic properties, researchers have investigated the interaction between probed molecules and perovskite surface to have information about the density, strength, and type of adsorption sites by multiple techniques such as micro-calorimetric measurements, FTIR for the adsorptions of CO_2/NH_3/Pyridine or temperature desorption of these molecules. Another approach is probed reaction such as the conversion of 2-propanol to propylene and acetone depending on acidity-basicity of the catalysts. 2-propanol can be dehydrated to form propylene and water on an acid site, it can also be dehydrogenated to form acetone and hydrogen on a base site. Accordingly, the ratio of selectivities of acetone and propylene can be used to estimate the base-to-acid ratio of each catalyst [158–161].

Most recently, Xiao *et al.* [162] evaluated the acido -basic properties of $LaFeO_3$, synthesized by carbon template and conventional sol-gel method, by NH_3 –TPD and CO_2-TPD experiments (Fig.1.11). $LaFeO_3$ prepared by carbon templating route exhibits porous structure with textural properties (S_{BET} = 38.7 m^2 g^{-1}, Vpore = 0.12 cm^3 g^{-1}, D_{pore} = 12.5 nm) better than sol-gel $LaFeO_3$ ((S_{BET} = 21.3 m^2 g^{-1}, Vpore = 0.07 cm^3 g^{-1}, D_{pore} = 11.7 nm). The higher ammonia and carbon dioxide yields are observed with the porous $LaFeO_3$ and the desorption is seen to occur at higher temperatures. This indicates that the $LaFeO_3$ synthesized by carbon template method has both stronger acid and basic sites than its rival. The authors suggested that the NH_3 desorption takes place from the acidic metal cations: La^{3+} and Fe^{4+}/Fe^{3+}, and CO_2 is adsorbed on surface oxygen vacancies. The presence of stronger acid and basic sites leads to enhanced performance on hydrogenation of furfural by 2-isopropanol as a hydrogen donor.

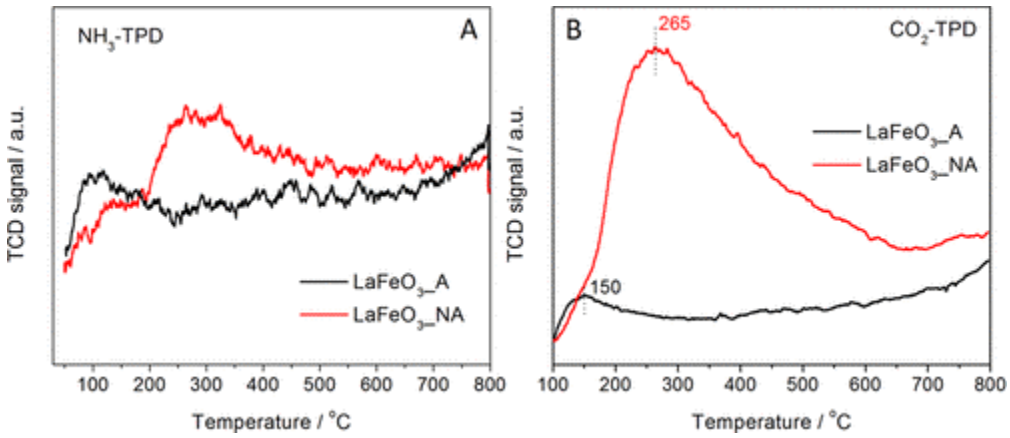

Figure 1.11 - NH_3-TPD (A) and CO_2-TPD (B) results from $LaFeO_3$ prepared by carbon templating ($LaFeO_3$_NA) and sol – gel ($LaFeO_3$_A) method [162].

On the study of CH_3OH – TPD over $La_{0.8}Co_{0.2}Fe_{1-x}Co_xO_3$ (x = 0.1, 0.2, 0.3) [163], methanol adsorbed at low temperature on the Lewis basic sites which is independent on Co substitution. The adsorbed methanol species on Lewis sites are assigned by in IR bands in 2951 and 2845 cm^{-1}. At higher 150 °C, these bands disappear, and a new band at 2350 cm^{-1} assigned to CO_2 appears since under experimental conditions CH_3OH is converted to CO_2 by taking lattice oxygen from the solid. The CO_2 temperature remains unchanged with different Co substitution whereas its amount varies not linearly with Co compositions. However, the nature of these basic sites is not covered in the study. Moreover, Natile *et al.* [164] reported the study of CO oxidation of $LaCoO_3$ monitored by diffuse reflectance infrared Fourier transform spectroscopy (DRIFT) [164]. A significant signal around 2058 cm^{-1} is assigned the interaction of CO with the Lewis acidic sites at room temperature. At higher than 150 °C, the CO contribution disappears and new bands in the region 2280 - 2400 cm^{-1} are assigned to CO_2, which can be linked to monodentate carbonates [6].

The basicity of $LaMnO_{3+\delta}$ perovskite is investigated by interactions between CO_2 and oxide surface using means of density functional theory calculation [165]. The authors claimed that (i) MnO_2 -terminated surfaces that are not enough basic to allow strong adsorption, (ii) two main anionic active sites are oxygen-deficient sites and surface oxygen; (iii) adsorption on cationic sites (La and Mn) leads to weakly adsorbed species. In a study of the influence of A-site on the basicity of $AMnO_3$ (A = Y, La, Pr, Sm, Dy) [139], CO_2-TPD profile of $LaMnO_3$ shows a signal of CO_2 at ~ 300 °C, whereas desorption peaks are located at around 230 °C for other samples (Fig.1.12). According to the temperature desorption of the first peak, the strength of basic properties is in order: La > Pr, Sm > Dy, Y. The authors proposed that

the difference in electronegativity between A and Mn^{n+} results in various polarity between Mn^{n+}- O^- bonding, and CO_2 is adsorbed in monodentate carbonate form. CO_2 desorption at high temperature seems to be associated with bidentate carbonates species.

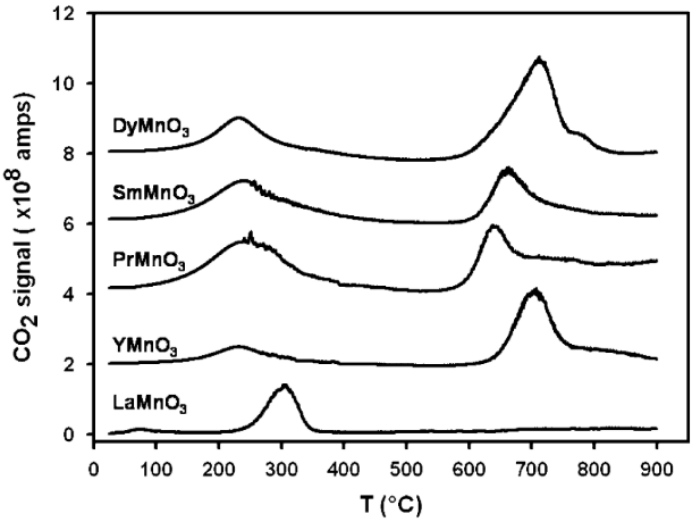

Figure 1.12 - CO_2-TPD of $AMnO_3$ [139].

The adsorption microcalorimetry is used to probe the concentration and strength of acid and base sites on perovskite oxides (Ba, Sr)(Ti,Zr)O_3 (Fig.1.13) [166]. Titanate perovskites have higher heat adsorption NH_3 than Zr samples, and Zr-based perovskites possess higher CO_2 heat adsorption up to a surface coverage of ~ 2 μmol m^{-2}. Among the samples, $SrTiO_3$ has the highest surface density of both acid and base sites, and all of the perovskite surfaces are dominated with base sites. Regarding the nature of acid sites, FTIR pyridine indicates that these sites belong to Lewis acid sites, and there are no apparent Brønsted acid sites present on these perovskite catalysts. Moreover, the FTIR of CO_2 adsorption shows that basic surface oxygen atoms are exposed on the surface by the formation of both bidentate and unidentate carbonates. There is no basic hydroxyl group by the absence of bicarbonate species. In term of isopropanol conversion over (Ba, Sr)(Ti,Zr)O_3 [166], propene and acetone are the major products, and the selectivity to acetone is higher than 70 % for each perovskite. This means that the reaction is more selective to dehydrogenation over dehydration. The authors concluded that the perovskite surfaces are dominated with intermediate and strong basic sites with the presence if some weak Lewis acid sites, due to the preferred exposure of SrO/BaO on the perovskite surfaces.

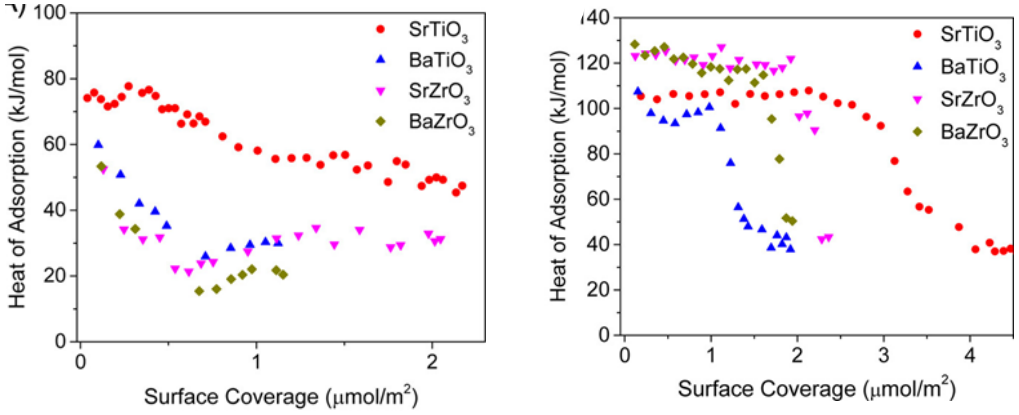

Figure 1. 13- Heat of adsorption of (left) NH_3 and (right) CO_2 on perovskite catalysts [166].

1.4 CATALYTIC APPLICATIONS

1.4.1 Perovskite catalysts for oxidation reactions

1.4.1.1 CO oxidation

Perovskite catalysts with the tunability of the valence states of B-sites are generally active for oxidation reactions. $LnBO_3$ series (Ln is a lanthanide and B is Co, Ni, Fe and Mn) are the most active perovskites for the CO oxidation [50]. For perovskite oxides, CO oxidation is considered as a model reaction for the suprafacial mechanism which occurs at low temperatures because the oxidation involves surface oxygen species which reacts with CO leaving oxygen anion vacancy at the perovskite surface.

Over $LaCoO_3$ synthesized by sol-gel with ethylene glycol and acid citric, CO oxidation starts above 70 °C and finishes below 200 °C [167]. Differences in oxidation activities between Co_3O_4 and $LaCoO_3$ are related to the arrangement of octahedrally coordinated Co^{3+} in a study of Ngamou *et al.* [168]. In $LaCoO_3$, Co^{3+} sites are interconnected through their vertex sharing one O^{2-} anion, whereas they are interconnected through their edges sharing two O^{2-} in Co_3O_4. The presence of Co^{4+} as an electron acceptor in the octahedral site of $LaCoO_3$ is expected to promote the oxygen adsorption at the perovskite surface. The CO oxidation over $LaCoO_3$ outperforms that of spinel is explained that the oxidation follows the suprafacial mechanism where the adsorbed oxygen allows the total CO oxidation. Addition divalent Sr^{2+} in $La_{1-x}Sr_xCoO_3$ perovskites enhances the presence of Co^{4+}, thus increases the catalytic performances in CO oxidation [169,170]. Isupova *et al.* [168] reported that with x = 0.3 and 0.8 the $La_{1-x}Sr_xCoO_3$ shows the best activity, while Borovskikh *et al.* [169] indicated that the catalytic activity increases with x and reaches the maximum with x = 0.5.

Doping Sr^{2+} in $LaCoO_3$ results in octahedral distortion, and closer structure to cubic, the easier is electron exchange between Co^{4+} and Co^{3+} through the p-orbital of oxygen [169], promoting the ability to adsorb the oxygen species. In another research, Magalhães *et al.* [171] substituted Ce^{4+} into the A site of $LaCoO_3$, which favors the oxygen vacancies and O^{2-} storage and hence enhances the selective CO oxidation reaction. Yan *et al.* [172] studied a series of B site substitutions over $LaCoO_3$ perovskite and showed that the doping of divalent Mn^{2+},Fe^{2+},Ni^{2+},Cu^{2+} could result in an enhancement in CO oxidation whereas that of Cr^{2+} deteriorates the performance.

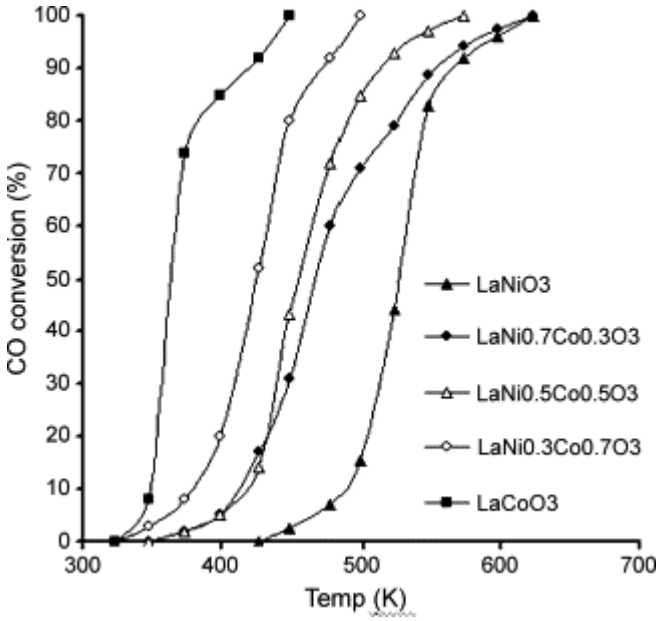

Figure 1.14 - CO conversion as a function of catalyst temperature [173].

$LaNiO_3$ is also studied for CO oxidation but less common than Co-base perovskites because of lower activity. It can be seen that substitution Co by Ni results in deterioration of catalytic performance in CO oxidation (Fig.1.14) [173]. However, in a study of Falcon *et al.* [174] on $LaNi_{1-x}Fe_xO_3$ for CO oxidation, the intrinsic activity for $LaNiO_3$ is higher than for $LaFeO_3$, and this is explained on the basis of the higher capability of Ni^{3+} ions to adsorb oxygen. The best CO oxidation activity is obtained with x=0.10 and x=0.50, which is related to the mixed valence states $Ni^{3+}$and Fe^{4+} generated in the solid solution. This cation mixture enhances the bonding with oxygen on the surface. The effects of A-substitution of $(Ln,Sr)NiO_3$ (Ln = Pr, Sm, Eu) on CO oxidation were investigated by the same authors [134]. $Pr_{0.95}Sr_{0.05}NiO_3$ has the highest activity, which is associated to the relative ease of oxygen removal and to the presence of oxygen vacancies.

Mn-based perovskites have been widely studied for oxidation reactions due to the flexible exchange Mn^{4+}/Mn^{3+} at B-sites [175,176]. The partial or total substitutions of Sr^{2+} for La^{3+} in $La_{1-x}Sr_xMnO_3$ leads to the formation of Mn^{4+}, positive holes or oxygen vacancies in the perovskite structures, enhancing the catalytic activity [177]. In a study on $La_{0.5}Sr_{0.5}CoO_3$ for CO and CH_4 oxidations by Liang *et al.* [177], the catalytic mechanism of CO oxidation is proposed that the adsorbed CO is oxidized by the lattice oxygen. Then, the chemisorbed oxygen is transformed into the lattice oxygen by MnO_6 octahedra to reinforce the consumed lattice oxygen. The authors compared the oxidation activity between cubes and nanoparticles $La_{0.5}Sr_{0.5}MnO_3$. O_2-TPD shows that Mn^{3+}/Mn^{4+} ratio is less in cubes than in nanoparticles, whereas Raman spectroscopy reveals that $Mn^{3+}O_6$ units give rise to Jahn-Teller distortion of the cubic structure, and $Mn^{4+}O_6$ octahedra have almost undistorted coordination. The better activity for nanoparticles is related to more distortion, generating more defects in the solid. The influence of B substitution of $LaMnO_3$ was investigated by Tarjomannejad *et al.* [178]. $LaMn_{0.7}Cu_{0.3}O_3$ perovskite shows the superior activity to Fe-doped perovskites (Fig.1.15), which is associated with reducibility at low temperatures, more oxygen vacancies and synergistic effect between Cu and Mn.

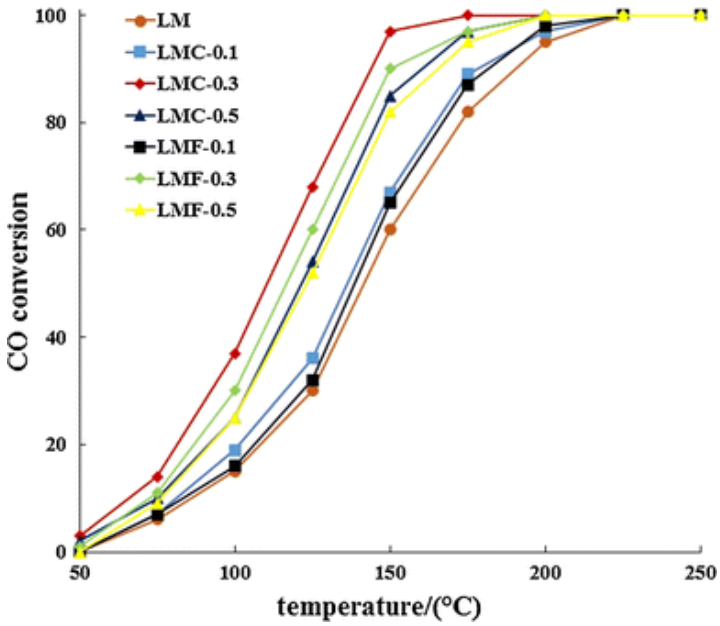

Figure 1.15 - CO oxidation over $LaMn_{1-x}B_xO_3$ (F=Fe; M=Mn; C=Cu) [178].

1.4.1.2 CH_4 oxidation

While CO oxidation reactions occur by the suprafacial mechanism (< 400 °C) involving surface oxygen species, CH_4 oxidation is reported to follow the intrafacial mechanism (>

400 °C) that is closely related to the amounts and mobility of surface lattice oxygen [35]. This mechanism also includes the migration of anion oxygen from the bulk to surface to fill the oxygen vacancies, so than all oxygen species can participate in the oxidation process [50].

Zhang *et al.* [179] studied methane oxidation over $LaCoO_3$ and $La_{0.9}Ca_{0.1}CoO_3$ to understand the role of Ca^{2+} substitution on the intrafacial reactions. It is showed that the substitution reduces the quantities of surface lattice oxygen and interior lattice oxygen and also has negative effects on reducibility. This substitution is not beneficial for methane oxidation in the study. Taguchi *et al.* [180] compared the effects of different substitutions (Ca^{2+}, Ba^{2+} and Sr^{2+}) at A site of $La_{1-x}A_xCoO_3$ (x=0.04 and 0.06). For x = 0.04, there is no difference between the samples, whilst x =0.06 the methane oxidation is in order $Ba^{2+} > Sr^{2+} > Ca^{2+}$ in line with the cation radii. The authors suggested that the difference in catalytic activity is linearly correlated with Co^{4+} content and O-Co-O angle in the octahedral, in agreement with another study on $La_{1-x}Nb_xCoO_3$ [181]. However, Gao and Wang [182] found that the Co^{4+} quantity is not the only factor for catalytic activity. They prepared a series of $La_{1-x}Sr_xCoO_3$ (x=0.0-0.3) by urea decomposition method. Perovskite with the highest substitution does not exhibit the best activity for methane oxidation, and catalytic performance of the oxides is in order of x = 0.1 > x = 0.2 > x = 0.0 and x = 0.3 which is not directly related to the amount of Co^{4+}, similar to a study of Forni *et al.* [150]. The authors showed that oxygen lattice vacancies and Co^{4+} increases with the degree of substitution. Lattice oxygen vacancy on the surface is to activate gaseous oxygen molecules into surface active oxygen species, and these species are able to oxidize methane. However, the authors suggested that activation process of gaseous oxygen on surface lattice oxygen vacancy would need electron transfer from neighboring cobalt ions at a lower oxidation state. Therefore, a compromise between Co^{3+} and Co^{4+} at the surface is decisive for the highest activity for $La_{0.9}Sr_{0.1}CoO_3$ [182].

Partial substitutions of La by Ce have been investigated in several articles [183–185], confirming that partial replacement leads to more active catalysts. According to Kirchnerova *et al.* [183], a significant improvement of activity with Ce substitution can only partially be explained by the formation of a defective perovskite structure permitting higher oxygen mobility. On the other hand, Bosomoiu *et al.* [184] synthesized $La_{0.9}Ce_{0.1}CoO_3$ by combustion method with α-alanine or urea fuels, yielding moderate surface areas. $La_{0.9}Ce_{0.1}CoO_3$ prepared by α-alanine has better activity than $LaCoO_3$, while the substitution of La with Ce prepared by urea method has not led to a significant increase of

catalytic activity. The reasons for difference in activity are supposed to textural properties of studied samples without mentioning the oxygen mobility. Machin *et al.* [185] studied Ce substitution of both La and Co in $La_xCe_yCo_{(2-x-y)}O_{3\pm\delta}$, showing that Ce doping at both A and B sites of perovskite gives better oxidation activity since $La_{0.1}Ce_{0.4}Co_{1.5}O_{3\pm\delta}$ and $La_{0.2}Ce_{0.3}Co_{1.5}O_{3\pm\delta}$ oxidize methane at lower temperatures than $La_{0.9}Ce_{0.1}CoO_3$.

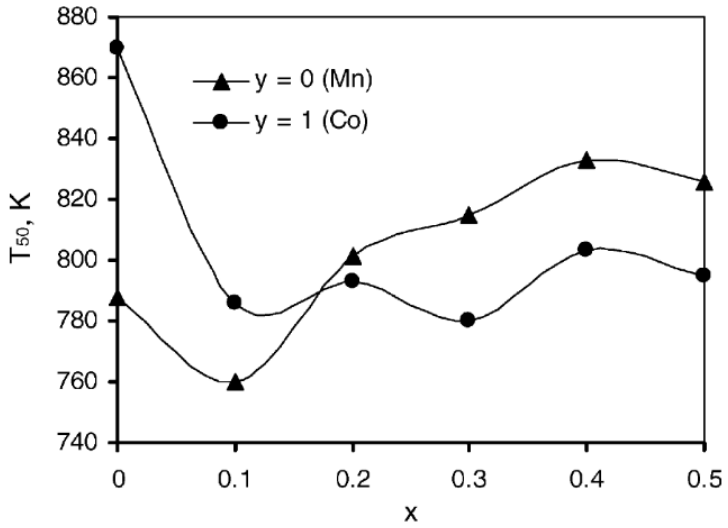

Figure 1.16 – Temperatures of 50 % of conversion of methane to CO_2 over $La_{1-x}Ce_xCoO_3$ and $La_{1-x}Ce_xMnO_3$ perovskites as a function of x [186].

Similar effects of substitution of B-site on catalytic performance can also be observed on a study by Alifanti *et al.* [186]. Coexistence of Mn and Co at B site in $La_{1-x}Ce_xMn_{1-y}Co_yO_3$ (x = 0.0, 0.1, 0.2, 0.3 and y = 0.3, 0.5, 0.7) does not improve the methane combustion performance compared to single substitution of $La_{1-x}Ce_xCoO_3$ and $La_{1-x}Ce_xMnO_3$. Moreover, partial substitution of Mn by Co significantly reduces the amount of β - oxygen (> 410 °C) which is generally reported as a responsible factor for the intrafacial reactions. However, $La_{0.8}Ce_{0.2}Co_{0.3}Mn_{0.7}O_3$ and $La_{0.7}Ce_{0.3}Co_{0.3}Mn_{0.7}O_3$ show higher quantities of β - oxygen than non-Co samples. The effects of Ce substitution on catalytic activity and textural properties are controversial. Ce substitution for La increases the amount of α-oxygen (< 410 °C) from 8.3 μmol g^{-1} for $LaMnO_3$ to 15.3, 38 and 48 μmol g^{-1} for $La_{0.9}Ce_{0.1}MnO_3$, $La_{0.8}Ce_{0.2}MnO_3$ and $La_{0.7}Ce_{0.3}MnO_3$ respectively, while significantly reduces the β - oxygen. For $La_{1-x}Ce_xCoO_3$, Ce doping increases both α-oxygen and β - oxygen. In the $La_{1-x}Ce_xBO_3$ (B =Mn and Co) sample, x = 0.4 is the most active catalyst (Fig.1.16). Further increase in the degree of substitution deteriorates the catalytic performance in both cases. The authors reported that no direct correlation between

physical characteristics of the mixed cobalt– manganese perovskites and their catalytic activity.

Substitution of La^{3+} by Sr^{2+} results in positive effects on catalytic activity not only for Co-based perovskites but also for Mn-based ones. By comparing two morphologies $La_{0.5}Sr_{0.5}MnO_3$: cubes and nanoparticles [177], the sample with higher β - oxygen desorption, referred to the reduction of Mn^{4+} ions to lower valences accompanied by the evolution of equivalent lattice oxygen, shows better catalytic activity on methane oxidation. The authors suggested the small degree of Jahn-Teller distortion of $La_{0.5}Sr_{0.5}MnO_3$ cubes results in the lower ratio of Mn^{3+}/Mn^{4+}, leading to lower O_2 desorption at a high temperature than that of nanoparticles. They also proposed that the oxidation of methane takes place by means of the adsorption and lattice oxygen from the catalyst, even in the presence of gaseous oxygen. The catalytic activities of $La_{0.5}Sr_{0.5}MnO_3$ catalysts are determined mainly by adsorbed oxygen and/or lattice oxygen.

1.4.1.3 Volatile Organic Compounds Elimination

Compared to CO and CH_4 oxidation, fewer investigations have been conducted for VOC (typically, aromatics) elimination over perovskite oxides. Spinicci *et al.* [187] studied the catalytic activity of two perovskites: $LaCoO_3$ and $LaMnO_3$ for total combustion of different types of VOCs: acetone, isopropanol, and benzene (Fig.1.17) [187]. The reactivity of VOCs towards oxidation is in order: acetone > isopropanol > benzene. In most cases, $LaMnO_3$ is more active than $LaCoO_3$ probably due to the higher surface area: 22 $m^2\ g^{-1}$ vs 15 $m^2\ g^{-1}$. Moreover, redox titration identifies the presence of Mn^{4+} (about 35 %) in $LaMnO_4$ resulting in the formation of cation vacancies which are able to adsorb gaseous oxygen species, whereas no Co^{4+} is detected. In another research, the substitution of Co by Mn improves the activity of isopropanol oxidation which is in order: $LaCoO_3$ < $LaCo_{0.9}Mn_{0.1}O_3$ < $LaCo_{0.5}Mn_{0.5}O_3$ < $LaCo_{0.75}Mn_{0.25}O_3$ [188]. The effects of B substitution in $LaCo_{0.5}B_{0.5}O_3$ (B = Mn, Cr, Cu) on toluene combustion is evident and the catalytic performances follow order: $LaMn_{0.5}Co_{0.5}O_3$ > $LaCr_{0.5}Co_{0.5}O_3$ > $LaCu_{0.5}Co_{0.5}O_3$ > $LaCoO_3$. However, there is no clear explanation in the study about the reason of the superior performance of dual Mn-Co-based perovskite over others [188]. The activity of $LaCoO_3$ for aromatics oxidation could be improved introducing supports. $LaCoO_3$ supported on $Ce_{1-x}Zr_xO_2$ (x = 0-0.3) samples were investigated for toluene and benzene oxidation by Alifanti *et al.* [189]. A small loading of $LaCoO_3$ (20 %) on $Ce_{0.9}Zr_{0.1}O_2$ leads to better activity due to (i) better dispersion at the

surface of ceria–zirconia solid solutions and (ii) the composition of the support that provides increased oxygen mobility.

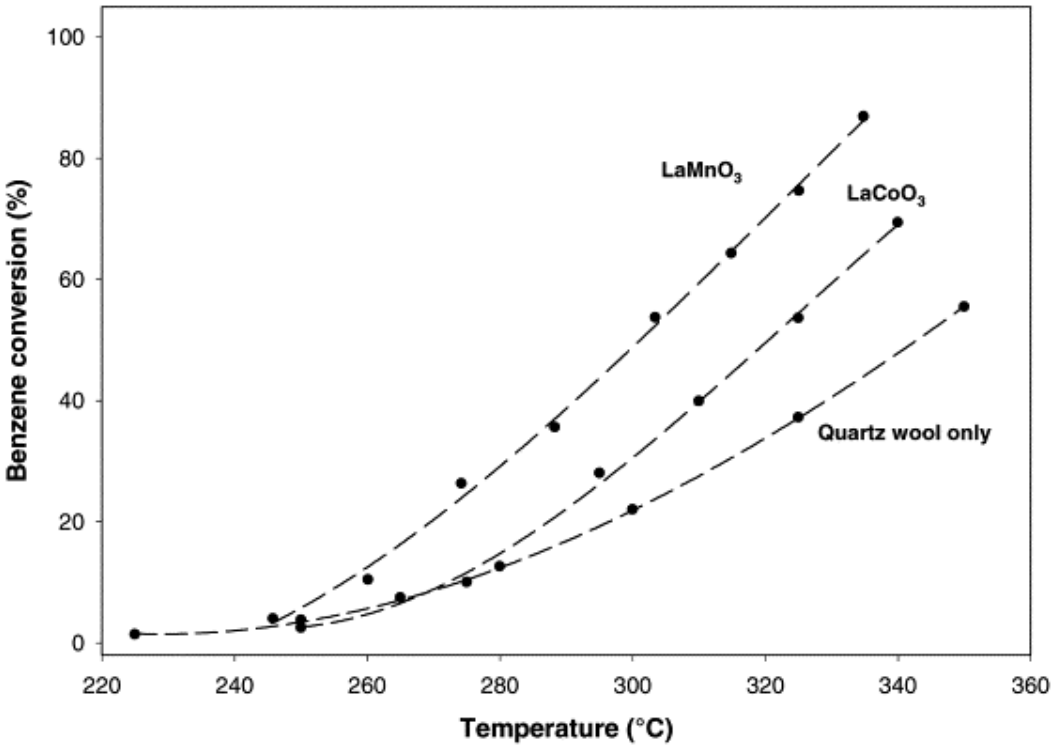

Figure 1.17 – Benzene combustion over $LaCoO_3$ and $LaMnO_3$ [187].

The effects of dual substitution of $La_{1-y}Ce_yCo_{1-x}Fe_xO_3$ (y = 0, 0.1 and x = 0, 0.2, 0.4, 1) were studied for VOCs (methanol, CO and CH_4) oxidations [190]. Ce allows an enhancement of the reducibility of the B-site cations in perovskite structure during H_2-TPR and an increase in the amount of β-O_2 desorbed during O_2-TPD while the addition of Fe in the perovskite structure causes a drop in reducibility and a decrease in the oxygen mobility in the bulk. Due to low temperatures at which CO and CH_3OH oxidations occur, the activity is found to be related to α-oxygen and the reducibility, whereas CH_4 combustion is linked to β-O_2. Consequently, the catalytic activity is enhanced by Ce and weakened by Fe additions. The influences of the co-existence of Fe and Ni in $LaFe_{1-y}Ni_yO_3$ (y=0, 0.1, 0.2 ,0.3 and 1) on catalytic performances of oxygenates (acetyl acetate and ethanol) combustion were investigated by Pecchi *et al.* [191]. All samples are prepared by citric acid method calcined at 700 C, and partial substitution of Fe by Ni results in a progressive decrease in the values of BET area. However, an increase in the reaction rate and parallel decrease in the ignition temperature of acetyl acetate and ethanol combustion was observed upon increasing the nickel substitution from 0 to 0.3.

1.4.1.4 NH_3 selective oxidation

Selective oxidation of NH_3 ($4NH_3 + 3O_2 = 2N_2 + 6H_2O$) to harmless N_2 over perovskite oxides has been widely studied for solving the problem of ammonia pollution. This reaction has been studied over different types of perovskites: manganites [192], colbatites [193] and ferrites [194]. Biausque *et al.* [193] conducted NH_3 oxidation over $LaCoO_3$ at high temperature (> 700 °C) to understand the reaction mechanism. $LaCoO_3$ yields good selectivity to NO and low selectivity to N_2O in the high- temperature oxidation of ammonia. The mechanism of the reaction is Mars and Van Krevelen, whereas the decomposition N_2O and NO leads to the formation of N_2.

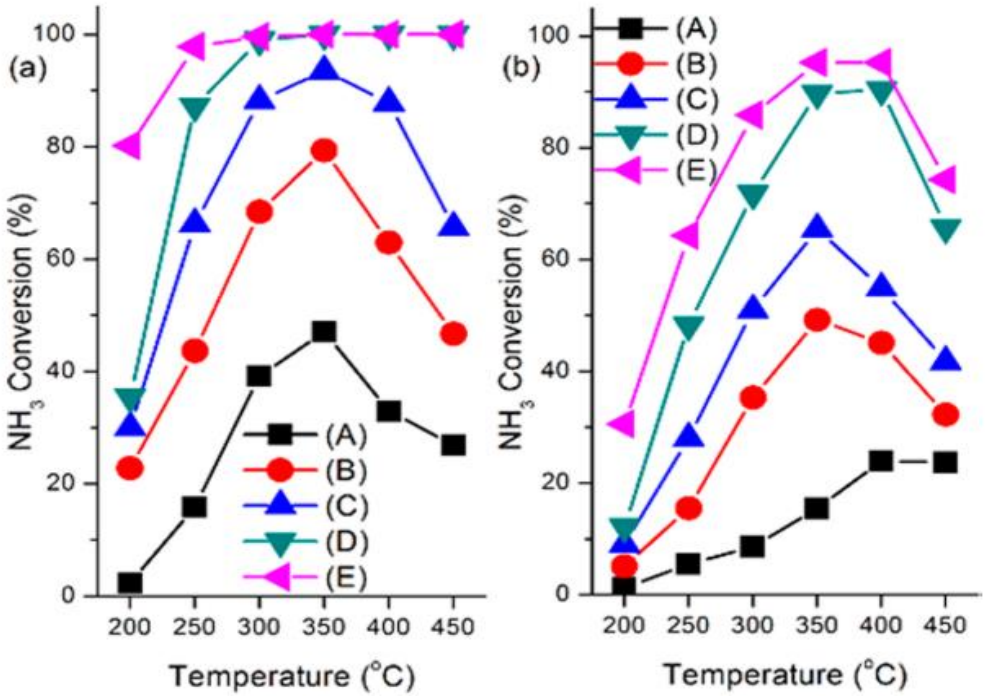

Figure 1.18 - NH_3 conversions of the $La_{1-x}Sr_xMnO_3$ under (a) dry and (b) wet conditions in the range 200−450 °C. (A) Fresh catalyst, (B) 0.1h immersed in HNO_3, (C) 1h- immersed in HNO_3, (D) 10h- immersed in HNO_3, and (E) 72h- immersed in HNO_3 [195].

In another study on NH_3 selective oxidation [195], $La_{1-x}Sr_xMnO_3$ was treated by immersion in HNO_3 in different period, and this procedure was suggested to have more B-site cations exposed on the catalyst surface. The treatment significantly increases the quantity of desorbed NH_3 during TPD experiments since NH_3 strongly and mostly bonded to the B-site cations of the perovskite framework rather than A-site cations. With increasing immersion time, the XPS peaks shifted to higher binding energy, and the Mn^{4+} increased while the O_{ads} decreased. Furthermore, the activity of catalyst increased with the immersion

time, samples with 10h and 72h of immersion 100% NH_3 conversions at the range of 300−450 °C under dry conditions (Fig.1.18). Under wet condition, activity dramatically decreased, especially at high temperature the NH_3 conversion significantly dropped. When the stream was introduced, partial H_2O molecules adsorbed competitively with NH_3 as hydroxyl groups inhibiting the effects of the catalyst.

Fe-based perovskites ($LaFe_{1-x}BO_3$, B=Cu, and Pd) and their supports on Al_2O_3 were investigated for NH_3 selective oxidation (Fig.1.19) [194]. In the study, $LaFeO_3$, $LaFe_{0.8}Cu_{0.2}O_3$, and $LaFe_{0.95}Pd_{0.05}O_3$ are prepared by high-temperature pyrolysis, using citric acid as a complexation agent, whilst $LaFe_{0.8}Cu_{0.2}O_3/Al_2O_3$ and $LaFe_{0.95}Pd_{0.05}O_3$ are supported on Al_2O_3 by the impregnation. Cu and Pd substitutions increase the reducibility of perovskite evidenced by shifting reduction peaks towards lower temperatures in H_2-TPR profiles. When the perovskites are dispersed on support Al_2O_3, a decrease in reducibility is observed owing to the strong interaction between the perovskite phase and supports. Interestingly, incorporation of Cu in the formulation results in slightly higher O_{ads}/O_{lat} from 0.52 for $LaFeO_3$ to 0.54 for $LaFe_{0.8}Cu_{0.2}O_3$ whereas Pd substitution leads to the opposite trend, O_{ads}/O_{lat} is decreased to 0.33. Consequently, Cu substitution seems to be more adequate to promote the formation of surface vacancies that are available for adsorption and dissociation of gaseous dioxygen molecule on its surface, Pd addition causes a decrease in surface sites. For $LaFeO_3$, NH_3 conversion starts between 150 °C and 200 °C, and increases up to a value of above 90% at T > 450 °C. Adding Cu and Pd the conversion is improved; however, those perovskites supported on Al_2O_3 show worse conversion due to low perovskite content (40 %). N_2 yield of $LaFe_{0.8}Cu_{0.2}O_3$ reaches 75 % at 250 °C but at higher temperature N_2 drops significantly together with NO_x formation. This evolution is associated to the high oxygen mobility displayed by Cu-containing solids that is in favor of N-H bond scission of adsorbed $-ONH_3$ species, leading to high NOx yield. For $LaFe_{0.95}Pd_{0.05}O_3$, the N_2 yield increases from ∼20% at 200 °C to 80–90% at 300 °C, and is maintained up to 600 °C. Supported samples show better catalytic performances in terms of N_2 yield at high temperature.

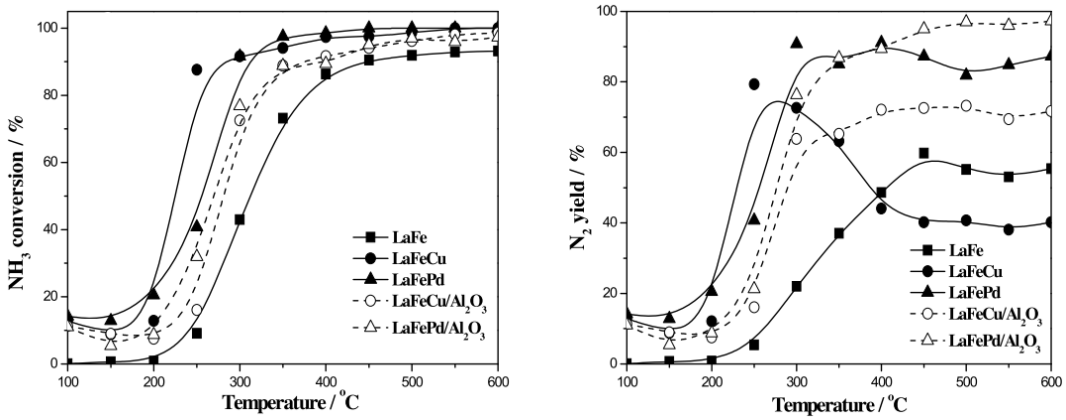

Figure 1.19 - NH_3 conversion and N_2 yield over different perovskite: $LaFeO_3$ (LaFe); $LaFe_{0.8}Cu_{0.2}O_3$ (LaFeCu); $LaFe_{0.95}Pd_{0.05}O_3$ (LaFePd); $LaFe_{0.8}Cu_{0.2}O_3$ supported on Al_2O_3 ($LaFeCu/Al_2O_3$) and $LaFe_{0.95}Pd_{0.05}O_3$ supported on Al_2O_3 ($LaFePd/Al_2O_3$) [194].

1.4.1.5 Soot Oxidation

Diesel engines offer superior fuel efficiency, higher durability, and lower greenhouse gas emission than gasoline engines. However, they can emit many air pollutants such as particulate matter (PM or soot), hydrocarbons, CO, nitrogen oxides (NO_x) and other toxic species [196]. For the reduction of soot emission, these engines are normally equipped with diesel particulate filters (DPF) which capture soot from the exhaust gases. This device should be regenerated by thermal treatments allowing the combustion of the soot deposited on the wall of DPF at high temperatures. Catalysts coated on the DPF wall assist to accelerate the soot combustion and decrease the regeneration temperature. Noble metals based catalysts have been widely used for diesel exhaust aftertreatment (Tab.1.4). Since a study of Kim *et al.* [197] perovskite oxide $La_{0.9}Sr_{0.1}CoO_3$ shows better catalytic performance than other noble rivals. Owning to strong redox properties, the formation and the high mobility of oxygen species, perovskite oxides are considered as promising candidates to replace noble metals coated on DPF to reduce the general costs of diesel vehicles.

In order to compare with $LaCoO_3$, Russo *et al.* [27] prepared a series of alkali-metal substituted perovskites $La_{1-x}A_xCoO_3$ (A = Na, K, and Rb) for the soot oxidation. $LaCoO_3$ prepared by combustion solution exhibits the ignition temperature ($T_{5\%}$ - temperature when 5 % of soot is combusted) of 402 and 459 °C for tight and loose contact respectively. The tight contact can be obtained by mixing soot and catalyst using ball milling in a certain period of time, but this condition does not represent the real catalyst-soot contact conditions

in diesel engines. On the other hand, loose contact can be achieved by gently shaking the soot and catalyst powders in a vessel. Alkaline-metal substitutions improved the catalytic

Table 1.4 – Some featured works on NO_x-assisted soot oxidation,

Catalysts	**NO assisted soot oxidation**						**NO oxidation**	
	$T_{10\%}$ (°C)	**$T_{50\%}$ (°C)**	**T_{max} (°C)**	**S_{CO2} (%)**	**NO_2/NO_x**	**Conditions**	**NO_2/NO_x**	**T_{max}(°C)**
Nano Pt-$Ce_{0.5}Pr_{0.5}$ [198]	396	456	450	-	-	550 ppm NO + 10% O_2 in N_2	0.6	350
5% Cu/CeO_2 [199]	384	540	580	-	0.5	550 ppm NO + 10% O_2 in N_2	0.7	380
Pt_3Sn/CeO_2-NC [200]	414	501	520	-	-	550 ppm NO + 10% O_2 in N_2	0.5	400
Pt/CeO_2-NC [200]	445	529	550	97	-	500 ppm NOx, 5% O_2	0.4	450
$BaMn_{0.7}Cu_{0.3}O_3$ [201]	400	511	-	100	-	1000 ppm of NO/10% O_2	0.45	400
Pt/Al_2O_3 [202]	350	474	-	99.5	-	800 ppm of NO/10%O_2/Ar	0.7	350
Pt/H-ZSM5 [202]	-	440	-	-	-	1000 ppm NO/10% O_2	-	400
Pt/MnO_x-CeO_2 [203]	399	-	420	99	-	1000 ppm NO/10% O_2	-	400
Pt/H-ZSM5 [204]	370	440	-	99	-	500 ppm NOx + 5%O_2	-	400
Pt/Al_2O_3 [204]	370	460	-	99	-	-	-	390
MnO_x–CeO_2–Al_2O_3 [205]	-	-	431	-	-	550 ppm NO + 10% O_2 in N_2	-	330
$Ce_{0.76}Zr_{0.24}O_2$ [206]	440	520	-	-	-	550 ppm NO + 10% O_2 in N_2	-	450
$La_{0.9}Sr_{0.1}CoO_3$ [197]	-	-	-	-	-	550 ppm NO + 10% O_2 in N_2	0.86	300

activity. Especially, $La_{0.9}Rb_{0.1}CoO_3$ reduces the ignition temperature by 71 °C and T_{max} (temperature with maximum CO_2 concentration) by 55 °C in the loose contact condition. The improved performance is linked to the higher reducibility of $La_{0.9}Rb_{0.1}CoO_3$ than other perovskites. In other research, small Sr-substitution in $La_{1-x}Sr_xCoO_3$ improves the catalytic activity, but with x = 0.2 the soot oxidation activity worsens as for un-doped $LaCoO_3$ [207]. However, the catalytic performance increases with the degree of Ce-substitution with T_{max} of 435 °C for $La_{0.8}Ce_{0.2}CoO_3$ compared with 454 °C for $La_{0.9}Ce_{0.1}CoO_3$ and 485 °C for $LaCoO_3$ in the tight contact treatment. Since the soot oxidation is observed at significantly lower temperatures of β-desorption, the diffusibility of surface oxygen may remarkably contribute to the activity. The authors suggested that soot combustion seems to be a suprafacial process involving α-O_2, the catalyst must have a high density of surface oxygen vacancies, which yields a higher capacity for adsorption of molecular oxygen, and Ce and Sr-substitutions raise the amount of α-O_2.

It is reported that the soot combustion can be enhanced by the presence of NO_x which is stronger oxidant than O_2, and a small quantity of NO_x in the inlet reaction mixture represents the real conditions. K –substitution in $LaCoO_3$ not only improves the basicity of the perovskite but also leads to the formation of Co^{4+} and oxygen vacancies to absorb gaseous oxygen [208]. Wang *et al.* [208] observed that an increasing substitution of K in $La_{1-x}K_xCoO_3$ (x= 0.05-0.3) gradually reduces the ignition temperature of the soot oxidation in the presence of NO_x, and simultaneously increases the XPS O_{ads}/O_{lat} ratio [208]. However, in the research, only a small proportion of NO_x can be converted to NO_2 (34.6 %) and considerable CO_2 selectivity (98.4 %) are observed. High NO_2 percentage is expected for afterbatement treatment for the NO_2 reduction. A similar catalytic system $La_{1-x}K_xCoO_3$ was investigated by Bin *et al.*[209], the authors concluded that the introduction of K ions into the A-site causes the enhancement of Co valence state, which is beneficial to improving the catalytic activity. However, with x > 0.4 Co_3O_4 appears and the activity starts declining. For $La_{0.7}K_{0.3}CoO_3$, ignition temperature is 286 °C and T_{max} of 389 °C, which is similar to the study of Wang group [208]. Besides, the authors also observed with the increasing K substitution, NOx conversion in the $La_{1-x}K_xCoO_3$ series shows a declining trend.

For the $LaCo_{1-y}Fe_xO_3$ system, the catalytic performances show a monotonously decreasing trend as a function of Fe substitution [209]. Upon Fe-substitution (y < 0.5), only the perovskite phase is observed due to a similar ionic radius of Fe^{3+} and Co^{3+} [210]. Contract to K-substitution where the ratio of adsorbed oxygen to lattice oxygen (O_{ads}/O_{lat}) increases with

K content, no obvious changes in O_{ads}/O_{lat} ratio are apparent for $LaCo_{1-y}Fe_yO_3$ series. The decrease in activity is probably also associated with the strong interaction between Co and Fe. At low Fe-doping ratios, the Co^{4+}/Co^{3+} couple plays an important role in catalytic performance. With increasing Fe content, the Fe^{4+}/Fe^{3+}couple gradually prevails over the Co^{4+}/Co^{3+} and consequently inhibits the simultaneous removal of NO_x and soot. In an effect to increase the activity of bi-transition metals Co-Fe perovskites, Le *et al.* [34] introduced Sr in $La_{1-x}Sr_xCo_{0.2}Fe_{0.8}O_3$ (x = 0.2-0.4) and the perovskite prepared by electrospinning technique to form three-dimensional (3D) fiber web structure that increases the high-contact area by trapping soot in the unique pore structure. It is observed that the addition of Sr increases the catalytic properties of perovskite oxides, which are probably related to the increase in O_{ads}/O_{lat} with Sr-substitution. The best performance is recorded with x = 0.4.

The effects of B-site on soot oxidation activity have been widely investigated. In the study on the soot oxidation, Mishra *et al.* [211] suggested the activity should be in order: $LaCoO_3$ > $LaFeO_3$ > $LaNiO_3$. Hernández *et al.*[212] also mentioned the effects of Mn in the $La_{0.6}Sr_{0.4}BO_3$ (B = Fe, Mn, and Ti) for the soot oxidation. The perovskites are prepared by the thermal decomposition of the chelated nitrate precursors. The better activity of Fe and Mn perovskites is explained by the presence of oxygen vacancies in $La_{0.6}Sr_{0.4}FeO_3$ and Mn^{4+} in $La_{0.6}Sr_{0.4}MnO_3$. Among the three samples, O_{ads}/O_{lat} of $La_{0.6}Sr_{0.4}TiO_3$ is extremely low, and there is no oxygen desorption due to non-redox behavior of the sample.

The co-existence of Fe-Mn in a perovskite structure ($LaMn_{1-x}Fe_xO_3$) have some positive effects on the soot oxidation [213]. Interestingly, Fe is a factor reducing the activity of $LaCo_{1-y}Fe_yO_3$ [210], the addition of Fe in $LaMnO_3$ improves the activity, reducing the T_{max} from 437 °C for $LaMn_{0.95}Fe_{0.05}O_3$ to 411 °C for $LaMn_{0.85}Fe_{0.15}O_3$ [213]. However, the reasons for better performance with Fe-substitution are not mentioned in the study. On the other hand, in $BaMn_{1-x}Cu_xO_3$, the introduction of Cu increases the number of oxygen vacancies, reducibility and maintains the oxygen state of Mn^{3+}. This may lead to the positive performance of $LaMn_{0.7}Cu_{0.3}O_3$ compared to lower Cu content perovskites [72]. A-site substitution of $LaMnO_3$ effects on diesel soot removal is also studied. $La_{1-x}K_xMnO_3$ exhibits lower T_{ign} and T_{max} with increase in K-substitution up to x = 0.25 [214]. The better performance is explained on the basic of the presence more Mn^{4+} and oxygen vacancies with the substitution of La^{3+} by K^+.

Table 1.5 – Soot oxidation performances of several perovskite oxides,

Perovskites	Reaction conditions	Tight contact		Loose contact		χ_{NO} (%)	S_{CO2} (%)
		T_{ign} (C)	T_{max} (C)	T_{ign} (C)	T_{max} (C)		
$LaCoO_3$ [27]	Catalyst:soot =9:1, heating rate 5 C/min, under 100 ml/min of air	402	455	459	518	-	-
$La_{0.9}Rb_{0.1}CoO_3$ [27]		330	393	388	463	-	-
$La_{0.8}Ce_{0.2}CoO_3$ [207]	Catalyst:soot = 9.5:1, 5 C/min; 10 % O_2/He	-	435	-	-	-	-
$La_{0.7}K_{0.3}CoO_3$ [208]	catalyst:soot = 5:1; 2 C/min; 5 % O_2, 2000 ppm of NO	-	-	289	400	34.6	98.4
$LaCo_{1-y}Fe_yO_3$	Catalyst: soot = 10:1; inert SiO_2 added; 10 % O_2; 800 ppm O_2; 2 C/min	-	-	309	409	32.8	93.7
$La_{1-x}Sr_xCo_{0.2}Fe_{0.8}O_3$ [34]	Catalyst:soot = 9.5:1; 6 %O_2; 10 C/min	397	490	-	-	-	-
$LaCo_{1-y}Pd_yO_3$ [215]	Catalyst:soot = 15:1; 0.5%NO; 5 % O_2 ; 1.5 C/min	265	-	-	-	-	-
$BaCoO_{3-\delta}$ [216]	Catalyst :soot = 20 :1 ; air ; 10 C/min	350	450	-	-	-	-
$La_{0.7}Ag_{0.3}MnO_3$ [217]	Cat :soot = 100.2 % NO ; 5 % O_2 ;	-	-	317	461	72.2	-
$La_{0.8}K_{0.2}Cu_{0.05}Mn_{0.95}O_3$ [218]	Cat:soot = 20:1; 0.25% NO ; 5 %O_2 ; 0.27 % C_3H_6 ; plasma assisted	-	325	-	-	-	-
$La_{1-x}A_xBO_3$ (A = Ce, Cs, Sr) (B = Co, Mn, Fe) [219]	Cat :soot = 9.5 :5 ; 5000 ppm NO ; 4 % O_2; 1 C/min	200	320	-	-	-	-
$La_{1-x}Ce_xNiO_3$ [68]	Cat :soot = 9:1 ; 0.5 %NO; 5 %O_2 ; 1 C/min	303	375	-	-	-	-
$La_2Ni_{1-y}Cu_yO_4$ [220]	Cat :soot = 9:1; 0.5 %NO; 5 %O_2 ; 1 C/min	246	-	-	-	15.6	-
$La_{2-x}K_xCuO_4$ [221]	Cat :soot = 5:1; 5 C/min; 5 %O_2; 2000 ppm NO	-	-	376	487	-	98.5

Ni-based perovskites take less attention for soot oxidation reactions probably due to the fact that they are less active than Fe and Co [211]. The partial substitution of Ce for La

increased the concentration of Ni^{2+} which is considered as an active center for the reaction, enhancing the catalytic activities [68]. Other studies on Ni-based perovskites as well as other metal-catalysts can be found in Table 1.5.

1.4.2 Perovskite oxides for reduction reactions

Great efforts have been devoted to developing perovskite catalysts to eliminate NO_x ($NO+NO_2$) during abatement treatments in vehicle engines. There are two main processes for NO_x elimination: NO_x storage reduction (NSR) and selective catalytic reduction (SCR). In the NSR, catalysts usually with noble metals allow the oxidation of NO into NO_2 which is later trapped by base sites (for example, Ba-based oxides/Ba-carbonates) in forms of nitrite or nitrate intermediates. The NSR catalysts operate in the transient lean/rich period. During the lean step, the standard exhaust gas from the lean-burn engine passes through the catalysts, and NO is oxidized to NO_2 over precious metals and trapped on the basic part of the catalysts. In the later step, the saturated trap is regenerated in the rich flow to reduce the stored NO_2 to N_2. The generation is begun by injecting pulses of fuels, oxidation of which increases internal temperatures which favor nitrate/nitrite desorption and its reduction. On the other hand, in the SCR, NO_x is continuously reduced with support of additional reducers such as hydrocarbons, urea (ammonia), hydrogen, or alcohols.

1.4.2.1 NO_x Storage Reduction

Model NSR catalysts usually contain a noble metal site oxidizing NO to NO_2, and a basic phase (Ba oxide, carbonate) to trap NO_2 in nitrite or nitrate forms. Both precious metals and basic phases are supported on a modified alumina substrate [222]. In addition to the high cost of noble metals, one of the disadvantages of the NSR catalysts is high sensibility to sulfur poisoning, leading to the deactivation of the catalysts [223]. Perovskite oxides have been considered as alternative options regarding to low cost materials and resistance to sulfur poisoning. In its formula ABO_3, A is usually La or Ba due to its strong basicity to storage NO_x, and B is transition metals (Co, Fe and Ce) owing to strong redox properties.

Milt *et al.* [216] investigated non-stoichiometric $BaCoO_{3-y}$ for NO_2 storage capacity. $BaCoO_3$ is obtained by calcination at 700 °C, increasing to 1000 °C resulted in the formation of $BaCoO_{2.74}$. The non-stoichiometric sample shows high NO_x storage capacity, two times higher than that of $BaCoO_3$. It is well known that oxygen vacancies can act as Lewis bases and become adsorption sites for O_2 and NO_2. The interaction between Ba and NO_2 to form bulk and surface nitrates resulted to partial destructions of the perovskite phase. However,

the decomposition of the nitrates can be achieved under reductive treatments either under H_2 atmosphere or with soot particles at temperatures lower than 400 C (Fig.1.20). In another study on Ba-Co-K/CeO_2 by the same group [224], the introduction of K supports the formation of $BaCoO_{2.93}$ perovskite phase which is responsible for enhanced NO_2 storage capacity and the instability of nitrate species, due to the formation of surface N-bound nitrate species. Interestingly, the decomposition of barium nitrates under heating does not cause destroying the perovskite phase of $BaSnO_3$ [225]. The process of absorption/desorption of NO_2 is reversible, repeatable. However, the prolonged contact of the perovskite with SO_2 led to a partial destruction of the perovskite structure, resulting in permanent deactivation [226].

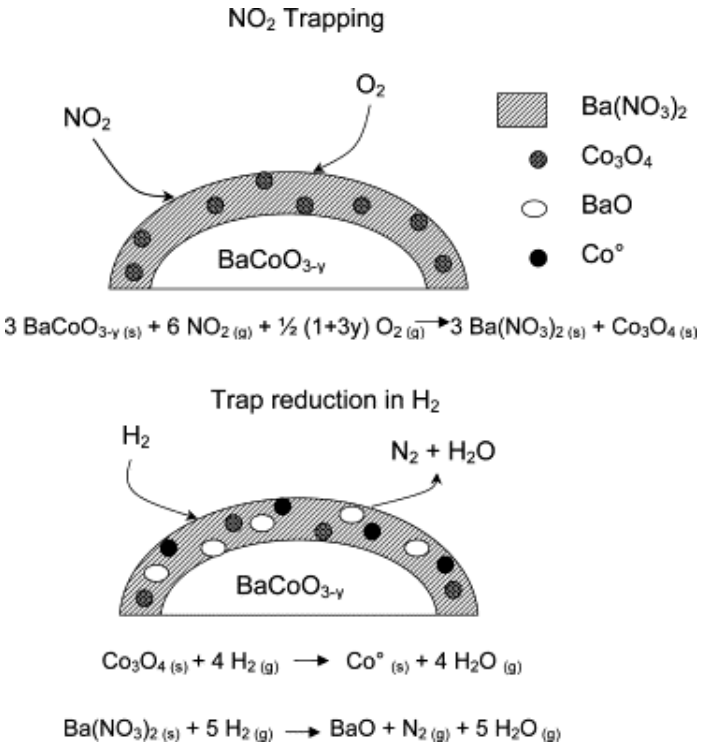

Figure 1.20 - Scheme for the NO_x trapping-regeneration process with the $BaCoO_{3-y}$perovskite [216].

The NO_x storage properties of $BaFeO_3$ were widely reported [227–230]. $BaFeO_{3-x}$ recently acquires a reputation for high NO_x storage capacity and sulfur resistance. Without SO_2, NO_x storage capacity of $BaFeO_3$ is not comparable with standard Pt/BaO/Al_2O_3 [230]. However, adding 100 ppm SO_2, the NSC of Pt/BaO/Al_2O_3 dropped dramatically whereas this capacity of $BaFeO_{3-x}$ is reasonable. In another research, the NO_x storage capacity of $BaFeO_{3-x}$ is slightly reduced by 11 % upon sulfation process with 200 ppm SO_2/O_2 in 1 h

[227]. The authors suggested that the NO_x mainly bonded with Ba atoms to form Ba nitrates, while during the sulfation process the sulfur mainly deposited on iron forming the $Fe_2(SO_4)_3$-like species. However, according to Xian *et al.* [229], not only the iron sulfate but also the barium sulfate are formed after exposing the perovskite catalyst in the SO_2/O_2 atmosphere. The Fe atoms surrounding the Ba atoms closely in the crystal lattice of the perovskite inhibit the sulfation of the barium, inducing a high sulfur tolerance [229]. In addition, Fe substituted by Ti is reported to significantly improve the NO_x absorbability and the sulfur resistance [228]. According to the authors [228], the NSC of $BaFe_{0.8}Ti_{0.2}O_{3-y}$ perovskite drops by only 5.1 % after sulfation pretreatment at 400 °C.

1.4.2.2 Selective Catalytic Reduction

One of the most promising ways for NO_x abatement is believed to be the catalytic reduction in the presence of hydrocarbons (CH_4, C_2H_4, C_3H_6), and alcohols (methanol and ethanol) because of their trace presence in the exhaust gas of vehicle engines. Another deNO_x possibility is to use H_2 as a reducing agent for the catalytic reduction of NO over a suitable catalyst, especially for the treatment of exhaust gas from a stationary source. Stathopoulos *et al*. [231] studied La–Sr–Fe perovskite systems for H_2 and CH_4-SCR. $La_{0.8}Sr_{0.3}FeO_{3-x}$ was synthesized by ceramic (LSF-1) and surfactant (LSF-2) methods with surface areas of 3 and 33 $m^2\ g^{-1}$ respectively. Over the whole temperature range, both samples exhibit higher N_2 selectivity under both CH_4 and H_2-SCR conditions in spite of remarkably different surface area (Fig.1.21). However, between 350-475 °C, LSF-2 shows better NO conversion under $CH_4/NO/O_2$ whereas in the presence of H_2, LSF-1 has superior performance. The difference in catalytic activity is explained by the presence of $SrFeO_{3-x}$ phase in both samples with various amounts, contributing to easier oxidation of adsorbed NO to NO_2 through mobile surface oxygen atoms, where the NO_2 species formed can be easier reduced by CH_4 than the adsorbed NO species. On a study on Ce^{4+} and Sr^{2+} substituting $LaFeO_3$ ($La_{1-x-y}Sr_xCe_yFeO_3$) [232], a noticeable improvement in NO conversion by substitution La^{3+} by Sr^{2+} and $Ce^{4+}$is observed. $La_{0.5}Sr_{0.2}Ce_{0.3}FeO_3$ exhibits the highest activity with 25 % of NO conversion and 93 % of N_2 selectivity. The authors concluded that Sr^{2+} largely contributes to the creation of oxygen vacancies.

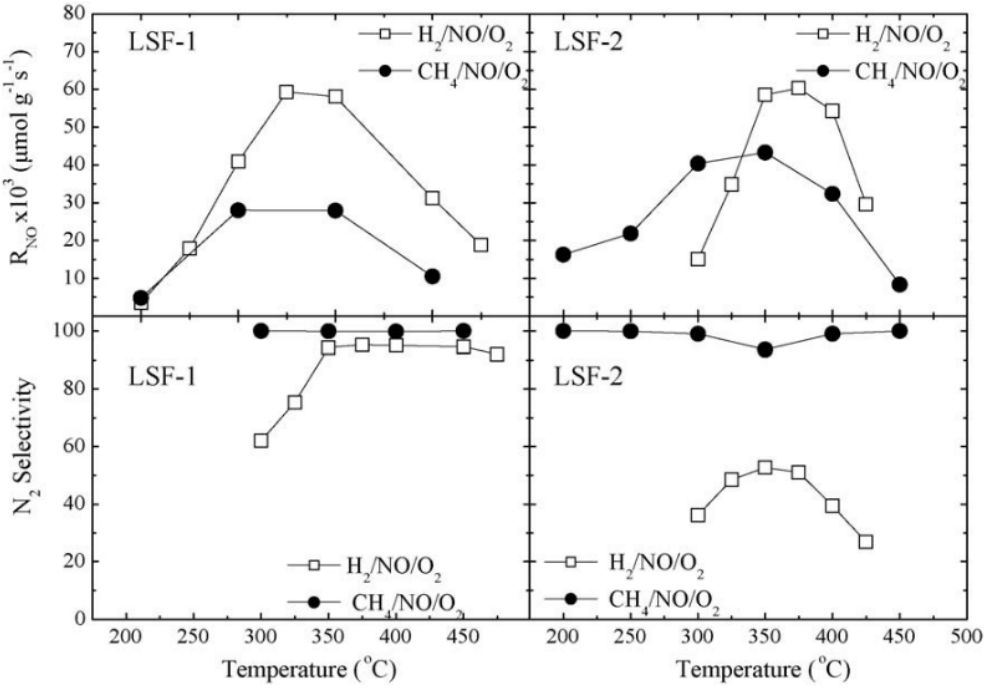

Figure 1.21 – Temperature profiles of the rates of NO conversion and N_2 selectivity of CH_4-SCR ($NH_4/NO/O_2$) and H_2-SCR ($H_2/NO/O_2$). Reaction conditions (0.67 mol % CH_4 + 0.5 mol % NO + 5 % O_2 or 1 mol % H_2 + 0.5 mol % NO + 10 % O_2) [231].

Wu *et al.* [233] studied deNO_x reduction by C_3H_8 in the presence of different amounts of oxygen over $La_{1-x}Sr_xMnO_3$. Generally, the addition Sr^{2+} improves the NO reduction rate but too much introduction ($x > 0.4$) results in deterioration of activity. $La_{0.7}Sr_{0.3}FeO_3$ exhibits the best activity with the highest NO reduction rate and considerable C_3H_8 oxidation. C_3H_8 can act as a reducer for NO reduction below 400 °C, but the NO reduction is severely weakened by increasing the O_2 concentration, especially at high temperatures. The NO reduction rate can reach 100% at 560 °C under 0.5% O_2 but under 10% O_2 it becomes zero (Fig.1.22). Using C_3H_6 as a reducer, Zhang *et al.* [38] investigated the catalytic behavior of $LaMn_{1-x}Cu_xO_3$. The incorporation of 20 % Cu in the lattice enhances the N_2 yield of $LaMnO_3$ by 24 % under condition (3000 ppm NO, 3000 ppm C_3H_6,1 % O_2 in helium and 500 °C). The better performance of Cu-substituted samples is likely to correspond to the facility in the formation of adsorbed nitrate species via the oxidation of NO by α-oxygen. However, the excessive α-oxygen content observed over $LaCo_{0.8}Cu_{0.2}O_3$ accelerates the unselective C_3H_6, which leads to a poor N_2 yield with respect to Mn-based perovskites [38].

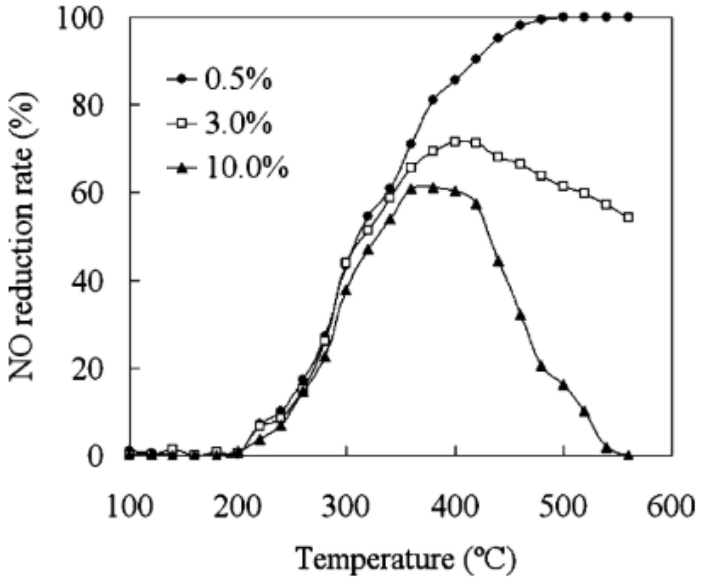

Figure 1.22 - NO reduction curves under various O2 concentrations over the $La_{0.7}Sr_{0.3}MnO_3$ [233].

NH_3-SCR for the $DeNO_x$ process is currently the leading technology to low-level NOx abatement in lean conditions but they have several drawbacks such as additional tanks for urea. In an effort to use perovskite oxides for NH3-SCR to replace commercial catalysts (V_2O_5–WO_3 (MoO_3)/TiO_2), Zhang *et al.* [234] prepared a series of $LaBO_3$ (B = Cu, Co, Mn and Fe) for NH_3-SCR reaction (inlet composition: 1000 ppm NO, 1000 ppm NH_3, 6% O_2) at low temperatures. The authors suggested that NH3 chemical adsorption is the rate-determining step, thus the NH3 adsorption ability of the perovskites is the key factor for the SCR performance. Among the studied samples, Mn-based perovskite exhibits the best catalytic activity, yielding 78 % NO conversion at 250 °C. In addition, nitrite/nitrate species formed on $LaMnO_3$ is another essential key for NH3-SCR, and monodentate nitrates are identified to be reactive with adsorbed NH_3 [235]. Moreover, $LaMnO_3$/CeO_2 exhibited an expectably high activity below 200 °C, which can be safely correlated to the enhancement of NO oxidation by CeO_2 at low-temperature zone.

1.4.3 Chemical transformations

The utilization of perovskite catalysts for chemical transformations of organic compounds of common interests is still limited in spite of many beneficial aspects such as high thermal stability, tolerance to partial substitution of cations and surface reconstruction [236]. Tab. 1.6

Table 1.6– Some chemical conversions over perovskite oxides,

Catalyst system	Reaction type	Products	Reaction conditions
$LaNi_xFe_{1-x}O_3$[7]	Steam reforming of toluene C_7H_8 / tar	H_2 CO	• Reduced at 600 °C • Test at 650 °C
$LaNi_{0.5}Mn_{o.5}O_3$[8]	Steam reforming of toluene C_7H_8 tar	H_2+CO	• Reduced at 1000 °C • Test at 700 °C
$Ni/La_{0.7}Sr_{0.3}AlO_{3-\delta}$[9]	Steam reforming of toluene C_7H_8	H_2 CO CO_2	• Reduced at 800 °C • Test at 600 °C
$LaNiO_3$[10]	Steam reforming of C_2H_5OH	H_2	• Reduced at 400 °C • Test at 225-400 °C
$La_{2-x}Sr_xNiO_{4-\delta}$[11]	Steam reforming of C_2H_5OH (chemical looping)	H_2	• Test at 650 °C
$LaFe_{1-x}Co_xO_3$[12]	Steam reforming of CH_4 (chemical looping)	H_2+CO	• Test at 850 °C
$LaNiO_3$[13]	Partial oxidation of CH_4	H_2+CO	• Test at 920 °C
$LaNiO_3$[14]	Partial oxidation of CH_4	H_2+CO	• RT-900 °C
$LaCo_{1-x}Cu_xO_3$[16]	Steam gasification of bio-oil/char (slurry)	H_2	• Test at 800 °C
$La_{0.8}Ce_{0.2}FeO_3$[17]	Steam gasification of bio-oil/char (slurry)	H_2	• Test at 800 °C
$La_{1-x}K_xMnO_3$[18]	Steam reforming of bio-oil	H_2+CO	• Test at 800 °C
$LaCoO_3$[20]	biomass (carbohydrates)---->lactic acid	Lactic acid	• 160-240 °C+400psi N_2, batched reactor
$LaNiO_3$[15]	Steam reforming of bioglycerol $C_3H_8O_3$	H_2	• Reduced and test at 550-650 °C • Gas phase
$LaNiO_3$[19]	Steam reforming of CH_3COOH/bio-oil	H_2 CO CH_4 CO_2 C_3H_6O	• Reduced at 700 °C • Test at 600 °C
$LaNi_{1-x}Fe_xO_3$[21]	HMF --> DMF	DMF	• 230 °C and 5 MPa • Batch reactor
$LaMnO_3$[22]	Oxidation lignin to aromatic aldehydes	Aldehydes	• Batched reactor, 20 bar • 120 °C
$LaCoO_3$[23]	Oxidation lignin to aromatic aldehydes	Aldehydes	• Batched , 15 bars
$La_{0.9}Sr_{0.1}Co_{1-x}Ni_xO_3$ [237]	Fischer-Tropsch synthesis to C_{2+}-alcohols	C_{2+}-alcohols	• reduced 450 °C • 5 MPa, 200 °C
$La_{1-x}Sr_xCo_{1-y}Fe_yO_{3-\lambda}$[67]	Photocatalysis of 2-propanol degradation		• Photoreactor
$La_{1-x}Sr_xCo_{1-y}F_yO_{3-\lambda}$[56]	Oxidative coupling of CH_4	C_2-species	• 850 °C • Membrane reactor

shows some applications in chemical valorization processes, mainly H_2 production via steam reforming of hydrocarbons, partial oxidation, hydrogenolysis of HMF, and oxidative coupling to synthesis heavy hydrocarbons.

1.4.3.1 Alcohol conversion

Due to the tunability of their surface properties, perovskites appear as a promising candidate to design multifunctional catalysts. Tesquet *et al.* [238] investigated $La_{1+x}FeO_{3+\delta}$ (x = 0.1, 0.3, 0.5, 0.8 and 1) for ethanol conversion using isopropanol conversion to study basic-acid properties. It can be seen that the excess of La content leads to the formation of La_2O_3; however, more La does not correlate to the increase in the basicity of the sample (x > 0.5). The reason is that the appearance of $La(OH)_3$ when doping high content of La, inducing the decrease in basic sites. The sample with highest basicity $La_{1.3}FeO_{3+\delta}$ exhibits the highest ethanol conversion, highest yield to butanol-1 and highest selectivity to pentanone-2. The authors suggested that the reaction pathway to butanol-1 is Guerbet reaction. However, there was no characterization to study the strength and density of acid-basic sites in the study.

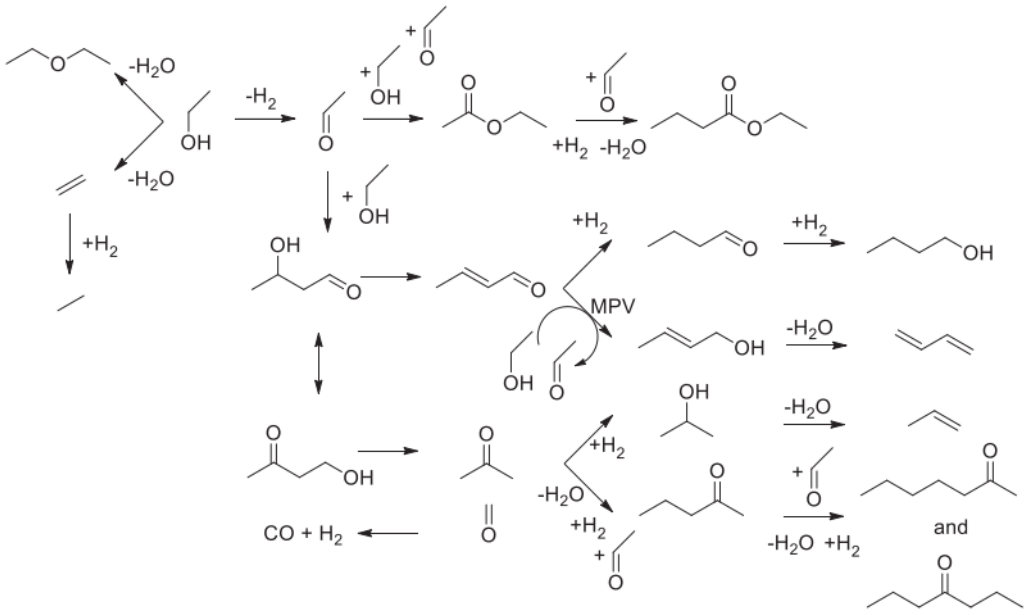

Figure 1.23– Generally accepted network of C – C coupling of ethanol [239].

More recently, Yu *et al.* [239] compared $LaFeO_3$ with $LaMnO_3$ and their silica-supported forms in ethanol conversion. The authors suggested the general pathway of ethanol conversion into chemicals in Fig.1.23. The catalytic activity of perovskite oxides is manipulated by tuning acidobasic properties. Both perovskites contain mainly surface

basic sites whereas supporting on silica results in the suppression of basicity and enhancement of acidity due to more concentration of B^{4+} cations. The concentration and strength of Lewis acids are positively correlated to the concentration of Mn^{4+} in $LaMnO_3$ solid solution [158]. Lewis/base pair (Mn^{4+}/nonstoichiometric oxygen) formed on $LaMnO_3/SiO_2$ are responsible for aldolization activities while Lewis/base pair was absent on $LaFeO_3/SiO_2$. Consequently, $LaMnO_3/SiO_2$ produces more aldolization products (butadiene-1,3 and butanol-1) than $LaFeO_3/SiO_2$. Furthermore, both $LaFeO_3$ and $LaMnO_3$ were active in base-catalyzed reactions leading to the formation of acetone, pentanone-2, ethyl acetate, while silica-supported perovskites were active in aldolization and dehydration of ethanol.

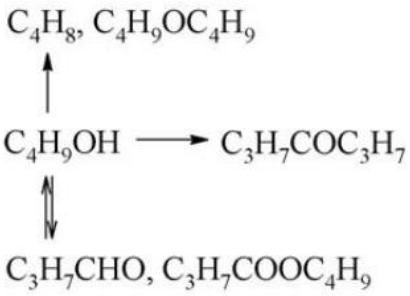

Figure 1.24– Reaction pathway of butanol-1 conversion [240].

In a work of Klimkiewicz *et al.* [240], the partial substitution of Cu, V or Sr into $LaMnO_3$ is able to control the acid–base surface properties of perovskites. The authors conducted butanol-1 conversion over perovskite catalysts (Fig. 1.24). Selectivity to butyraldehyde can be related to the share of basic sites whilst selectivity to dipropyl ketone is affected both by the acidity and concentration of acidic sites. In the study, the substitution of Mn by Cu increases the basic site and decreases the acidity, while substitution of La^{3+} by Sr^{2+}reduces both acidic and basic sites. These observations are contrary to the study of Yu *et al.* [239] since these substitutions may result in the presence of more Mn^{4+} species which are related to acidity of perovskite oxides. It should be mentioned that the authors used the decomposition reaction of cyclohexanol to determine the acid-basic properties of the catalyst surface. Acid sites are involved in dehydration of cyclohexanol, while dehydrogenation to cyclohexanone proceeds over both acid and basic sites. The authors also developed carbon-supported $LaMnO_3$ for butanol-1 ketonization to heptanone-4 via butylaldehyde [241]. It was shown that the combination of carbon black with perovskite $LaMnO_3$ could produce a high yield of heptanone-4.

1.4.3.2 Alkylation

Zawadzki *et al.* [242] studied the phenol methylation on perovskite $La_{0.6}Sr_{0.4}Co_{0.2}Fe_{0.8}O_3$ prepared by the combustion synthesis and by the reactive grinding method. Among products (Fig.1.25), ortho-cresol is the most desirable due to its applications in the industry [236]. It is known that ortho-selectivity of phenol alkylation is governed by the type of phenol adsorption on the catalyst surface, depending on its acidic strength. The perovskite prepared by reactive grinding shows the best catalytic performance (41 % of conversion and 90 % ortho-cresol selectivity) due to the optimal ratio between acid and base sites. According to Tanabe *et al.* [243], phenol adsorbs on acid-base pairs with the hydrogen of –OH binding the surface basic oxygen and ring bound to acidic sites. More acidity of the catalysts causes the phenolate ring to lay closer to the catalysts surface, promoting alkylation at ortho-, meta- and para-positions, whereas more basicity enhances the adsorption of phenolate ring at a vertical position and the ortho-substitution is preferred.

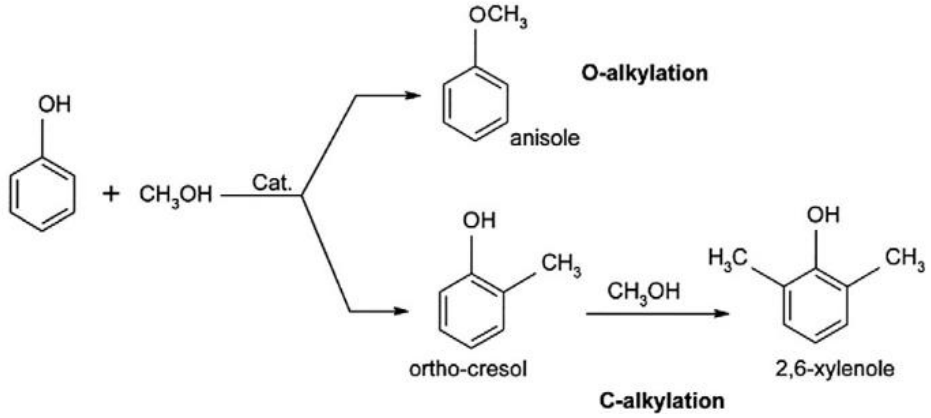

Figure 1.25– Main reaction pathway of phenol methylation [242].

1.4.3.3 Hydrogenolysis of 5-hydroxymethylfurfural.

Chen *et al.* [21] investigated the hydrogenolysis of C–O and C=O in 5-hydroxymethylfurfural (HMF) for the production of furan biofuel 2,5- dimethylfuran (DMF) over $Ni/LaFeO_3$. HMF is an important bio-based compound which is one of the top 10 platform molecules derived from biomass. DMF is considered as an appealing candidate as a biofuel. Hydrogenolysis of HMF to DMF may lead to the formation of side products (Fig.1.26), and many studies have been conducted over expensive noble metal catalysts. In the study of Chen *et al.* [21], $Ni/LaFeO_3$ reveals the best catalytic activity with 99 % of conversion and 98 % of DMF yield. Compared to Ni/Fe_2O_3, Ni/La_2O_3 and $LaFeO_3$, the $Ni/LaFeO_3$ possesses superior activity, suggesting the synergetic interaction between Ni and $LaFeO_3$.

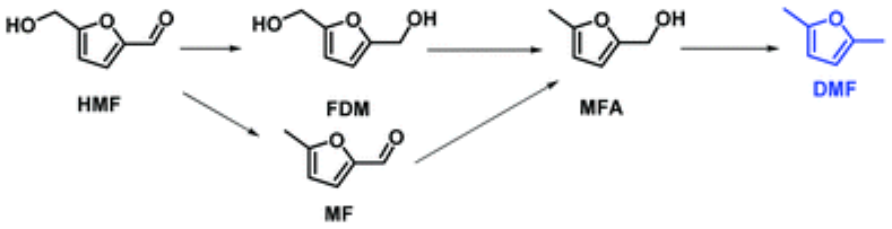

Figure 1.26- Possible reaction pathways for the hydrogenolysis of HMF [21].

1.5. CONCLUSIONS AND PERSPECTIVES

The unique structure, the versatility of compositions and tunability to surface properties make perovskite oxides appealing materials for a wide range of applications. Many efforts have been devoted to their applications in heterogeneous catalysis. Good performances have been mostly reported for oxidation reactions due to high redox properties such as CO, hydrocarbon, VOC total oxidation. Recently, more works have been focused on using perovskite catalysts for environment treatment including three-way catalysts, soot oxidation, selective reduction catalysts or photo-degradation on Ti- or Ta-based perovskites. Applications of perovskite oxides in chemical transformations to useful products or intermediates are still limited. One of the traditional disadvantages of perovskite oxides is low surface area, typically in the range of 10 – 20 m^2 g^{-1} inhibiting them to be utilized widely in the industry. Scientists have worked to prepare high surface perovskites, of which specific areas being reached up to 100 m^2 g^{-1} or more. The new synthesis routes such as nanocasting or templating methods allow forming meso/macro-porous perovskite catalysts, providing the possibilities to increase the catalytic performances. In the meanwhile, modern characterization techniques allow researchers to understand deeply perovskite systems: its properties and behaviors in different media such as reducing atmospheres.

The performances of perovskite catalysts in some cases reached those of noble metals [244]. Total replacement of noble catalysts by perovskite ones are still under consideration since both of them have their own advantages. Combination them into all-in-one catalysts with multifunctional properties may offer a considerable advantageous technology for different types of reactions. Furthermore, a few studies on acidobasic properties of perovskite oxides have been developed. Tuning the acidity-basicity tailoring to specific applications may be promising developments for perovskite oxides in the near future.

In addition to cation substitutions, partial replacement of perovskite anions such as oxyhydrides [245,246,255–260,247–254] have recently attracted many scientists. Many new

properties of these materials have been discovered. For instance, replacing O^{2-} by H^- reduces the oxidation states of the transitional metals to unusual values [261] or $BaTiO_{3-x}H_x$ allows to synthesize oxynitrites at soft conditions [258]. Applications of dual cation/anion substituted perovskites in catalysis may be an appealing topic in science. In fact, in the year 2018, Tang *et al.* applied oxyhydrides as supports to significantly enhance CO_2 methanation activity [262] or for ammonium synthesis [263]. However, similar studies have not been reported yet, thus these applications should be more deeply and widely investigated.

1.6 REFERENCES

1 H. Wang, J. Zhang, J. W. Liu, L. Z. Ouyang and M. Zhu, *J. Alloys Compd.*, 2013, **580**, S197–S201.
2 A. Oleaga, A. Salazar and D. Skrzypek, *J. Alloys Compd.*, 2015, **629**, 178–183.
3 J. M. Polfus and R. Haugsrud, *Solid State Commun.*, 2012, **152**, 1921–1923.
4 S. H. Porter, Z. Huang, Z. Cheng, M. Avdeev, Z. Chen, S. Dou and P. M. Woodward, *J. Solid State Chem.*, 2015, **226**, 279–285.
5 J. Zhu, H. Li, L. Zhong, P. Xiao, X. Xu, X. Yang, Z. Zhao and J. Li, *ACS Catal.*, 2014, **4**, 2917–2940.
6 M. A. Pena and J. L. G. Fierro, *Chem. Rev.*, 2001, **101**, 1981–2017.
7 U. Oemar, P. S. Ang, K. Hidajat and S. Kawi, *Int. J. Hydrogen Energy*, 2013, **38**, 5525–5534.
8 C. P. B. Quitete, R. L. Manfro and M. M. V. M. Souza, *Int. J. Hydrogen Energy*, 2017, **42**, 9873–9880.
9 Yasushi, D. Mukai, Y. Murai, S. Tochiya, Y. Izutsu, K. Sekiguchi, N. Hosomura, H. Arai, E. Kikuchi and Y. Sugiura, *Appl. Catal. A Gen.*, 2013, **451**, 160–167.
10 K. H. Lin, C. Bin Wang and S. H. Chien, *Int. J. Hydrogen Energy*, 2013, **38**, 3226–3232.
11 Q. Zhang, L. Li, B. Jiang, K. Wang, D. Tang and B. Dou, *Int. J. Hydrogen Energy*, 2017, **42**, 17102–17111.
12 K. Zhao, F. He, Z. Huang, G. Wei, A. Zheng, H. Li and Z. Zhao, *Appl. Energy*, 2016, **168**, 193–203.
13 L. D. Vella, J. A. Villoria, S. Specchia, N. Mota, J. L. G. Fierro and V. Specchia, *Catal. Today*, 2011, **171**, 84–96.
14 T. H. Nguyen, A. Łamacz, P. Beaunier, S. Czajkowska, M. Domański, A. Krztoń, T. Van Le and G. Djéga-Mariadassou, *Appl. Catal. B Environ.*, 2014, **152**–**153**, 360–369.
15 S. Ramesh and N. J. Venkatesha, *ACS Sustanaible Chem. Eng.*, 2017, **5**, 1339–1346.
16 J. Yao, J. Liu, H. Hofbauer, G. Chen, B. Yan, R. Shan and W. Li, *Energy Convers. Manag.*, 2016, **117**, 343–350.
17 G. Chen, J. Yao, J. Liu, B. Yan, R. Shan and W. Li, *Bioresour. Technol.*, 2015, **198**, 108–114.
18 G. Chen, J. Yao, J. Liu, B. Yan and R. Shan, *Renew. Energy*, 2016, **91**, 315–322.
19 K. A. Resende, C. N. Vila-Neto, R. C. Rabelo-Neto, F. B. Noronha and C. E. Hori, *Catal. Today*, 2015, **242**, 71–79.
20 X. Yang, L. Yang, W. Fan and H. Lin, *Catal. Today*, 2016, **269**, 56–64.
21 M.-Y. Chen, C.-B. Chen, B. Zada, Y. Fu, M. H. Qiao, K. N. Fan, X. X. Zhang, B.

N. Zong, A. Sarkar, M. K. Nazeeruddin, M. Grätzel and S. I. Seok, *Green Chem.*, 2016, **18**, 3858–3866.
22 H. Deng, L. Lin, Y. Sun, C. Pang, J. Zhuang, P. Ouyang, Z. Li and S. Liu, *Catal. Letters*, 2008, **126**, 106–111.
23 H. Deng, L. Lin, Y. Sun, C. Pang, J. Zhuang, P. Ouyang, J. Li and S. Liu, *Energy & Fuels*, 2009, **23**, 19–24.
24 J. A. Onrubia and J. R. González-velasco, *Appl. Catal. B, Environ.*, 2017, **213**, 198–210.
25 X. Yang, L. Luo and H. Zhong, *Catal. Commun.*, 2005, **6**, 13–17.
26 A. K. Ladavos and P. J. Pomonis, *Appl. Catal. A Gen.*, 1997, **165**, 73–85.
27 N. Russo, S. Furfori, D. Fino, G. Saracco and V. Specchia, *Appl. Catal. B Environ.*, 2008, **83**, 85–95.
28 S. Irusta, M. P. Pina and M. Men, *J. Catal.*, 1998, **412**, 400–412.
29 B.-S. Jiang, R. Chang and Y.-C. Lin, *Ind. Eng. Chem. Res.*, 2012, 120427144845004.
30 M. Popa, J. Frantti and M. Kakihana, *Solid State Ionics*, 2002, **155**, 135–141.
31 J. Shi, G. Liu, N. Wang and C. Li, *J. Mater. Chem.*, 2012, **22**, 18808.
32 P. Tang, Y. Tong, H. Chen, F. Cao and G. Pan, *Curr. Appl. Phys.*, 2013, **13**, 340–343.
33 F. Fang, N. Feng, L. Wang, J. Meng, G. Liu, P. Zhao, P. Gao and J. Ding, *Appl. Catal. B Environ.*, 2018, **236**, 184–194.
34 C. Lee, Y. Jeon, S. Hata, J. Park, R. Akiyoshi, H. Saito, Y. Teraoka, Y. Shul and H. Einaga, *Appl. Catal. B Environ.*, 2016, **191**, 157–164.
35 R. J. H. Voorhoeve, J. P. Remeika and L. E. Trimble, *Ann. New York Acad. Sci.*, 1976, 3.
36 G. Lee, E. Park, S. Yang, J. Park, S. Bu and M. Lee, *Nat. Publ. Gr.*, 2017, 1–11.
37 S. Royer, F. Bérubé and S. Kaliaguine, *Appl. Catal. A Gen.*, 2005, 282, 273–284.
38 R. Zhang, A. Villanueva, H. Alamdari and S. Kaliaguine, *Appl. Catal. A Gen.*, 2006, **307**, 85–97.
39 N. Tien-thao, H. Alamdari and S. Kaliaguine, *J. Solid State Chem.*, 2008, **181**, 2006–2019.
40 L. Zhang, Z. Xu, L. Cao and X. Yao, *Mater. Lett.*, 2007, **61**, 1130–1133.
41 N. Tien-thao, M. H. Zahedi-niaki, H. Alamdari and S. Kaliaguine, *J. Catal.*, 2007, **245**, 348–357.
42 M. Crespin and W. K. Hall, *J. Catal.*, 1981, **370**, 359–370.
43 J. Shu and S. Kaliaguine, *Appl. Catal. B Environ.*, 1998, **16**, 303–308.
44 S. Kaliaguine, A. Van Neste, V. Szabo, J. E. Gallot, M. Bassir and R. Muzychuk, *Appl. Catal. A Gen.*, 2001, **209**, 345–358.
45 Q. Zhang and F. Saito, *J. Mater. Sci.*, 2001, **36**, 2287–2290.
46 Q. Zhang, J. Lu and F. Saito, *Powder Technol.*, 2002, **122**, 145–149.
47 V. Szabo, M. Bassir, A. Van Neste and S. Kaliaguine, *Appl. Catal. B Environ. 43*, 2003, **43**, 81–92.
48 R. Zhang, A. Villanueva, H. Alamdari and S. Kaliaguine, *J. Catal.*, 2006, **237**, 368–380.
49 S. Royer, B. Levasseur, H. Alamdari, J. B. Jr, D. Duprez and S. Kaliaguine, *Appl. Catal. B Environ. 80*, 2008, **80**, 51–61.
50 S. Royer, D. Duprez, F. Can, X. Courtois, C. Batiot-dupeyrat, S. Laassiri and H. Alamdari, *Chem. Rev.*, 2014, **114**, 10292–10368.
51 M. Panneer Selvam and K. J. Rao, *Adv. Mater.*, 2000, **12**, 1621–1624.
52 R. K. J, B. Vaidhyanathan, M. Ganguli and P. A. Ramakrishnan, *Chem. Mater.*, 1999, **11**, 882–895.

53 L. K. Templeton and J. A. Pask, *J. Am. Ceram. Soc*, 1959, **42**, 212.
54 A. Kaddouri and S. Ifrah, *Catal. Commun.*, 2006, **7**, 109.
55 Y. Zhu, Y. Sun, X. Niu, F. Yuan and H. Fu, *Catal. Lett.*, 2010, **135**, 152.
56 Y. Zeng, Y. S. Lin and S. L. Swartz, *J. Memb. Sci.*, 1998, **150**, 87–98.
57 J.-W. Lee, Y.-T. Hsieh, N. De Marco, S.-H. Bae, Q. Han and Y. Yang, *J. Phys. Chem. Lett.*, 2017, **8**, 1999–2011.
58 L. Guironnet, P. Geffroy, N. Richet and T. Chartier, *Chem. Eng. Sci.*, 2016, **156**, 128–135.
59 U.S. Patent 3,330,697, 1967.
60 N. T. and P. V. Xin-Gang Li, Yan-Hua Dong, Hui Xian, Willinton Yesid Hern andez, Ming Meng, Hong-Hu Zou, Ai-Jing Ma, Tian-Yong Zhang, Zheng Jiang, *Energy Environ. Sci.*, 2011, **4**, 3351–3354.
61 A.-J. Ma, S. Z. Wang, C. Liu, H. Xian, Q. Ding, L. Guo, M. Meng, Y. S. Tan, N. Tsubaki, J. Zhang, L. R. Zheng and X. G. Li, *Appl. Catal. B Environ.*, 2014, **146**, 24–34.
62 J. A. Villoria, M. C. Alvarez-Galvan, S. M. Al-Zahrani, P. Palmisano, S. Specchia, V. Specchia, J. L. G. Fierro and R. M. Navarro, *Appl. Catal. B Environ.*, 2011, **105**, 276–288.
63 Z. Li, M. Meng, F. Dai, T. Hu, Y. Xie and J. Zhang, *Fuel*, 2012, **93**, 606–610.
64 G. Lee, I. Kim, I. Yang, J.-M. Ha, H. Bin Na and J. C. Jung, *Appl. Surf. Sci.*, 2017, **429**, 55–61.
65 Y. Li, S. Yao, W. Wen, L. Xue and Y. Yan, *J. Alloys Compd.*, 2010, **491**, 560–564.
66 A. Schön, J.-P. Dacquin, C. Dujardin and P. Granger, *Top. Catal.*, 2017, **60**, 300–306.
67 P. Ciambelli, S. Cimino, S. De Rossi, L. Lisi, G. Minelli, P. Porta and G. Russo, *Appl. Catal. B*, 2001, **29**, 239–250.
68 B. Zhao, R. Wang and X. Yang, *Catal. Commun.*, 2009, **10**, 1029–1033.
69 Y. Peng, W. Si, J. Luo, W. Su, H. Chang, J. Li, J. Hao and J. Crittenden, *Environ. Sci. Technol.*, 2016, **50**, 6442–6448.
70 J. Chen, M. Shen, X. Wang, J. Wang, Y. Su and Z. Zhao, *Catal. Commun.*, 2013, **37**, 105–108.
71 X. Zhu, X. Tu, M. Chen, Y. Yang, C. Zheng, J. Zhou and X. Gao, *Catal. Commun.*, 2017, **92**, 35–39.
72 C. M. Marcos, V. T. Rivero, V. A. Fuentes, M. S. S. Adsuar and M. J. I. Gómez, *Top. Catal.*, 2018, **0**, 0.
73 H. Taguchi, H. Yoshioka, D. Matsuda and M. Nagao, *J. Solid State Chem.*, 1993, **104**, 460–463.
74 Y. Shimizu and T. Murata, *J. Am. Ceram. Soc.*, 1997, **80**, 2702–2704.
75 S. K. Tiwari, P. Chartier and R. N. Singh, *J. Electrochem. Soc.*, 1995, **142**, 148–153.
76 M. J. Koponen, T. Venalainen, M. Suvanto and K. Kallinen, *J. Mol. Catal. A Chem.*, 2006, **258**, 246–250.
77 G. Xiong, Z. L. Zhi, X. Yang, L. Lu and X. Wang, *J. Mater. Sci. Lett.*, 1997, **16**, 1064–1068.
78 Y. Teraoka, H. Kakebayashi, I. Moriguchi and S. Kagawa, *J. Alloys Compd.*, 1993, **193**, 70–72.
79 W. Y. Hernandez, M. N. Tsampas, C. Zhao, A. Boreave, F. Bosselet and P. Vernoux, *Catal. Today*, 2015, **258**, 525–534.
80 T. Puangpetch, T. Sreethawong, S. Yoshikawa and S. Chavadej, *J. Mol. Catal. A Chem.*, 2009, **312**, 97–106.
81 S. N. Tijare, M. V. Joshi, P. S. Padole, P. A. Mangrulkar, S. S. Rayalu and N. K.

Labhsetwar, *Int. J. Hydrogen Energy*, 2012, **37**, 10451–10456.
82 A. Rabenau, *Angew. Chemie Int. Ed.*, 1985, **24**, 1026–1040.
83 J. C. Rendón-Angeles, ed. Z. Matamoros-Veloza, IntechOpen, Rijeka, 2016, p. Ch. 2.
84 J. Deng, L. Zhang, H. Dai and C. T. Au, *Catal. Letters*, 2009, **130**, 622–629.
85 R. Wang, Y. Zhu, Y. Qiu, C. F. Leung, J. He, G. Liu and T. C. Lau, *Chem. Eng. J.*, 2013, **226**, 123–130.
86 B. Paul and K. H. Choo, *Catal. Today*, 2014, **230**, 138–144.
87 J. W. Liu, G. Chen, Z. H. Li and Z. G. Zhang, *Int. J. Hydrogen Energy*, 2007, **32**, 2269–2272.
88 W. Wang, S. Liang, K. Ding, J. Bi, J. C. Yu, P. K. Wong and L. Wu, *J. Mater. Sci.*, 2014, **49**, 1893–1902.
89 L. F. da Silva, W. Avansi, J. Andrés, C. Ribeiro, M. L. Moreira, E. Longo and V. R. Mastelaro, *Phys. Chem. Chem. Phys.*, 2013, **15**, 12386.
90 H. Yu, S. Ouyang, S. Yan, Z. Li, T. Yu and Z. Zou, *J. Mater. Chem.*, 2011, **21**, 11347.
91 Y. Wang, H. Xu, X. Wang, X. Zhang, H. Jia and L. Zhang, *J. Phys. Chem. B*, 2006, **110**, 13835–13840.
92 Q. Kuang and S. Yang, *ACS Appl. Mater. Interfaces*, 2013, **5**, 3683–3690.
93 T. Ma, H. Li, T. Ren and Z. Yuan, *RSC Adv.*, 2012, **2**, 2790–2796.
94 X. Zhang, Y. Gong, S. Li and C. Sun, *ACS Catal.*, 2017, **7**, 7737–7747.
95 J. Kim, X. Chen, P. Shih and H. Yang, *ACS Sustain. Chem. Eng.*, 2017, **5**, 10910–10917.
96 J. Zhang, Y. Zhao, X. Zhao, Z. Liu and W. Chen, *Sci. Rep.*, 2014, **4**, 2–7.
97 M. S. Batista, M. Wallau, E. A. Sanches and Y. P. Mascarenhas, *Appl. Catal. B Environ.*, 2009, **90**, 441–450.
98 Y. Wang, J. Ren, Y. Wang, F. Zhang, X. Liu, Y. Guo and G. Lu, *J. Phys. Chem. C*, 2008, **112**, 15293–15298.
99 T. Valdes-Solıs, G. Marban and A. B. Fuertes, *Chem. Mater.*, 2005, **17**, 2003–2006.
100 Y. Wang, H. Arandiyan, H. A. Tahini, J. Scott, X. Tan, H. Dai, J. D. Gale, A. L. Rohl, S. C. Smith and R. Amal, *Nat. Commun.*, 2017, **8**, 1–7.
101 T. Yokoi, J. Sakuma, K. Maeda, K. Domen, T. Tatsumi and J. N. Kondo, *Phys. Chem. Chem. Phys.*, 2011, **13**, 2563.
102 M. Sadakane, T. Asanuma, J. Kubo and W. Ueda, *Chem. Mater.*, 2005, 3546–3551.
103 H. Arandiyan, Y. Wang, H. Sun, M. Rezaei and H. Dai, *Chem. Commun.*, 2018, **54**, 6484–6502.
104 Y. Chang, K. Yu, C. Zhang, Z. Yang, Y. Feng and H. Hao, *Appl. Catal. B, Environ.*, 2017, **215**, 74–84.
105 J. Zheng, J. Liu, Z. Zhao, J. Xu, A. Duan and G. Jiang, *Catal. Today*, 2012, **191**, 146–153.
106 K. Ji, H. Dai, J. Deng, X. Li, Y. Wang, B. Gao, G. Bai and C. Tong, *Appl. Catal. A, Gen.*, 2012, **447**–**448**, 41–48.
107 E. O. Chi, Y. N. Kim, J. C. Kim and N. H. Hur, *Chem. Mater.*, 2003, **15**, 0–2.
108 H. Arandiyan, H. Dai, J. Deng, Y. Liu, B. Bai, Y. Wang, X. Li, S. Xie and J. Li, *J. Catal.*, 2013, **307**, 327–339.
109 X. Li, H. Dai, J. Deng, Y. Liu, S. Xie, Z. Zhao, Y. Wang, G. Guo and H. Arandiyan, *Chem. Eng. J.*, 2013, **228**, 965–975.
110 H. Arandiyan, H. Dai, J. Deng, Y. Wang, S. Xie and J. Li, *Chem. Commun.*, 2013, **49**, 10748–10750.
111 K. Ji, H. Dai, J. Dai, J. Deng, F. Wang, H. Zhang and L. Zhang, *Catal. Today*, 2013, **201**, 40–48.

112 Y. Wei, J. Liu, Z. Zhao, Y. Chen, C. Xu and A. Duan, *Angew. Chemie - Int. Ed.*, 2011, 2326–2329.
113 K. Ji, H. Dai, J. Deng, H. Jiang, L. Zhang, H. Zhang and Y. Cao, *Chem. Eng. J.*, 2013, **214**, 262–271.
114 J. Chen, M. Shen, X. Wang, G. Qi, J. Wang and W. Li, *Appl. Catal. B Environ.*, 2013, **134**–**135**, 251–257.
115 J. Bassat, P. Odier, A. Villesuzanne, C. Marin and M. Pouchard, *Solid State Ionics*, 2004, **167**, 341–347.
116 H. Kondou, M. Fujimoto, H. Haneda and S. Shirasaki, *Jpn. J. Appl. Phys.*, 1989, **28**, 52.
117 M. Crespin, P. Levitz and L. Gatineau, *J. Chem. Soc. Faraday Trans. 2 Mol. Chem. Phys.*, 1983, **79**, 1181–1194.
118 T. Moriga, O. Usaka, I. Nakabayashi, T. Kinouchi, S. Kikkawa and F. Kanamaru, *Solid State Ionics*, 1995, **79**, 252–255.
119 J. Du, T. Zhang, F. Cheng, W. Chu, Z. Wu and J. Chen, *Inorg. Chem.*, 2014, **53**, 9106–9114.
120 J. Kim, X. Yin, K. Tsao, S. Fang and H. Yang, *J. Am. Chem. Soc.*, 2014, **3**, 8–11.
121 B. C. Tofield and W. R. Scott, *J. Solid State Chem.*, 1974, **10**, 183–194.
122 T. Inprasit, S. Wongkasemjit, S. J. Skinner, M. Burriel and P. Limthongkul, *RSC Adv.*, 2015, **5**, 2486–2492.
123 T. Nakamura, G. Petzow and L. J. Gauckler, *Mat. Res. Bull.*, 1979, **14**, 649–659.
124 N. A. Merino, B. P. Barbero, P. Ruiz and L. E. Cadús, *J. Catal.*, 2006, **240**, 245–257.
125 J. Zhang, X. Weng, Z. Wu, Y. Liu and H. Wang, *Appl. Catal. B Environ.*, 2012, **126**, 231–238.
126 S. Ivanova, A. Senyshyn, E. Zhecheva, K. Tenchev, V. Nikolov, R. Stoyanova and H. Fuess, *J. Alloys Compd.*, 2009, **480**, 279–285.
127 N. A. Merino, B. P. Barbero, P. Grange and L. E. Cadús, *J. Catal.*, 2005, **231**, 232–244.
128 B. Białobok, J. Trawczyński, W. Miśta and M. Zawadzki, *Appl. Catal. B Environ.*, 2007, **72**, 395–403.
129 B. Levasseur and S. Kaliaguine, *Appl. Catal. A Gen.*, 2008, **343**, 29–38.
130 L. B. Sis, G. P. Wirtz and S. C. Sorenson, *J. Appl. Phys.*, 1973, **44**, 5553.
131 L. Huang, M. Bassir and S. Kaliaguine, *Appl. Surf. Sci.*, 2005, **243**, 360–375.
132 R. Lago, G. Bini, M. A. Peña and J. L. G. Fierro, *J. Catal.*, 1997, **167**, 198–209.
133 Y. Cui, V. Galvita, L. Rihko-Struckmann, H. Lorenz and K. Sundmacher, *Appl. Catal. B Environ.*, 2009, **90**, 29–37.
134 H. Falcón, M. J. Martínez-Lope, J. A. Alonso and J. L. G. Fierro, *Solid State Ionics*, 2000, **131**, 237–248.
135 J. Chen, M. Shen, X. Wang, J. Wang, Y. Su and Z. Zhao, *Catal. Commun.*, 2013, **37**, 105–108.
136 B. P. Barbero, J. A. Gamboa and L. E. Cadús, *Appl. Catal. B Environ.*, 2006, **65**, 21–30.
137 S. M. de Lima and J. M. Assaf, *Catal. Letters*, 2006, **108**, 63–70.
138 B. Izadkhah, A. Niaei, M. J. Illán-Gómez, D. Salari, A. Tarjomannejad and V. Albaladejo-Fuentes, *Ind. Eng. Chem. Res.*, 2017, **56**, 3880–3886.
139 B. Levasseur and S. Kaliaguine, *J. Solid State Chem.*, 2008, **181**, 2953–2963.
140 L. Lisi, G. Bagnasco, P. Ciambelli, S. De Rossi, P. Porta, G. Russo and M. Turco, *J. Solid State Chem.*, 1999, **146**, 176–183.
141 Y.-H. Dong, H. Xian, J.-L. Lv, C. Liu, L. Guo, M. Meng, Y.-S. Tan, N. Tsubaki and X.-G. Li, *Mater. Chem. Phys.*, 2014, **143**, 578–586.

142 Y. Lu, Q. Dai and X. Wang, *Catal. Commun.*, 2014, **54**, 114–117.
143 S. Ponce, M. A. Peña and J. L. G. Fierro, *Appl. Catal. B Environ.*, 2000, **24**, 193–205.
144 P. Ciambelli, S. Cimino, S. De Rossi, M. Faticanti, L. Lisi, G. Minelli, I. Pettiti, P. Porta, G. Russo and M. Turco, *Appl. Catal. B Environ.*, 2000, **24**, 243–253.
145 R. Zhang, A. Villanueva, H. Alamdari and S. Kaliaguine, *Appl. Catal. B Environ.*, 2006, **64**, 220–233.
146 R. Pereñíguez, J. L. Hueso, F. Gaillard, J. P. Holgado and A. Caballero, *Catal. Letters*, 2012, **142**, 408–416.
147 Y. Lu, A. Ma, Y. Yu, R. Tan, C. Liu, P. Zhang, D. Liu and J. Gui, *ACS Sustain. Chem. Eng.*, 2019, **7**, 2906–2910.
148 T. Nitadori and M. Misono, *J. Catal.*, 1985, **93**, 459–466.
149 Q. Shen, Y. Zhang, H. Ding, L. Wu, Y. Xu, B. Shi, Y. Zheng and J. Yuan, *Energies*, 2017, **10**, 164.
150 D. Ferri and L. Forni, *Appl. Catal. B Environ.*, 1998, **16**, 119–126.
151 R. Zhang, H. Alamdari and S. Kaliaguine, *J. Catal.*, 2006, **242**, 241–253.
152 R. M. García de la Cruz, H. Falcón, M. A. Peña and J. L. G. Fierro, *Appl. Catal. B Environ.*, 2001, **33**, 45–55.
153 Y. Yi, H. Liu, B. Chu, Z. Qin, L. Dong, H. He, C. Tang, M. Fan and L. Bin, *Chem. Eng. J.*, 2019, **369**, 511–521.
154 T. Nakamura, M. Misono and Y. Yoneda, *Bull. Chem. Soc. Jpn.*, 1982, **55**, 394–399.
155 S. O. Choi, M. Penninger, C. H. Kim, W. F. Schneider and L. T. Thompson, *ACS Catal.*, 2013, **3**, 2719–2728.
156 T. Nitadori, S. Kurihara and M. Misono, *J. Catal.*, 1986, **98**, 221–228.
157 I. Kuritsyna, V. Sinitsyn, A. Melnikov, Y. Fedotov, E. Tsipis, A. Viskup, S. Bredikhin and V. Kharton, *Solid State Ionics*, 2014, **262**, 349–353.
158 R.-K. Chen, T.-F. Yu, M.-X. Wu, T.-W. Tzeng, P.-W. Chung and Y.-C. Lin, *ACS Sustain. Chem. Eng.*, 2018, **6**, 11949–11958.
159 A. Gervasini and A. Auroux, *J. Catal.*, 1991, **131**, 190–198.
160 M. A. Aramendía, V. Borau, C. Jiménez, J. M. Marinas, A. Porras and F. J. Urbano, *J. Catal.*, 1996, **161**, 829–838.
161 J. E. Rekoske and M. A. Barteau, *J. Catal.*, 1997, **165**, 57–72.
162 P. Xiao, J. Zhu, D. Zhao, Z. Zhao, F. Zaera and Y. Zhu, *ACS Appl. Mater. Interfaces*, 2019, **11**, 15517–15527.
163 J. N. Kuhn and U. S. Ozkan, *J. Catal.*, 2008, **253**, 200–211.
164 M. M. Natile, E. Ugel, C. Maccato and A. Glisenti, *Appl. Catal. B Environ.*, 2007, **72**, 351–362.
165 R. Hammami, H. Batis and C. Minot, *Surf. Sci.*, 2009, **603**, 3057–3067.
166 G. S. Foo, F. Polo-Garzon, V. Fung, D. Jiang, S. H. Overbury and Z. Wu, *ACS Catal.*, 2017, **7**, 4423–4434.
167 H. Taguchi, S. Yamasaki, A. Itadani, M. Yosinaga and K. Hirota, *Catal. Commun.*, 2008, **9**, 1913–1915.
168 P. H. T. Ngamou and N. Bahlawane, *Chem. Mater.*, 2010, **22**, 4158–4165.
169 L. Borovskikh, G. Mazo and E. Kemnitz, *Solid State Sci.*, 2003, 5, 409–417.
170 L. A. Isupova, G. M. Alikina, S. V Tsybulya, N. N. Boldyreva, G. N. Kryukova, I. S. Yakovleva, V. P. Isupov and V. A. Sadykov, *Int. J. Inorg. Mater.*, 2001, **3**, 559–562.
171 R. N. S. H. Magalhães, F. S. Toniolo, V. T. da Silva and M. Schmal, *Appl. Catal. A Gen.*, 2010, **388**, 216–224.
172 X. Yan, Q. Huang, B. Li, X. Xu, Y. Chen, S. Zhu and S. Shen, *J. Ind. Eng. Chem.*,

2013, **19**, 561–565.
173 T. Vaz and A. V Salker, *Mater. Sci. Eng. B*, 2007, **143**, 81–84.
174 H. Falcón, J. Baranda, J. M. Campos-Martín, M. A. Peña and J. L. G. Fierro, in *12th International Congress on Catalysis*, eds. A. Corma, F. V Melo, S. Mendioroz and J. L. G. B. T.-S. in S. S. and C. Fierro, Elsevier, 2000, vol. 130, pp. 2195–2200.
175 C. N. R. Rao, *J. Phys. Chem. B*, 2000, **104**, 5877–5889.
176 S. Cimino, S. Colonna, S. De Rossi, M. Faticanti, L. Lisi, I. Pettiti and P. Porta, *J. Catal.*, 2002, **205**, 309–317.
177 S. Liang, F. Teng, G. Bulgan and Y. Zhu, *J. Phys. Chem. C*, 2007, **111**, 16742–16749.
178 A. Tarjomannejad, A. Niaei, A. Farzi, D. Salari and P. R. Zonouz, *Catal. Letters*, 2016, **146**, 1544–1551.
179 J. Zhang, D. Tan, Q. Meng, X. Weng and Z. Wu, *Appl. Catal. B, Environ.*, 2015, **172**–**173**, 18–26.
180 H. Taguchi, K. Matsu-ura, M. Takada and K. Hirota, *J. Solid State Chem.*, 2012, **190**, 157–161.
181 H. Taguchi, S. Matsuoka, M. Kato and K. Hirota, *J. Mater. Sci.*, 2009, **44**, 5732–5736.
182 Z. Gao and R. Wang, *Appl. Catal. B Environ.*, 2010, **98**, 147–153.
183 J. Kirchnerova, M. Alifanti and B. Delmon, *Appl. Catal. A Gen.*, 2002, **231**, 65–80.
184 M. Bosomoiu, G. Bozga, D. Berger and C. Matei, *Appl. Catal. B Environ.*, 2008, **84**, 758–765.
185 N. E. Machin, C. Karakaya and A. Celepci, *Energy & Fuels*, 2008, **22**, 2166–2171.
186 M. Alifanti, R. Auer, J. Kirchnerova, F. Thyrion, P. Grange and B. Delmon, *Appl. Catal. B Environ.*, 2003, **41**, 71–81.
187 R. Spinicci, M. Faticanti, P. Marini, S. De Rossi and P. Porta, *J. Mol. Catal. A Chem.*, 2003, **197**, 147–155.
188 S. A. Hosseini, D. Salari, A. Niaei and S. A. Oskoui, *J. Ind. Eng. Chem.*, 2013, **19**, 1903–1909.
189 M. Alifanti, M. Florea and V. I. Pârvulescu, *Appl. Catal. B Environ.*, 2007, **70**, 400–405.
190 B. Levasseur and S. Kaliaguine, *Appl. Catal. B Environ.*, 2009, **88**, 305–314.
191 G. Pecchi, P. Reyes, R. Zamora, L. E. Cadús and J. L. G. Fierro, *J. Solid State Chem.*, 2008, **181**, 905–912.
192 T. Hou, H. Yang, X. Fan and X. Zhang, *Catal. Letters*, 2011, **141**, 1215–1218.
193 G. Biausque and Y. Schuurman, *J. Catal.*, 2010, **276**, 306–313.
194 P. Li, R. Zhang, N. Liu and S. Royer, *Appl. Catal. B Environ.*, 2017, **203**, 174–188.
195 D. Wang, Y. Peng, Q. Yang, S. Xiong, J. Li and J. Crittenden, *Environ. Sci. Technol.*, 2018, **52**, 7443–7449.
196 Z. H. Zhang, C. S. Cheung, T. L. Chan and C. D. Yao, *Atmos. Environ.*, 2010, **44**, 1054–1061.
197 C. H. Kim, G. Qi, K. Dahlberg and W. Li, *Science (80-.).*, 2010, **327**, 1624–1627.
198 T. Andana, M. Piumettia, S. Bensaida, L. Veyre, C. Thieuleux, N. Russo, D. Fino, E. A. Quadrelli and R. Pirone, *Appl. Catal. B Environ.*, 2018, **226**, 147–161.
199 T. Andana, M. Piumetti, S. Bensaid, L. Veyre, C. Thieuleux, N. Russo, D. Fino and E. A. Q. R. Pirone, *Appl. Catal. B, Environ.*, 2017, **216**, 41–58.
200 T. Andana, M. Piumetti, S. Bensaid, L. Veyre, C. Thieuleux, N. Russo, D. Fino, E. Alessandra and R. Pirone, *Appl. Catal. B Environ.*, 2017, **209**, 295–310.
201 V. Torregrosa-Rivero, V. Albaladejo-Fuentes, M. S. Sánchez-Adsuar and M. J. Illán-Gómez, *RSC Adv.*, 2017, **7**, 35228–35238.
202 S. Liu, X. Wu, H. Luo, D. Weng and R. Ran, *J. Phys. Chem. C*, 2015, **119**, 17218–

17227.
203 H. Zhang, Y. Zhu, S. Wang, M. Zhao, M. Gong and Y. Chen, *Fuel Process. Technol. J.*, 2015, **137**, 38–47.
204 S. Liu, X. Wu, D. Weng, M. Li and R. Ran, *ACS Catal.*, 2015, **5**, 909–919.
205 F. Lin, X. Wu, S. Liu, D. Weng and Y. Huang, *Chem. Eng. J.*, 2013, **226**, 105–112.
206 I. Atribak, B. Azambre and A. B. Lo, *Appl. Catal. B, Environ.*, 2009, **92**, 126–137.
207 R. Zhang, N. Luo, B. Chen and S. Kaliaguine, *Energy and Fuels*, 2010, **24**, 3719–3726.
208 H. Wang, Z. Zhao, P. Liang, C. Xu, A. Duan, G. Jiang, J. Xu and J. Liu, *Catal. Letters*, 2008, **124**, 91–99.
209 F. Bin, C. Song, G. Lv, J. Song, C. Gong and Q. Huang, *Ind. Eng. Chem. Res.*, 2011, **50**, 6660–6667.
210 R. D. Shannon, *Acta Cryst.*, 1976, 751.
211 A. Mishra and R. Prasad, *Bull. Chem. React. Eng. Catal.*, 2017, **12**, 469–477.
212 W. Y. Hernández, M. N. Tsampas, C. Zhao, A. Boreave, F. Bosselet and P. Vernoux, *Catal. Today*, 2015, **258**, 525–534.
213 J. Xu, J. Liu, Z. Zhao, J. Zheng, G. Zhang, A. Duan and G. Jiang, *Catal. Today*, 2010, **153**, 136–142.
214 H. Wang, Z. Zhao, C. M. Xu and J. Liu, *Catal. Letters*, 2005, **102**, 251–256.
215 W. Yao, R. Wang and X. Yang, *Catal. Letters*, 2009, **130**, 613–621.
216 V. G. Milt, M. A. Ulla and E. E. Miro, *Appl. Catal. B Environ. 57*, 2005, **57**, 13–21.
217 K. Wang, L. Qian, L. Zhang, H. Liu and Z. Yan, *Catal. Today*, 2010, **158**, 423–426.
218 X. Peng, H. Lin, Z. Huang and W. Shangguan, *Chem. Eng. Technol.*, 2006, **29**, 1262–1266.
219 S.-S. Hong and G.-D. Lee, *Catal. Today*, 2000, **63**, 397–404.
220 B. Zhao, R. Wang, W. Yao, X. Yang and B. Zhou, *Catal. Letters*, 2009, **132**, 41–49.
221 J. Liu, Z. Zhao, C. Xu, A. Duan, T. Meng and X. Bao, *Catal. Today*, 2007, **119**, 267–272.
222 S. Matsumoto, *CATTECH*, 2000, **4**, 102–109.
223 S. Elbouazzaoui, E. C. Corbos, X. Courtois, P. Marecot and D. Duprez, *Appl. Catal. B Environ.*, 2005, **61**, 236–243.
224 V. G. Milt, C. A. Querini, E. E. Miró and M. A. Ulla, *J. Catal.*, 2003, **220**, 424–432.
225 S. Hodjati, C. Petit, V. Pitchon and A. Kiennemann, *Appl. Catal. B Environ.*, 2000, **27**, 117–126.
226 S. Hodjati, C. Petit, V. Pitchon and A. Kiennemann, *Appl. Catal. B Environ.*, 2001, **30**, 247–257.
227 H. Xian, F.-L. Li, X.-G. Li, X.-W. Zhang, M. Meng, T.-Y. Zhang and N. Tsubaki, *Fuel Process. Technol.*, 2011, **92**, 1718–1724.
228 C. Ge, L. Li, H. Xian, H. Yan, M. Meng and X. Li, *Fuel Process. Technol.*, 2014, **120**, 1–7.
229 H. Xian, X. Zhang, X. Li, L. Li, H. Zou, M. Meng, Q. Li, Y. Tan and N. Tsubaki, *J. Phys. Chem. C*, 2010, **114**, 11844–11852.
230 X. Li, J. Chen, P. Lin, M. Meng, Y. Fu, J. Tu and Q. Li, *Catal. Commun.*, 2004, **5**, 25–28.
231 V. N. Stathopoulos, V. C. Belessi, T. V Bakas, S. G. Neophytides, C. N. Costa, P. J. Pomonis and A. M. Efstathiou, *Appl. Catal. B Environ.*, 2009, **93**, 1–11.
232 V. C. Belessi, C. N. Costa, T. V Bakas, T. Anastasiadou, P. J. Pomonis and A. M. Efstathiou, *Catal. Today*, 2000, **59**, 347–363.

233 X. Wu, L. Xu and D. Weng, *Catal. Today*, 2004, **90**, 199–206.
234 R. Zhang, N. Luo, W. Yang, N. Liu and B. Chen, *J. Mol. Catal. A Chem.*, 2013, **371**, 86–93.
235 R. Zhang, W. Yang, N. Luo, P. Li, Z. Lei and B. Chen, *Appl. Catal. B Environ.*, 2014, **146**, 94–104.
236 F. Polo-Garzon and Z. Wu, *J. Mater. Chem. A*, , DOI:10.1039/C7TA10591F.
237 M. Ao, G. H. Pham, V. Sage and V. Pareek, *Fuel*, 2017, **206**, 390–400.
238 G. Tesquet, J. Faye, F. Hosoglu, A.-S. Mamede, F. Dumeignil and M. Capron, *Appl. Catal. A Gen.*, 2016, **511**, 141–148.
239 T.-F. Yu, C.-W. Chang, P.-W. Chung and Y.-C. Lin, *Fuel Process. Technol.*, 2019, **194**, 106117.
240 R. Klimkiewicz and J. Trawczyński, *Appl. Catal. A Gen.*, 2009, **360**, 199–204.
241 A. Cyganiuk, R. Klimkiewicz and J. P. Lukaszewicz, *Mater. Res. Bull.*, 2011, **46**, 327–332.
242 M. Zawadzki, H. Grabowska and J. Trawczyński, *Solid State Ionics*, 2010, **181**, 1131–1139.
243 K. Tanabe and T. Nishizaki, The Chemical Society, London, 1977, p. 863.
244 C. H. Kim, G. Qi, K. Dahlberg and W. Li, *Science (80-.).*, 2010, **327**, 1624–1627.
245 M. A. Hayward, E. J. Cussen, J. B. Claridge, M. Bieringer, M. J. Rosseinsky, C. J. Kiely, S. J. Blundell, I. M. Marshall and F. L. Pratt, *Science (80-.).*, 2002, **295**, 1882–1884.
246 C. A. Bridges, G. R. Darling, M. A. Hayward and M. J. Rosseinsky, *J. Am. Chem. Soc.*, 2005, **127**, 5996–6011.
247 C. A. Bridges, F. Fernandez-Alonso, J. P. Goff and M. J. Rosseinsky, *Adv. Mater.*, 2006, **18**, 3304–3308.
248 R. M. Helps, N. H. Rees and M. A. Hayward, *Inorg. Chem.*, 2010, **49**, 11062–11068.
249 J. Bang, S. Matsuishi, H. Hiraka, F. Fujisaki, T. Otomo, S. Maki, J. I. Yamaura, R. Kumai, Y. Murakami and H. Hosono, *J. Am. Chem. Soc.*, 2014, **136**, 7221–7224.
250 T. Katayama, A. Chikamatsu, K. Yamada, K. Shigematsu, T. Onozuka, M. Minohara, H. Kumigashira, E. Ikenaga and T. Hasegawa, *J. Appl. Phys.*, , DOI:10.1063/1.4961446.
251 F. Denis Romero, A. Leach, J. S. Möller, F. Foronda, S. J. Blundell and M. A. Hayward, *Angew. Chemie - Int. Ed.*, 2014, **53**, 7556–7559.
252 C. Tassel, Y. Goto, D. Watabe, Y. Tang, H. Lu, Y. Kuno, F. Takeiri, T. Yamamoto, C. M. Brown, J. Hester, Y. Kobayashi and H. Kageyama, *Angew. Chemie - Int. Ed.*, 2016, **55**, 9667–9670.
253 C. Tassel, Y. Goto, Y. Kuno, J. Hester, M. Green, Y. Kobayashi and H. Kageyama, *Angew. Chemie - Int. Ed.*, 2014, **53**, 10377–10380.
254 Y. Goto, C. Tassel, Y. Noda, O. Hernandez, C. J. Pickard, M. A. Green, H. Sakaebe, N. Taguchi, Y. Uchimoto, Y. Kobayashi and H. Kageyama, *Inorg. Chem.*, 2017, **56**, 4840–4845.
255 T. Sakaguchi, Y. Kobayashi, T. Yajima, M. Ohkura, C. Tassel, F. Takeiri, S. Mitsuoka, H. Ohkubo, T. Yamamoto, J. Kim, N. Tsuji, A. Fujihara, Y. Matsushita, J. Hester, M. Avdeev, K. Ohoyama and H. Kageyama, *Inorg. Chem.*, 2012, **51**, 11371–11376.
256 Y. Kobayashi, O. J. Hernandez, T. Sakaguchi, T. Yajima, T. Roisnel, Y. Tsujimoto, M. Morita, Y. Noda, Y. Mogami, A. Kitada, M. Ohkura, S. Hosokawa, Z. Li, K. Hayashi, Y. Kusano, J. E. Kim, N. Tsuji, A. Fujiwara, Y. Matsushita, K. Yoshimura, K. Takegoshi, M. Inoue, M. Takano and H. Kageyama, *Nat. Mater.*, 2012, **11**, 507–511.

257 T. Yajima, A. Kitada, Y. Kobayashi, T. Sakaguchi, G. Bouilly, S. Kasahara, T. Terashima, M. Takano and H. Kageyama, *J. Am. Chem. Soc.*, 2012, **134**, 8782–8785.
258 T. Yajima, F. Takeiri, K. Aidzu, H. Akamatsu, K. Fujita, W. Yoshimune, M. Ohkura, S. Lei, V. Gopalan, K. Tanaka, C. M. Brown, M. A. Green, T. Yamamoto, Y. Kobayashi and H. Kageyama, *Nat. Chem.*, 2015, **7**, 1017–1023.
259 N. Masuda, Y. Kobayashi, O. Hernandez, T. Bataille, S. Paofai, H. Suzuki, C. Ritter, N. Ichijo, Y. Noda, K. Takegoshi, C. Tassel, T. Yamamoto and H. Kageyama, *J. Am. Chem. Soc.*, 2015, **137**, 15315–15321.
260 T. Yamamoto, R. Yoshii, G. Bouilly, Y. Kobayashi, K. Fujita, Y. Kususe, Y. Matsushita, K. Tanaka and H. Kageyama, *Inorg. Chem.*, 2015, **54**, 1501–1507.
261 Y. Kobayashi, O. Hernandez, C. Tassel and H. Kageyama, *Sci. Technol. Adv. Mater.*, 2017, **18**, 905–918.
262 Y. Tang, Y. Kobayashi, C. Tassel, T. Yamamoto and H. Kageyama, *Adv. Energy Mater.*, 2018, **8**, 1–7.
263 Y. Tang, Y. Kobayashi, N. Masuda, Y. Uchida and H. Okamoto, *Adv. Energy Mater.*, 2018, **8**, 1801772.

Chapter II - Experimental Section

2.1 Catalysts preparation

2.1.1. Solid state synthesis of $LaSrCoO_4$ and $BaTiO_3$

$LaSrCoO_4$ powder was synthesized by conventional solid-state method. Stoichiometric quantities of La_2O_3 (Alfa Aesar, 99.99 %), $SrCO_3$ (Aldrich, 99.9 %) and Co_3O_4 (Aldrich, 99.9 %) were mixed in ethanol, and La_2O_3 was previously dried overnight at 900 °C to remove absorbed species. Due to slight volatility at high sintering temperature, 1 % extra of Co_3O_4 is required for the reaction. The mixture was grinded by an agate mortar and pestle for 60 min, pelletized at pressure of 10 MPa, and annealed in a Carbolite tube furnace under Ar-flow in at 1000 °C in 15 h with a heating rate of 10 °C min^{-1} (Fig. 2.1). After the first heating, the powder is re-ground in the mortar in 90 min without ethanol and pelletized under 10 MPa pressure. Pellets, each of about 1.0 gram, are reheated in the argon furnace at 1200 °C and 1250 °C in 15 h at each temperature with heating rate of 15 °C min^{-1}.

Figure 2.1 – The Ar-flow furnace setup for $LaSrCoO_4$ synthesis and mortar pestle machine.

Perovskite $BaTiO_3$ was also prepared by solid-state reaction at 1200 °C. $BaCO_3$ (Aldrich, 99.98 %) and anatase-TiO_2 (Aldrich, 99.8 %) were stoichiometrically mixed in ethanol, grinded for 60 min. After grinding, the mixed powder was then heated at 800 °C in 12 h following by pelletizing under 10 MPa pressure. The pellets were later annealed at 1200 °C in 24 h and finally dried at 80 °C and stored in the vacuum.

2.1.2. Oxyhydride $LaSrCoO_{4-x}H_y$ and $BaTiO_{3-x}H_x$ synthesis

Oxyhydride $LaSrCoO_{4-x}H_y$ was synthesized by reducing $LaSrCoO_4$ with a strong reducing agent CaH_2. The reduction is begun by mixing and grinding $LaSrCoO_4$ (0.967 g) with CaH_2 (0.233 g, Aldrich 95 %) in an argon glovebox with a ratio of 1:2 (Fig. 2.2). Argon atmosphere in the glovebox prevents any contact between reducing agent and air because CaH_2 is strongly reactive with the air oxygen. The process is followed by placing the ground powder in a glass Pyrex tube (150 mm of length, 17-mm outer diameter and wall thickness of 2 mm) and sealed (Fig. 2.3). The amount of CaH_2 should be controlled to be lower than 0.24 g to avoid possible explosion caused by H_2 released from the reaction, breaking the tube. The argon-filled-tube was removed from the glovebox, evacuated in 10 min and flame welded. The tube was covered by a metallic tube to protect the oven in case of explosion of the Pyrex tube. The tube was kept at 350 °C in 3 h and 450 °C in 48 h. The reacted powder after annealed was carefully taken out of the furnace and cooled down. Because of the high pressure inside the tube, the glass tube could be broken down into tiny pieces and they may mix with the powder, resulting in a hard separation of the products from glass pieces. The hydride powder is washed and filtered by 100 ml of 0.1 M NH_4Cl in methanol and additional 50 ml CH_3OH to remove excess CaH_2 and by-product CaO.

Figure 2.2 – Argon glovebox and a flame sealed tube.

Similarly, $BaTiO_{3-x}H_x$ was also synthesized by reducing $BaTiO_3$ with CaH_2. Prior to the reaction, $BaTiO_3$ is dried in an oven at 200 °C overnight. $BaTiO_3$ (0.28 g) and CaH_2 (0.15 g) are mixed and ground in molar ratio of 1:3 in the argon glovebox. The powder is pelletized under the pressure of around 10 MPa and placed in a Pyrex tube. All steps were

conducted in glove box. The experiment is followed by evacuating the tube in 30 mins and flame sealing it. The tube is then heated at the temperatures of about 530 °C for 6-7 days. The synthesis is finalized by washing and filtering the product by 100 ml of 0.1M NH_4Cl/CH_3OH, 50 ml CH_3OH respectively to remove excess CaH_2 and CaO. The washed compound is dried in oven at 120 °C in 3 h.

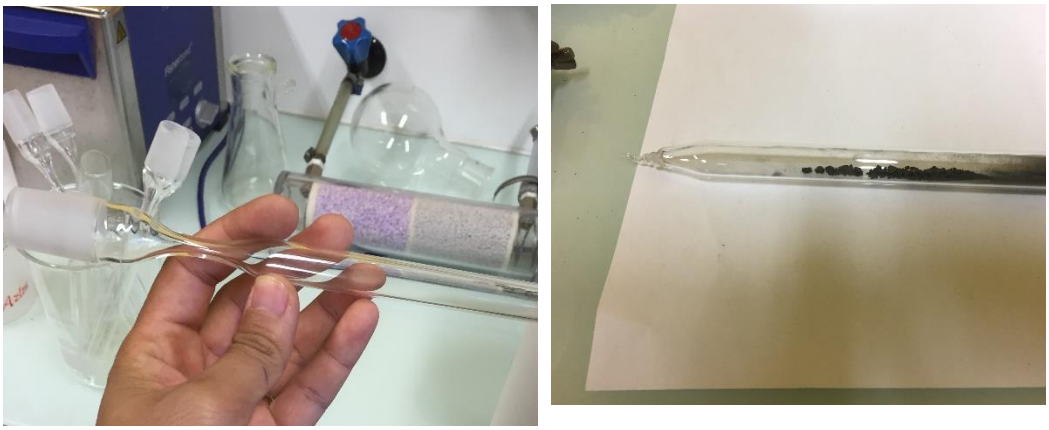

Figure 2.3 – An empty glass tube (150 x 17 x 2 mm of length x diameter x thickness) and sealed sample tube which was previously evacuated.

2.1.3 Sol-gel synthesis of perovskite oxides

Table 2.1 – Materials' weights for the synthesis of perovskite oxides by the sol-gel approach.

Catalysts	**Materials (g)**				
	$La(NO_3)_3$ $6H_2O$	$Al(NO_3)_3$· $9H_2O$	$Co(NO_3)_2$ $\cdot 6H_2O$	$Ga(NO_3)_3$ $\cdot xH_2O$	$C_6H_8O_7$ $\cdot H_2O$
$LaAlO_3$	1.5000	1.2990	-	-	2.9105
$LaAl_{0.75}Co_{0.25}O_3$	1.5000	0.9742	0.2519	-	2.9105
$LaAl_{0.5}Co_{0.5}O_3$	1.5000	0.6495	0.5039	-	2.9105
$LaAl_{0.25}Co_{0.75}O_3$	1.5000	0.3247	0.7558	-	2.9105
$LaCoO_3$	1.5000	-	1.0077	-	2.9105
$LaAl_{0.75}Ga_{0.25}O_3$	1.5000	0.9742	-	0.3071	2.9105

$LaAl_{1-x}Co_xO_3$ (x= 0, 0.25, 0.5, 0.75 and 1) and $LaAl_{0.75}B_{0.25}O_3$ (B = Co, Ga) were prepared by a sol–gel method with citric acid. $La(NO_3)_3 \cdot 6H_2O$ (Sigma-Aldrich,99%), $Al(NO_3)_3 \cdot 9H_2O$ (Sigma-Aldrich, 99%), $Co(NO_3)_2 \cdot 6H_2O$ (Sigma-Aldrich,99%) $Ga(NO_3)_3 \cdot xH_2O$ (Alfa, 99.99%) were used as metal precursors and citric acid $C_6H_8O_7 \cdot H_2O$ as a gel-forming agent. Before the synthesis, $Ga(NO_3)_3 \cdot xH_2O$ was treated by thermal gravimetric analysis to determine H_2O quantity. Quantities of materials can be seen in Tab. 2.1. In brief, the stoichiometric amounts of nitrate salts were dissolved in deionized water (~ 80 mL). A suitable amount of citric acid (citric acid:metal = 2 mol/mol) was added to the solution

where the pH was kept at 7.5 ± 0.5 by dropwise of ammonia addition. The solution was stirred and evaporated at 80 °C until the gel was formed. The gel was then kept at 150 °C for 3 h and at calcination temperature (500, 600 and 700 °C) for 5 h with ramp-up of 5 °C min^{-1}.

2.2 Catalysts characterization

2.2.1 Oxyhydride perovskites $LaSrCoO_{4-x}H_y$ and $BaTiO_{3-x}H_x$

X-ray diffraction (XRD). X-ray diffraction analysis was performed using a PANalytical X'Pert PRO system with an X'Celerator detector operating in the Bragg–Brentano geometry (θ/2θ) using Cu K_α (45 kV and 40 mA) (Fig. 2.4). The diffraction was recorded from 20 ° to 80 ° of 2θ angle with a step size of 0.017 ° and time-per-step of 50 s. The data analysis was carried out by Rietveld refinement using FullProf software with Thompson-Cox-Hastings pseudo-Voigt shape function. The space group of I4/mmm for $LaSrCoO_4$, Immm for $LaSrCoO_{4-x}H_y$, and P4mm for both $BaTiO_3$ and $BaTiO_{3-x}H_x$.

Figure 2.4– Empyrean PANalytical diffractometer for in-situ XRD experiments

In-situ XRD studies were performed on an Empyrean PANalytical diffractometer with Cu-K_α source (30 mA, 45 kV) in a continuous mode under 5% H_2/N_2 (20 mL min^{-1}) and air during heating to 700 °C with heating rate of 10 °C min^{-1}. A pattern was recorded at room temperature from 12 to 60 ° of 2θ with a step size of 0.026 ° and step time of 296 s. The next measurement was recorded at 150 °C with the same parameters, and the following

patterns were measured every 50 °C. A final record was conducted after cooling down to room temperature. Further High Resolution *in-situ* XRD measurements were also conducted at specific temperatures (450, 750, 1050 °C) under the same reducing condition. For the HR in-situ XRD experiments, the patterns were recorded from 20 to 70 ° of 2θ with a step size of 0.026 and step time of 1200 s.

Magnetic measurement. Magnetic properties were measured on a Superconducting Quantum Interference Design (SQUID) magnetometer MPMS XL7. DC magnetization-magnetic field (M-H) loops were carried at 2 K and 300 K in a range of 0- 5 T of external magnetic field. For the magnetic susceptibility ZFC (zero-field cooled)-FC (field cooled) measurements, samples were cooled in zero-field down to 2 K and then the required fields (0.01 T or 0.05 T) were applied, and data were recorded during heating until 400 K for ZFC curve. After reaching 400 K, data were recorded during cooling down to 2K in the applied field for the FC data.

Fourier-transform infrared spectroscopy (FT-IR). (FT-IR) spectra of powder samples mixed in KBr pellets were recorded at 2 cm^{-1} resolutions on a Bruker FTIR Equinox 55 spectrometer, equipped with a DTGS (deuterated-triglycine sulfate) cryodetector.

Thermogravimetric mass spectroscopic (TG-MS) measurements. TGA-MS experiments were carried out on a NETSCH thermobalance Jupiter STA 449C, equipped with a PFEIFFER VACUUM ThermoStar mass spectrometer (MS) using heating rate 10 °C min^{-1} under air from ambient temperature to 800 °C.

Scanning Electron Microscopy / Energy Dispersive X-Ray Spectroscopy (SEM/EDS) data were collected on a Zeiss Supra 40 Merlin microscope equipped with a Gemini II column with source of 20 kV

Temperature programmed reduction (H_2-TPR). Reducibility of the oxyhydrides was investigated using a TPD/R/O 1100 ThermoQuest instrument with a thermal conductivity detector (TCD). In a typical experiment, a quartz tube reactor was loaded with ca. 50-60 mg sample and heated between 50 and 1050 °C with ramp of 10 °C min^{-1}, under 20 ml min^{-1} of 5% H_2/Ar, hold for 60 min before cooling down to room temperature.

X-ray photoelectron spectroscopy (XPS). Surface characterization was studied by a PHI 5000 Versaprobe scanning X-ray photoelectron spectrometer (monochromatic Al Kα X-ray source with 1486.6 eV energy). A spot size of 100 μm was used in order to collect the

photoelectron signal for both the high resolution (HR) and the survey spectra. Different pass energy values were exploited: 187.85 eV for survey spectra and 23.5 eV for HR peaks. All samples were analyzed with a combined electron and Ar ion gun neutralizer system, in order to reduce the charging effect during the measurements. The XPS spectra were calibrated with adventitious C 1s peak at 284.5 eV.

2.2.2 Perovskite oxides $LaAl_{1-x}Co_xO_3$ and $LaAl_{0.75}B_{0.25}O_3$ (B = Co, Ga)

X-ray diffraction (XRD). X-ray diffractions analysis were collected at ambient conditions on a Bruker D8 Advance diffractometer operated with a Cu K-α source (40 mA and 40 kV). The patterns were measure from 20 ° to 80 ° of 2θ angle with a step size of 0.02 s and time per step of 53 s. The data analysis was carried out by Rietvield refinement using FullProf software with Thompson-Cox-Hastings pseudo-Voigt shape function. The data analysis was carried out by Rietvield refinement using FullProf software with Thompson-Cox-Hastings pseudo-Voigt shape function.

The BET surface area was determined by N_2 adsorption at -196 °C using Micrometrics Tristar instrument. Samples were previously degassed at 250 °C in 3 hours.

H_2 - Temperature Programmed Reduction. The reducibility of perovskite oxides was studied by temperature programmed reduction (H_2-TPR) using ThermoQuest TPDRO 1100 equipment equipped with TCD detector. The quartz tube reactor was loaded with about 50 mg of sample and pretreated with 10 mL min^{-1} of N_2 at 500°C for 30 min, and then cooled down to 50 °C. Samples were then heated from room temperature to 950 °C with 5 °C min^{-1} heating rate under 20 mL min^{-1} of 5 % H_2/Ar.

The O_2-Temperature Programmed Desorption (TPD) was conducted in the same instrument. The samples were previously treated under pure O_2 flow (40 mL min^{-1} at 600 °C for 30 min before cooling down to ambient temperature under O_2 flow. The desorption was performed from room temperature to 950 °C under He flow (20 mL min^{-1}) with heating rate of 5 °C min^{-1}.

The NO_x-TPD experiments were conducted under flow-gas reactor system equipped with ABB Limas and Uras UV and NDIR analyzers to detect NO, NO_2, N_2O, CO, and CO_2 gases separately. Catalysts were placed at the middle position of 10 mm i.d. tubular reactor with thermocouple inserted into the catalytic bed to measure the reaction temperature. In a typical experiment, 200 mg of sample was used. For the NO_x desorption tests, NO_x (250

ppm NO; 250 ppm NO_2, balance N_2; total flow 300 mL min^{-1}) was adsorbed at 250 °C until the concentration of NO_x unchanged and cooled down to room temperature under N_2 flow. The sample was then heated under N_2 flow (300 mL min^{-1}) from room temperature to about 600 °C at 5 °C min^{-1}. CO_2 desorption experiments were conducted in the same instrument by simply heating the samples with 5 °C min^{-1} under N_2 flow (300 ml min^{-1}) from room temperature to around 800 °C due to the limitation of the instrument.

Isopropanol Test. In order to investigate the acidity and the basicity of the catalysts, a conversion test of isopropanol was conducted. 100 mg of catalysts was introduced into a fixed bed quartz reactor. 4 % of isopropanol in N_2 (total flow of 27 ml min^{-1}) was flow through the catalysts at 325 °C . The products (acetone and propylene) were online analyzed by GC Varian 3800 equipped with a Super Q-Plot (30 m length x 0.32 mm id) with a FID detector.

The XPS experiments were done as reported elsewhere [1]. Briefly, XPS analysis was carried out on an XPS PHI 5000 Versa probe apparatus, using the band-pass energy of 187.85 eV, a 45° take off angle and a 100.0 μm diameter X-ray spot size for survey spectra. High-resolution XP spectra were recorded in the following conditions: pass energy of 23.5eV, resolution of 0.1 eV, and a step of 0.2 eV. Sample charging effects were eliminated by referring to the spectral line shift of the C 1 s binding energy (BE) value at 284.5 eV.

2.3 Catalytic Tests

2.3.1 Hydrodealkylation of toluene over oxyhydride perovskite

Reactivity investigations were studied by the chemical titration of toluene by hydride from the catalysts over $LaSrCoO_{4-x}H_y$ and $BaTiO_{3-x}H_x$ at 300 °C. The hydrodealkylation of toluene in the presence of H_2 in feeding gas was also studied over $LaSrCoO_{4-x}H_y$ and $LaSrCoO_4$ at 350 °C. Both tests were conducted in a continuous-flow fixed-bed microreactor (Fig. 2.5). Briefly, the reactor (210 mm length and 6.5 mm i.d. stainless steel cylinder) was loaded with 500 mg of samples with inert quartz (Sigma–Aldrich, 274739, 50–70 mesh particle size) and placed in the middle part of the reactor, the upper and lower parts being filled with quartz in extrusions. A thermocouple was placed inside the reactor at the catalyst bed level to monitor the reaction temperature. For the chemical titration test, toluene (250 ppm in 100 ml min^{-1} of N_2) was supplied by a liquid-injection system called CEM (controlled evaporation and mixing; Bronkhorst High-Tech). The catalytic activity

was evaluated in terms of toluene conversion and CH_4 product using on-line gas chromatography (Varian CP-3800) equipped with TCD and FID. For the hydrodealkylation of toluene, feeding flow (1.4 % of toluene, 100 ml of 5 % H_2/N_2) and 150 mg of catalyst were used.

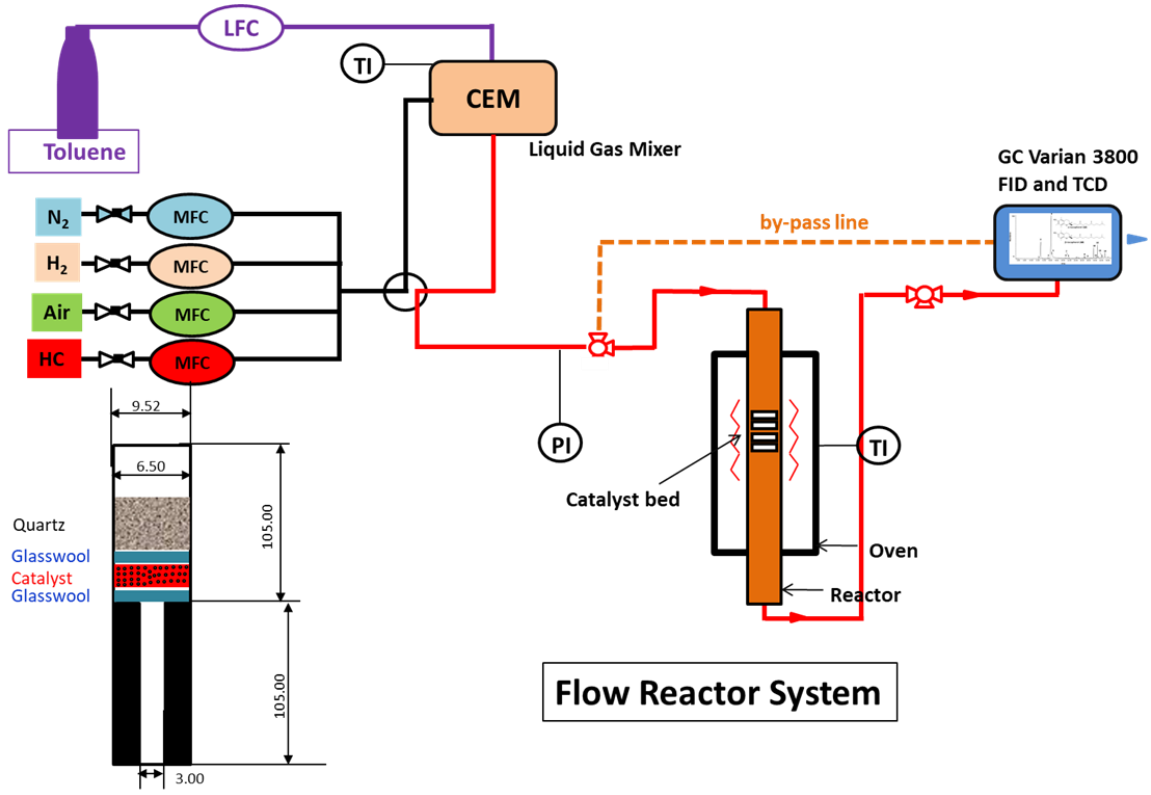

Figure 2.5 – Catalytic Testing System

2.3.2 NOx – assisted soot oxidation over LaAl1-xCoxO3 (x = 0, 0.25, 0.50, 0.75 and 1)

The NO oxidation tests were conducted in isothermal mode one the same system for NO_x-TPD experiments mentioned above. The feed gas contains 650 ppm of NO and 5 % of O_2 balanced with N_2 (total flow 254 $ml.min^{-1}$) and 200 mg of catalyst was used. The temperature range for the oxidation was 150-400 °C. At each temperature, the stabilization time is about 20 -30 min for reaching the steady state reaction in order to avoid the adsorption/desorption effect of NO_x on catalysts. NO oxidation was also performed in the temperature ramping mode, in this case the reaction conditions matched those of the NO_x assisted soot oxidation: the feed gas contained 500 ppm NO and 4 % O_2 in N_2 with total flow 600 mL min^{-1} and 200 mg of catalyst with ramping rate 5 °C min^{-1}. Besides the $LaAl_{1-}$

$_xCo_xO_3$ catalysts Pt/Al_2O_3 with 5% Pt loading (Sigma-Aldrich 205974) was used as commercial reference.

The activity of the catalysts NO_x-assisted soot oxidation tests was determined by Temperature Programmed Reaction (TPR) with a heating rate of 5 °C min^{-1}. The soot oxidation was studied by mixing 20 mg of soot (Printex U, a carbon black used as model soot) with 180 mg of catalyst or SiC for the reference non-catalytic test (catalyst:soot = 9:1), in loose contact with a spatula. Feed gas contains 500 ppm of NO and 4 % of oxygen in flow N_2 balance gas, the total flow is 600 mL min^{-1}. The tests were conducted between 200 °C and 700 °C with a ramp of 5 °C min^{-1}. The soot conversion and CO_2 selectivity were calculated as followed:

$$\text{Soot conversion (\%)} = \frac{\sum_0^t (co_2+co)}{(co_2+co)_{total}} 100 \qquad CO_2 \text{ selectivity (\%)} = \frac{\sum_0^t (co_2)}{(co_2+co)_{total}} 100$$

2.3.3. Ethanol Conversion over $LaAl_{0.75}B_{0.25}O_3$ (B=Co and Ga)

The ethanol conversion was performed in a fixed bed quartz reactor with an internal diameter of 4 mm and a length of 250 mm under atmospheric pressure. The system is as described for hydrodealkylation of toluene, but with a quartz reactor instead of the stainless steel reactor. Nitrogen was the carrier gas, and flow rate was changed with different space velocity. Before the introduction of ethanol, 0.1 g of catalyst was loaded intro the quartz reactor and preheated under nitrogen gas at 500 °C in 1 h, and cooled down to reaction temperature (350 and 400 °C). The catalytic reactions were carried out for 4 h on the stream with 1 % ethanol in N_2. The products were kept at around 150 °C to prevent condensation, then were online analyzed by GC Varian 3800 equipped with a Super Q-Plot (30 m length x 0.32 mm id) with a FID detector.

Chapter III - NO_x assisted Soot Oxidation over $LaAl_{0.75}B_{0.25}O_3$ (B=Co, Ga) catalysts

3.1. INTRODUCTION

Perovskite oxides have general formula ABO_3, where the 12-fold cubo-octahedral A site is usually occupied by alkaline earth/alkaline or larger cations and the octahedral B-site by smaller cations [1]. The ideal structure of perovskite is cubic with tolerance factor t (so-called Goldschmidt factor) of 1 ($t = (r_A + r_O)/(\sqrt{2}(r_B + r_O))$, where r_A, r_B and r_O are ionic radii of A, B, and oxygen, respectively) [2]. A t parameter between 0.75 and 1 is necessary to form perovskite structures, with decreasing symmetry for $t < 1$ [1]. Thanks to the wide range of metals able to adapting in the perovskite structures (about 90 % of metallic elements in the periodic table), the physicochemical properties of perovskite oxides can be finely tuned and they find enormous applications in catalysis for, *e. g.*, steam reforming of toluene [3–5], ethanol [6,7], CH_4 [8–10] and bioglycerol [11]; valorization of bio-oil [12–15], biomass [16] and HMF [17], lignin partial oxidation [18 19] and environmental treatments [20–24].

Particulate matter (PM) which is normally referred as soot (although the latter strictly refers only to its carbonaceous fraction) is a noxious emission of diesel engines, which find enormous applications thanks to their high energy efficiency in fuel consumption [25]. PMs can cause a number of respiratory diseases [26] and deactivation of post-treatment's catalysts for the NO_x (NO and NO_2) reduction processes [27]. Thus, the control of PMs emission is necessary for diesel engine future developments. Generally, there are two steps of PMs treatment: filtration and regeneration [28]. Filtration consists of capturing soot in a Diesel Particulate Filter (DPF), followed by the regeneration which refers to combustion soot at relatively high temperature (around 600 °C [29]) to avoid backpressure across the filter [25]. Alternatively, the Continuously Regenerating Trap (CRT) is able to continuously oxidize soot at lower temperature by using NO_2 as a stronger oxidant instead of O_2 [30,31]. On the other hand, NO_x gases, which are also included in diesel exhaust in extremely small quantity, are highly toxic pollutants. NO_x elimination is a technical problem because of mandatory requirements to add extra elements to aftertreatment systems, leading to an increase in overall cost of vehicles.

A conventional diesel aftertreatment system combines both oxidation catalysts to oxidize trace substances (unburnt hydrocarbon, soot, CO, NO) and consecutive NO_x reduction catalysts. Many efforts have been made to reduce NO_x in lean-rich exhaust cycles such as using lean NO_x trap (LNT) or NO_x storage/reduction (NSR) catalysts. An alternative way is to employ Selective Catalytic Reduction (SCR) by using extra reductants such as NH_3 from injected urea solution or itself as NO_2 [32]. These treatments are only productive in case of a large proportion of NO_2 present in the exhaust gases [25,33,34]. Therefore, finding catalysts for soot combustion at low temperature while maintaining a high proportion of NO_2 for further reduction processes is highly desirable.

NO_x-assisted soot oxidation is a simultaneous approach which involves NO to NO_2 conversion and subsequent soot oxidation by formed NO_2 from the gas phase, at relatively low temperature [28]. Many works have investigated this reaction using noble metal catalysts which are able to reduce the ignition temperature of soot oxidation ($T_{10\%}$ - temperature when 10% of soot is combusted) down to 370°C, depending on the operating conditions [28,35–38]. However, no high NO_2 yields of the soot oxidation reaction have been reported whereas a high proportion of NO_2 is beneficial for further NO_x elimination processes (for instance, NH_3 SCR). Obviously, the applications of noble metals are limited by their prohibitively expensive cost and strategic limitations of availability. Recently, Kim et al. suggested that perovskite $La_{0.9}Sr_{0.1}CoO_3$ can be reasonably priced alternative since it can oxidize about 86 % of NO at lower temperature (300 °C) than noble metal rival Pt/Al_2O_3[39]. The study has been followed by other works on doped perovskites for low temperature soot oxidation such as $LaMn_{0.9}Co_{0.1}O_3$ [40] , $BaMn_{0.7}Cu_{0.3}O_3$ [41], $La_{0.9}ACoO_3$ (A=Na, K and Rb)[23], $La_{1-x}B_xO_3$ (B=Ce and Sr)[27] and $BaCoO_{3-\lambda}$[42] , focusing on the substitution of A- or B-sites to promote redox properties of perovskite oxides by generating either defective structure or multiple oxidation state cations.

Furthermore, modified $LaCoO_3$ is generally accepted as a highly active catalyst for NO oxidation [20,43,44], whereas Al_2O_3 supported oxides are reportedly able to catalyze NO_x-assisted soot oxidation at relatively low temperature [45]. The combination of Al and Co in La-based perovskite oxides may be a promising approach for the NO_x-assisted soot oxidation at low temperature. The present work investigates Co-doped $LaAlO_3$ perovskite oxides for soot oxidation in the presence of NO_x gases to correlate the catalytic activity with crystallinity, redox properties and the role of lattice oxygen. The experimental section

of the current chapter can be found in the chapter 2. The results reported in this chapter have been published in Applied Catalysis A: General, volume 589.

3.2. RESULTS AND DISCUSSION

3.2.1 Effects of the substitutions

3.2.1.1 Structural Properties

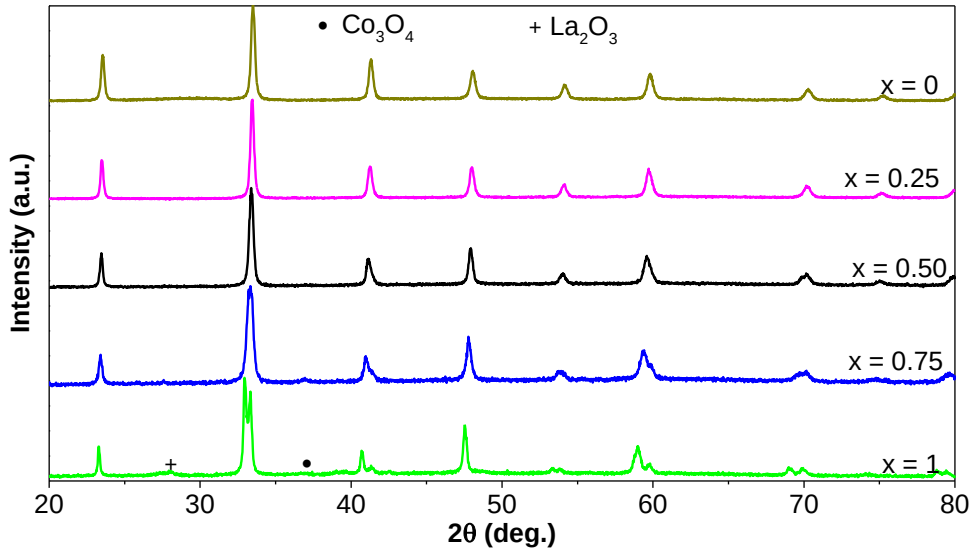

Figure 3.1– X-Ray diffractions of $LaAl_{1-x}Co_xO_3$ calcined at 700 °C.

X-ray diffraction patterns of all catalysts $LaAl_{1-x}Co_xO_3$ (x = 0, 0.25, 0.5, 0.75 and 1) calcined at 700 °C are shown in Fig. 3.1. All catalysts exhibit a well-crystallized perovskite phase, which is the only phase present from x = 0 to 0.5 and is accompanied in $LaAl_{0.25}Co_{0.75}O_3$ and $LaCoO_3$ by two minor peaks at about 36.7 and 28.1 °2θ, which belong respectively to Co_3O_4 and La_2O_3. The perovskite phase presents symmetric diffraction peaks in the case of $LaAlO_3$, whereas peak splitting is observed with increasing cobalt. Rietveld analysis has been conducted on all catalysts calcined at 700 °C to understand the lowering of symmetry with Co-doping. The refinement was done with the Thompson-Cox-Hastings pseudo-Voigt peak profile and two space groups: rhombohedral R-3c and cubic Pm-3m. The refinement data reported in Tab. 3.1 confirm the change of perovskite symmetry with the composition, $LaAlO_3$ being cubic and all other samples being rhombohedral. Interestingly, all samples would be expected presenting R-3c space group at room temperature [46]. Rhombohedral perovskite normally evolves towards cubic structure when the octahedral tilting is reduced at higher temperature. $LaAlO_3$ is normally rhombohedral at room temperature reaching space group Pm-3m at nearly 530 °C [46,47].

The presence of cubic phase at room temperature is probably due to a metastability effect. Substituted LaAl perovskites remain rhombohedral also at very high temperature and, in the case of $LaCoO_3$, the rhombohedral structure is also stable above 970 °C [47,48]. In the case of solid solutions intermediate between $LaAlO_3$ and $LaCoO_3$, Aswin *et al.* observed that the rhombohedral phase was accompanied by a secondary monoclinic perovskite phase [49]. No monoclinic phase was observed in our samples. It is tempting to assume that the presence of such a phase is a secondary result of sintering at 1030 °C in the preparation of Aswin *et al*.

The volume of the formula units $LaAl_{1-x}Co_xO_3$ calculated from the cell parameters, taking into account Z = 1 for Pm-3m and Z = 6 for R-3c space groups, are reported in Tab. 3.1 and highlighted in Fig. 3.2. They show a systematic increase of volume from $LaAlO_3$ to $LaCoO_3$ once the R-3c symmetry is established, indicating that Co is well incorporated inside the perovskite framework. In fact, trivalent Co is larger than Al^{3+} [50], so the substitution of Al by Co tends to expand the unit cell.

Table 3.1- Refinement parameters of $LaAl_{1-x}Co_xO_3$ calcined at 700 °C,

$LaAl_{1-x}Co_x-O_3$ (x)	**Space group**	**a (Å)**	**c (Å)**	**formula unit volume (Å^3)**
0	**Pm-3m**	3.7927	-	54.555
0.25	**R-3c**	5.3652	13.1402	54.596
0.5	**R-3c**	5.3730	13.1605	54.938
0.75	**R-3c**	5.3887	13.1940	55.299
1	**R-3c**	5.4367	13.1181	55.966

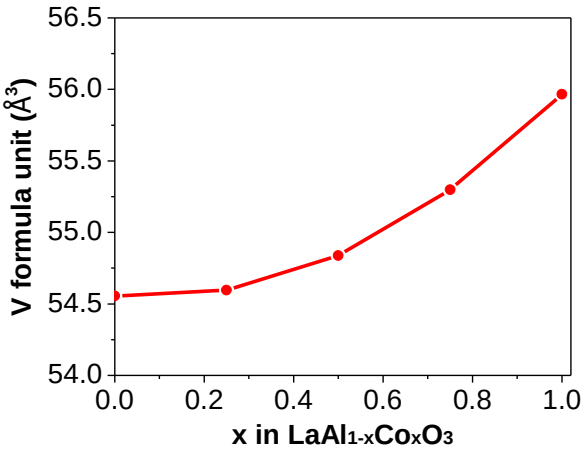

Figure 3.2 –Volume of the formula units $LaAl_{1-x}Co_xO_3$ as a function of the cobalt fraction.

Textural properties of $LaAl_{1-x}Co_xO_3$ calcined at 700 °C are listed in Tab.3.2. The average crystallite size of $LaAl_{1-x}Co_xO_3$ is calculated from the Rietveld refinement by the Williamson-Hall method. Crystallite size d_c slightly varies around 30 nm for x=0 to 0.75, before jumping up for the total introduction of cobalt. The surface areas of all samples, measured by N_2 sorption, are between 10 – 15 $m^2 g^{-1}$, as expected for samples annealed at high temperature [51]. It can be observed that the observed variation in crystallite size does not correspond to any equivalent change in surface area. Indeed, taking into account the density of the perovskite, the observed surface areas correspond to grain size between 60 and 80 nm, in good agreement only with the crystallite size of $LaCoO_3$. It is tempting to advance the hypothesis that, in the case of all other samples, the 30 nm crystallites are the result of splitting of larger grains during the thermal treatment.

Table 3.2- Textural properties of $LaAl_{1-x}Co_xO_3$ calcined at 700 °C,

$LaAl_{1-x}Co_xO_3$(x)	d_c (nm)	S_{BET} ($m^2 g^{-1}$)	V_p ($cm^3 g^{-1}$)
0	30.5	14.4	0.10
0.25	32.1	11.4	0.09
0.50	36.8	11.6	0.09
0.75	28.7	13.1	0.08
1.0	73.7	12.3	0.08

3.2.1.2. Redox properties

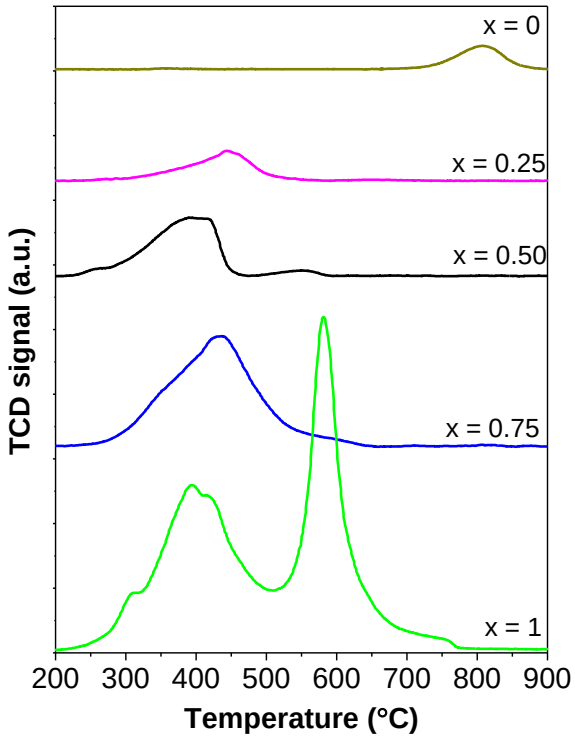

Figure 3.3 – H_2-TPR profiles of the samples $LaAl_{1-x}Co_xO_3$ calcined at 700 °C.

Fig. 3.3 summarizes the H_2-TPR profiles of $LaAl_{1-x}Co_xO_3$ (x =0, 0.25, 0.5, 0.75, 1) calcined at 700°C. In the literature, the reduction of Co^{3+} in $LaCoO_3$ was generally proposed by two different pathways, implying one or two steps. In the two-steps route, Co^{3+} is converted to Co^0 via Co^{2+} in two distinguished temperature regions at around 420 °C for Co^{3+} to Co^{2+} and 550 °C for Co^{2+} to Co^0 with the formation of intermediate brownmillerite $LaCoO_{2.5}$ [16,52–56]. This two-steps mechanism should be confirmed by the area ratio of the first peak to the second one of 1:2 [57]. However, the H_2 consumption at high-temperature reduction region is usually found lower than expected [44,54,58], suggesting that Co^0 might be partially formed in the first stage at lower temperature [54,59]. Indeed, the Co^{3+} reduction was also proposed as one-step mechanism, in which Co^0 can be produced directly from Co^{3+} with the formation of oxygen-deficient compound $LaCoO_{3-y}$, bypassing the Co^{2+} species [59], and splitting of the reduction peak can be attributed to different structural Co^{3+} species related to the distortion of perovskite structure and oxygen defects [60].

The TPR profile of the as-prepared $LaCoO_3$ reveals two separate peaks with maxima at ca. 395 and 580 °C (Fig. 3.3). The H_2-consumption, reported in Table 3.3, corresponds to a 1.5 H_2/Co ratio, indicating that all Co^{3+} has been reduced to Co°. The H_2-consumption ratio between the first and second reduction peaks is 1.04/1, indicating that the first peak does not correspond only to the reduction of Co^{3+} to Co^{2+} but includes some further reduction of Co^{2+}. The mechanism of reduction seems hence to be a mixed one-step and two-steps process. The first reduction peak presents several components: the small shoulder located at 310 °C can be ascribed to microcrystalline part or chemisorbed oxygen in the catalyst surface [20]. The two overlapping components at 391 and 418 °C probably include the formation of Co^0 at relatively low temperature [54,59].

Table 3.3 – H_2-consumption of $LaAl_{1-x}Co_xO_3$ with different composition,

Catalysts	X	Peak temperature (°C)	H_2-consumption ($\mu mol\ g^{-1}$)	H_2/Co mol/mol
$LaAlO_3$	0.00	-	-	-
$LaAl_{0.75}Co_{0.25}O_3$	0.25	445	1202	1.07
$LaAl_{0.50}Co_{0.50}O_3$	0.50	394	2909	1.34
$LaAl_{0.25}Co_{0.75}O_3$	0.75	437	4909	1.56
$LaCoO_3$	1.00	395, 580	6379	1.57

When Al partially replaces Co in $LaCoO_3$, the H_2-TPR profiles of $LaAl_{1-x}Co_xO_3$ follow the one–step reduction mechanism from around 210 °C to 600 °C. The H_2/Co ratio (Tab.3.3) is close to the values of total reduction for $LaAl_{0.25}Co_{0.75}O_3$, indicating that Co^{3+} is completely reduced to Co° up to around 600 °C. This suggests that, in bimetallic Al-Co

perovskites, Co^{3+} can be reduced to metallic species at low temperature without any clear intermediate formation of Co^{2+}, and the asymmetry of peak shape may be due to variously distinct Co^{3+} species in perovskite lattice [60]. $LaAl_{0.5}Co_{0.5}O_3$ and $LaAl_{0.75}Co_{0.25}O_3$, the most Al-rich mixed samples, present a H_2-consumption lower than the value expected for complete reduction of Co^{3+} (Tab. 3.3). This effect could be attributed to a lower than expected average oxidation state of cobalt, probably related to cation vacancies. In the case of the Co-free $LaAlO_3$, a small peak observed above 800 °C is not related to reduction phenomena but corresponds to CO_2 release from decomposition of carbonate species from the surface of this highly basic solid.

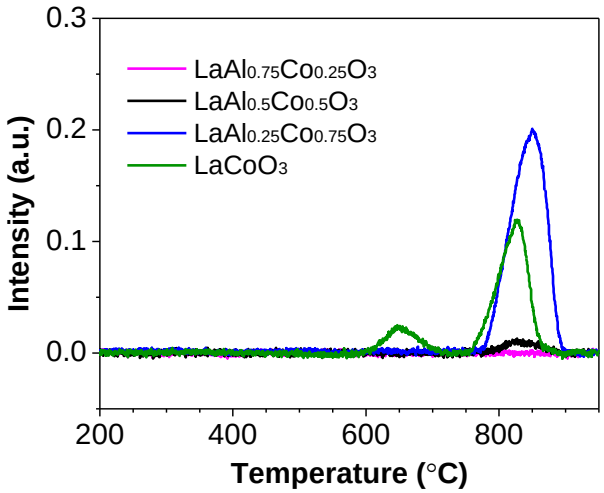

Figure 3.4- O_2-TPD profiles of $LaCo_{1-x}Al_xO_3$ samples calcined at 700 °C.

It is generally accepted that perovskite $LaCoO_3$ exhibits two type of desorbed oxygen. The α-oxygen, which is desorbed below 750 °C, is usually ascribed to oxygen weakly bound to perovskite surface. β-oxygen is lattice oxygen which diffuses from bulk and is considered as an indicator of oxygen mobility in the structure [53,58,61,62]. The latter species can come from inner bulk oxygen vacancies or can be directly associated with the B-site cation reduction in the perovskite oxide framework [55]. $LaCoO_3$ shows two desorption peaks at around 650 °C and 827 °C, probably corresponding to α- and β-oxygen, respectively (Fig. 3.4). $LaCoO_3$ releases 77.5 μmol g^{-1} of β-oxygen (nearly 2% of bulk oxygen), as a result of Co^{3+} to Co^{2+} reduction and anion vacancy generation [20,61]. The amount of β-oxygen release from $LaCoO_3$ and the desorption temperature are comparable with the results of other groups [63 64]. Decreasing the cobalt fraction x from 1 to 0.75 significantly raises the quantity of β-oxygen, $LaAl_{0.25}Co_{0.75}O_3$ releasing 158.1 μmol g^{-1} at a desorption temperature of 849 °C. The oxygen species in $LaAl_{0.25}Co_{0.75}O_3$ occupies almost 3.7 % of

total oxygen anion in perovskite, revealing the highest oxygen mobility among the studied samples. it should be noticed that Royer et al. suggested that β-oxygen is likely to originate from grain boundaries between two neighbor crystal domains due to higher oxygen diffusivity within boundaries than bulk, and the feature was significantly enhanced by substituting 20 % of Co by Fe to form $LaCo_{0.8}Fe_{0.2}O_3$ [63]. Therefore, the highest amount of lattice oxygen for $LaAl_{0.25}Co_{0.75}O_3$ may be related to the smallest crystallite size among the studied samples. For further decrease of cobalt content, the oxygen evolution dramatically drops to 9.1 μmol g^{-1} when 50 % of Co is replaced by Al and no β-oxygen is measured when only 25% cobalt is left (Tab. 3.4). $LaAl_{0.75}Co_{0.25}O_3$ exhibits no oxygen evolution during the experiment, as it is the case for $LaAlO_3$ due to non-reducibility of aluminum cations. The decrease of β-oxygen with the increase of cobalt content closely matches the decrease of H_2-consumption in H_2-TPR and confirms that the cobalt-richest samples present abundant cation vacancies and a lower than expected cobalt oxidation state.

Table 3.4 – Calculated quantity of desorbed oxygen of $LaAl_{1-x}Co_xO_3$ obtained by integration of O_2-TPD profiles,

Samples	β-O_2-desorption (μmol g^{-1})	O-percentage (mol.%)	Temperature (°C)
$LaAl_{0.75}Co_{0.25}O_3$	-	-	-
$LaAl_{0.50}Co_{0.50}O_3$	9.1	0.2	827
$LaAl_{0.25}Co_{0.75}O_3$	158.1	3.7	849
$LaCoO_3$	77.5	1.9	827

3.2.1.3. Surface properties

The Fig. 3.5a shows XPS profiles of $LaAl_{1-x}Co_xO_3$ (x =0.25, 0.5, 0.75 and 1) with Co $2p_{3/2}$ and $2p_{1/2}$ binding energy at 780-780.4 eV and 795.4 eV respectively, both ascribed to Co^{3+} species [64,65] . Moreover, distorted $2p_{3/2}$ Co pattern is distinctive for Co^{3+} species [66], with a similar gap between $2p_{1/2}$ - $2p_{3/2}$ of 15.4 eV [67] and no Co^{2+} shake up peaks at 785-788 eV [66 68], suggesting that mainly Co^{3+} species can be detected at the surface of the prepared samples. However, the satellite signal at 790.2 eV and broadening region at about 805 eV can be seen in $LaAl_{0.5}Co_{0.5}O_3$, and more pronounced in the sample with more cobalt: $LaAl_{0.25}Co_{0.75}O_3$. This profile is reported for Co_3O_4 [69], indicating that there may be some cobalt oxides not incorporated in perovskite structure when more than 50 % of Al is replaced by Co, which is in agreement with XRD profiles. Tab. 3.5 listed the ratios of surface Co/Al which increase from 0.4 for $LaAl_{0.75}Co_{0.25}O_3$ to 3.2 for $LaAl_{0.25}Co_{0.75}O_3$. The

ratio of $LaAl_{0.75}Co_{0.25}O_3$ is higher than its bulk composition (0.33) by around 20 % and the surface is slightly enriched with Co. By contrast, $LaAl_{0.5}Co_{0.5}O_3$ has surface Co lower than in the bulk composition: 0.6 in comparison with theoretical 1.0.

Table 3.5 – Relative abundances of oxygen species derived from the deconvolution of O 1s XPS spectra and Co/Al surface ratio,

Sample	$(Co/Al)_{surf.}$	Co $2p_{3/2}$	O_{ads}		O_{lat}		O_{ads}/O_{lat}
		BE (eV)	BE (eV)	%-atom	BE (eV)	%-atom	
$LaAlO_3$	0	-	531.1	43.5	529.3	56.5	0.77
$LaAl_{0.75}Co_{0.25}O_3$	0.4	780.4	531.2	44.4	529.2	55.6	0.80
$LaAl_{0.5}Co_{0.5}O_3$	0.6	780.4	531.3	39.4	529.1	60.6	0.65
$LaAl_{0.25}Co_{0.75}O_3$	3.2	780.0	531.1	42.9	529.1	57.1	0.75
$LaCoO_3$	-	779.5	531.2	66.2	528.7	25.4	2.60

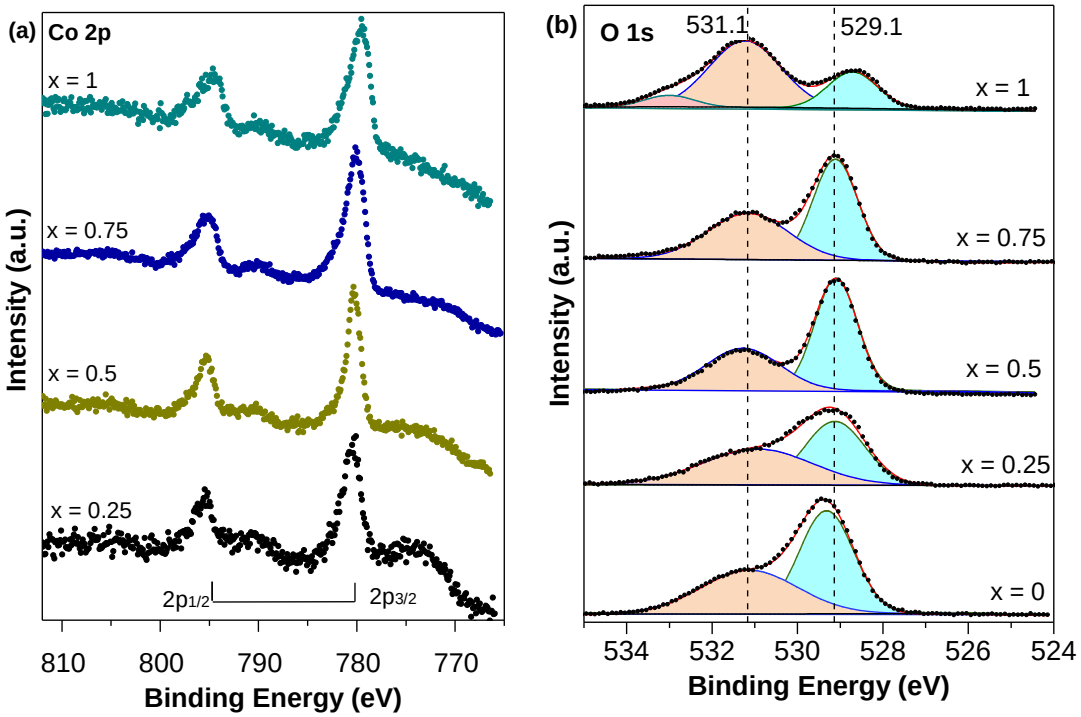

Figure 3.5 – XPS spectra of Co 2p (a) and O 1s (b) of $LaAl_{1-x}Co_xO_3$.

The O 1s XPS spectra are deconvoluted to two oxygen species: peaks at 529.1-529.3 eV are characteristic of surface lattice oxygen (denoted as O_{lat}) and signals at 531.1-531.3 eV can be ascribed to oxygen adsorbed on perovskite surface (denoted as O_{ads})[70,71] (Fig. 3.5b). The XP spectrum of the $LaCoO_3$ perovskite showed a significant shoulder at the higher binding energies, conversely not present in the $LaAlO_3$ substituted perovskites. This indicates the presence of high binding energy species, namely under-coordinated oxygen

on the surface of the perovskite that can be associated to superficial segregated oxides, clearly identified in the XRD pattern of the sample. The ratios O_{ads}/O_{lat} of $LaAl_{1-x}Co_xO_3$ with x = 0, 0.25, 0.5 and 0.75 are 0.77, 0.80, 0.65 and 0.75, respectively (Tab. 3.5). These four samples, with similar surface area, show O_{ads}/O_{lat} ratios in the same range, whereas the $LaCoO_3$ sample, with much lower surface area, shows a much higher O_{ads}/O_{lat} surface ratio. These data clearly indicate that the oxygen distribution at the surface in non-reactive conditions poorly reflects the bulk mobility of oxygen as revealed by H_2-TPR or O_2-desorption experiments. Quantity of O_{ads} is relatively related to surface area values which are similar for $LaAlO_3$.

3.2.1.4. NOx- Temperature Programmed Desorption

For the NO_x – TPD measurement, the samples were adsorbed by equal quantities of NO and NO_2 (about 250 ppm of each balanced by N_2) at 250 °C until the saturation, cooled down under N_2, and followed by heating up under N_2 atmosphere with a rate of 5 °C min^{-1}. Fig. 3.6a reveals the NO_x - TPD profiles of $LaAl_{1-x}Co_xO_3$ (x up to 0.75), while a similar figure for $LaCoO_3$ is plotted in Fig. 3.6b. The first small NO_x desorption can be ascribed to physically adsorbed species which peaks at about 150 °C for $LaAlO_3$, and decreases by around 60 °C when Al is substituted by Co. It is reported that the NO_x desorption below 250 °C is mostly related to B-site of perovskite, while at high temperature the basic A-site may take a role [44]. The adsorbed species is reportedly in dependence with adsorption temperature [72]. When NO_x is adsorbed below 250 °C, it is mainly stored as nitrite species, which can convert into nitrate at higher adsorption temperature [72]. In contrast, at high temperatures NO_x can be released by nitrate decomposition followed by oxides formation and the destruction of perovskite structure. [42]. It is also suggested that at low adsorption temperature NO_x is stored as chemisorbed NO_x and converted to nitrate by interaction with surface hydroxyl groups [73]. This chemisorbed species may be unstable which can be released by TPD experiment up to 350 °C. Generally, NO_2 is desorbed at a lower temperature in all studied samples compared to NO [74], and its desorption temperature drops with increased Co doping, from 351 °C for $LaAlO_3$ to 275 °C for $LaAl_{0.25}Co_{0.75}O_3$, and almost disappears in case of $LaCoO_3$ (Tab. 3.6). The quantity of desorbed gases is similar in all cases except $LaCoO_3$, varying from around 53-75 μmol g^{-1}. The values partially depend on surface area which may be not promoted by high calcination temperature of perovskite oxides. Furthermore, deficient perovskites favor NO adsorption on oxygen vacancies before oxidizing to NO_2 [43,75] which may not be found in our compounds

persevering charge neutrality. NO desorption temperature has the same trend of NO_2 but at a higher temperature. It decreases with Co content from 412 °C for $LaAlO_3$ to similar range of 347-350 °C for both $LaAl_{0.75}Co_{0.25}O_3$ and $LaAl_{0.5}Co_{0.5}O_3$, and drops to the minimum of 320 °C for $LaAl_{0.25}Co_{0.75}O_3$. Surprisingly, a decrease in Al quantity weakens the bond with acidic NO_x, leading to lower desorption temperature. Introduction of Co may induce some modifications of the perovskite surface which leads to variation in desorption temperature of NO_x [44]. It is reported that calcination temperature up to 1000 °C induces the formation of oxygen-deficient $BaCoO_{3-\lambda}$ which promotes the trap of NO_x on oxygen vacancies; however, when synthesis temperature lower than 700 °C surface areas may significantly contribute to the quantity of absorbed species [42]

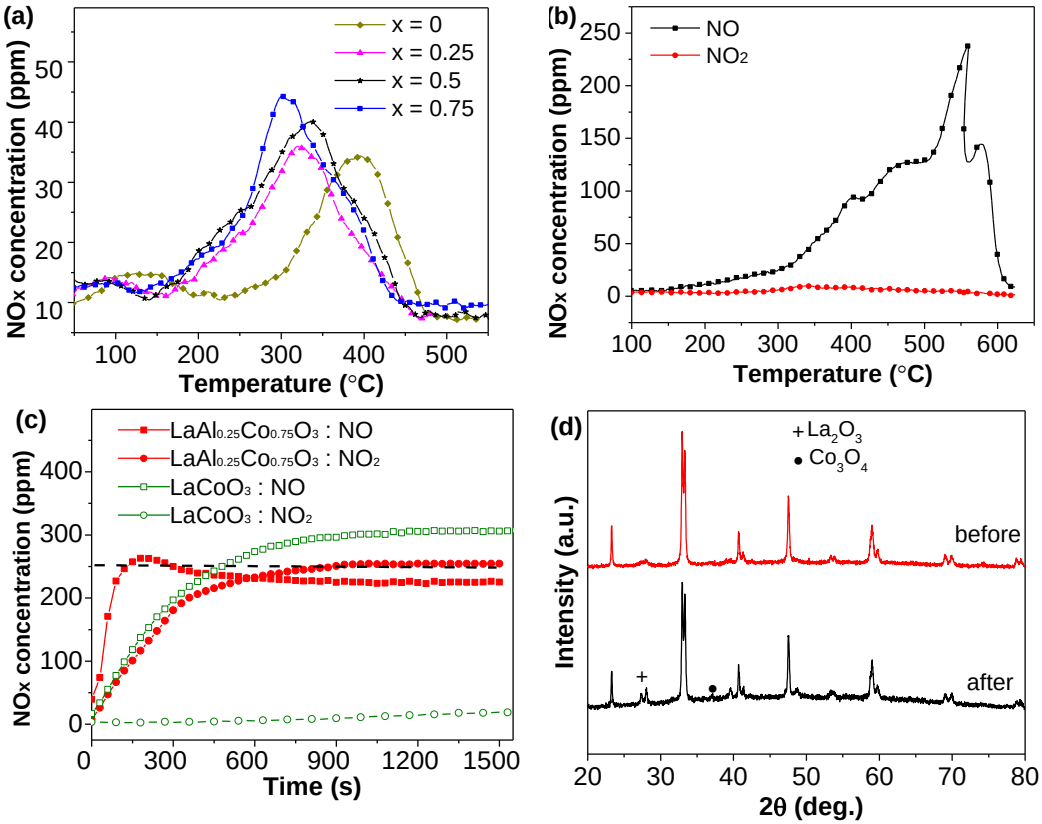

Figure 3.6 – NO_x desorption curves of $LaCo_{1-x}Al_xO_3$ calcined at 700 °C (a), NOx desorption of $LaCoO_3$ at 250 °C with time (b) (250 ppm of NO_x and 250 ppm of NO_2 balance in N_2; 250 °C); NO_x adsorption on $LaCoO_3$ and $LaAl_{0.25}Co_{0.75}O_3$ at 250 °C (c), and XRD pattern of $LaCoO_3$ after the NO_x-TPD experiment (d).

In many works for NO_x storage and reduction, NO is fed with O_2 to be oxidized to NO_2 which is more readily trapped by basic catalysts [74]. In the present study, NO and NO_2 are supplied in an approximately equal amount at 250 °C without the presence of O_2. However,

NO_2 almost disappears while NO is higher than its original value (250 ppm) during the adsorption process over $LaCoO_3$ (Fig. 3.6c). This behavior cannot be found in other samples (for example $LaAl_{0.25}Co_{0.75}O_3$ in Fig. 3.6c) where both NO and NO_2 gets saturated after around 10 minutes. This suggests that during the NO_x adsorption at 250 °C, NO_2 may be adsorbed and partially reduce it to NO. This is confirmed by the presence of more intense peaks of Co_3O_4 and La_2O_3 phases in XRD pattern of $LaCoO_3$ after TPD treatment. Moreover, the NO_x-TPD of $LaCoO_3$ shows no NO_2 peaks whereas NO is desorbed at significantly higher than those of other samples (Fig. 3.6b). The difference between NO adsorption (calculated by integration of NO adsorption curve with time) and desorption is 88.2 μmol g^{-1}, indicating the additional amount of NO from NO_2 reduction. It should be mentioned that NO_2 can be adsorbed by basic La_2O_3 observed in XRD pattern for $LaCoO_3$ to form nitrate salt, which can be decomposed at higher temperature than that in the experiment (Fig. 3.6d) [76]. It may be suggested that NO_2 may be adsorbed on $LaCoO_3$ and completely reduced to other species together with both Co^{4+} formation and partially perovskite structure collapse.

Table 3.6 – Desorbed NO_x quantity and its desorption temperature,

Catalysts	NO_2		NO		Total
	Amount (μmol.g^{-1})	T_{max} (°C)	Amount (μmol.g^{-1})	T_{max} (°C)	(μmol.g^{-1})
$LaAlO_3$	26.8	351	26.2	412	53.0
$LaAl_{0.75}Co_{0.25}O_3$	27.8	294	25.8	347	52.9
$LaAl_{0.5}Co_{0.5}O_3$	36.5	289	38.7	350	75.2
$LaAl_{0.25}Co_{0.75}O_3$	24.7	275	36.3	320	61.0
$LaCoO_3$	-	-	410.2	558	411.7

3.2.1.5. Catalytic Activities

a. NO oxidation

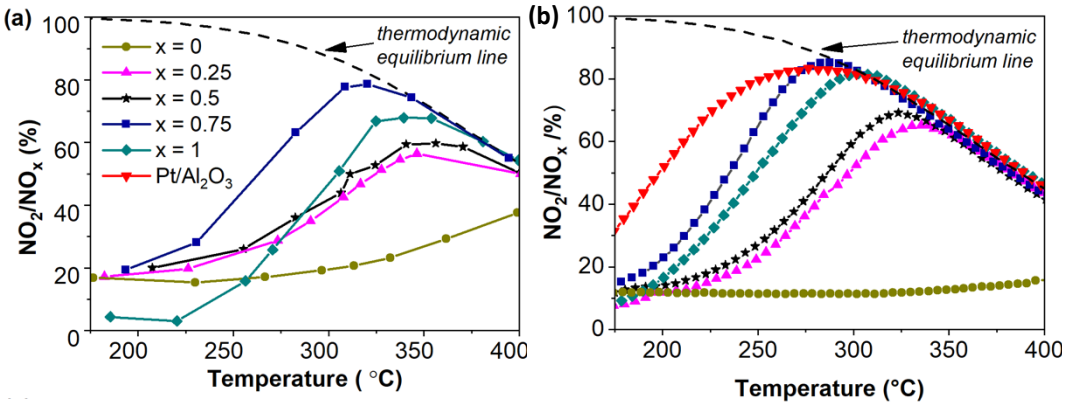

Figure 3.7 – NO_2 percentage of $LaAl_{1-x}Co_xO_3$ calcined at 700 °C in (a) steady state conditions and (b) dynamic conditions.

The NO oxidation tests aim at investigating the NO_2 production at low temperatures, which is beneficial for the NO_x storage/reduction process and soot combustion [74]. Fig. 3.7a shows NO to NO_2 conversion profiles obtained from the isothermal mode, whereas the broken line represents the thermodynamic equilibrium of NO oxidation reaction as a reference. The peaks of the curves indicate the temperatures where maximum NO_2 generation is achieved. At temperatures below the peak temperature the NO oxidation is kinetically limited, while at higher temperatures the thermodynamic equilibrium is the limiting factor. Among the as-prepared samples, $LaAl_{0.25}Co_{0.75}O_3$ perovskite presents the best performance (Tab.3.7), with a maximum NO conversion of about 78 % at 320 °C. In contrast, $LaAlO_3$ exhibits the worst activity with 38 % at a remarkably high temperature of about 399°C and the NO conversion increases with Co, from 38 % for $LaAlO_3$ to 56 and 60 % for $LaAl_{0.75}Co_{0.25}O_3$ and $LaAl_{0.5}Co_{0.5}O_3$ catalysts, respectively. The conversion reaches the maximum value for $LaAl_{0.25}Co_{0.75}O_3$ before reverting to 68 % when Al is totally substituted by Co as reported for $LaCoO_3$ [20]. The same catalysts were also tested in the temperature ramping mode and under lower residence time (Fig. 3.7b) in order to obtain the same test conditions as the soot oxidation tests and to get a closer correlation between the two kind of experiments. As can be appreciated, the order of the catalytic performance ($LaAl_{0.25}Co_{0.75}O_3$ > $LaCoO_3$ > $LaAl_{0.5}Co_{0.5}O_3$ > $LaAl_{0.75}Co_{0.25}O_3$ > $LaAlO_3$) remained unvaried from steady state to dynamic conditions.

Furthermore, by comparing the $LaAl_{0.25}Co_{0.75}O_3$ sample with a Pt/Al_2O_3 commercial oxidation catalyst, the NO oxidation rate of the perovskite is obviously lower although the equilibrium is reached by both catalysts at almost the same temperature, which is the one of interest for the soot oxidation, offering a viable alternative for the PGM-based catalysts under certain conditions.

Table 3.7 – NO_x performances of $LaCo_{1-x}Al_xO_3$ calcined at 700 °C,

Catalysts	**$LaAl_{1-x}Co_xO_3$ (x)**	**NO_2/NO_x (%)**	**Temperature (°C)**
$LaAlO_3$	0	38	399
$LaAl_{0.75}Co_{0.25}O_3$	0.25	56	346
$LaAl_{0.5}Co_{0.5}O_3$	0.5	60	356
$LaAl_{0.25}Co_{0.75}O_3$	0.75	78	320
$LaCoO_3$	1	68	339

It should be noticed that NO-to-NO_2 oxidation ability is due to the generation of oxygen defects and redox property [77], which can be created by adjusting cation doping at A or B sites in perovskite compounds. Others suggest that higher oxidation capacity is associated with higher oxygen mobility and exchange between lattice oxygen and gas phase oxygen [20]. This may be related to $LaAl_{0.25}Co_{0.75}O_3$ with the higher amount of β-oxygen desorption (Tab. 3.4), implying the pivotal role of lattice oxygen species in the improvement of the oxidation reaction. Furthermore, all samples have negligible α-oxygen quantity released during O_2-TPD experiment, but still possess comparable NO oxidation activity. This result indicates that surface oxygen may not play a critical role in NO oxidation but the diffusion of lattice oxygen to the surface is more important [78].

However, $LaCoO_3$ desorbs significantly more oxygen than its rivals ($LaAl_{0.75}Co_{0.25}O_3$ and $LaAl_{0.5}Co_{0.5}O_3$) but its oxidation activity worsens despite more Co content. The higher NO_x desorption temperature for $LaCoO_3$ indicates strong interactions between NO_x and the catalyst, while partial doping Al slightly weakens the bonds facilitating the NO_x release at low temperatures. Thus, oxygen mobility may be not the only factor for NO oxidation but the synergetic interaction between two B-site cations (Al and Co) may enhance oxidation performance of the catalysts, as suggested by Ma et al. with a small substitution of Co by Fe to promote NO conversion [79]. Furthermore, under H_2/Ar flow in H_2-TPR experiment, $LaAl_{0.25}Co_{0.75}O_3$ is reduced at a temperature of 437 °C, higher than 394 °C for $LaAl_{0.75}Co_{0.25}O_3$. However, the NO conversions of these samples reveal different trend from reduction temperature, which may imply the negligible effects of reducibility on NO oxidation. Furthermore, $LaCoO_3$ produces less NO_2 at low temperatures but higher above

275 °C than $LaAl_{0.75}Co_{0.25}O_3$ and $LaAl_{0.5}Co_{0.5}O_3$ (Fig. 3.7). This may be related to the fact that $LaCoO_3$ can adsorb NO_2 at low temperatures and partially reduce to NO as can be seen in the NO_x-TPD experiment. Besides, the temperature at maximum NO_2 production is lowest for $LaAl_{0.25}Co_{0.75}O_3$ at 320 °C, and increases by around 30 °C with x = 0.25 and 0.5 (Tab.3.7). A similar trend can be found for NO desorption profiles (Tab.3.6), where NO desorbs at 320 °C for $LaAl_{0.25}Co_{0.75}O_3$ and increase to 350 and 347 °C for $LaAl_{0.5}Co_{0.5}O_3$ and $LaAl_{0.75}Co_{0.25}O_3$ respectively. This highlights the suggestion in which the oxidation reaction commences with the chemisorption of reactants NO and O_2, followed the dissociation of O_2 and NO_2 on the surface [28].

b. Soot Oxidation

Fig. 3.8 reveals the results of soot oxidation tests over $LaAl_{0.25}Co_{0.75}O_3$ (calcined at 700 °C) in the presence and absence of NO_x gas. Tab.3.8 shows the testing outputs: $T_{10\%}$ is ignition temperature when 10 % of soot is burnt; $T_{50\%}$ and $T_{90\%}$ are temperatures when 50 % and 90 % of soot is consumed respectively; T_{max} when maximum CO_2 production is achieved, and $(NO_2/NO)_{max}/T$ is the maximum percentage of NO_2 over NO_x mixture and its temperature. Generally, the NO_x-assisted soot oxidation reaction commences with the oxidation of adsorbed NO to produce NO_2, which is a stronger oxidant than O_2 [38,45,82] . Soot can be also oxidized by O_2 but at a relatively higher temperature than with NO_2. In the presence of NO_2, it interacts with soot surface to form surface oxygen complexes (SOC), which decomposes further to CO, CO_2 and NO [28,83]. O_2 is first adsorbed at the catalyst's surface and undergoes the dissociation to form active oxygen species. This species is possibly transferred to the surface of soot forming SOC via spill-over mechanism [83]. The results clearly show that soot is oxidized at a significantly lower temperature in the presence of NO_x ($T_{10\%}$ are 377 and 513 °C for with and without NO_x respectively). Moreover, NO_x also remarkably supports to reduce the temperature of 50 % of soot conversion by around 111 °C although at higher temperatures the role of NO_x in soot oxidation becomes less prominent with the decrease of $T_{90\%}$ by only 27 °C because of limited NO_x availability (Tab.3.8). In terms of CO_2 production, NO_x promotes total oxidation with CO_2 selectivity of 99.8 % compared to 98.5 % of that without NO_x. Without the presence of NO_x, the T_m increases by around 120 °C and the formation of CO is significant. The results highlight the vital role of NO_2 in soot oxidation and its further applications in NO_x reduction process by the selective catalytic reduction reaction.

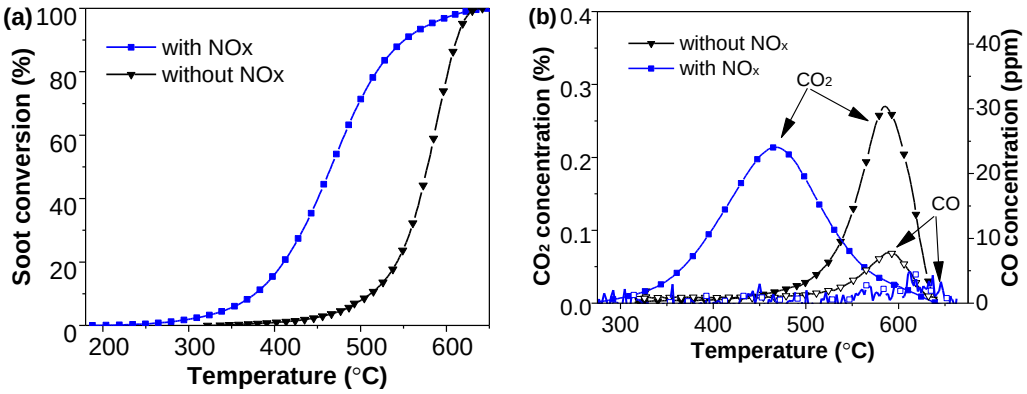

Figure 3.8- Soot conversion (a), CO_2 and CO concentration (b) as functions of temperature during soot oxidation catalytic tests with and without NO_x supply over $LaAl_{0.25}Co_{0.75}O_3$ catalyst.

Fig.3.9 summarizes soot conversion, NO_2/NO_x percentage, CO and CO_2 concentrations as functions of temperature during the experiments with NO_x-assisted soot oxidation over $LaAl_{1-x}Co_xO_3$ catalysts. Among the prepared solids, $LaAlO_3$ possesses certainly the lowest activity with $T_{10\%}$, $T_{50\%}$ and $T_{90\%}$ of 470, 562 and 623 °C respectively. Doping Co shifts the reaction temperature to lower ranges, $LaAl_{0.75}Co_{0.25}O_3$ obviously outperforms $LaAlO_3$ by reducing these temperature values by about 60-80 °C. The improvement in oxidation activity is likely to relate to not only the better performance in the NO_x oxidation but also the NO_x adsorption [35], as the Co doping reduces the NO_x desorption temperature thereby facilitating the oxidation reactions at a lower temperature range (Fig. 3.6). As expected, both samples $LaAl_{0.75}Co_{0.25}O_3$ and $LaAl_{0.5}Co_{0.5}O_3$ (violet and black curves) exhibit similar soot oxidation activity, which is in line with the NO_x-TPD experiments. This suggests that the NO_x-assisted soot oxidation is mainly governed by the adsorption of NO_x on the catalyst's surface and directed to the soot-catalyst interface before initiation of the oxidation [35]. $LaAl_{0.25}Co_{0.75}O_3$ is the most active catalyst with $T_{10\%}$ of 377 °C, which is 12 °C lower than that of $LaCoO_3$. The complete substitution of Al by Co deteriorates the soot oxidation performance at low temperatures while there is no difference at middle temperature with $T_{50\%}$ of 467 °C for both $LaAl_{0.25}Co_{0.75}O_3$ and $LaCoO_3$. The difference between these two catalysts is signified in terms of NO_2 production which plays an essential role in abatement reduction. $LaAl_{0.25}Co_{0.75}O_3$ maintains high formation of NO_2 with NO_2/NO_x of 0.71 at 321 °C compared to 0.42 at 352 °C for $LaCoO_3$. The low ignition temperature allows to uninterruptedly oxidize soot while keeping high NO_2 production. In comparison with soot-free NO oxidation, NO_2 production obtained from NO_x-soot

oxidation for all catalysts is lower, confirming the participation of NO_2 as a strong oxidant in the reaction leading to its consumption. $LaAlO_3$ shows no formation of NO_2 at all, explaining that the soot oxidation is practically the same as non-catalytic [83]. The outstanding performance of $LaAl_{0.25}Co_{0.75}O_3$ is likely to be associated with the prominent lattice oxygen mobility which may be facilitated by co-incorporation of Co-Al elements in perovskite structure[83,84].

Table 3.8 – Catalytic performances of $LaCo_{1-x}Al_xO_3$ calcined at 700 C,

$LaAl_{1-x}Co_xO_3$	X	$T_{10\%}$ (°C)	$T_{50\%}$ (°C)	T_{max} (°C)	$T_{90\%}$ (°C)	$(NO_2/NO_x)_{max}$/T(°C)	CO_2 selectivity (%)
$LaAlO_3$	0	470	562	563	623	0.08 / 376	82.3
$LaAl_{0.75}Co_{0.25}O_3$	0.25	402	484	481	560	0.39 / 383	98.7
$LaAl_{0.5}Co_{0.5}O_3$	0.5	401	487	482	570	0.44 / 379	98.1
$LaAl_{0.25}Co_{0.75}O_3$	0.75	377	467	467	585	0.71 / 321	99.8
$LaCoO_3$	1	389	467	493	624	0.40 / 352	93.8
Without NO_x	-	513	578	587	612	-/-	98.5

Fig. 3.9c and 3.9d show the CO_2 and CO concentration evolutions during the NO_x-assisted oxidation tests over the catalysts with various Co content. Obviously, $LaAlO_3$ has the highest T_{max} (the temperature at which maximum CO_2 is produced) at 563 °C with low quantity of CO_2 formed, evidenced by the CO_2 selectivity of 82.3 %. The substitution of Co by Al shifts the T_m to lower range by about 81 °C for x=0.25 and 0.5, and by around 96 °C for $LaAl_{0.25}Co_{0.75}O_3$. However, $LaCoO_3$ shifts the temperature towards 493 °C which is similar to reported elsewhere [27] and produces relatively a large amount of CO at high temperature. The CO_2 evolution profile for $LaCoO_3$ has a relatively similar trend as NO desorption curve with a broader shoulder at a low-temperature range (Fig. 3.6b), indicating the key role of NO adsorption on soot oxidation. When SiC was used as a reference for the non-catalytic soot oxidation, the promotional effect of NO_x was lost as the peak of the soot oxidation rate was shifted to 626 °C coupled with a very high CO production.

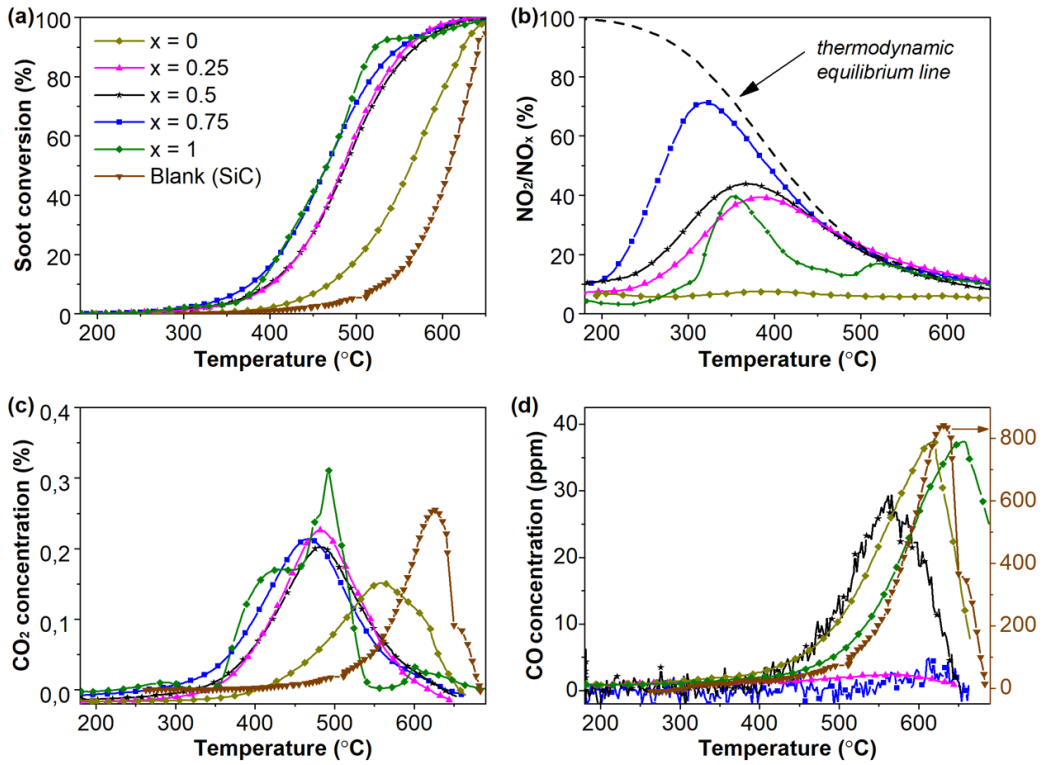

Figure 3.9- Soot oxidation (a), NO_2 percentage (b), CO_2 (c) and CO (d) concentrations (both Y axes) of $LaAl_{1-x}Co_xO_3$ calcined at 700 C.

3.2.2 Effects of the calcination temperatures

3.2.2.1. Structural Properties

The effect of calcination temperature on the formation of the perovskite phase is highlighted in Fig. 3.10, in which the diffraction patterns of $LaAl_{0.25}Co_{0.75}O_3$ calcined at 500, 600 and 700 °C are shown. The diffraction pattern at 500°C present no perovskite peaks but exhibits broad bands of Co_3O_4 and La_2O_3 phases. Evaluation of the peaks of these phases by the Scherrer method suggests sizes of 27 nm for Co_3O_4 and 2.6 nm for La_2O_3, a signature of nano-crystalline form for this last phase. At 600 °C, perovskite structure emerges beside traces of La_2O_3 phase, better crystallized than at 500°C. La_2O_3 disappears altogether at a calcination temperature of 700 °C, leaving perovskite as the only crystalline phase. A rise of calcination temperature results to the reduction of the BET surface areas (Tab.3.9) from 21.9 to 16.3 $m^2 g^{-1}$ for 500 and 600 °C respectively.

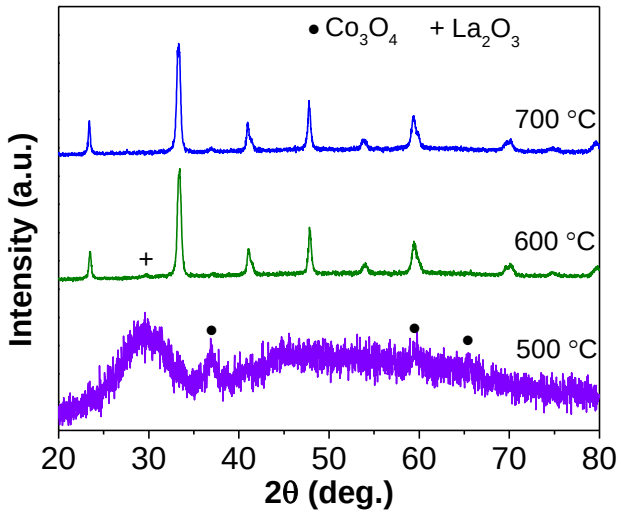

Figure 3.10 - Diffraction patterns of $LaAl_{0.25}Co_{0.75}O_3$ calcined at different temperatures.

Table 3.9 – Textural properties of $LaAl_{0.25}Co_{0.75}O_3$ calcined at different temperatures,

Calcination Temperature (°C)	d_c (nm)	S_{BET} ($m^2 g^{-1}$)	V_p ($cm^3 g^{-1}$)
500	-	21.9	0.08
600	26.4	16.3	0.10
700	28.7	13.1	0.08

3.2.2.2. Redox properties

Table 3.10 – H_2-consumption of $LaAl_{1-x}Co_xO_3$ with different composition,

Calcination Temperature (°C)	Peak temperature (°C)	H_2-consumption ($\mu mol\ g^{-1}$)	H_2/Co mol/mol
500	388, 646	7229	2.29
600	350, 398	4536	1.44
700	437	4909	1.56

Fig. 3.11 shows H_2-TPR profiles of $LaAl_{0.25}Co_{0.75}O_3$ calcined at 500, 600 and 700 °C. The sample annealed at 500 °C exhibits two peaks at 388 and 646 °C (Tab. 3.10). The first peak closely correspond to the expected temperature for reduction of the Co_3O_4 phase observed in the sample [85]. The second peak does not correspond to a reduction peak but it is at the temperature expected for the decarbonation of the carbonate species at the surface of the extremely dispersed La_2O_3 evidenced by the XRD pattern [86]. $LaAl_{0.25}Co_{0.75}O_3$ calcined at 600 °C reveals two overlapped peaks at 350 and 398 °C. This corresponds to the formation of Co^0 by reduction of perovskite $LaAl_{0.25}Co_{0.75}O_3$ at a temperature nearly 90 °C lower than in the case of the same material calcined at 700 °C. This may be linked with lower surface

area, narrower crystal size distribution and higher crystal size with higher calcination temperature, which leads to more diffusional resistance [24].

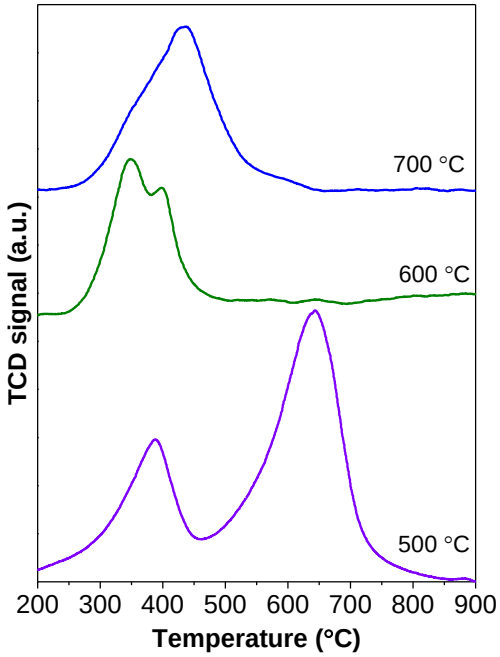

Figure 3.11 – H_2-TPR profiles of $LaAl_{0.25}Co_{0.75}O_3$ calcined at different temperatures

3.2.2.3. NOx- Temperature Programmed Desorption

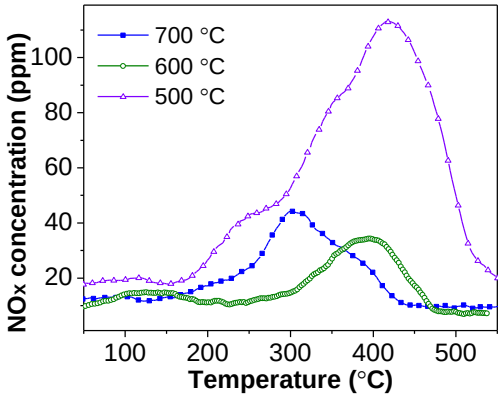

Figure 3.12 - NO_x desorption curves of $LaAl_{0.25}Co_{0.75}O_3$ calcined at different temperatures.

For the sample $LaAl_{0.25}Co_{0.75}O_3$ calcined at different temperatures (Fig. 3.12), the one annealed at 500 °C releases the most NO_x at 258 μmol g^{-1} in comparison with 45 and 61 μmol g^{-1} of $LaAl_{0.25}Co_{0.75}O_3$ calcined at 600 and 700 °C respectively. On the other hand, the specific surface areas of the sample decrease from ~ 22 to ~ 16 $m^2 g^{-1}$ with calcination temperature from 500 to 600 °C, and drops to 13.1 $m^2 g^{-1}$ at 700 °C (Tab. 3.9). Furthermore,

it can be seen that calcination temperature from 700 to 600 °C shifts desorption peak of NO_x by around 96 °C, whereas sample calcined at 500 °C possesses the highest desorption temperature at 420 °C. The presence of La_2O_3 in the samples calcined at low temperatures may be attributed to a stronger bond with NO_x and higher adsorbed quantity since La_2O_3 is supposed as the main NO_x storage site [43] (Tab. 3.11). The desorbed quantities increase with the decrease in calcination temperatures, probably associated with the surface areas.

Table 3.11 - Desorbed NO_x quantity and its desorption temperature,

Calcination Temperature (°C	NO_2		NO		Total ($\mu mol.g^{-1}$)
	Amount ($\mu mol.g^{-1}$)	T_{max} (°C)	Amount ($\mu mol.g^{-1}$)	T_{max} (°C)	
500	77.7	307	178.0	424	255.7
600	24.0	355	25.5	413	49.5
700	24.7	275	36.3	320	61.0

3.2.2.4. Catalytic Activities

a. NO oxidation

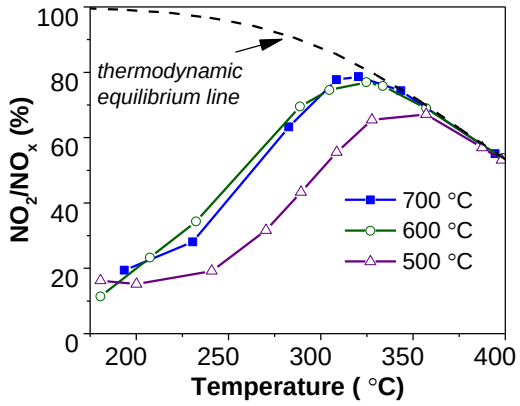

Figure 3.13 - NO_2 percentage of $LaAl_{0.25}Co_{0.75}O_3$ calcined at different temperatures.

Many works have found that substitutions of A-site generate oxygen vacancies, for example $La_{1-x}Sr_xBO_3$ [20,43], or of B-site to support the co-existence of multivalent states, e.g. $LaCo_{1-x}Mg_xO_3$ [64], in order to promote NO oxidation. Furthermore, it was shown that the partial substitution of cations can promote the formation of preferential oxidation active states (e.g. metallic isolated or biactive sites) that can promote the NO oxidation [80,81]. However, there are fewer investigations regarding the effect of the degree of perovskite crystallinity on the NO oxidation. Fig. 3.13 shows profiles of NO_2 molar percentage in the NO_x mixture of $LaAl_{0.25}Co_{0.75}O_3$ which is calcined at 500, 600 and 700 °C. It is clear that the sample annealed at 500 °C reveals the lowest oxidation activity, with about 66 % at ~

350 °C despite the highest surface area (21.9 $m^2 g^{-1}$), probably due to the presence of segregated phases such as Co_3O_4 and La_2O_3 (Tab. 3.12) [20]. The samples calcined at 600 °C show superior oxidation performances at low temperatures, but at above 300 °C the solid calcined at 700 °C slightly outperforms. Despite the reduction in surface area, the calcination temperature up to 700 °C has positive effects on oxidation activity, which may be associated with higher crystallinity and less minor phases as detected in XRD profiles (Fig. 3.10). However, further increase calcination temperature beyond 700 °C may lead to deterioration of oxidation activity due to low surface area as studied elsewhere [20].

Table 3.12 – NO_x performances of $LaCo_{1-x}Al_xO_3$ calcined at 700 °C

Calcination Temperature (°C	NO_2/NO_x (%)	Temperature (°C)
500	66.9	350
600	76.9	324
700	78	320

b. Soot oxidation

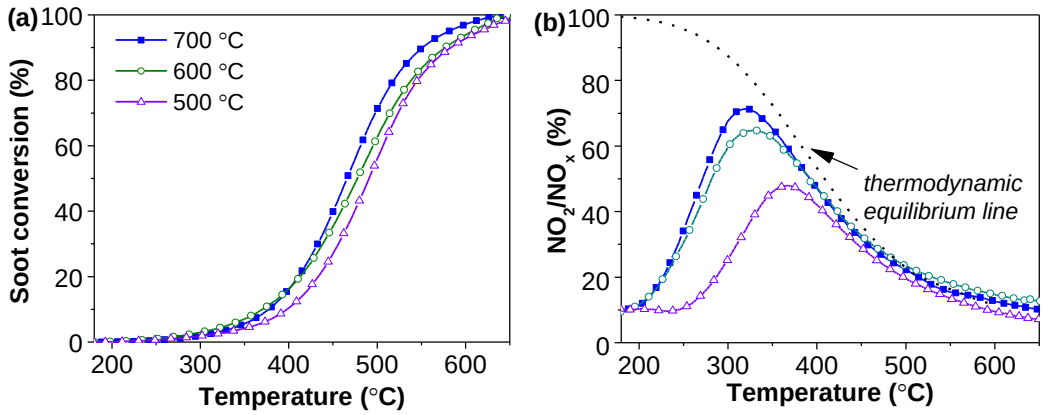

Figure 3.14- Soot oxidation (a), NO_2 percentage (b) of $LaAl_{0.25}Co_{0.75}O_3$ calcined at different temperature.

Fig. 3.14 summarizes soot conversion and NO_2/NO_x percentage as functions of temperature over catalyst $LaAl_{0.25}Co_{0.75}O_3$ calcined at different temperatures, and Tab. 3.13 sums up the oxidative characteristics of the catalyst. Calcination at lower temperatures enhances the surface areas but deteriorates the oxidation activity. The sample annealed at 500 °C has the highest $T_{10\%}$, $T_{50\%}$ and $T_{90\%}$ at 399, 492 and 583 °C respectively, compared to 370, 478 and 578 °C for $LaAl_{0.25}Co_{0.75}O_3$ calcined at 600 °C. Moreover, the treatment at 600 and 700 °C shows similar soot oxidation but the NO_2 production of the later is ameliorated with 71 % compared to 64.9 % for the former. It is already mentioned that $LaAl_{0.25}Co_{0.75}O_3$ calcined

at the lowest temperature adsorbs the largest amount of NO due to high surface area but releases this gas at the highest temperature, suggesting that stronger interaction between NO_x and substrate surface does not support the oxidation reaction and the products fail to dissociate as it can be described by the Sabatier principle [87]. This finding emphasizes the crucial role of crystallinity promoted by high calcination temperature in both NO and NO_x-assisted soot oxidation.

Table 3.13 – Catalytic performances of $LaAl_{0.25}Co_{0.75}O_3$ at different calcination temperatures

Calcination Temperature (°C)	$T_{10\%}$ (°C)	$T_{50\%}$ (°C)	T_{max} (°C)	$T_{90\%}$ (°C)	$(NO_2/NO_x)_{max}/T$ (%/°C)	CO_2 selectivity (%)
700	377	467	467	585	71.0 /321	99.8
600	370	478	478	578	64.9/330	99.5
500	399	492	499	583	47.9/368	98.7

3.3 CONCLUSIONS

Among the prepared catalysts, $LaAl_{0.25}Co_{0.75}O_3$ exhibits superior catalytic activity for both NO oxidation and NO_x-assisted soot oxidation. For the NO oxidation, NO_2 production can reach 78 % at relatively low temperature (320 °C) which is considered as a potential alternative for noble metal catalysts. Furthermore, $LaAl_{0.25}Co_{0.75}O_3$ is also the most active catalyst for NO_x-assisted soot oxidation with $T_{10\%}$ of 377 °C and NO_2/NO_x of 0.71, and results in almost 100 % of CO_2 selectivity. The correlation between NO_x desorption and oxidation activity is well established suggesting that NO_x adsorption on catalyst surface is a key role in soot oxidation with NO_x. The presence of NO_2 for soot oxidation is obvious, the absence of which remarkably decreases the oxidation activity. The excellent performance of $LaAl_{0.25}Co_{0.75}O_3$ is likely to be linked with high lattice surface oxygen supported by well-crystallized perovskite structure. Full replacement of Al by Co deteriorates the catalytic activity, suggesting that the combination of Al-Co has synergetic effects on the catalysis.

3.4 REFERENCES

1 M. A. Pena and J. L. G. Fierro, *Chem. Rev.*, 2001, **101**, 1981–2017.

2 J. Zhu, H. Li, L. Zhong, P. Xiao, X. Xu, X. Yang, Z. Zhao and J. Li, *ACS Catal.*, 2014, **4**, 2917–2940.

3 U. Oemar, P. S. Ang, K. Hidajat and S. Kawi, *Int. J. Hydrogen Energy*, 2013, **38**, 5525–5534.

4 C. P. B. Quitete, R. L. Manfro and M. M. V. M. Souza, *Int. J. Hydrogen Energy*, 2017, **42**, 9873–9880.

5 Yasushi, D. Mukai, Y. Murai, S. Tochiya, Y. Izutsu, K. Sekiguchi, N. Hosomura, H. Arai, E. Kikuchi and Y. Sugiura, *Appl. Catal. A Gen.*, 2013, **451**, 160–167.

6 K. H. Lin, C. Bin Wang and S. H. Chien, *Int. J. Hydrogen Energy*, 2013, **38**, 3226–3232.

7 Q. Zhang, L. Li, B. Jiang, K. Wang, D. Tang and B. Dou, *Int. J. Hydrogen Energy*, 2017, **42**, 17102–17111.

8 K. Zhao, F. He, Z. Huang, G. Wei, A. Zheng, H. Li and Z. Zhao, *Appl. Energy*, 2016, **168**, 193–203.

9 L. D. Vella, J. A. Villoria, S. Specchia, N. Mota, J. L. G. Fierro and V. Specchia, *Catal. Today*, 2011, **171**, 84–96.

10 T. H. Nguyen, A. Łamacz, P. Beaunier, S. Czajkowska, M. Domański, A. Krztoń, T. Van Le and G. Djéga-Mariadassou, *Appl. Catal. B Environ.*, 2014, **152**–**153**, 360–369.

11 S. Ramesh and N. J. Venkatesha, *ACS Sustanaible Chem. Eng.*, 2017, **5**, 1339–1346.

12 J. Yao, J. Liu, H. Hofbauer, G. Chen, B. Yan, R. Shan and W. Li, *Energy Convers. Manag.*, 2016, **117**, 343–350.

13 G. Chen, J. Yao, J. Liu, B. Yan, R. Shan and W. Li, *Bioresour. Technol.*, 2015, **198**, 108–114.

14 G. Chen, J. Yao, J. Liu, B. Yan and R. Shan, *Renew. Energy*, 2016, **91**, 315–322.

15 K. A. Resende, C. N. Vila-Neto, R. C. Rabelo-Neto, F. B. Noronha and C. E. Hori, *Catal. Today*, 2015, **242**, 71–79.

16 X. Yang, L. Yang, W. Fan and H. Lin, *Catal. Today*, 2016, **269**, 56–64.

17 M.-Y. Chen, C.-B. Chen, B. Zada, Y. Fu, M. H. Qiao, K. N. Fan, X. X. Zhang, B. N. Zong, A. Sarkar, M. K. Nazeeruddin, M. Grätzel and S. I. Seok, *Green Chem.*, 2016, **18**, 3858–3866.

18 H. Deng, L. Lin, Y. Sun, C. Pang, J. Zhuang, P. Ouyang, Z. Li and S. Liu, *Catal. Letters*, 2008, **126**, 106–111.

19 H. Deng, L. Lin, Y. Sun, C. Pang, J. Zhuang, P. Ouyang, J. Li and S. Liu, *Energy & Fuels*, 2009, **23**, 19–24.

20 J. A. Onrubia and J. R. González-velasco, *Appl. Catal. B, Environ.*, 2017, **213**, 198–210.

21 X. Yang, L. Luo and H. Zhong, *Catal. Commun.*, 2005, **6**, 13–17.

22 A. K. Ladavos and P. J. Pomonis, *Appl. Catal. A Gen.*, 1997, **165**, 73–85.

23 N. Russo, S. Furfori, D. Fino, G. Saracco and V. Specchia, *Appl. Catal. B Environ.*, 2008, **83**, 85–95.

24 S. Irusta, M. P. Pina and M. Men, *J. Catal.*, 1998, **412**, 400–412.

25 A. Russell and W. S. Epling, *Catal. Rev. - Sci. Eng.*, 2011, **53**, 337–423.

26 A. Namdeo and M. C. Bell, *Environ. Int.*, 2005, **31**, 565–573.

27 R. Zhang, N. Luo, B. Chen and S. Kaliaguine, *Energy and Fuels*, 2010, **24**, 3719–3726.

28 T. Andana, M. Piumetti, S. Bensaid, L. Veyre, C. Thieuleux, N. Russo, D. Fino, E. Alessandra and R. Pirone, *Appl. Catal. B Environ.*, 2017, **209**, 295–310.

29 E. Xue, K. Seshan and J. R. H. Ross, *Appl. Catal. B Environ.*, 1996, **11**, 65–79.

30 M. V. Twigg, *Catal. Today*, 2006, **117**, 407–418.

31 A. Setiabudi, M. Makkee and J. A. Moulijn, *Appl. Catal. B Environ.*, 2004, **50**, 185–194.

32 M. Koebel, M. Elsener and M. Kleemann, *Catal. Today*, 2000, **59**, 335–345.

33 M. Koebel, G. Madia and M. Elsener, *Catal. Today*, 2002, **73**, 239–247.

34 M. K. Majewski, W.A.; Khair, in *Diesel Emissions and Their Control. SAE International:*, Warrendale, PA, 2006.

35 T. Andana, M. Piumettia, S. Bensaida, L. Veyre, C. Thieuleux, N. Russo, D. Fino, E. A. Quadrelli and R. Pirone, *Appl. Catal. B Environ.*, 2018, **226**, 147–161.
36 S. Liu, X. Wu, H. Luo, D. Weng and R. Ran, *J. Phys. Chem. C*, 2015, **119**, 17218–17227.
37 H. Zhang, Y. Zhu, S. Wang, M. Zhao, M. Gong and Y. Chen, *Fuel Process. Technol. J.*, 2015, **137**, 38–47.
38 S. Liu, X. Wu, D. Weng, M. Li and R. Ran, *ACS Catal.*, 2015, **5**, 909–919.
39 C. H. Kim, G. Qi, K. Dahlberg and W. Li, *Science (80-.).*, 2010, **327**, 1624–1627.
40 J. Wang, Y. Su, X. Wang, J. Chen, Z. Zhao and M. Shen, *Catal. Commun.*, 2012, **25**, 106–106.
41 M.-S. S.-A. M.-J. I. G. Veronica Torregrosa-Rivero, Vicente Albaladejo-Fuentes, *RSC Adv. Open*, 2017, **7**, 35228–35238.
42 V. G. Milt, M. A. Ulla and E. E. Miro, *Appl. Catal. B Environ. 57*, 2005, **57**, 13–21.
43 N. T. and P. V. Xin-Gang Li, Yan-Hua Dong, Hui Xian, Willinton Yesid Hern andez, Ming Meng, Hong-Hu Zou, Ai-Jing Ma, Tian-Yong Zhang, Zheng Jiang, *Energy Environ. Sci.*, 2011, **4**, 3351–3354.
44 J. Chen, M. Shen, X. Wang, J. Wang, Y. Su and Z. Zhao, *Catal. Commun.*, 2013, **37**, 105–108.
45 F. Lin, X. Wu, S. Liu, D. Weng and Y. Huang, *Chem. Eng. J.*, 2013, **226**, 105–112.
46 H. Lehnert, H. Boysen, J. Schneider, F. Frey, D. Hohlwein, P. Radaelli and H. Ehrenberg, *Zeitschrift fur Krist.*, 2000, **215**, 536.
47 C. J. Howard, B. J. Kennedy and B. C. Chakoumakos, *J. Phys. Condens. Matter*, 2000, **12**, 349–365.
48 G. Thornton, B. C. Tofield and A. W. Hewat, *J. Solid State Chem.*, 1986, **61**, 301–307.
49 V. Aswin, P. Kumar, P. Singh, A. Gupta, S. Rayaprol and A. Dogra, *J. Mater. Sci.*, 2015, **50**, 366–373.
50 R. D. Shannon, *Acta Cryst.*, 1976, 751.
51 X. Zhu, X. Tu, M. Chen, Y. Yang, C. Zheng, J. Zhou and X. Gao, *Catal. Commun.*, 2017, **92**, 35–39.
52 N. A. Merino, B. P. Barbero, P. Ruiz and L. E. Cadús, *J. Catal.*, 2006, **240**, 245–257.
53 J. Zhang, X. Weng, Z. Wu, Y. Liu and H. Wang, *Appl. Catal. B Environ.*, 2012, **126**, 231–238.
54 S. Ivanova, A. Senyshyn, E. Zhecheva, K. Tenchev, V. Nikolov, R. Stoyanova and H. Fuess, *J. Alloys Compd.*, 2009, **480**, 279–285.
55 N. A. Merino, B. P. Barbero, P. Grange and L. E. Cadús, *J. Catal.*, 2005, **231**, 232–244.
56 B. Białobok, J. Trawczyński, W. Miśta and M. Zawadzki, *Appl. Catal. B Environ.*, 2007, **72**, 395–403.
57 T. Nakamura, G. Petzow and L. J. Gauckler, *Mat. Res. Bull.*, 1979, **14**, 649–659.
58 B. Levasseur and S. Kaliaguine, *Appl. Catal. A Gen.*, 2008, **343**, 29–38.
59 L. B. Sis, G. P. Wirtz and S. C. Sorenson, *J. Appl. Phys.*, 1973, **44**, 5553.
60 L. Huang, M. Bassir and S. Kaliaguine, *Appl. Surf. Sci.*, 2005, **243**, 360–375.
61 R. Zhang, A. Villanueva, H. Alamdari and S. Kaliaguine, *Appl. Catal. B Environ.*, 2006, **64**, 220–233.
62 R. Pereñíguez, J. L. Hueso, F. Gaillard, J. P. Holgado and A. Caballero, *Catal. Letters*, 2012, **142**, 408–416.
63 S. Royer, F. Bérubé and S. Kaliaguine, *Appl. Catal. A Gen.*, 2005, 282, 273–284.
64 J. Zhang, D. Tan, Q. Meng, X. Weng and Z. Wu, *Appl. Catal. B, Environ.*, 2015,

172–**173**, 18–26.
65 R. R. Solís, F. J. Rivas and O. Gimeno, *"Applied Catal. B, Environ.*, 2017, **200**, 83–92.
66 M. O'Connell, A. . Norman, C. . Hüttermann and M. . Morris, *Catal. Today*, 1999, **47**, 123–132.
67 C. A. F. Vaz, D. Prabhakaran, E. I. Altman and V. E. Henrich, *Phys. Rev. B - Condens. Matter Mater. Phys.*, 2009, **80**, 1–7.
68 C. A. Chagas, F. S. Toniolo, R. N. S. H. Magalhães and M. Schmal, *Int. J. Hydrogen Energy*, 2012, **37**, 5022–5031.
69 M. C. Biesinger, B. P. Payne, A. P. Grosvenor, L. W. M. Lau, A. R. Gerson and R. S. C. Smart, *Appl. Surf. Sci.*, 2011, **257**, 2717–2730.
70 F. Fang, N. Feng, L. Wang, J. Meng, G. Liu, P. Zhao, P. Gao and J. Ding, *Appl. Catal. B Environ.*, 2018, **236**, 184–194.
71 C. Lee, Y. Jeon, S. Hata, J. Park, R. Akiyoshi, H. Saito, Y. Teraoka, Y. Shul and H. Einaga, *Appl. Catal. B Environ.*, 2016, **191**, 157–164.
72 X. He, M. Meng, J. He, Z. Zou, X. Li, Z. Li and Z. Jiang, *Catal. Commun.*, 2010, **12**, 165–168.
73 R. You, Y. Zhang, D. Liu, M. Meng, Z. Jiang, S. Zhang and Y. Huang, *Chem. Eng. J.*, 2015, **260**, 357–367.
74 S. Roy and A. Baiker, *Chem. Rev.*, 2009, **109**, 4054–4091.
75 J. Liu, Z. Zhao, C. Xu, A. Duan and G. Jiang, *J. Phys. Chem. C*, 2008, **112**, 5930–5941.
76 S. Mentus, D. Jelić and V. Grudić, *J. Therm. Anal. Calorim.*, 2007, **90**, 393–397.
77 Y. Peng, W. Si, J. Luo, W. Su, H. Chang, J. Li, J. Hao and J. Crittenden, *Environ. Sci. Technol.*, 2016, **50**, 6442–6448.
78 J. Chen, M. Shen, X. Wang, G. Qi, J. Wang and W. Li, *Appl. Catal. B Environ.*, 2013, **134**–**135**, 251–257.
79 A.-J. Ma, S. Z. Wang, C. Liu, H. Xian, Q. Ding, L. Guo, M. Meng, Y. S. Tan, N. Tsubaki, J. Zhang, L. R. Zheng and X. G. Li, *Appl. Catal. B Environ.*, 2014, **146**, 24–34.
80 J. Xiong, Q. Wu, X. Mei, J. Liu, Y. Wei, Z. Zhao, D. Wu and J. Li, *ACS Catal.*, 2018, **8**, 7915–7930.
81 P. Ciambelli, S. Cimino, G. Lasorella, L. Lisi, S. De Rossi, M. Faticanti, G. Minelli and P. Porta, *Appl. Catal. B Environ.*, 2002, **37**, 231–241.
82 K. Tikhomirov, O. Kröcher, M. Elsener and A. Wokaun, *Appl. Catal. B Environ.*, 2006, **64**, 72–78.
83 N. D. Wasalathanthri, T. M. SantaMaria, D. A. Kriz, S. L. Dissanayake, C. H. Kuo, S. Biswas and S. L. Suib, *Appl. Catal. B Environ.*, 2017, **201**, 543–551.
84 C. M. Marcos, V. T. Rivero, V. A. Fuentes, M. S. S. Adsuar and M. J. I. Gómez, *Top. Catal.*, 2018, **0**, 0.
85 O. O. James and S. Maity, *J. Pet. Technol. Altern. Fuels*, 2016, **7**, 1–12.
86 R. Sarbajna, A. S. Devi, K. Purandhar and M. V Suryanarayana, *Int. J. ChemTech Res.*, 2013, **5**, 2810–2820.
87 G. Rothenberg, *Catalysis: Concepts and Green Applications*, WILEY-VCH Verlag, 2008.

Chapter IV - Oxyhydride perovskites $BaTiO_{3-x}H_x$ and $LaSrCoO_{4-x}H_y$

4.1 INTRODUCTION

The term "oxyhydride'' might early originate from the work of J.F. Brice and A. Moreau in 1982 about the solid-state synthesis of LaHO under pure H_2 at 900 °C [1]. Two years later, using X-ray and neutron diffraction, they discovered the unusual average length of O-H of 2.85 Å which is much larger than O^{2-}—H^+ distance in OH^- group ranging from 1.32 to 1.37 Å [2]. This confirmed that they were dealing with hydride-oxide simultaneously associating with O^{2-} and H^- in a ternary combination of LaHO. Later on, a few materials containing both oxide and hydride anions have been reported such as Ba_3AlO_4H [3], $Ba_{21}Ge_2O_5H_{24}$ [4] synthesized under drastically reducing conditions (hydrogen pressure ~ 1 bar and 800 – 1100 °C).

Recent years have seen rapid growth in studies on oxyhydride perovskites, mostly based on transition metals: Co [5–8], V [9–11], Mn[12], Cr[13], Sc[14], and Ti[15–20]. Besides the structural stability of hydride-hosting compounds, these materials also possess intriguing characteristics. $LaSrCoO_3H_{0.7}$ (Fig. 4.1a) enhances the Néel temperature to 380 K from 110 K of $LaSrCoO_{3.5-x}$ [21] originated from exchange interactions mediated by hydride anions [5,6]. This oxyhydride and its successors $LnSrCoO_{3+\alpha}H_\beta$ (Ln = Pr, Nd) [22] and $Sr_3Co_2O_{4.33}H_{0.84}$ [8] exhibits unusually low oxidation states of cobalt +1.7 and + 1.75 respectively. Kobayashi *et al.* [16,23] synthesized $BaTiO_{3-x}H_x$ (Fig. 4.1b) with a mixed Ti^{3+}/Ti^{4+}, exhibiting hydride exchange and electronic conductivity. Furthermore, $SrCrO_2H$ exhibits higher antiferromagnetic order than other Cr-oxides due to octahedral tilting cause by hydride intercalation [13]. Pure H^- conductivity is also evidenced in the K_2NiF_2-oxyhydride $La_{2-x-y}Sr_{x+y}LiO_{3-y}H_{1-x+y}$ [24], which may lead to applications in ionic transport devices. Furthermore, hydride mobility in $LaSrCoO_{4-x}H_y$ can be probed above 400 °C and estimated as high as 4 $S.cm^{-1}$ [7]. Remarkably, $ATi(O,H)_3$ (A=Ca, Sr, Ba) series have no vacancies but the hydride anions are diffused and exchangeable with other gaseous species such as N_2; HF; NH_3 at ~400 °C [18,19,16]. They also reveal excellent electrical conductivity, which may be promising as mixed ionic/electronic conductors (MIEC). Finally, the lability of hydrides in $BaTi(O,H)_3$ allows milder conditions of oxynitrides preparation, which conventionally requires high temperature (800-1300 °C) via NH_3 route [18,19].

The preparation of oxyhydride perovskites requires strongly reducing conditions, leading to the possibility of the total reduction of transition cations to metallic phases. In addition, many hydride compounds can be decomposed via hydrogen release at high temperatures, thus special cares should be considered. Initially, hydrogen was used to reduce oxides at high temperatures to form oxyhydrides. More recently, using hydrides in forms of NaH, CaH_2 or TiH_2 and parent perovskite oxides allow forming oxyhydrides at significantly lower temperatures. Generally, there are two main approaches to preparing oxyhydride perovskites. The first route is the topochemical reduction, in which hydride anions of reducers (for instance, CaH_2) partially occupy O^{2-} positions of perovskite precursors while general frameworks of the parents are preserved. The second approach involves mixing hydride and metal oxide precursors under high pressure. This route does not require the synthesis of perovskite precursors, but it requires special equipment and should satisfy the condition: one of the cations of oxyhydrides (A or B-site) should be the metal of reducing agents such as Ca^{2+} or Ti^{4+} [25].

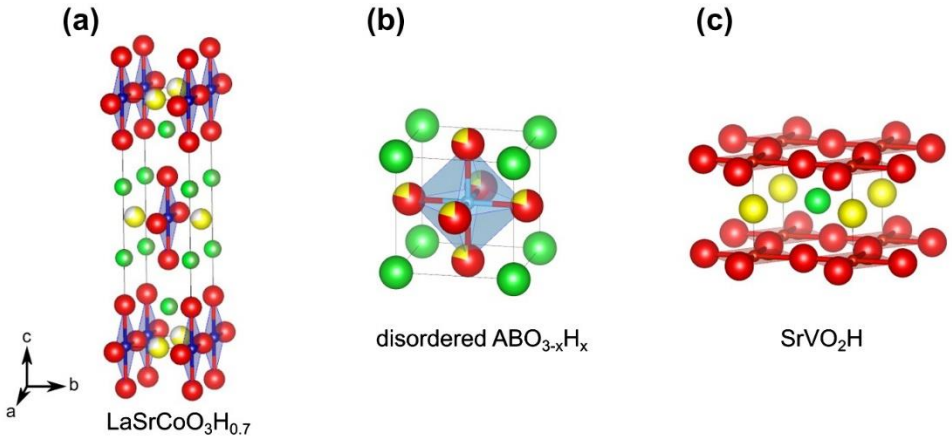

Figure 4.1 – Some structures of oxyhydride perovskites: hydride is shown by yellow spheres and oxide is shown by red spheres; La and Sr cations are shown by shades of green [25].

In 2000, Rosseinsky and Hayward [5] reported the first transition metal oxyhydride $LaSrCoO_3H_{0.7}$ which was prepared by topochemical reduction of $LaSrCoO_4$ using CaH_2 in 2002. Two years earlies, with the same approach but using NaH as a reducing agent, they synthesized the defected structure $LaSrCoO_{3.5}$ with the absence of hydride species [21]. Other subsequent oxyhydrides prepared by topotactic reactions have been reported such as $ATiO_{3-x}H_x$ (A=Ba, Ca, Sr, Eu) [15,20,23], $SrVO_2H$ (Fig. 4.1c) [10]. This method involves grinding perovskite parents with CaH_2 and pelletizing in a glovebox to eliminate the oxidation of CaH_2 by air, and followed by sealing pellets in evacuated Pyrex tubes. Heating the tubes at

300 – 600 °C yields oxyhydrides and by-product CaO which must be washed by methanol solution of a weak acid (ammonium chloride). This method is also applied to prepare oxyhydrides in forms of thin films. Typically, thin films of parent perovskite are prepared by pulsed-laser deposition, then immersed with CaH_2 and sealing in evacuated Pyrex tubes before heating at suitable temperatures. Some oxyhydrides thin films have been investigated such as $SrVO_2H$ [10], $ATiO_{3-x}H_x$ (A = Ba, Sr, Ca) [17], and $LaSrCoO_{4-x}H_x$ [26]. The benefits of the topochemical reaction to the synthesis of oxyhydride perovskites are simple without requiring special equipment. However, the drawback is the reduction nature of the process itself, resulting in the possibilities of metallic formation. In addition, controlling the hydride quantity doped in structures is challenging since it strongly depends on reaction temperatures, CaH_2 quantities and pressures inside Pyrex tubes.

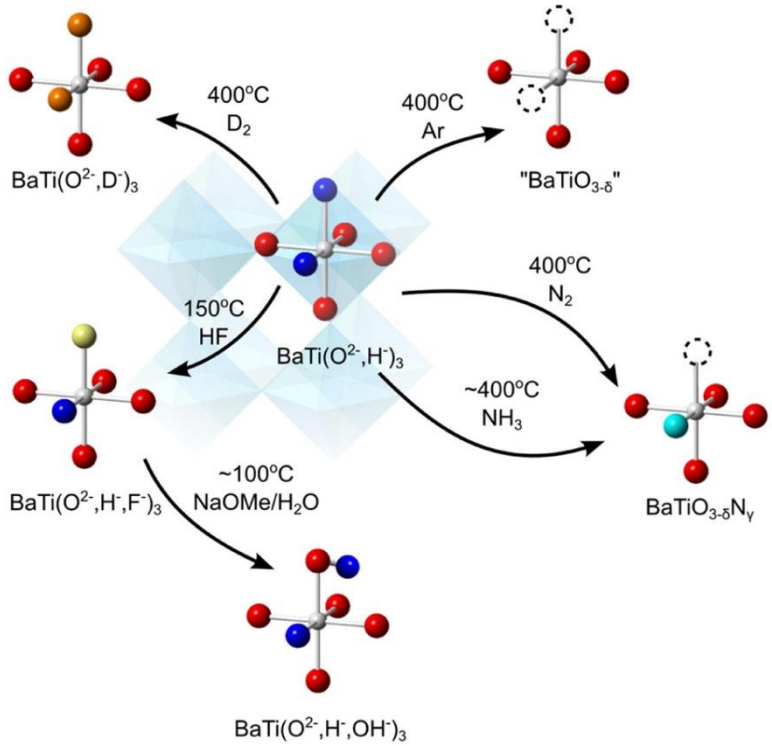

Figure 4.2 - Anion exchange routes of $BaTi(OH)_3$ [25].

Another approach is direct synthesis which involves mixing reducers and metal oxides, bypassing the preparation step of parent perovskites. The quantity of hydride in obtained oxyhydride is estimated by the used metal hydrides. The method involves enclosing precursors' mixtures in a solid container with no headspace to prevent the loss of hydrogen under heating. The mixtures should be compressed under high pressures and heated at high temperatures. Another advantage of this method is no requirement for washing products,

but special equipment to sustain high pressures is needed. $BaScO_2H$ is prepared from BaH_2, BaO and Sc_2O_3 [14]. Another example is $Sr_2VO_{4-x}H_x$ obtained from SrO, VO_2 and SrH_2 [9].

The chemical reactivity of oxyhydrides lies on the nature of hydride anions. The redox potential of H^-/H_2 is highly negative (-2.23 V), it is easily oxidized to H_2 gas. The oxidant may be the transition metal within the compound, however, most oxyhydride perovskites are stable in ambient conditions. Under heating, $BaTiO_{2.4}H_{0.6}$ can release H_2 at 400 °C and form presumably $BaTiO_{3-\delta}$ under flowing Ar [16]. Under flowing D_2, hydrides are exchangeable with D_2 to form $BaTiO_{3-x}H_yD_z$ [16]. Similar exchange routes with N_2 and HF can be found in a work of Masuda *et al.* (Fig. 4.2) [19]. The exchangeability of oxyhydrides with external gases allow synthesizing oxynitride $BaTiO_{2.4}N_{0.4}$ from $BaTiO_{2.6}H_{0.4}$ exchanged with NH_3 at temperatures of 375-550 °C which are significantly lower than normal routes (800 -1300 °C) [18].

However, the chemical reactivity of oxyhydrides or hydride species itself has not been investigated. In 2018, Tang *et al.* [27] used $BaTiO_{2.4}H_{0.6}$ as a new support for catalytic CO_2 methanation. The authors compared the methanation activity between Ru, Ni/$BaTiO_3$ and Ru,Ni/ $BaTiO_{2.4}H_{0.6}$. Before the tests, the samples were reduced at 400 °C in 30 min for Ni-based and 2 h for Ru-based catalysts. With the oxyhydride support, the activity for Ni and Ru increases by a factor of 2–7 when compared to the $BaTiO_3$ oxide support. However, the reasons for the enhancement of the activity of catalysts supported on the oxyhydride was not mentioned. Probably, during the reduction step of catalysts at 400 °C, hydride species as a strong reducer may release and support to reduce Ni and Ru sites to produce more metallic phase compared to unhydride support. In another work, the same group used Ru, Fe, Co/$BaTiO_{3-x}H_x$ for ammonia synthesis [28]. A similar observation was found: the activity of $BaTiO_{2.5}H_{0.5}$ as support is significantly higher than $BaTiO_3$. The authors suggested that the function of hydride as a strong electron donor is one of the reasons for the enhancement of catalytic activity [28].

In this part of the thesis, two oxyhydride perovskites $LaSrCoO_{4-x}H_y$ ($y-x \leq 0.5$) and $BaTiO_{3-x}H_x$ bearing Ruddlesden-Popper A_2BX_4 and ABX_3 structures, respectively, are prepared by the topochemical route. Their characteristics are deeply explored by various techniques: X-Ray diffraction, magnetic measurements, Fourier-transform infrared spectroscopy (FT-IR), thermogravimetric mass spectroscopic (TGA-MS), X-ray photoelectron spectroscopy (XPS) and H_2-temperature programmed reduction (H_2-TPR). The present work shows that

these oxyhydrides own different levels of thermal stability under reducing conditions: perovskite framework of $BaTiO_{3-x}H_x$ is sustainable during thermal treatment, whereas its counterpart $LaSrCoO_{4-x}H_y$ has seen the simultaneous transformation to defected $LaSrCoO_{3.5}$ and mixed oxides/Co^0. However, under oxidative thermal treatment, both oxyhydrides are converted to stable perovskite structures. Interactions of hydrides with supports lead to questions about possible reactivity of oxyhydrides towards hydro-related reactions. In this study, the reactive potentiality is investigated by the chemical titration of toluene by the hydride reservoir of the oxyhydrides at 300 °C and hydrodealkylation of toluene over the oxyhydride $LaSrCoO_{4-x}H_y$ and oxide $LaSrCoO_4$. $LaSrCoO_{4-x}H_y$ produces some hydrogenated products but $BaTiO_{3-x}H_x$ shows no activity under the adopted reaction conditions, and the perovskite structure remains after hydride release. In the presence of H_2 in feeding gas, $LaSrCoO_{4-x}H_y$ exhibits better catalytic activity than $LaSrCoO_4$. The observed activity of $LaSrCoO_{4-x}H_y$ is likely linked to the metallic sites formed by thermal decomposition and detected by the magnetic measurements, and reactivity of oxyhydrides may be ignored. Furthermore, XPS confirms extraordinarily low oxidation states of transition metals hosted in the oxyhydride frameworks, which is consistent with low H_2 consumption during H_2-TPR experiments. Additionally, the amount of hydride as estimated by means of H_2-TPR in the two oxyhydrides is close to that found in reported compounds [5,15]. The experimental parts can be found in Chapter II of the thesis.

4.2 RESULTS AND DISCUSSION

4.2.1 Structural Analysis

4.2.1.1 Oxyhydride $BaTiO_{3-x}H_x$

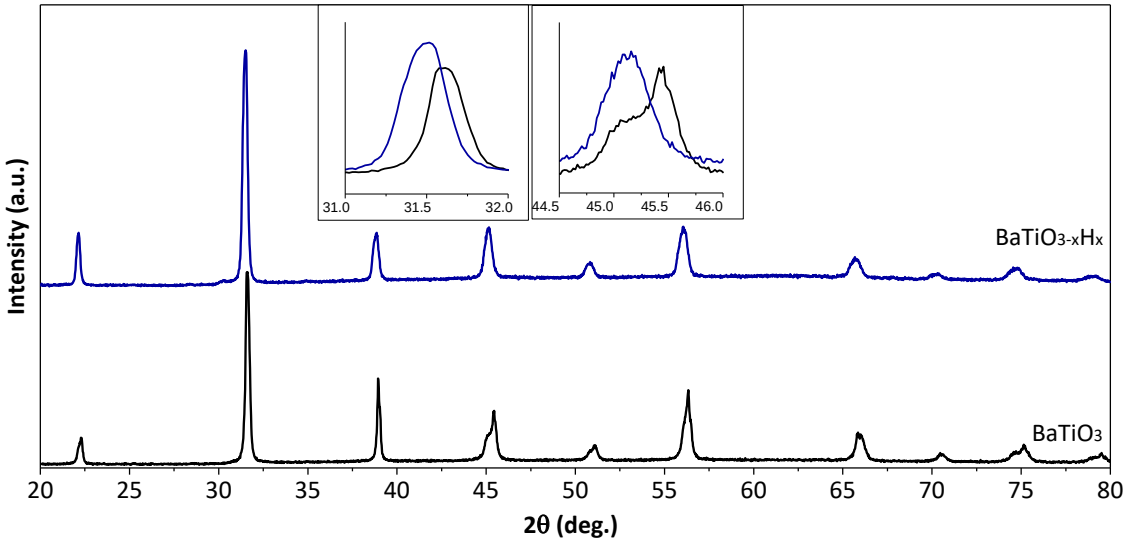

Figure 4.3 - XRD patterns of the oxyhydride $BaTiO_{3-x}H_x$ and $BaTiO_3$. Inset: examples of some peaks.

Fig. 4.3 compares XRD patterns between $BaTiO_3$ and $BaTiO_{3-x}H_x$. It is obvious that there is a shift to lower angles after hydride intercalation (Inset in Fig. 4.3) caused by an expansion of cell parameters (Tab. 4.1). The presence of hydride may lead to the reduction in oxidation states of transition metal Ti and therefore larger cation. These effects may result in an increase in lattice parameters or a change in the structure[15] . Additionally, two peaks at 44.5-46.0 ° ((002) and (200)) become almost overlapped after reduction, indicating that the c and a parameters tend to be mostly identical (c/a ≈ 1) tending forwards cubic structure. the nearly cubic structure.

Table 4.1 - Fitting parameters from Rietvield refinements of the oxyhydride $BaTiO_{3-x}H_x$ and $BaTiO_3$,

Sample	a (Å)	b (Å)	c (Å)	c/a	V (Å^3)	Space Group
$BaTiO_3$	3.9980	3.9980	4.0291	1.0078	64.401	P4mm
$BaTiO_{3-x}H_x$	4.0143	4.0143	4.0311	1.0042	64.961	P4mm

4.2.1.2 Oxyhydride $LaSrCoO_{4-x}H_y$

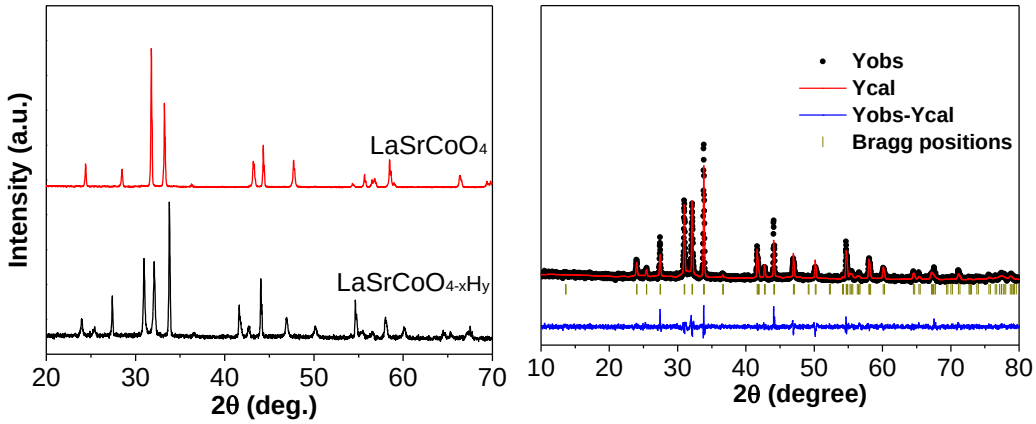

Figure 4.4 - XRD patterns of $LaSrCoO_{4-x}H_y$ and $LaSrCoO_3H_{0.7}$ (ICSD 95598) and Rietveld refinement for the prepared $LaSrCoO_{4-x}H_y$.

Fig. 4.4 illustrates the XRD patterns of parent $LaSrCoO_4$, the prepared oxyhydride $LaSrCoO_{4-x}H_y$, and Rietveld Refinement results. The perovskite $LaSrCoO_4$ matches well with reference data (ICSD 01-083-2409) [29]. It should be mentioned that the topotactic intercalation of hydride into the planar square CoO_2 sheet to replace axial O^{2-}, the tetragonal phase of $LaSrCoO_4$ I/4mmm is transformed into orthorhombic Immm of $LaSrCoO_{4-x}H_y$, together with an increase in unit volume (Tab. 4.2) [5]. This may be a consequence of different effects: interaction between H^- and Co species along b-axis, interlayer interactions, and the formation of lower oxidation state cations of cobalt, which are larger than Co^{3+} species. In comparison with reported data [5], the prepared oxyhydride has higher value of b-axis and lower c value, probably because of variation in either hydride quantity or vacancies in structure [7]. Because of the invisibility of hydrogen under X-ray especially in the presence of heavy atoms such as La, the refinement is not able to give any information of hydride quantity [25]. Assuming oxygen occupancy and ignoring the presence of hydride, the stoichiometric formula of the oxyhydride is $LaSrCoO_{3.2}$ which is obtained via structural refinement.

Table 4.2 – Lattice parameters of the $LaSrCoO_{4-x}H_y$ and $LaSrCoO_4$ synthetized in this study (*) in comparison with the literature,

Sample	Space group	a (Å)	b (Å)	c (Å)	V(Å³)
$LaSrCoO_4$ *	I4/mmm	3.8065	3.8065	12.5211	181.423
$LaSrCoO_{4-x}H_y$*	Immm	3.8668	3.6352	13.0027	182.771
$LaSrCoO_3H_{0.7}$ [5]	Immm	3.8709	3.6034	13.0151	181.541

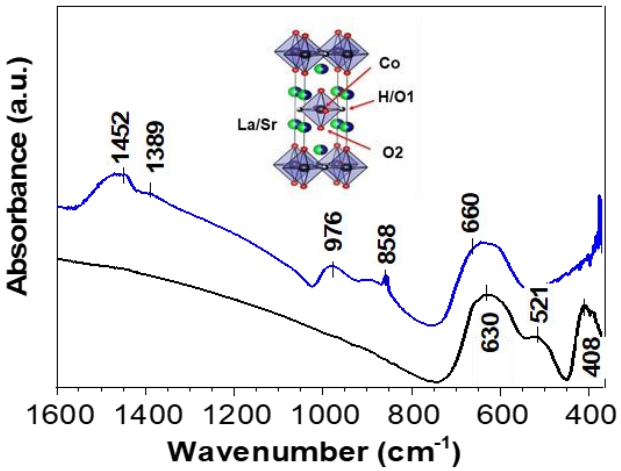

Figure 4.5 - FTIR of $LaSrCoO_4$ (black) and $LaSrCoO_{4-x}H_y$ (blue)

Fig. 4.5 shows the FT-IR profiles of $LaSrCoO_4$ and $LaSrCoO_{4-x}H_y$. Both present a broad absorption centered at about 650 cm^{-1}. Two additional signature peaks are observed in the IR spectrum of $LaSrCoO_4$ at lower wavenumbers (521 and 408 cm^{-1}). In the CoO_6 octahedra of $LaCoO_3$, bands in the 170 - 350 cm^{-1} range are assigned to Co rotational mode, and those above 350 cm^{-1} are assigned to Co–O stretching [30]. According to literature reports on $La_{2-x}Sr_xCoO_4$, the Co–O vibration modes are associated with planar oxygen O1 [31], where hydrides can replace oxide anions, these are located between 350-700 cm^{-1}. Therefore, 4 signature peaks of $LaSrCoO_4$ appear in the 400-650 cm^{-1} IR range, probably attributed to $Co–O_{axial}$ vibrations, which are in good agreement with the literature [31]. Upon reduction, those signatures typical of Co–O–Co bending modes in the ab-plane disappear in oxyhydride $LaSrCoO_{4-x}H_y$, suggesting that there is a high possibility of structural change in CoO_2 plane associated with axial oxygen replaced by hydride intercalation[5]. Moreover, $LaSrCoO_{4-x}H_y$ shows 4 extra peaks at 858, 976, 1389 and 1452 cm^{-1}. These bands may be assigned to unidentate carbonates absorbed on La–O sites [32].

4.2.2 Thermal Stability under Oxidative Environment

4.2.2.1 Oxyhydride $BaTiO_{3-x}H_x$

In the TG experiment, $BaTiO_3$ reveals almost no mass change with temperature, whereas the figure of the oxyhydride shows a slow increase in mass after 400 °C [16] (Fig. 4.6). Since no vacancies, this mass rise is directly associated with H_2 release/O_2 uptake [14], demonstrating the presence of the hydride species in the structure. The mass rise of 2.23 % implies the composition of $BaTiO_{2.7}H_{0.3}$, in good agreement with the results arising from

Rieveld Refinement. The oxidation process undergoes at a slow pace, starts at around 400 °C and finishes at almost 800 °C. The XRD of the oxyhydride after the TGA experiment in comparison with fresh oxide $BaTiO_3$ is shown in Fig.4.6. Both spent $BaTiO_{3-x}H_x$ and $BaTiO_3$ exhibit clear peak splitting of tetragonal structure and the peaks shift towards higher angles. These observations indicate that under oxidative atmosphere, the oxyhydride $BaTiO_{3-x}H_x$ is converted back to its parent $BaTiO_3$ by releasing hydride and uptaking the oxygen to fill the anion positions in the structure. Moreover, the color of the solid changes from black to white of $BaTiO_3$, evidencing total oxidation.

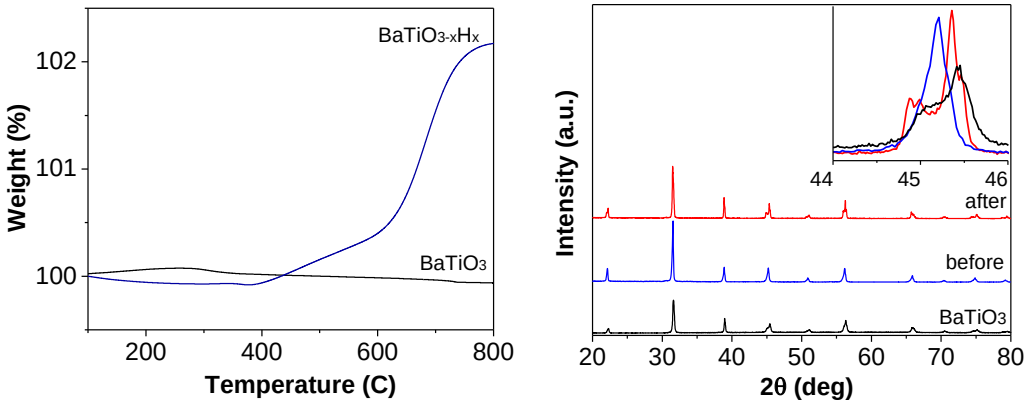

Figure 4.6 - TGA (under air) profiles $BaTiO_3$ and the oxyhydride $BaTiO_{3-x}H_x$; and X-Ray diffractions of the oxyhydride before/after the TGA experiment.

4.2.2.2 The oxyhydride $LaSrCoO_{4-x}H_y$

While $LaSrCoO_4$ shows almost no mass change during the TGA experiment under airflow (not shown), the oxyhydride exhibits an interesting behavior (Fig. 4.7). A mass loss at below 200 °C is probably attributed to adsorbed H_2O, and above 200 °C hydride starts to be released as H_2O detected by a broad shoulder of the H_2O peak. From 300 °C, a remarkable explosion of weight (~ 2.1 wt.%) indicates the occurrence of a rapid exothermal reaction, corresponding to hydride release/O_2 uptake as reported by Tassel *et al.* on $SrCrO_2H$ [13]. The hydride presence in the structure is confirmed by water and H_2 peaks in mass spectroscopy between 350 - 400 °C, and H_2O is produced from the chemical oxidation of released H_2 with air [5]. Latter mass reduction is probably attributed for β-oxygen desorption (> 550 °C), which accounts for oxygen from inner layers of lattice [33]. CO_2 in the mass spectrum may be linked to the decomposition of carbonate species above 650 °C, and in good agreement with elementary analysis (0.5 wt.% C) [33] and IR spectra. XRD measurement carried out on the $LaSrCoO_{4-x}H_y$ after the TGA experiment confirms the

complete transformation of $LaSrCoO_{4-x}H_y$ to stable perovskite phase $LaSrCoO_4$ under air. Compared to $BaTiO_{3-x}H_x$, the oxidation takes place at significantly higher speed and both oxyhydrides preserve the perovskite structures after the thermal treatment.

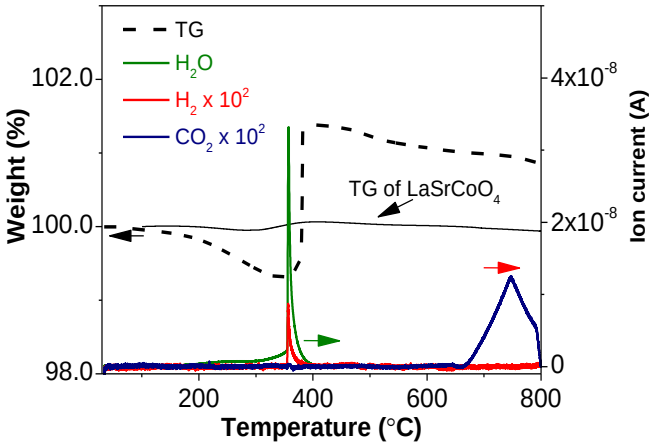

Figure 4.7 - TGA-MS profile of $LaSrCoO_{4-x}H_y$ under air.

In addition, the *in situ* X-ray data from heating $LaSrCoO_{4-x}H_y$ under oxidation atmosphere (Fig. 4.8) demonstrates that the oxyhydride phase is unchanged below ~ 200 °C. Above 200 °C, two typical peaks of oxyhydride at 30.9 ° and 32.0 ° become gradually broadened, indicating the beginning of phase transformation. At 300 °C, this structural change is more significant with the contribution of the major peak of $LaSrCoO_4$ phase. It should be noticed that in the TG experiment the oxyhydride $LaSrCoO_{4-x}H_y$ starts to uptake oxygen at a temperature above 200 °C, and completely transforming to the more stable phase of $LaSrCoO_4$ at ~ 400 °C, which can be seen by the change of the distinctive peak of oxyhydride at 32.1 ° 2θ. At elevated temperature, all reflections shifts to lower angles because of thermal expansion of the lattice parameters, but lattice planes are shifted in different angles evidencing the anisotropy in thermal expansion of the solid [34]. No other phases than $LaSrCoO_4$ can be detected after annealing the oxyhydride under air. In conclusion, taking into account the TGA-MS and XRD f(T) experiments the following reaction schema can be proposed for the thermal transformation of $LaSrCoO_{4-x}H_y$ in the air**:**

$$LaSrCoO_{4-x}H_y + 0.5(x+0.25y)O_2 \xrightarrow{200-400\,°C} LaSrCoO_4 + 0.25y\ H_2O + 0.25y\ H_2 \quad (4.1)$$

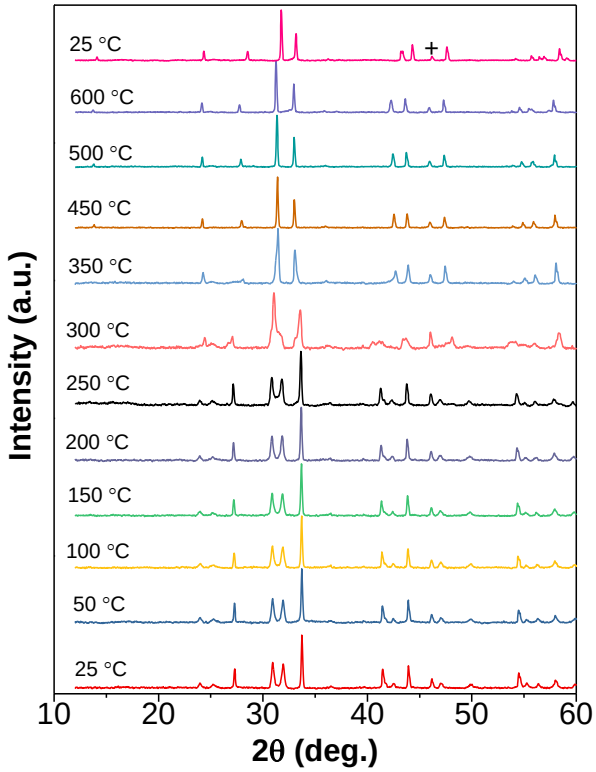

Figure 4.8 - In-situ X-ray diffraction of $LaSrCoO_{4-x}H_y$ under air, peak at 46.2 (+) belongs to metallic Pt sample holder (ICSD 01-087-0642).

4.2.3 Thermal Stability under Reductive Atmosphere

4.2.3.1 Oxyhydride $BaTiO_{3-x}H_x$

In H_2-TPR experiments, $BaTiO_3$ clearly cannot be reduced under the present conditions [35] while the negative peak of the oxyhydride evidences for the hydride release from 400 °C, associating to the hydride mobility at the same temperature of other works (Fig. 4.9) [16,19] . Hydride amount calculated by integration of the negative peak accounts for 0.13 wt.%, corresponding with the chemical composition $BaTiO_{2.7}H_{0.3}$ [16] and consistent with TG and refinement results. Moreover, the shoulders of the negative peak may be contributed by different size distribution which is evident in SEM images (Fig. 4.13). We also made XRD of the oxyhydride after the experiment which indicates peak splitting of tetragonal phase (Fig. 4.9). However, our spent solid displays gray/blue color which is similar to the reported $BaTiO_{3-\lambda}$ [36]. It should be mentioned that heating under H_2/Ar pushes out the hydride species and leaves vacant sites $BaTiO_{3-x}V_x$ (V=vacancies) which can be filled up by oxygen [19]. Moreover, under reduction condition at extremely high temperature (>1250 °C) [35], $BaTiO_3$ can be reduced to form defected structure $BaTiO_{3-\lambda}$ [35,37], while boron-doped

$BaTiO_3$ reduces the temperature to 850 °C to form blue/gray $BaTiO_{3-\lambda}$ [36]. It is suggested that with the support of hydride, $BaTiO_{3-\lambda}$ can be formed at much lower temperature in Ar-flow as described in ref. [19].

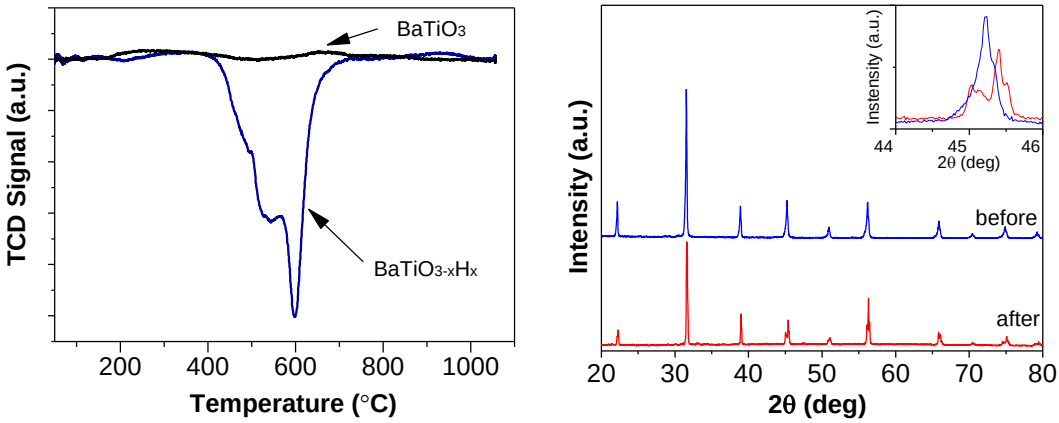

Figure 4.9 - H_2-TPR of profiles $BaTiO_3$ and the oxyhydride $BaTiO_{3-x}H_x$ and XRD profiles after the experiment

4.2.3.2 Oxyhydride $LaSrCoO_{4-x}H_y$

In-situ XRD experiments were conducted at 450 °C, 750 °C and 1050 °C under 5 %H_2/N_2 over $LaSrCoO_4$ and $LaSrCoO_{4-x}H_y$ to understand their structural evolution with temperature (Fig. 4.10). It is reported that the reduction of $LaSrCoO_4$ can be split into two consequent steps from Co^{3+} to Co^{2+} with the formation of $LaSrCoO_{3.5}$ at 400-450 °C (Equation 4.2), followed by complete reduction to metallic Co, La_2O_3 and SrO above 850 °C (Equation 4.3) [21]. In Fig. 4.10, at 450 °C, the only phase that can be found is $LaSrCoO_{3.5}$ which is confirmed by the refinement result of $LaSrCoO_{3.5}$ (Fig. 4.11). According to Hayward *et al.* [21], the appearance of $LaSrCoO_{3.5}$ can be obtained by the reduction of $LaSrCoO_4$ by 8 % H_2/N_2 from 450 °C and it starts to decompose at about 750 °C. In the present study, at 750 °C $LaSrCoO_{3.5}$ is partially decomposed into La_2O_3 (ICSD 01-073-2141), SrO (ICSD 00-048-1477) and Co^0 (ICSD 01-088-2325), which is followed by total decomposition at high temperatures. It should be mentioned that Co^0 peak can be seen in *in-situ* XRD of $LaSrCoO_4$ at 750 °C, which is lower than reported H_2-TG experiment [21], because of significantly longer duration needed for XRD measurements.

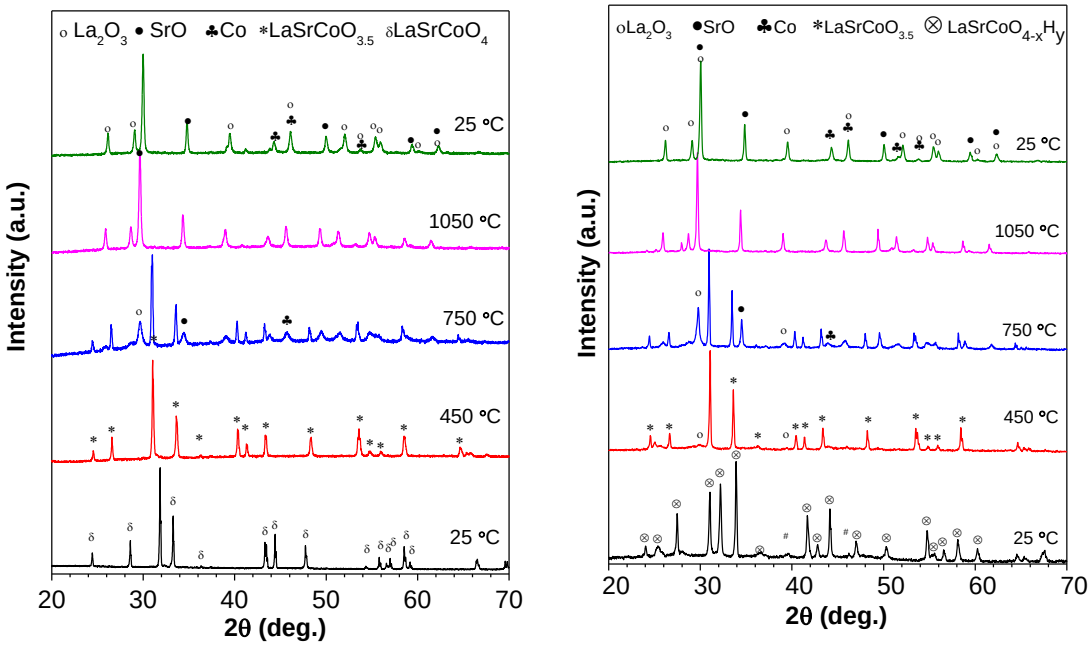

Figure 4.10 – (a) In-situ X-ray diffractions of $LaSrCoO_4$ (left) and $LaSrCoO_{4-x}H_y$ (right) under 5% H_2/N_2.. La_2O_3 (ICSD 01-073-2141), SrO (ICSD 00-048-1477) and metallic Co (ICSD 01-088-2325 and ICSD 00-015-0806). # stands for sample-Pt holder peaks.

In the case of $LaSrCoO_{4-x}H_y$, at 450 °C La_2O_3 clearly appears together with the $LaSrCoO_{3.5}$ phase (Fig. 4.10). It is reported that hydride escaped from the structure will leave a vacancy and electron which may transfer to the transition metal and promote its reduction [38]. Equation 4.4 suggests partial decomposition of the oxyhydride to form the $LaSrCoO_{3.5}$ phase, and hydride release internally reduces Co species under reductive environments. This suggestion may be supported by the presence of both $LaSrCoO_{3.5}$ and La_2O_3 at 450 °C in the in-situ XRD experiment. At 750 °C, the presence of minor phases (La_2O_3, SrO and Co) is more profound confirming the decomposition of $LaSrCo_{4-x}H_y$ follows equation 4.4. The XRD pattern of the reduced oxyhydride is similar to the reduced $LaSrCoO_4$ but with more intense oxide peaks, suggesting that the oxyhydride is more easily reduced than $LaSrCoO_4$. The oxyhydride is totally decomposed into oxides and Co^0 at 1050 °C.

$$LaSrCoO_4 + 0.5\ H_2 \xrightarrow{400-750\ ^\circ C} LaSrCoO_{3.5} + 0.5H_2O \quad (4.2)$$

$$LaSrCoO_{3.5} + H_2 \xrightarrow{>750\ ^\circ C} 0.5La_2O_3 + SrO + Co + H_2O \quad (4.3)$$

$$LaSrCoO_{4-x}H_y + 0.5(1-y)\ H_2 \xrightarrow{300\ C} (1-x)LaSrCoO_{3.5} + 0.5xLa_2O_3 + xSrO + xCo + 0.5H_2O \quad (4.4)$$

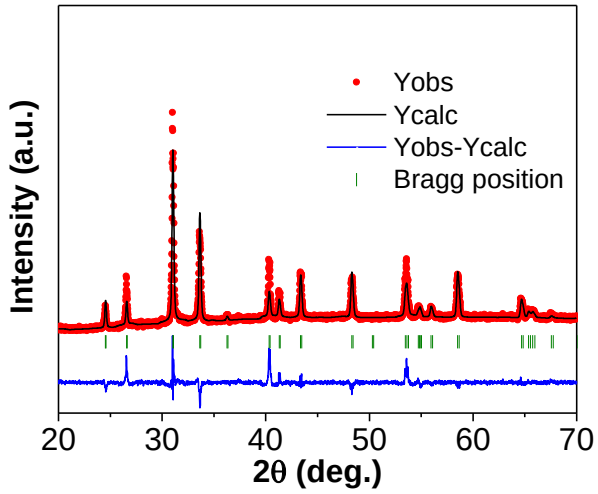

Figure 4.11 - Rietveld refinement of $LaSrCoO_4$ reduced at 450 °C under 5 $\%H_2/N_2$ ($LaSrCoO_{3.5}$ I4/mmm, a = 3.77 Å, c = 13.41 Å).

The H_2-TPR of $LaSrCoO_4$ under 5 $\%H_2$/Ar shows two reduction regions: 450-650 and above 800 °C (Fig. 4.12). The first peak is assigned to the transformation from $LaSrCoO_4$ to $LaSrCoO_{3.5}$ (Equation 4.2)[17], while the latter peak is a total reduction to La_2O_3, SrO and Co^0 (Equation 4.3)[21,33]. The X-ray diffraction of spent $LaSrCoO_4$ (not shown) exhibits La_2O_3, SrO and Co phases as in *in-situ* XRD study. The value of H_2/Co ratio is around 1.5 for totally reducing $Co^{3+} \rightarrow Co^0$ (Tab. 4.3). In the H_2-TPR profile of $LaSrCoO_{4-x}H_y$, the negative peak below 450 °C is attributed to the hydride release (Fig. 4.12). Integrating the peak yields 0.23 wt.% of hydrides, compared to 0.21 wt.% of $LaSrCoO_3H_{0.7}$ [5], and the peak asymmetry may be related to different particle size or thermal diffusibility. Hydride mobility in $LaSrCoO_3H_{0.7}$ can be probed at above 400 °C [7] matching with the tip of the negative reduction peak. The ratio of H_2/Co is remarkably low at 1.16, suggesting the presence of low oxidation state species of cobalt.

Moreover, *in-situ* XRD shows that hydride release undergoes together with the transformation of $LaSrCoO_{4-x}H_y$ to $LaSrCoO_{3.5}$ and La_2O_3 (Fig. 4.12). Furthermore, lower ration H_2/Co than that of $LaSrCoO_4$ suggests the co-existence of lower valent Co in $LaSrCoO_{4-x}H_y$ and internal contribution from H^- to the reduction [38]. On the other hand, the 450-750 °C reduction region matches with $LaSrCoO_4$ but more significant H_2 consumption, implying that there are other reducing processes rather than simple Co^{3+} to Co^{2+} (Tab. 4.3). *In-situ* XRD of $LaSrCoO_{4-x}H_y$ at 750 °C confirms the formation of Co^0 which may be obtained during the reduction by Equation 4.4. The reduction to Co^0 at early stages is supported by a small quantity of hydrogen consumption at the final reduction step

due to a small amount of remained Co cations after 750 °C or H_2 spillover with Co metallic particles. By comparison the total amount of hydrogen consumed in the H_2-TPR experiment between $LaSrCoO_4$ with Co^{3+} and $LaSrCoO_{4-x}H_y$, the mean oxidation state of Coin $LaSrCoO_{4-x}H_y$ is roughly estimated as +2.2 which is higher than +1.7 of $LaSrCoO_3H_{0.7}$. The deviation may be due to variation in hydride/vacancy quantities or the presence of small Co^{2+} in $LaSrCoO_4$ which may deviate the estimation. Further reduction at above 800 °C may be assigned to complete reduction of remaining Co^{2+} species to Co^0 which is confirmed by X-ray diffraction.

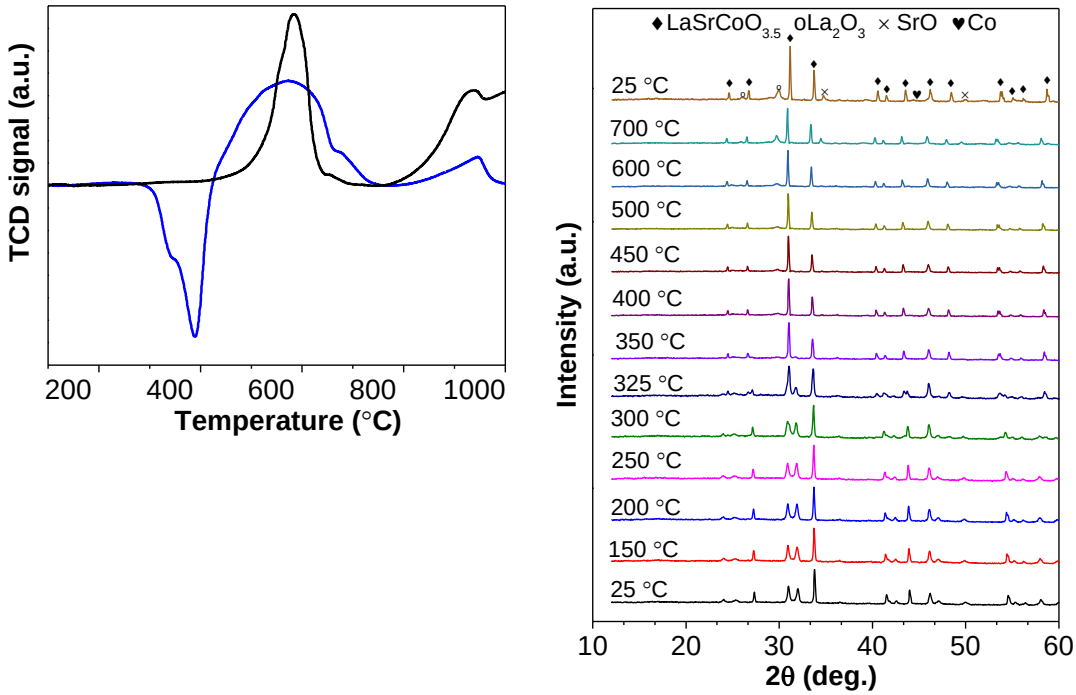

Figure 4.12- H_2-TPR profile of $LaSrCoO_{4-x}H_y$ (blue) and $LaSrCoO_4$ (black) in-situ XRD of $LaSrCoO_{4-x}H_y$ under 5 %H_2/N_2 at 5 °C.min^{-1}; and *in-situ* XRD of $LaSrCoO_{4-x}H_y$ under 5 %H_2/N_2 at 5 °C min^{-1}.

Table 4.3 – Hydrogen consumption of the reduction of $LaSrCoO_4$ and $LaSrCoO_{4-x}H_y$ calculated from H_2-TPR profiles,

Sample	**H_2/Co (mol.)**	**Negative peak (300-450 °C) (µmol.H_2.g^{-1})**	**First (+) peak (450-750 °C) (µmol.H_2.g^{-1})**	**Second(+) peak (>750 °C) (µmol.H_2.g^{-1})**	**Co^{3+} /Co**	**H^- (wt.%)**
$LaSrCoO_4$	1.60	-	1509.3	3166.4	0.48	-
$LaSrCoO_{4-x}H_y$	1.16	1239.0	2808	589	-	0.23

Hydrogen consumption calculated by integration of reduction peaks: integration of the negative peak, Co^{3+}/Co is ratio between the first positive peak of $LaSrCoO_4$ over total hydrogen consumption

4.2.4 Surface Characteristics

4.2.4.1 Oxyhydride perovskite $BaTiO_{3-x}H_x$

The particle size of parent $BaTiO_3$ may decide hydride quantity and symmetry of $BaTiO_{3-x}H_x$: nano-$BaTiO_3$ helps to form cubic oxyhydride $BaTiO_{2.4}H_{0.6}$ [16]; micro-$BaTiO_3$ (20 – 30 μm) can produce tetragonal $BaTiO_{2.7}H_{0.3}$ [15]. The oxyhydride obtained from micro-$BaTiO_3$ may have a similar quantity of hydride [15] (Fig. 4.13). However, the surface compositions of both $BaTiO_3$ and $BaTiO_{3-x}H_x$ are different from the nominal compositions (Tab. 4.4). Both samples exhibit the enrichment of Ba and O at the surface whereas the presence of Ca in the surface of $BaTiO_{3-x}H_x$ may be the result of uncomplete washing of CaO withNH_4Cl/CH_3OH solution.

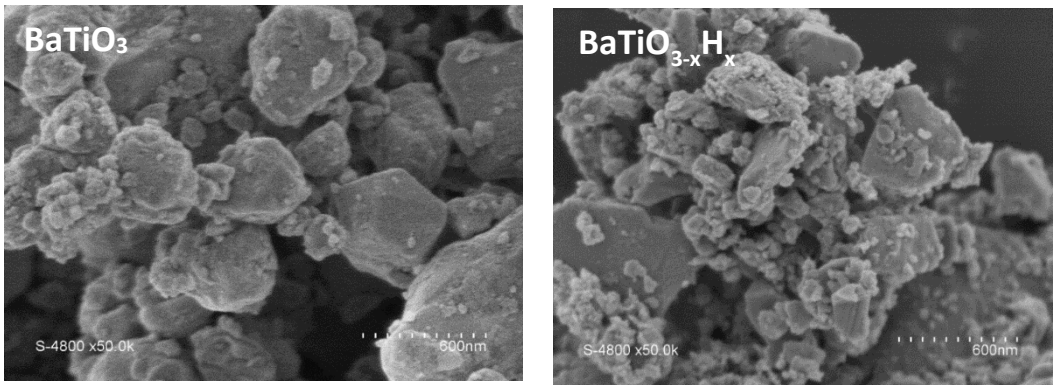

Figure 4.13 - SEM images of $BaTiO_3$ and $BaTiO_{3-x}H_x$.

Table 4.4 - Composition of $BaTiO_3$ and its oxyhydride determined by EDX,

Samples	Atomic Composition (%)			
	Ba	**Ti**	**O**	**Ca**
$BaTiO_3$	31.99	24.25	43.76	-
$BaTiO_{3-x}H_x$	25.73	22.94	48.49	2.42

We also investigated the surface characteristics of $BaTiO_{3-x}H_x$ by XPS measurements. The Ti $2p_{3/2}$ peaks of TiO_2 have been generally accepted between 458.3-458.7 eV [39], while in our work the Ti $2p_{3/2}$ was located slightly lower at 457.6 Ev (Fig. 4.14). However, the doublet splitting of 5.8 eV [40] in $BaTiO_3$ is similar to those reported on Ti^{4+} [40,41] . Meanwhile, studied $BaTiO_3$ reveals the unique peak feature with more broadening of Ti $2p_{1/2}$ than Ti $2p_{3/2}$, which is distinctive for Ti^{4+} in $BaTiO_3$ [42]. On the other hand, Ti 2p XPS of $BaTiO_{3-x}H_x$ has a similar feature with the exception of a shoulder peak at lower BE, which could be attributed to Ti^{3+} $2p_{3/2}$ [36,43]. The O 1s peak of $BaTiO_{3-x}H_x$ can be fitted by three Gaussian peaks at 529.02 ± 0.02, 531.17 ± 0.07 and 532.5 ± 0.67 eV respectively (Fig. 4.15). The low binding energy component positioned at 529.02 ± 0.02 (O_{lat}) could be ascribed to the

lattice oxygen which could be found for the $BaTiO_3$[36]. The peak at highest BE at 532.5 ± 0.67 eV (O_{dis}) usually belongs to chemisorbed or dissociated oxygen, or OH type species on the oxyhydride [44]. Finally, the middle peak at 531.17 ± 0.07eV (O_{ads}) is associated with O^{2-} defect of the structure [45,46] which evidences the reduction of Ti^{4+} to Ti^{3+} in the oxyhydride. The oxyhydride $BaTiO_{3-x}H_x$ exhibits the highest proportion of O_{ads}, and higher than that of parent $BaTiO_3$, evidencing the presence of Ti^{3+} in the surface of the oxyhydride (Tab. 4.5).

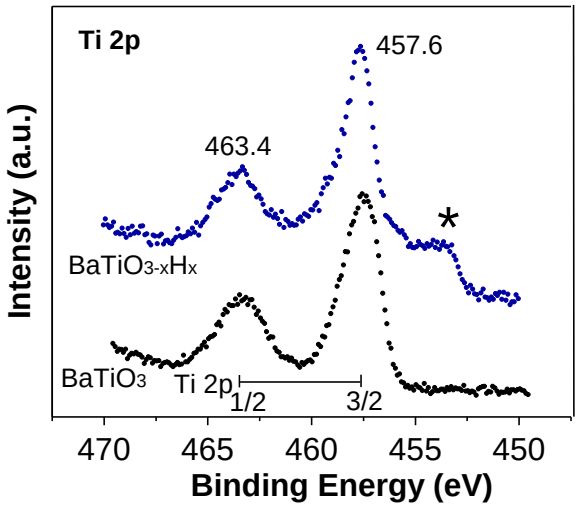

Figure 4.14 – Ti 2p XPS profiles of $BaTiO_3$ and $BaTiO_{3-x}H_x$.

Table 4.5 – O1s deconvolution of $BaTiO_3$ and $BaTiO_{3-x}H_x$,

Samples	**Percentage (Binding Energy) / %(eV)**		
	O_{lat}	**O_{ads}**	**O_{dis}**
$BaTiO_3$	27.5 (528.4)	32.4 (529.4)	40.0 (530.8)
$BaTiO_{3-x}H_x$	24.4 (529.0)	62.7(531.2)	12.9 (532.5)

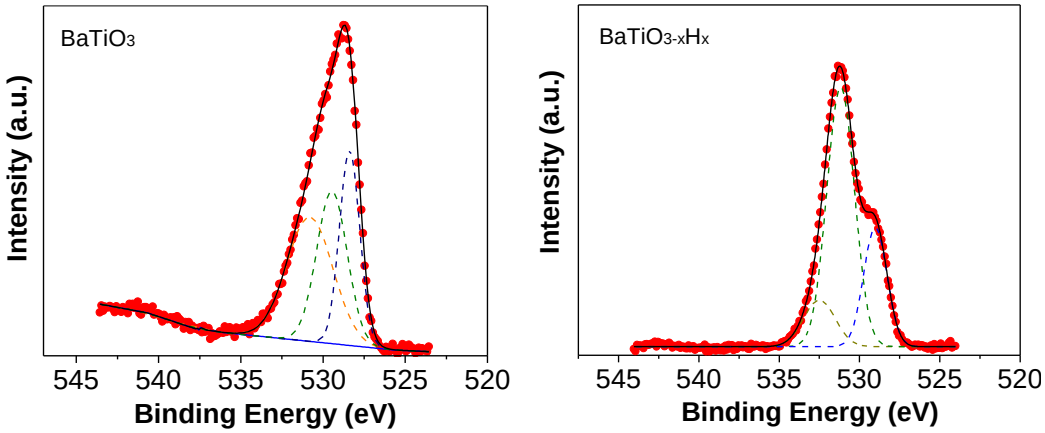

Figure 4.15 – O1s XPS profiles of $BaTiO_3$ and $BaTiO_{3-x}H_x$

4.2.4.2 Oxyhydride $LaSrCoO_{4-x}H_y$

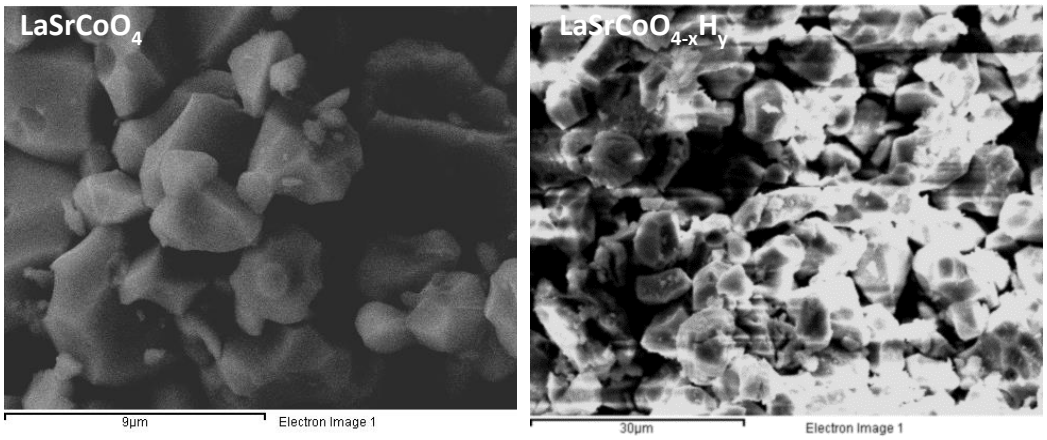

Figure 4.16 – SEM images of $LaSrCoO_4$ and $LaSrCoO_{4-x}H_y$.

Table 4.6 - Composition of $LaSrCoO_4$ and its oxyhydride determined by EDX,

Samples	Atomic Composition (%)				
	La	Sr	Co	O	Ca
$LaSrCoO_4$	14.85	14.00	14.19	56.96	-
$LaSrCoO_{4-x}H_y$	16.46	12.54	16.31	53.91	0.78

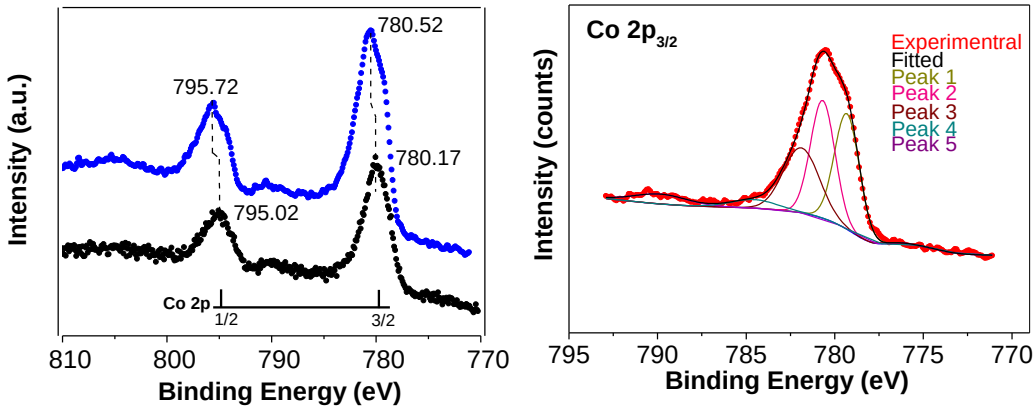

Figure 4.17 - XPS Co 2p of $LaSrCoO_4$ (black) and $LaSrCoO_{4-x}H_y$ (blue); deconvolution of Co $2p_{3/2}$ of the oxyhydride $LaSrCoO_{4-x}H_y$.

Fig. 4.16 shows the SEM images of both $LaSrCoO_4$ and $LaSrCoO_{4-x}H_y$, possessing microscale particles which are signature of solid-state synthesis at high temperature (1200 °C). After reduction by CaH_2, the overall size of particles stays intact but smaller fragments can be observed. The composition of $LaSrCoO_4$ is consistent with nominal values (Tab. 4.6) whereas the proportions of components in the oxyhydride at the surface are variable

with enrichment of La and Co at the surface. The presence of Ca may be due to not totally washing the by-products of the reduction (CaO) by the solution of NH_4Cl in methanol.

Table 4.7 - Co 2p3/2 fitting parameters: BE is binding energy, Δ is difference from peak 1. (a) is from reference [47],

	$LaSrCoO_{4-x}H_y$		**Co_3O_4[a]**	
	Binding Energy (eV)	%	Binding Energy (eV)	%
Peak 1	779.3	32.1	779.6	40.5
Peak 2	780.7	32.0	780.9	29.1
Peak 3	781.9	25.9	782.2	15.2
Peak 4	784.5	4.4	785.2	8.1
Peak 5	789.8	5.6	789.5	7.2

In literature, binding energy (BE) values of $2p_{3/2}$ Co^{3+} is 779.6 eV [48], Co^{2+} is 780.3 eV [48], Co^0 is 778.2 eV [49] and Co_3O_4 is 780.2 eV [50]. The Co 2p line of $LaSrCoO_4$ shows a similar trend with those reported for $La_{0.5}Sr_{0.5}CoO_{3-\delta}$, where Co^{3+} has a main $2p_{3/2}$ line at 780.2 eV and satellite peak at around 790 eV [51]. Moreover, distorted $2p_{3/2}$ Co is distinctive for Co^{3+} species [50], with a similar gap between $2p_{1/2}$ - $2p_{3/2}$ of 14.9 eV as reported for $LaCoO_3$ [52] and no Co^{2+} shake-up peaks at 785-788 eV [50], leading to the conclusion that probably only Co^{3+} species can be detected at the surface of $LaSrCoO_4$. On the other hand, the 2p Co line of $LaSrCoO_{4-x}H_y$ was more asymmetric with a major contribution of higher BE peaks for both $2p_{1/2}$ and $2p_{3/2}$ (Fig. 4.17) This may be associated with the superposition of Co^{3+} profile as in $LaSrCoO_4$ with other lower oxidation state Co species. In comparison with an XPS study of Co_3O_4 [47], the $LaSrCoO_{4-x}H_y$ shows similar spectrum, but reverse peak shape with more contribution of high binding energy zones, suggesting that the oxidation state of Co in the oxyhydride is lower than +2.67 of Co_3O_4. The authors[37] fitted the $2p_{2/3}$ by 5 peaks with different BE (Tab. 4.7). According to the researchers,[37] peak at 779.6 eV is dominant which may be attributed at Co^{3+}, and a small peak at 785.2 eV may be the signature satellite peak for Co^{2+}. Nevertheless, $LaSrCoO_{4-x}H_y$ showed an equal contribution between 779.3 eV and 780.7 eV, suggesting that lower oxidation state of Co species are more abundant than those in Co_3O_4.

4.2.5 Chemical Reactivity of the oxyhydrides $LaSrCoO_{4-x}H_y$ and $BaTiO_{3-x}H_x$

4.2.5.1 Chemical titration and toluene hydrodealkylation

$$C_6H_5\text{-}CH_3 \xrightarrow{oxyhydrides} C_6H_6 + CH_4 \quad (4.5)$$

In the chemical titration reaction, toluene has flowed through a large amount of oxyhydride (500 mg) at 300 °C, at which the hydride species starts mobilize and release from the perovskite structure. Reactions between toluene and hydride are expected to prove the chemical reactivity of the present oxyhydrides: $BaTiO_{3-x}H_x$ and $LaSrCoO_{4-x}H_y$. Under the oxidation environment, both oxyhydrides are converted to parent perovskites. However, $BaTiO_{3-x}H_x$ still keeps general perovskite framework with the release of hydride whereas $LaSrCoO_{4-x}H_y$ tends to decompose to oxides and metallic Co with the evolution of hydride under heating.

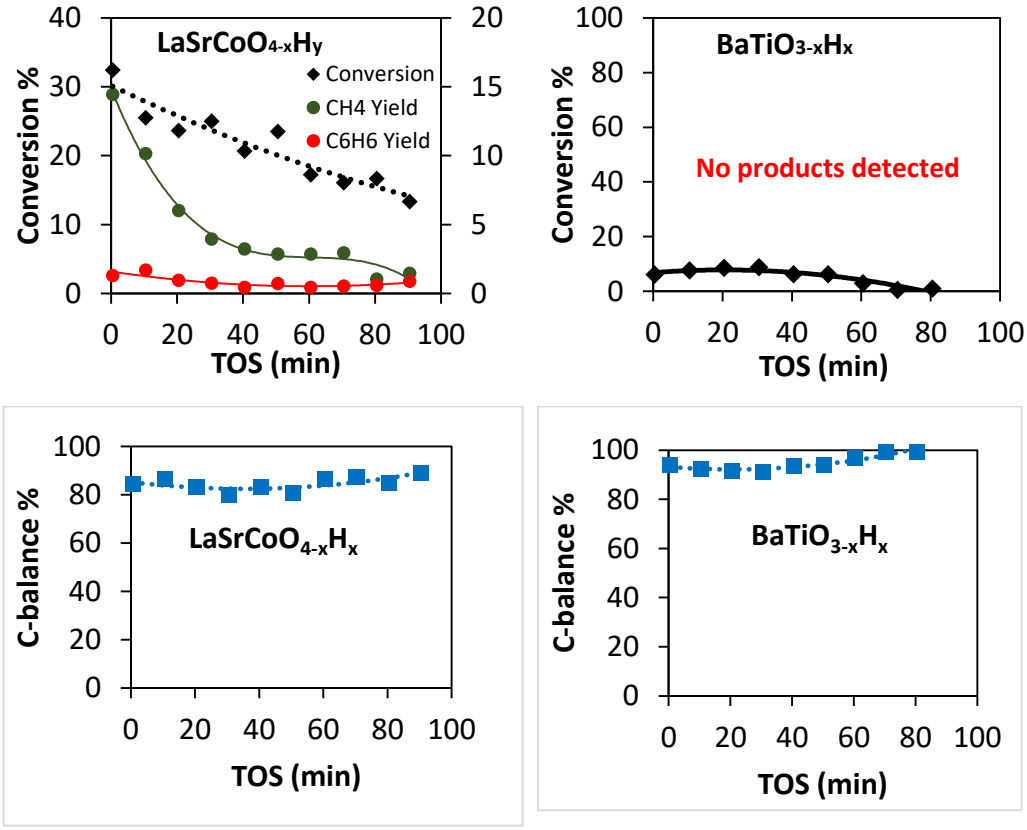

Figure 4.18– Toluene conversion and yields of products with time on stream of the chemical titration of oxyhydrides $LaSrCoO_{4-x}H_y$ and $BaTiO_{3-x}H_x$ (500 mg of the oxyhydride; 250 ppm of toluene in 100 $ml.min^{-1}$ of N_2 flow at atmospheric pressure, T = 300 °C); and C-balance

Fig. 4.18 illustrates the evolution of toluene conversions with time on stream and yields of products at 300 °C on $LaSrCoO_{4-x}H_y$ and $BaTiO_{3-x}H_x$. Better performance is recorded over $LaSrCoO_{4-x}H_y$ and toluene conversion gradually decreases, while there are no products detected form toluene chemical titration over $BaTiO_{3-x}H_x$ Furthers, the continuous

depletion of hydrogen supply over reaction time may negatively affect toluene conversion since the hydrodealkylation activity strongly relies on the partial pressure of H_2 [53]. The low quantities of C_6H_6 in comparison with CH_4 may be related to the absorption phenomenon of aromatic rings on oxide catalysts. Fig. 4.19 compares the hydrodealkylation of toluene activity over the oxyhydride $LaSrCoO_{4-x}H_y$ and oxide $LaSrCoO_4$ in the presence of H_2 gas. In the presence of H_2 gas. It is obvious that the oxyhydride catalyst has better catalytic performances in terms of conversion and products' yields. Tang *et al.* [27,28] showed that using the oxyhydride $BaTiO_{3-x}H_x$ as support for metallic catalysts significantly improves the catalytic activity for CO_2 methanation and NH_3 synthesis. The authors suggested that the function of hydride as a strong electron donor is one of the reasons for the enhancement of catalytic activity, probably promoting the reduction of doped foreign metals (Ni, Ru and Co) [28]. In the present case, no metallic phase is impregnated in the perovskite solids but remarkably better performance is obtained for $LaSrCoO_{4-x}H_y$ than $BaTiO_{3-x}H_x$. Furthermore, compared to the oxide $LaSrCoO_4$, the oxyhydride $LaSrCoO_{4-x}H_y$ exhibits better activity in hydrodealkylation of toluene.

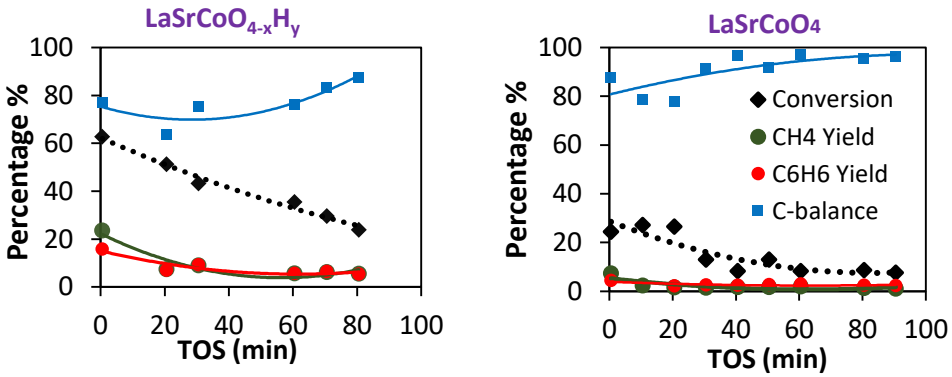

Figure 4.19 – Hydrodealkylation of toluene over perovskite $LaSrCoO_4$ and its oxyhydride $LaSrCoO_{4-x}H_y$ (Toluene 1.4 %, 5 % H_2/N_2; 150 mg of catalyst, T = 350 °C).

4.2.5.2 Characterization of spent catalysts

Fig. 4.20 compares the X-ray patterns of $LaSrCoO_{4-x}H_y$ before and after the chemical titration of toluene at 300 °C. Peak at 31.2° 2θ is distinctive for the oxyhydride phase, which is less intense after the chemical titration ,which may suggest more thermal decomposition at high temperature. By equation 4.4, the oxyhydride can be decomposed to $LaSrCoO_{3.5}$, La_2O_3, SrO and Co at intermediate temperatures. However, peaks for Co^0, SrO and La_2O_3 are not clearly identified probably due to superposition. Rietveld analysis against diffraction pattern of spent $LaSrCoO_{4-x}H_y$ at 300 °C with 5 phases: $LaSrCoO_{3.5}$,

$LaSrCoO_{4-x}H_y$, La_2O_3, Co and SrO, showing the dominance of $LaSrCoO_{3.5}$ and $LaSrCoO_{4-x}H_y$ (Tab. 4.8). The release of H^- as an electron donator helps to internally reduce the transition Co to the metallic phase which may be an active phase for the chemical titration reaction. Compared to $LaSrCoO_{3.5-x}H_y$, $Ti^{3+/4+}$ in $BaTiO_{3-x}H_x$ cannot be reduced to Ti^0, therefore no activity can be shown in case of chemical titration over $BaTiO_{3-x}H_x$. It should be mentioned that between $LaSrCoO_4$ and $LaSrCoO_{4-x}H_y$, the oxyhydride reveals better activity towards hydrodealkylation. It may play as a support for the reaction over Co^0 which is *in-situ* formed by the hydride evolution. These findings are consistent with the works of Tang *et al*. [27,28] in which the catalysts (Ni, Co, Ru) / $BaTiO_{3-x}H_x$ always shows better catalytic performance than (Ni, Co, Ru) / $BaTiO_3$ probably due to the reduction of active phases supported by hydride release during the pretreatment of catalysts at 400 °C under H_2/N_2 flow.

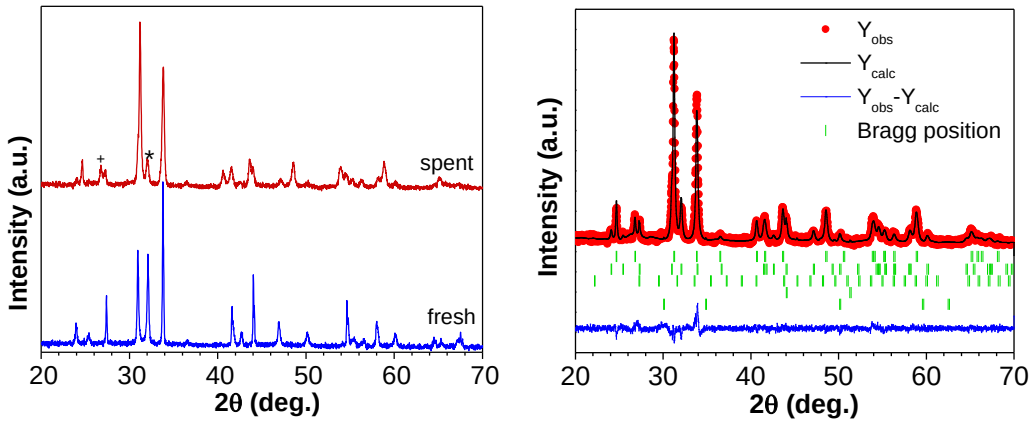

Figure 4.20 - X-ray diffractions of fresh and spent $LaSrCoO_{4-x}H_y$, refinement of oxyhydride $LaSrCoO_{4-x}H_y$ spent at 300 C of chemical titration (Bragg positions top to bottom: $LaSrCoO_{3.5}$, $LaSrCoO_{4-x}H_y$, La_2O_3, Co and SrO).

Table 4.8 - Phase compositions obtained from Rietveld refinement of spent $LaSrCoO_{4-x}H_y$ and fitting parameters (χ^2 of 1.96 and R-factor of 2.84),

	$LaSrCoO_{3.5}$	**$LaSrCoO_{4-x}H_y$**	**La_2O_3**	**Co**	**SrO**
Phase compositions (%)	62.81	36.22	0.31	0.48	0.18

The presence of Co^0 inside the spent $LaSrCoO_{4-x}H_y$ is hard to be detected by X-ray diffraction technique due to the co-existence of multiple phases leading to the superposition (Fig. 4.20). Therefore, M-H magnetic measurements were conducted on $LaSrCoO_4$, fresh and spent $LaSrCoO_{4-x}H_y$ (Fig. 4.21). $LaSrCoO_4$ has reportedly paramagnetic ground state

[54] and experimental values of μ_{eff} = 2.6 μ_B [55] or μ_{eff} = 2.7 μ_B [54], being consistent with intermediate spin state Co^{3+} and $LaSrCoO_3H_{0.7}$ exhibits antiferromagnetism [5]. Among different oxidation states of Co, only Co^0 possessed ferromagnetic properties [56]. Fig. 20 shows that a significantly high magnetic field (~ 10000 Oe) is required to saturate the ferromagnetic Co^0, and the M-H curve of Co^0 also exhibit hysteresis which is a signature of ferromagnetic components [57]. The M-H curves of $LaSrCoO_{4-x}H_y$ shows magnetic saturation at a magnitude which is much lower than required field to saturate non-magnetic material, while there is no magnetization saturation for $LaSrCoO_4$ in the applied field (Fig. 4.21). The hysteresis loop of $LaSrCoO_{4-x}H_y$ also shows coercivity at low fields. This behavior is the most distinctive property of ferromagnetic component [57] which is possibly due to the metallic Co in the sample. It should be reminded that $LaSrCoO_3H_{0.7}$ exhibits antiferromagnetism[5], and Co^0 can be found by the $LaSrCoO_4$ reduction with NaH at 550 °C due to unreacted Co_3O_4 [21]. The presence of a small amount ferromagnetic component in the studied $LaSrCoO_{4-x}H_y$ probably due to the reduction of minor cobalt oxides or overreduction of $LaSrCoO_4$ during the synthesis by CaH_2. Linear fitting gives a possible amount of Co^0 impurity as 1.69 (mol.%) (Tab. 4.9).

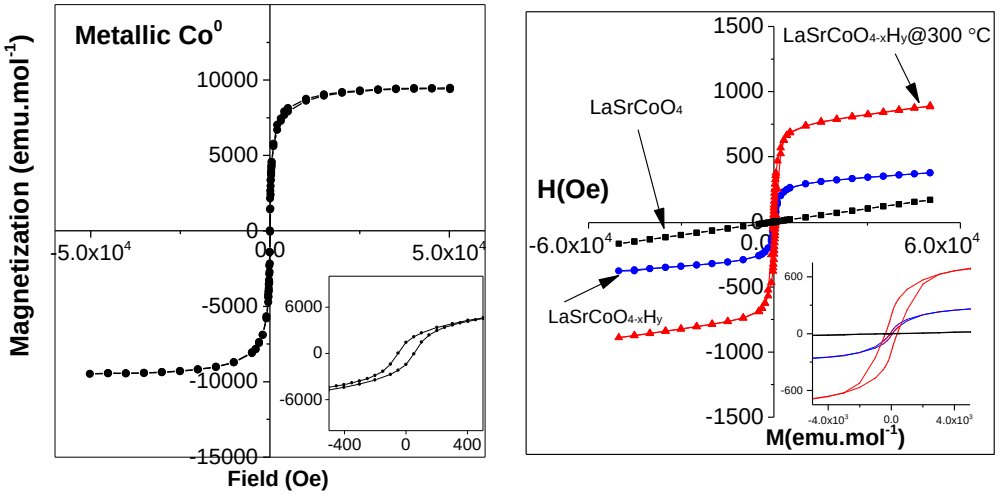

Figure 4.21 – M-H curves of metallic Co^0 and $LaSrCoO_4$, fresh and spent $LaSrCoO_{4-x}H_y$ at ambient temperature.

The M-H loop of the spent catalysts exhibits enhanced magnetization saturation and coercivity H_c which may imply more contribution from ferromagnetic component (Fig.21). Linear fitting of saturation region of the M-H isotherm results in that the quantity of Co^0 in the spent sample at 300 °C is almost three times higher than that in the starting material (Tab. 4.9). Formation of Co^0 during thermal treatment is in line with our proposed reaction (Equation 4.4). Surprisingly, metallic Co can be formed by reducing $LaSrCoO_4$ with 8

$\%H_2/N_2$ at remarkably more elevated temperature (>800 °C) [21]. In the oxyhydride, transferring e^- from internal H^- to Co site moderates the reduction process, allowing to form metallic sites at a lower temperature. The formation of the Co^0 may be directed to the activity of the oxyhydride but it is compensated by the H_2 shortage. The absence of metallic sites results in no activity in the chemical titration of toluene for $BaTiO_{3-x}H_x$ or low catalytic performances of hydrodealkylation of toluene for $LaSrCoO_4$.

Table 4.9 - Fitting parameters from M-H isotherm of fresh and spent $LaSrCoO_{4-x}H_y$ (2-5 Tesla of applied field). Co^0 is calculated based of magnetization saturation of Co^0 (M_s = 1400 G [57,58]),

Samples	Magnetization saturation ($emu.mol^{-1}$)	Co^0 (mol.%)	Fitting quality (R)
Fresh	285	1.69	0.9987
Spent	777	4.62	0.9983

It should be noted that thermal treatment stimulates hydrides to escape from $LaSrCoO_{4-x}H_y$ in a form of H_2 gas, simultaneously forms metallic Co^0 which can absorb H_2 for further reactions. However, thermal decomposition of the oxyhydride to $LaSrCoO_{3.5}$ and metallic Co is remarkably dominant than chemical processes. Supposedly, contributions to catalytic performances are probably shared among hydride species, H_2 gas and metallic sites. Similar tests were conducted on $BaTiO_{3-x}H_x$ which possesses a sustainable perovskite framework and no metallic sites can be formed during heating, exhibiting no products. These findings indicate that hydride-doped on stable support shows no activity towards the hydrodealkylation of toluene. The comparison between the two oxyhydrides highlights that the activity of oxyhydrides significantly depends on metallic sites on the supports, without it no catalytic performance can be recorded at reaction temperatures. The oxyhydride $LaSrCoO_{4-x}H_y$ supports the formation of Co^0 via *in-situ* reduction at low temperatures, resulting in the enhancement of catalytic activity.

4.3 CONCLUSIONS

The topochemical reaction allows synthesizing two oxyhydrides $LaSrCoO_{4-x}H_y$ and $BaTiO_{3-x}H_x$ at mild conditions. $BaTiO_{3-x}H_x$ is likely to maintain the perovskite structure under reduction condition, whereas $LaSrCoO_{4-x}H_y$ undergoes thermal decomposition to $LaSrCoO_{3.5}$, oxides, and Co^0 with hydride release. Hydride as an electron donator escaped from inside structure surprisingly supports the low-temperature formation of metallic Co.

Under H_2 flow, *in-situ* XRD illustrates mainly structural transformation of $LaSrCoO_{4-x}H_y$ to $LaSrCoO_{3.5}$ at between 250 – 400 °C, which is consistent with the H_2-TPR temperature range. Moreover, H_2-TPR suggests the presence of lower valence Co in $LaSrCoO_{4-x}H_y$ and this technique can estimate the hydride quantities. Evidence of extraordinarily low valent states of Co and Ti can also be confirmed by surface by XPS. Besides that, under oxidative environment, both oxyhydrides are converted to stable perovskite structures. The reactivity of the oxyhydrides towards hydrodealkylation of toluene are likely associated with the presence of active metallic sites, which can be determined by magnetic measurements. The shortage of H_2 source with time has negative impacts on toluene conversion over $LaSrCoO_{4-x}H_y$, while stable perovskite framework of $BaTiO_{3-x}H_x$ evidences no activity during the experiments. In the presence of H_2 in feeding gas mixture, $LaSrCoO_{4-x}H_y$ reveals the better catalytic performance than that of $LaSrCoO_4$ at 350 °C, confirming the pivotal role of formed Co^0 in the catalytic activity of the oxyhydride perovskite.

4.4 REFERENCES

1 J. F. Brice and A. Moreau, *Ann Chim Fr*, 1982, **7**, 623–634.
2 B. Malaman and J. F. Brice, *J. Solid State Chem.*, 1984, **53**, 44–54.
3 B. Huang and J. D. Corbett, *J. Solid State Chem.*, 1998, **141**, 570–575.
4 B. Huang and J. D. Corbett, *Inorg. Chem.*, 1998, **37**, 1892–1899.
5 M. A. Hayward, E. J. Cussen, J. B. Claridge, M. Bieringer, M. J. Rosseinsky, C. J. Kiely, S. J. Blundell, I. M. Marshall and F. L. Pratt, *Science (80-.).*, 2002, **295**, 1882–1884.
6 C. A. Bridges, G. R. Darling, M. A. Hayward and M. J. Rosseinsky, *J. Am. Chem. Soc.*, 2005, **127**, 5996–6011.
7 C. A. Bridges, F. Fernandez-Alonso, J. P. Goff and M. J. Rosseinsky, *Adv. Mater.*, 2006, **18**, 3304–3308.
8 R. M. Helps, N. H. Rees and M. A. Hayward, *Inorg. Chem.*, 2010, **49**, 11062–11068.
9 J. Bang, S. Matsuishi, H. Hiraka, F. Fujisaki, T. Otomo, S. Maki, J. I. Yamaura, R. Kumai, Y. Murakami and H. Hosono, *J. Am. Chem. Soc.*, 2014, **136**, 7221–7224.
10 T. Katayama, A. Chikamatsu, K. Yamada, K. Shigematsu, T. Onozuka, M. Minohara, H. Kumigashira, E. Ikenaga and T. Hasegawa, *J. Appl. Phys.*, , DOI:10.1063/1.4961446.
11 F. Denis Romero, A. Leach, J. S. Möller, F. Foronda, S. J. Blundell and M. A. Hayward, *Angew. Chemie - Int. Ed.*, 2014, **53**, 7556–7559.
12 C. Tassel, Y. Goto, D. Watabe, Y. Tang, H. Lu, Y. Kuno, F. Takeiri, T. Yamamoto, C. M. Brown, J. Hester, Y. Kobayashi and H. Kageyama, *Angew. Chemie - Int. Ed.*, 2016, **55**, 9667–9670.
13 C. Tassel, Y. Goto, Y. Kuno, J. Hester, M. Green, Y. Kobayashi and H. Kageyama, *Angew. Chemie - Int. Ed.*, 2014, **53**, 10377–10380.
14 Y. Goto, C. Tassel, Y. Noda, O. Hernandez, C. J. Pickard, M. A. Green, H. Sakaebe, N. Taguchi, Y. Uchimoto, Y. Kobayashi and H. Kageyama, *Inorg. Chem.*, 2017, **56**, 4840–4845.
15 T. Sakaguchi, Y. Kobayashi, T. Yajima, M. Ohkura, C. Tassel, F. Takeiri, S.

Mitsuoka, H. Ohkubo, T. Yamamoto, J. Kim, N. Tsuji, A. Fujihara, Y. Matsushita, J. Hester, M. Avdeev, K. Ohoyama and H. Kageyama, *Inorg. Chem.*, 2012, **51**, 11371–11376.

16 Y. Kobayashi, O. J. Hernandez, T. Sakaguchi, T. Yajima, T. Roisnel, Y. Tsujimoto, M. Morita, Y. Noda, Y. Mogami, A. Kitada, M. Ohkura, S. Hosokawa, Z. Li, K. Hayashi, Y. Kusano, J. E. Kim, N. Tsuji, A. Fujiwara, Y. Matsushita, K. Yoshimura, K. Takegoshi, M. Inoue, M. Takano and H. Kageyama, *Nat. Mater.*, 2012, **11**, 507–511.

17 T. Yajima, A. Kitada, Y. Kobayashi, T. Sakaguchi, G. Bouilly, S. Kasahara, T. Terashima, M. Takano and H. Kageyama, *J. Am. Chem. Soc.*, 2012, **134**, 8782–8785.

18 T. Yajima, F. Takeiri, K. Aidzu, H. Akamatsu, K. Fujita, W. Yoshimune, M. Ohkura, S. Lei, V. Gopalan, K. Tanaka, C. M. Brown, M. A. Green, T. Yamamoto, Y. Kobayashi and H. Kageyama, *Nat. Chem.*, 2015, **7**, 1017–1023.

19 N. Masuda, Y. Kobayashi, O. Hernandez, T. Bataille, S. Paofai, H. Suzuki, C. Ritter, N. Ichijo, Y. Noda, K. Takegoshi, C. Tassel, T. Yamamoto and H. Kageyama, *J. Am. Chem. Soc.*, 2015, **137**, 15315–15321.

20 T. Yamamoto, R. Yoshii, G. Bouilly, Y. Kobayashi, K. Fujita, Y. Kususe, Y. Matsushita, K. Tanaka and H. Kageyama, *Inorg. Chem.*, 2015, **54**, 1501–1507.

21 M. A. Hayward and M. J. Rosseinsky, *Chem. Mater.*, 2000, **12**, 2182–2195.

22 A. Bowman, J. B. Claridge and M. J. Rosseinsky, *Chem. Mater.*, 2006, **18**, 3046–3056.

23 Y. Kobayashi, O. J. Hernandez, T. Sakaguchi, T. Yajima, T. Roisnel, Y. Tsujimoto, M. Morita, Y. Noda, Y. Mogami, A. Kitada, M. Ohkura, S. Hosokawa, Z. Li, K. Hayashi, Y. Kusano, J. eun Kim, N. Tsuji, A. Fujiwara, Y. Matsushita, K. Yoshimura, K. Takegoshi, M. Inoue, M. Takano and H. Kageyama, *Nat. Mater.*, 2012, **11**, 507.

24 G. Kobayashi, Y. Hinuma, S. Matsuoka and A. Watanabe, *Science (80-.).*, 2016, **351**, 1314–1317.

25 Y. Kobayashi, O. Hernandez, C. Tassel and H. Kageyama, *Sci. Technol. Adv. Mater.*, 2017, **18**, 905–918.

26 G. Bouilly, T. Yajima, T. Terashima, Y. Kususe, K. Fujita, C. Tassel, T. Yamamoto, K. Tanaka, Y. Kobayashi and H. Kageyama, *CrystEngComm*, 2014, **16**, 9669–9674.

27 Y. Tang, Y. Kobayashi, C. Tassel, T. Yamamoto and H. Kageyama, *Adv. Energy Mater.*, 2018, **8**, 1–7.

28 Y. Tang, Y. Kobayashi, N. Masuda, Y. Uchida and H. Okamoto, *Adv. Energy Mater.*, 2018, **8**, 1801772.

29 G. Demazeau, P. Courbin, G. le, Flem, J. L. Pouchard, M., Hagenmueller, P., Soubeyroux, I. G. Main and .A. Robins, *Nouv. J. Chim*, 1979, **3**, 171.

30 X. Wang, Y. Han, X. Song, W. Liu and H. Cui, *Comput. Mater. Sci.*, 2017, **136**, 191–197.

31 S. Castro-Garcia, M. Sanchez-Andujar, C. Rey-Cabezudo, M. A. Senarıs-Rodrıguez and C. Julien, *J. Alloys Compd.*, 2001, **324**, 710–713.

32 Y. Ono and H. Hattori, *Solid Base Catalysis*, Springer Science & Business Media, 2012.

33 J. A. Onrubia and J. R. González-velasco, *Appl. Catal. B, Environ.*, 2017, **213**, 198–210.

34 C. Tealdi, C. Ferrara, L. Malavasi, P. Mustarelli, C. Ritter, G. Chiodelli and Y. A. Diaz-Fernandez, *Phys. Rev. B*, 2010, **82**, 174118.

35 H. Arend and L. Kihlborg, *J. Am. Ceram. Soc.*, 1969, **52**, 63–65.

36 Z. Q. Zheng and X. P. Zhou, *J. Am. Ceram. Soc.*, 2013, **96**, 3504–3510.

37 H. Arend, G. Montemezzani, K. Szot and H. Turcicova, *Ferroelectrics*, 1997, **202**,

1–10.
38 S. Yamaguchi, *Science (80-.).*, 2016, **351**, 1262–1263.
39 C. Badini, S. M. Deambrosis, O. Ostrovskaya, V. Zin, E. Padovano, E. Miorin, M. Castellino and S. Biamino, *Ceram. Int.*, 2017, **43**, 5417–5426.
40 M. C. Biesinger, L. W. M. Lau, A. R. Gerson and R. S. C. Smart, *Appl. Surf. Sci.*, 2010, **257**, 887–898.
41 M. E. Pilleux, C. R. Grahmann and V. M. Fuenzalida, *J. Am. Ceram. Soc.*, 1994, **77**, 1601–1604.
42 H. Jena, V. K. Mittal, S. Bera, S. V. Narasimhan, K. V. G. Kutty and T. R. N. Kutty, *Appl. Surf. Sci.*, 2008, **254**, 7074–7079.
43 F. Guillemot, M. C. Porté, C. Labrugère and C. Baquey, *J. Colloid Interface Sci.*, 2002, **255**, 75–78.
44 S. Major, S. Kumar, M. Bhatnagar and K. L. Chopra, *Appl. Phys. Lett.*, 1986, **49**, 394–396.
45 M. Chen, X. Wang, Y. H. Yu, Z. L. Pei, X. D. Bai, C. Sun, R. F. Huang and L. S. Wen, *Appl. Surf. Sci.*, 2000, **158**, 134–140.
46 H. Tan, Z. Zhao, W. Bin Zhu, E. N. Coker, B. Li, M. Zheng, W. Yu, H. Fan and Z. Sun, *ACS Appl. Mater. Interfaces*, 2014, **6**, 19184–19190.
47 M. C. Biesinger, B. P. Payne, A. P. Grosvenor, L. W. M. Lau, A. R. Gerson and R. S. C. Smart, *Appl. Surf. Sci.*, 2011, **257**, 2717–2730.
48 E. A. Lombardo, K. Tanaka and I. Toyoshima, *J. Catal.*, 1983, **80**, 340–349.
49 M. Oku and Y. Sato, *Appl. Surf. Sci.*, 1992, **55**, 37–41.
50 M. O'Connell, A. . Norman, C. . Hüttermann and M. . Morris, *Catal. Today*, 1999, **47**, 123–132.
51 G. Vovk, X. Chen and C. A. Mims, *J. Phys. Chem. B*, 2005, 2445–2454.
52 C. A. F. Vaz, D. Prabhakaran, E. I. Altman and V. E. Henrich, *Phys. Rev. B - Condens. Matter Mater. Phys.*, 2009, **80**, 1–7.
53 D. C. Grenoble, *J. Catal.*, 1979, **56**, 32–39.
54 A. V. Chichev, M. Dlouhá, S. Vratislav, K. Knížek, J. Hejtmánek, M. Maryško, M. Veverka, Z. Jirák, N. O. Golosova, D. P. Kozlenko and B. N. Savenko, *Phys. Rev. B - Condens. Matter Mater. Phys.*, 2006, **74**, 1–8.
55 Y. Moritomo, K. Higashi, K. Matsuda and A. Nakamura, *Phys. Rev. B*, 1997, **55**, R14725–R14728.
56 S. C. Petitto, E. M. Marsh, G. A. Carson and M. A. Langell, *J. Mol. Catal. A Chem.*, 2008, **281**, 49–58.
57 C. Kittel, in *Introduction to Solid State Physics*, Wiley: New York (US), 2004, p. 322.
58 S. P. Parker, *Solid-State Physics Source Book*, McGraw-Hill: New York (US), 1988.

Chapter V- Co- and Ga-doping of $LaAlO_3$ perovskite orients ethanol conversion towards dehydrogenation products

5.1 INTRODUCTION

The fermentation of renewable biomass to ethanol provides one of the largest volume liquid biofuels produced [1,2]. The ethanol global production is expected to increase by 4-6 % annually to 30 billion gallons in the next few years [3,4]. The demand for using bioethanol as an additive for automobile fuel has increased rapidly all over the world. Blending bioethanol with conventional fuels is the most common and efficient way to emit less carbon dioxide than combusting pure fossil fuels. Another approach for sustainable development is the catalytic conversion of bioethanol to valuable chemicals or intermediates [5]. Some attractive chemicals obtained by chemical conversion of bioethanol are 1-butanol for blending agent with gasoline [4], olefins (ethylene, propylene, butadiene,1,3) [6–9] for polymer productions, and solvents (acetone, pentanone-2, ethyl acetate) [10–12]. Different catalytic systems guide the ethanol conversion by different routes towards various products [4,5,7,13–15]. The design of catalysts should consider the complexity of reaction pathways such as dehydration, dehydrogenation, aldolization, Tischenko reaction, etc. which can be controlled by surface properties.

Perovskite structure with a general formula ABO_3 is able to adopt different types of elements until it satisfies the Goldschmidt rule [16]. Following to this principle, both A (alkaline earth/alkaline and larger cations) and B (transition cations) should yield a tolerance factor t ($t = (r_A + r_O)/((\sqrt{2}(r_B + r_O))$ and r_A , r_B and r_O are ionic radii of A, B, and O respectively) in a range between 0.75 and 1 [17]. About 90 % of metallic elements in the periodic table can be crystallized in the perovskite frameworks [16]. Thanks to a wide range of metals adopting in the structures allowing tuning physicochemical properties, the perovskite solids find enormous applications in catalysis for: steam reforming of toluene [18–20], ethanol [21,22], CH_4 [23–25], bioglycerol [26]; valorization of bio-oil [27–30], biomass [31], HMF [32]; lignin partial oxidation [33,34]; electrocatalysis [35] and environmental treatment [36–40]. One of the limitations of perovskite oxides is low surface area due to high-temperature synthesis, inhibiting its applications to other chemical reactions. This can be overcome by preparation

routes such as using templates [41–44]. The versability to compositions and tunability to physicochemical properties make perovskite oxides appealing candidates for heterogeneous catalysis.

To our knowledge, the ethanol valorization over perovskite catalysts was investigated by a limited number of studies. Tesquet *et al.* [45] investigated ethanol conversion over $LaFeO_3$-base perovskites, indicating that high quantities of basic sites on the perovskite surface lead to an increase in butanol-1 selectivity via the Guerbet mechanism. Chen *et al.* [46] discovered that over $LaMnO_4$ Mn^{4+}-nonstoichiometric oxygen pair as a Lewis acid-base couple is active for the aldolization of ethanol to form C_4 products. More recently, Yu *et al.* [47] compared $LaMnO_3$ with $LaFeO_3$ and silica-supported perovskites ($LaMnO_3/SiO_2$ and $LaFeO_3/SiO_2$) for ethanol aldolization. They found that both perovskites contain majorly basic sites and supporting on SiO_2 may suppress the basicity and increase acidities due to an enhanced B^{4+} as Lewis sites. Un-supported perovskites promote the formation of acetone, pentanone-2, ethyl acetate, and ethyl butyrate while supporting on SiO_2 results in more products of dehydration and aldolization processes. However, only Mn^{4+} or Fe^{4+} which are Lewis acid sites do not favor the aldolization reactions towards C_4 products (butadiene-1,3 and butanol-1). Non-stoichiometric oxygen on the surface is another key factor in the reactions. The authors concluded that supporting perovskite oxides on SiO_2 is able to tune the surface acid-base properties, tailoring different products.

In the present study, we investigated substituted perovskite catalysts ($LaAl_{0.75}B_{0.25}O_3$ with B = Co, Ga) for the ethanol valorization. The prepared perovskites are dominated by the basic sites by the nature of A-site cation. $LaAlO_3$ has the highest acidity whereas substitution of Al by Ga and Co results in a reduction in acidity. All catalysts were tested for the ethanol valorization yielding both olefins and oxygenates products with excellent conversions. The quantities of olefins may be controlled by the acidity of the catalysts whilst the formation of oxygenates depends on the nature of cation substitutions. Acetone is the major product over reducible Co-doped perovskite, and further transformed products (monoolefins>C2, pentanone-2, and C_7-oxygenates) from acetone are limited on this catalyst. On the other hand, $LaAl_{0.75}Ga_{0.25}O_3$ is an effective catalyst of aldol coupling of acetaldehyde to crotonaldehyde and further reaction to butadiene. At a high temperature of the reaction, Ga-doped perovskite becomes an effective catalyst for the formation of odd-C oxygenate products by acetone-acetaldehyde aldolization. The present study suggests the

potential possibilities to tune the surface acid-base properties of perovskite catalysts by substitutions in order to tailor the production of desired products.

5.2 RESULT AND DISCUSSIONS

5.2.1 Physicochemical properties

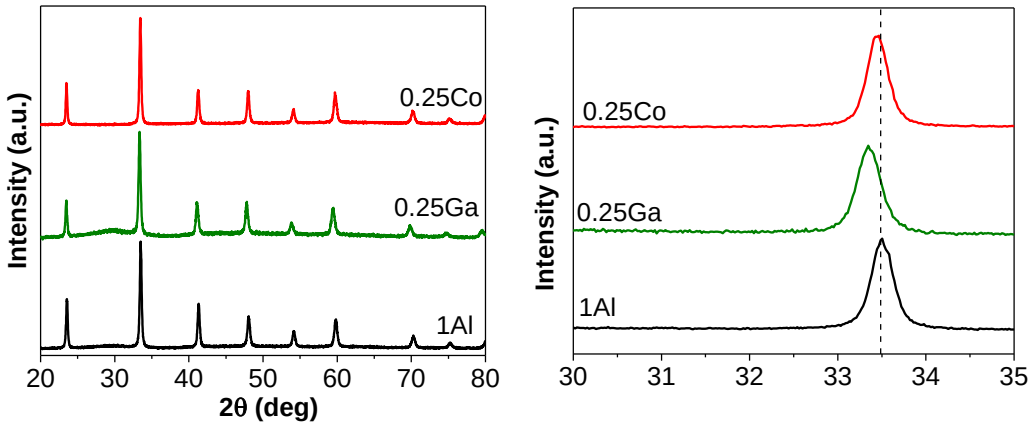

Figure 5.1 – X-ray diffraction patterns of $LaAlO_3$ (1Al), $LaAl_{0.75}Co_{0.25}O_3$ (0.25Co) and $LaAl_{0.75}Ga_{0.25}O_3$ (0.25Ga) and their magnifications.

Fig. 5.1 shows the XRD patterns of studied perovskite samples, indicating the pure perovskite phase present in the prepared catalysts. In the magnification pattern, the partial substitutions of Al^{3+} by Ga^{3+} and Co^{3+} shift peak towards lower angles due to the expansion of the unit cells. In fact, Ga^{3+} and Co^{3+} cations with radii of 0.62 and 0.546 Å [48] respectively replace smaller Al^{3+} (0.535 Å) leading to the enlargement of the unit cells. This observation indicates that Ga^{3+} and Co^{3+} cations are incorporated in the crystalline structure upon synthesis.

Table 5.1- Refinement parameters of perovskites calcined at 700 °C,

Sample	a (Å)	c (Å)	cell volume (Å^3)
$LaAlO_3$	3.360(1)	13.107(5)	326.1(2)
$LaAl_{0.75}Co_{0.25}O_3$	5.3594(23)	13.1705(9)	327.62(3)
$LaAl_{0.75}Ga_{0.25}O_3$	5.397(2)	13.21(1)	333.1(4)

Moreover, Fig. 5.2 shows a linear relationship between ionic radii and cell parameters, suggesting that all foreign cations are well introduced into the perovskite phase of $LaAlO_3$ upon substitutions. The cell parameters were obtained by Rietveld analysis with the Thompson-Cox-Hastings pseudo-Voigt peak profile and R-3c space group.

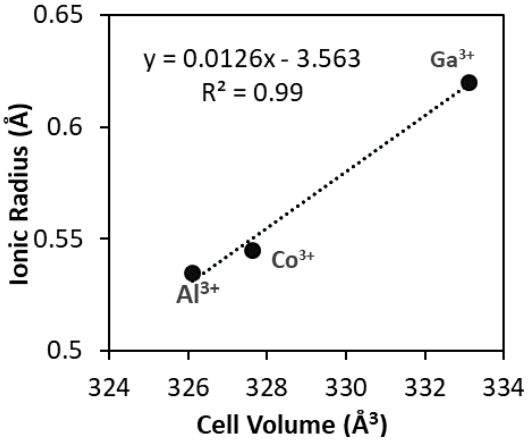

Figure 5.2 – Correlation between cell volume and ionic radii of the three samples.

Tab. 5.2 shows the textural properties of the prepared samples calcined at 700 °C. The surface specific areas of all samples are between 11 – 15 $m^2\ g^{-1}$, which are expected for samples annealed at high temperatures [49]. The average crystallite size is calculated by the Scherrer method. Crystallite size slightly varies between the samples around 30 nm.

Table 5.2 – Textural properties of the studied perovskite oxides,

Catalysts	Formula	S_{BET} ($m^2\ g^{-1}$)	V_{pore} ($cm^3\ g^{-1}$)	d(nm)*
1Al	$LaAlO_3$	14.4	0.10	30.3
0.25Co	$LaAl_{0.75}Co_{0.25}O_3$	11.4	0.09	32.0
0.25Ga	$LaAl_{0.75}Ga_{0.25}O_3$	11.0	0.06	28.2

* Crystallite size by Scherrer calculation

H_2-TPR measurements were performed to investigate the reduction behavior of the catalysts. The results are presented in Tab. 5.3 and Fig. 5.3. Co-substituted perovskite shows an asymmetric reduction peak from around 300 to 500 °C, in which 0.387 mmol H_2 / g catalyst are consumed, corresponding to the amount needed for the reduction $Co^{3+} \rightarrow Co^{2+}$. Further reduction takes place in two shallow phenomena, in which further 0.360 mmol $H_2\ g^{-1}$ are consumed until 900°C, corresponding to the reduction of nearly half Co^{2+} to Co^0. It is generally accepted that Co^{3+} reduction to Co^0 can undergo through Co^{2+} in form of intermediate brownmillerite $LaCoO_{2.5}$ [31,50–54]. This route is also referred to the two-process mechanism where the hydrogen consumption of the second step ($Co^{2+} + H_2 \rightarrow Co^0$) is the double amount of that used for the first step ($Co^{3+} + 0.5H_2 \rightarrow Co^{2+}$). On the other hand, Co^{3+} can be totally reduced via an one-process mechanism, in which Co^0 can be also formed at low temperature [55]. It can be observed that cobalt in $LaAl_{0.75}Co_{0.25}O_3$ is significantly less reducible than Co_3O_4, which reduction begins at nearly 200°C and is

completely reduces to Co^0 before 400°C, corresponding to a significant stabilization of Co^{2+} in the perovskite framework [56].

Table 5.3 - H_2-TPR data and the attribution to desorption of CO_2 of the signals on 1Al and 0.25Ga (CO_2 detected by ABB Limas and Uras UV and NDIR analyzers under thermal treatment in N_2 in a quartz tube reactor)

Sample	H_2 (µmol g^{-1})	H_2 molecule/nm^2	H_2 molecule/ formula unit	CO_2 (umol g^{-1})	CO_2 molecule/nm^2	CO_2 molecule/ formula unit	CO_2 % w/w
1Al	-	-	-	18	0.77	0.004	0.081
0.25Co	691	36.39	0.15	-	-	-	-
0.25Ga	-	-	-	42	2.30	0.010	0.188

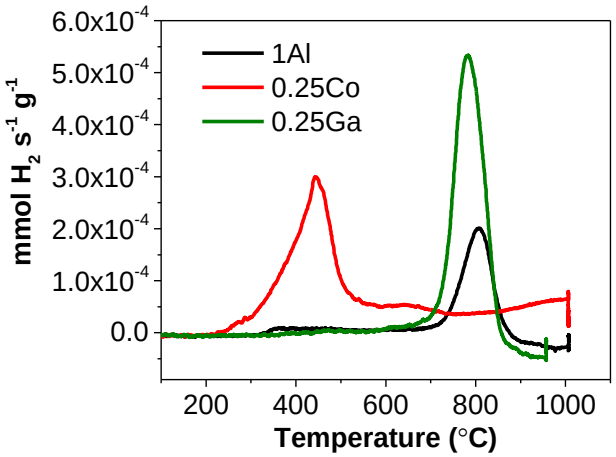

Figure 5.3 - H_2-Temperature Reduction profiles of $LaAlO_3$ (1Al), $LaAl_{0.75}Co_{0.25}O_3$ (0.25Co) and $LaAl_{0.75}Ga_{0.25}O_3$ (0.25Ga) (Samples were pretreated at 500 °C under N_2 in 30 min)

In H_2-TPR, 0.25Ga and 1Al present a sharp peak between 700 and 850°C. These results have to be interpreted at the light of parallel experiment of O_2-TPD, in which 0.25Co showed no peak in that region, while 0.25Ga and 1Al presented a sharp phenomenon of CO_2 desorption. The attribution of the peak above 700 °C to CO_2 desorption also in the case of the H_2-TPR experiment is justified by the poor reducibility of La^{3+}, Al^{3+}, and Ga^{3+}, with standard reduction potential -2.38, -1.66, and -0.53 V, respectively, to be compared with +1.82 and -0.28 V for the reduction of, respectively, $Co^{3+} \rightarrow Co^{2+}$ and $Co^{2+} \rightarrow Co^0$. It can be safely concluded that $LaAlO_3$ and $LaAl_{0.75}Ga_{0.25}O_3$ are non-reducible under the experimental conditions of H_2-TPR. The amount of desorbed CO_2 in Tab. 5.3 has been evaluated by the relative thermal conductivity of H_2 and CO_2 in the Wheatstone bridge of the TPR detector.

The desorption of CO_2 around 750°C in some samples has been confirmed by thermogravimetric analysis (TG) data shown in Fig. 5.4. 1Al and 0.25Ga present initial slow mass losses of, respectively. 0.7 and 0.9 % before 400°C, possibly corresponding to the loss of hydroxyls. A further sharp mass loss is observed between 750 and 850°C: 0.025 % for 1Al and 2.5% for 0.25Ga. The presence of carbonates in the samples is probably not related to the synthesis procedure, as no alkaline solutions able to trap CO_2 have been used. It seems reasonable that carbonates have been formed at the surface of the perovskite or of any hypothetical X-ray amorphous residue during the calcination in flow of room air.
In the air flow of the TG experiment, 0.25Co presents a constant mass until 600°C and shows a slow mass increase at higher temperatures, reaching a mass gain of 0.3 % at 900 °C. If attributed to the acquisition of oxygen, this gain of mass would correspond to an increase of oxidation state of cobalt from an initial mixed Co^{2+} and Co^{3+} oxidation state. This would imply the presence of oxygen vacancies in the 0.25Co sample. Assuming that, after oxidation at 900 °C, the oxidation state of cobalt is Co^{3+}, the observed mass increase would imply an initial composition $LaAl_{0.75}Co_{0.25}O_{2.96}$ for 0.25Co.

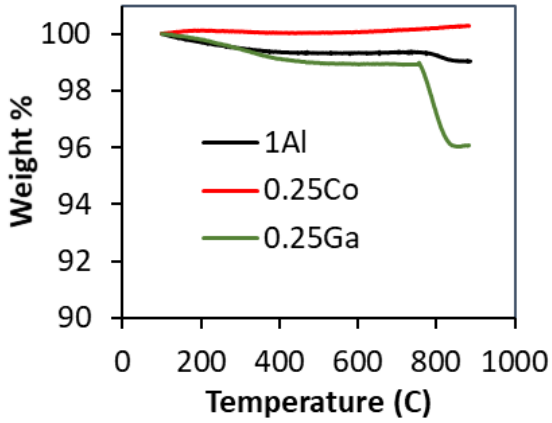

Figure 5.4 - Thermal gravimetric analysis of the three catalysts

The acid and base characteristics of the perovskite oxides were investigated using isopropanol conversion as a test reaction. Propene and acetone are the main products, and the selectivity depends on the acidity and basicity of the catalysts: the dehydration process is preferred over acidic sites and the dehydrogenation is favored on basic sites in proximity with acid sites [57,58]. The results obtained on the studies catalyst are reported in Tab. 5.4. The major product is acetone, showing that these catalysts have predominantly basic sites. 0.25Ga and 0.25Co samples present a nearly complete conversion and a selectivity of dehydration products (ethylene and low amount of diisopropylether) lower the 8%. $LaAlO_3$

has the lowest conversion and a 26% selectivity to propene, exhibiting significant acidity despite the main basic character. The basicity of the $LaAlO_3$ system, pure or doped, has not been thoroughly studied in most reports on the acid-base properties of perovskites [59]. By analyzing the products of isopropanol conversion over (Ba, Sr)(Ti,Zr)O_3, Foo *et al.*[60] suggested that the perovskite surfaces are dominated with intermediate and strong basic sites with the presence of some weak Lewis acid sites, due to the preferred exposure of SrO/BaO on the perovskite surfaces. Highly basic lanthanum oxide sites can play a similar role in $LaAlO_3$ materials, despite transition metal-bearing lanthanum perovskites have much weaker basic sites than pure La_2O_3 [61].

Table 5.4 –Products distribution of isopropanol conversion over the three catalysts (4 % isopropanol in N_2, 325°C, WHSV 1.6, 90 min of TOS),

Sample	Selectivity %			Conversion	C-balance
	Acetone	Propylene	diisopropyl ether	%	%
1Al	73.52	26.48	0.00	65.68	96.44
0.25Ga	92.81	5.75	1.44	96.03	94.87
0.25Co	92.55	6.26	1.19	98.82	99.40

5.2.2 Catalytic transformations of ethanol

Fig. 5.5 shows the evolution of conversion of ethanol and carbon balance with time over the studied catalysts at 350°C and WHSV 0.17 h^{-1}. On all catalysts, conversion decreases with time on stream until reaching stable values after 150-200 minutes. Steady-state Ga-substituted perovskite exhibits the highest activity with ~ 80 % of conversion after about 180 min, whereas $LaAl_{0.75}Co_{0.25}O_3$ reveals a lower conversion at about 57 %. Not-doped perovskite $LaAlO_3$ has the lowest conversion, around 30 %, suggesting that substitution of Al^{3+} by Ga^{3+} and Co^{3+} remarkably enhances the ethanol conversion. However, high conversions lead to the deterioration of carbon balance, especially evident in the case of $LaAl_{0.75}Ga_{0.25}O_3$. The carbon balance of all catalysts improves with time-on-stream, reaching stable values in correspondence with the stabilization of the conversion. The C-balance on $LaAlO_3$, the less active catalyst, reaches high values at around 95 % after 180 min whilst that of Co-substituted perovskite increases to a similar value upon 250 min and the C-balance of $LaAl_{0.75}Ga_{0.25}O_3$ never rise above 75%.

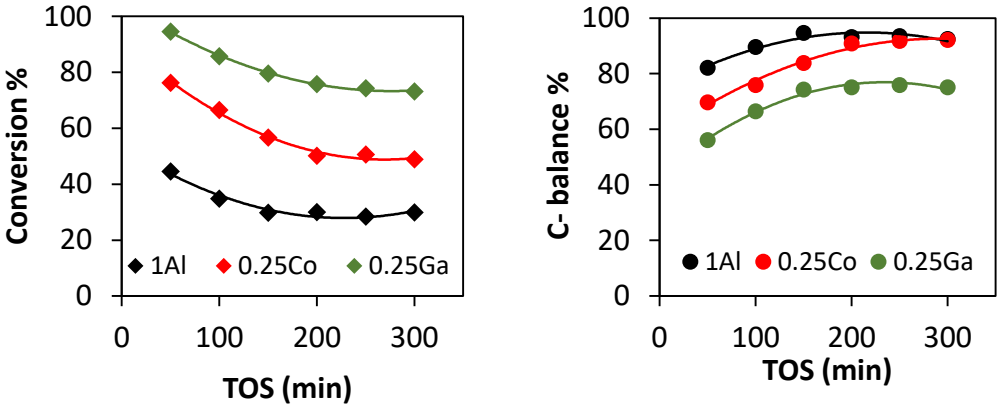

Figure 5.5 – Conversion and C-balance versus time on stream (1% ethanol in N_2, 100 mg of catalysts, T = 350°C; WHSV = 0.17 h^{-1}).

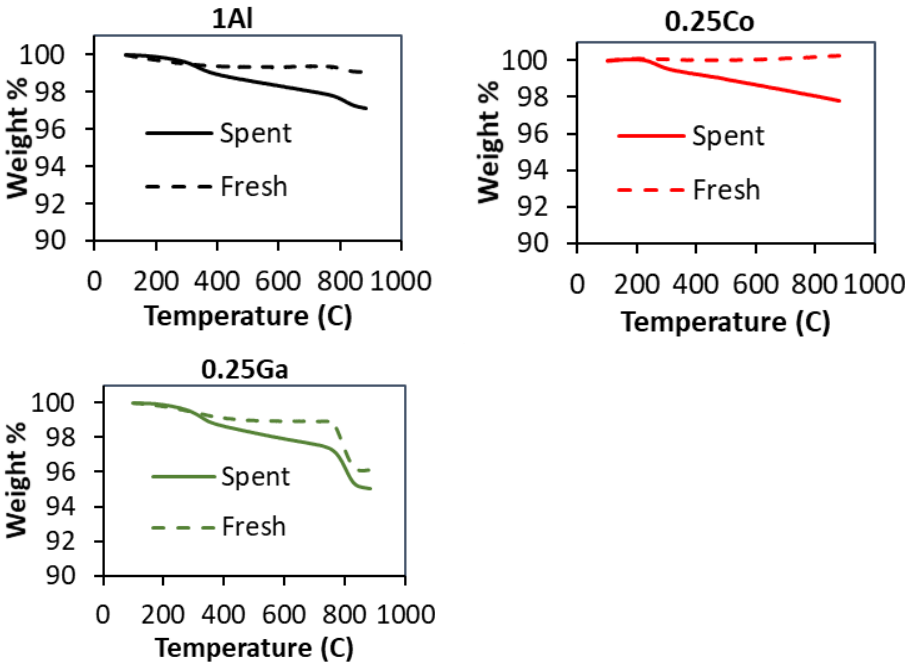

Figure 5.6 – Comparison of the TG curves for fresh and used catalysts.

This behavior suggests that highly active catalytic sites, present in the fresh catalyst, lead to the formation of carbon deposits, which decrease the carbon balance and passivate the same sites on which carbon is formed until a stable steady state is reached. Thermal gravimetry of the used catalysts confirms the presence of carbon deposit. The TG curves, reported in Fig. 5.6, appear as the sum of the TG curves of the fresh catalysts plus a mass loss peak between 250 and 350°C followed by a continuous mass loss until 900°C. The difference in mass loss between used and fresh catalyst is reported in Tab 5.5 for the three catalysts. These data confirm the correlation between deactivation of the catalysts and

carbon deposition: the decrease in ethanol conversion upon 3 h is proportional to the amount of carbon deposited on the catalysts.

Table 5.5 – Correlation between carbon deposited by TG and conversion reduction,

Catalysts	Δw used-fresh (w/w)	Mg(C)/100mg(catalyst)	$\Delta_{conversion\ \%}$ after 3h
1Al	-0.020	1.96	7.36
0.25Co	-0.025	2.50	9.38
0.25Ga	-0.011	1.09	4.08

The conversion of ethanol followed the main pathways represented in Fig. 5.7. Ethylene and acetaldehyde were the primary products of, respectively, dehydration and dehydrogenation reactions. Further reactions of acetaldehyde can follow different pathways, through aldol coupling followed by hydrogen transfer to form butadiene, or Tischenko coupling and ketonisation to form acetone. Monoolefins higher than ethylene can be formed by different pathways, either dimerization/metathesis of ethylene or dehydration/hydrogenation of carbonylic compounds.

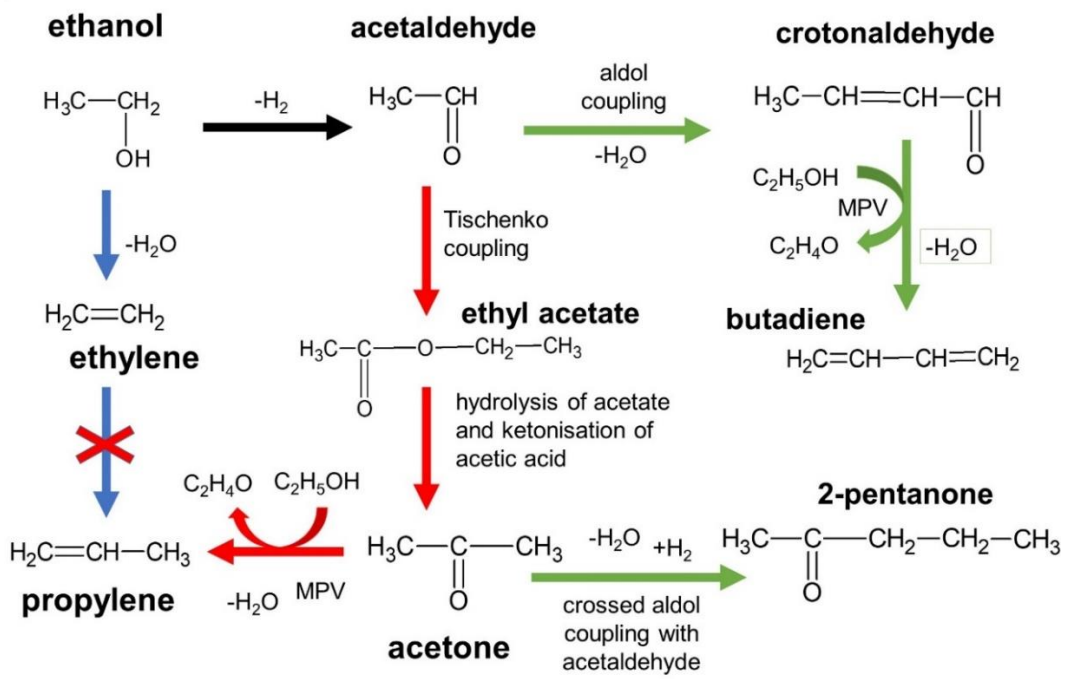

Figure 5.7 - Main reaction pathways in the conversion of ethanol on Ga- and Co-doped $LaAlO_3$ perovskites.

The pathways followed and the corresponding distributions of products are very different from one catalyst to another. Fig. 5.8 shows the yield of the most abundant products over the different catalysts as a function of conversion. It can be seen that ethylene and acetone

are major products for $LaAlO_3$ and $LaAl_{0.75}Co_{0.25}O_3$ respectively. For $LaAl_{0.75}Ga_{0.25}O_3$, acetaldehyde is the main product and it is converted to other products at high conversions. Over Ga-substituted perovskite, C_4-oxygenates increase more steeply than other products, and at high conversions they are dominant. For $LaAl_{0.75}Co_{0.25}O_3$ acetaldehyde yield gradually decreases with conversions whilst C_3-C_7 olefins and C_{4+} oxygenates slightly increases. The Co-doped perovskite supports the formation of acetone. Ga-doped perovskite, instead, accelerates the formation of heavy products from acetaldehyde at high conversion. For $LaAlO_3$, except ethylene, other products do not increase with the conversion. The strong differences in product distribution between the catalysts underline the importance of Ga- and Co-substitution in the modification of the active sites. These effects can be better understood by following the evolution of the selectivity of each product with conversion on the three catalysts.

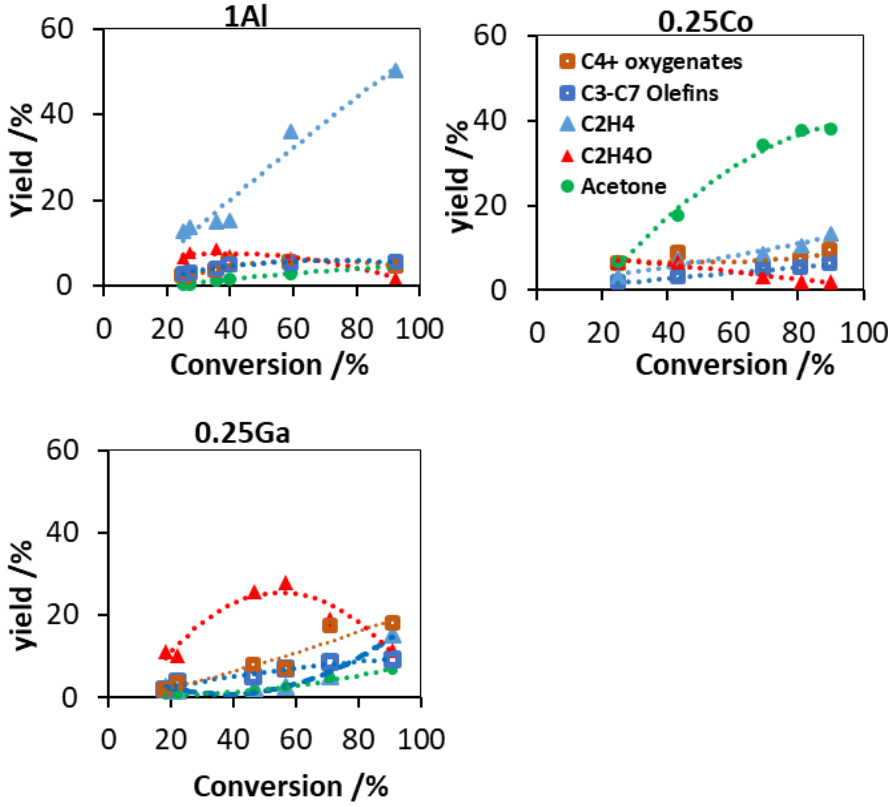

Figure 5.8 - Main product distributions with conversion over the three catalysts.

In Fig. 5.9, the selectivities of ethylene and acetaldehyde are reported as functions of the conversion of ethanol, which is varied by changing space velocity and temperature of the reaction. For a better understanding of the results, space velocity and temperature of the experimental points in these figures and the following one, showing the selectivities of

different products, are reported in Tab. 5.6. The selectivity of ethylene, between 40 and 60%, is much higher on 1Al than on the other catalysts, in good agreement with the results of the tests on isopropanol, indicating higher acidity of the 1Al catalyst, on which a maximum ethylene yield of about 50 %. On the other hand, ethylene selectivity over 0.25Co is around 15 %, significantly lower than that of 1Al. For Ga-substituted perovskite, the selectivity of ethylene is lower than 10 % at low conversions and increases sharply to nearly 15% at conversion higher 70%, where the reaction temperature is raised from 350 to 400 °C. A similar increase of selectivity of ethylene with temperature is observed on 1Al. This may suggest that the formation of more Lewis acidic sites at higher temperatures may accelerate the formation of ethylene, in parallel with literature reports that above 357 °C additional ethylene can be originated from diethyl ether over La_2O_3/Al_2O_3 [15].

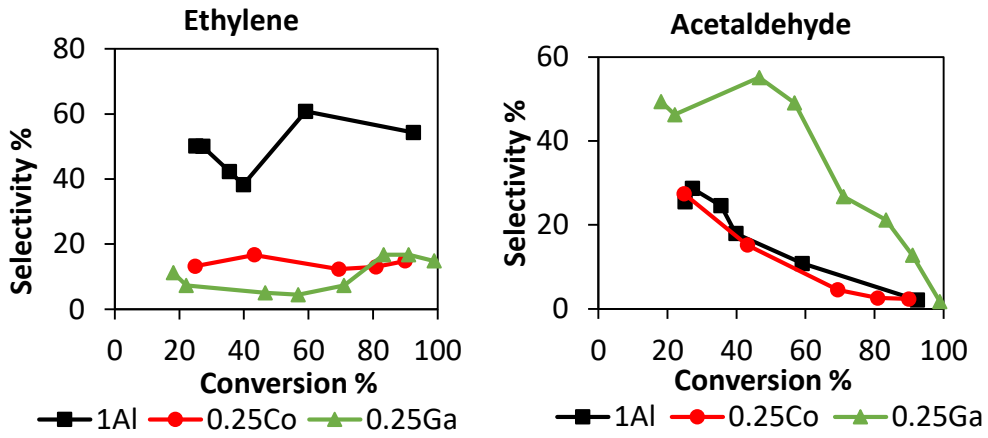

Figure 5.9 - Selectivities of ethylene and acetaldehyde as functions of the conversion of ethanol on different catalysts.

In the case of acetaldehyde, 0.25Ga provides the highest selectivity, nearly 50% at low levels of conversion. On all catalysts, the selectivity to acetaldehyde decreases with conversion, indicating acetaldehyde as a primary product converted to other products as the conversion increased. In the case of 0.25Ga catalyst, the decrease of acetaldehyde selectivity becomes significant at high conversion, especially beyond 70% conversion, when the temperature is raised from 350 to 400 °C. On both 1Al and 0.25Ga, the decrease of acetaldehyde selectivity at higher temperature parallels the observed increase of the ethylene selectivity, suggesting a modification of the dehydration/dehydrogenation activity ratio of the catalysts.

The understanding of the high yield of acetone over 0.25Co can be improved by observing the evolution of selectivity of ketones with ethanol conversion on the three catalysts (Fig. 5.10).

Table 5.6 - Conditions of catalytic tests. Conversion data are reported for easier identification of the experimental points on the figure graphs,

Catalyst	Temperature °C	WHSV h^{-1}	Conversion %
1Al	350	0.46	25.09
1Al	350	0.3	27.24
1Al	350	0.17	35.53
1Al	350	0.11	39.82
1Al	375	0.23	59.08
1Al	400	0.23	92.44
0.25Co	350	0.46	24.88
0.25Co	350	0.23	43.18
0.25Co	350	0.15	69.37
0.25Co	350	0.11	80.87
0.25Co	375	0.11	89.88
0.25Ga	350	0.92	18.13
0.25Ga	350	0.69	22.15
0.25Ga	350	0.46	46.60
0.25Ga	350	0.23	56.84
0.25Ga	350	0.11	70.99
0.25Ga	400	0.92	83.29
0.25Ga	400	0.69	91.02
0.25Ga	400	0.23	98.91

The selectivity of acetone on 0.25Co at 350 °C increases with the contact time in parallel with a decrease of selectivity of acetaldehyde, in correspondence with a mechanism of consecutive reactions, until a 50% selectivity of acetone is reached at 70% conversion. In the same time, the selectivity to pentanone and C7-oxygenates decreases. These products can be considered as results of consecutive aldol condensation of acetone with acetaldehyde. It is reported that pentanone-2 can be formed by aldo-condensation of acetaldehyde and acetone. C_7-oxygenates can be produced by condensation of pentanone-2 with acetaldehyde as described in the study of He *et al.* [11] over K-Pd/MnO_x-ZrO_2-ZnO catalyst and Tesquet *et al.* [45] over $La_{1+x}FeO_{3+\delta}$. The decrease of pentanone and higher odd-oxygenates with contact time can be related both to a decreased availability of acetaldehyde and to the formation of heavier products of further condensation, as suggested by the worsening of carbon balance shown in Fig. 5.11. Conversions higher than 70% are observed for a higher temperature of 400°C. In these conditions, with nearly no acetaldehyde still present, the selectivity of acetone decreases with the contact time and the

selectivities of further condensation products increases, confirming the consecutive mechanism of their formation.

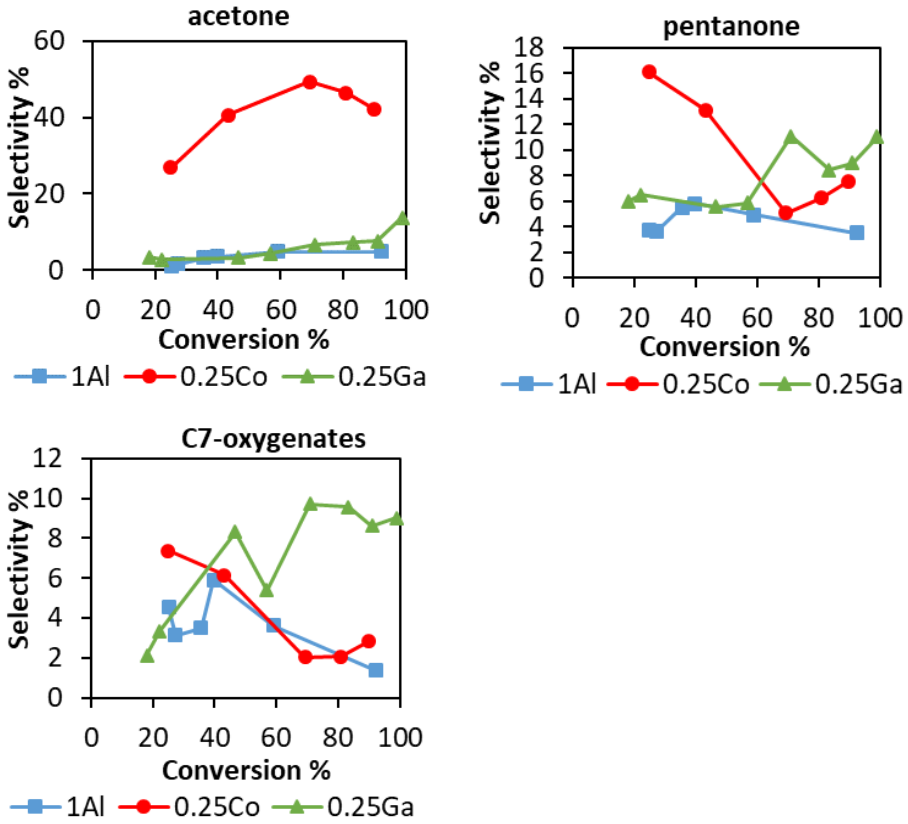

Figure 5.10 - Selectivity of odd-oxygenates vs. ethanol conversion on the three catalysts.

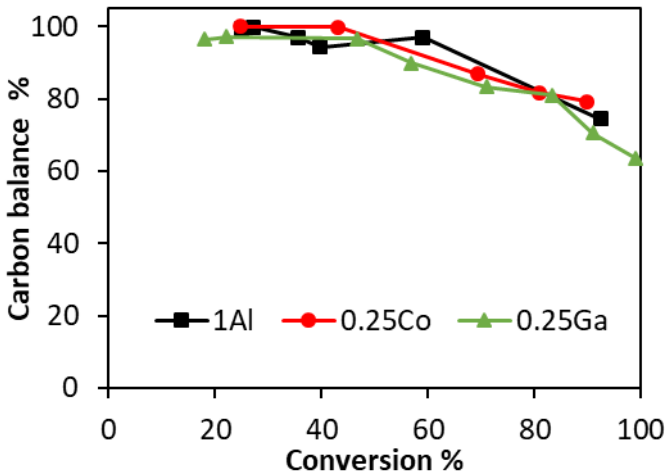

Figure 5.11 - Carbon balance vs. ethanol conversion on the three catalysts.

The selectivity of acetone is much lower on 1Al and 0.25Ga catalysts, following two well different patterns. On 1Al, the sum of the selectivities of C3-C7 odd oxygenates is virtually

constant at nearly 10%, with the fraction of acetone decreasing with the contact time and the fraction of higher oxygenates correspondingly increasing. On 0.25Ga, the selectivity of each odd oxygenate increases with ethanol conversion. The sum of their selectivities moves from less than 10% at 20% conversion to nearly 30% at a total conversion of ethanol. This increase more than compensates the decrease of selectivity of acetaldehyde, clearly indicating that other products are formed by reactions of acetaldehyde.

It is generally accepted that ethanol-acetone conversion follows the Tishchenko mechanism, which is the dimerization of aldehyde to form ethyl acetate, a reaction normally occurring on basic sites [62]. The mechanism of the Tishchenko coupling, developed for homogeneous catalysis by Ogata and Kawasaki [63] and extended to heterogeneous catalysis by Tanabe and Saito [64], implies the formation of an alkoxide complex on the basic site, followed by the nucleophilic attack of the complex by an acetaldehyde molecule and the desorption of ethyl acetate. The formation of the surface carboxylate has been shown to be favoured on bifunctional basic-Lewis acid sites, as can be formed by high-temperature treatment of basic oxides [65]. Interestingly, ethyl acetate can also be formed directly from ethanol, without isolation of an acetaldehyde intermediate, on the surface of bifunctional redox-acid catalysts like copper chromite [66,67].

The ethyl acetate formed by Tishchenko coupling is rapidly hydrolysed to acetic acid and ethanol, leading to the adsorption of acetate and its conversion to enolic CH_2COO^{2-} and acylic $CH_3C{=}O$ surface groups, which condensate to form β-keto butenoic acid, which can easily decarboxylate to form acetone [68] . Modelling the reaction on ZrO_2 surface, Tosoni and Pacchioni [68] highlighted the relevance of oxygen vacancies for the critical step of adsorption of the acetate intermediate.

In a different approach to the formation of acetone, self-condensation of acetaldehyde forms butan-1-al-3-ol, which is converted to keto-form by hydrogen transfer. By removing HCHO, this intermediate can be converted to acetone, condensation of which with acetaldehyde to form pentanone-2 [6]. Using temperature-programmed surface reaction of adsorbed ethanol on K-Pd/MnO_x-ZrO_2-ZnO catalyst with the detection of acetaldehyde, formaldehyde and acetone, He *et al.* [11] proposed the reaction pathway follows the second route. This pathway is similar to the study of Murthy *et al.* [10] over Ca/Mn-promoted Fe_2O_3 catalyst with the absence of acetic acid.

In order to verify if the Tishchenko mechanism is followed, its main intermediate, ethyl acetate, has been fed into the reactor over the three catalysts, obtaining majorly ethanol, acetone, and acetaldehyde. No acetic acid and limited amounts of ethylene, propylene, and

higher odd oxygenates and olefins are observed. The selectivity of ethanol, nearly 50 %, is the result expected from the cleavage of the ester bond to give ethanol and acyl groups, these last further reacting on surface hydroxyls of the catalyst. The conversion is higher for 0.25Ga, which also presents the higher selectivity in the back-reaction to acetaldehyde. The formation of acetone and higher odd oxygenates from ethyl acetate confirms that the Tishchenko mechanism is a reasonable pathway in our experimental conditions.

Table 5.7– Catalytic transformation of ethyl acetate over the three catalysts (1 % ethyl acetate in N_2 flow; 350 °C, WHSV 0.17 h^{-1}),

		Samples		
		1Al	**0.25Co**	**0.25Ga**
	χ (%)	11.3	13.4	21.1
	C-balance (%)	99.1	98.4	96
Selectivity (%)	**C_2H_4**	0.92	0.81	1.3
	C_3H_6	0.11	0	0.14
	CH_3CHO	4.82	6.84	12.97
	C_2H_5OH	57.56	55.03	50.25
	C_3H_6O	35.15	35.18	32.21
	$C_5H_{10}O$	0.11	0.37	1.4
	C_{7+}Olefins	0.83	0.95	0.65
	C_{7+}Oxygenates	0.5	0.69	0.89

It can be remarked that the selectivity of acetone from ethyl acetate on the different catalysts does not follow the same order than when starting from ethanol. Indeed, by the reaction of ethyl acetate, 1Al and 0.25Ga present the highest selectivity to acetone, while a reversed trend is observed by converting ethanol. It seems clear that the high selectivity of acetone from ethanol on 0.25Co is the result of a more effective Tishchenko mechanism, providing an easy formation of ethyl acetate. The property that more differentiates 0.25Co from the other catalysts is its higher reducibility, highlighted by H_2-TPR data. The special status of Co-bearing perovskite is confirmed by the XRD of the used catalysts, whose cell parameters are reported in Tab. 5.8.

Tab**le 5.8**- Refinement parameters of perovskites calcined at 700 °C and used as catalysts (3h at 350°C in an ethanol flow of WHSV 0.23 h^{-1}),

Sample	a (Å)	c (Å)	cell volume ($Å^3$)
$LaAlO_3$	5.364(2)	13.109(2)	326.7(1)
$LaAl_{0.75}Co_{0.25}O_3$	5.3382(1)	13.139(3)	329.6 (1)
$LaAl_{0.75}Ga_{0.25}O_3$	5.3979(1)	13.254(2)	333.58(7)

By comparing the cell volume of the used catalysts with the cell volume of the fresh catalysts reported in Tab. 5.1, differences lower than 0.2% are observed in the case of 1Al and 0.25Ga, whereas the cell volume of 0.25Co has increased by 0.6% in the catalytic test. This effect can be attributed to the formation of oxygen defects by partial reduction of Co^{3+} by ethanol vapours. Moreover, the quantitative evaluation of the H_2-TPR data has suggested that an amount of oxygen vacancies is already present in the fresh catalyst. Oxygen vacancies in ZrO_2 have been suggested by Tosoni and Pacchioni [68] to favour the formation of acetone from ethanol by favouring the adsorption on the catalyst of acetate issued from the decomposition of ethyl acetate. However, the differences in acetone selectivity when ethanol or ethyl acetate are fed indicate that the formation of ethyl acetate, and not its following reactions, is the step favoured on the more reducible 0.25Co catalyst. Properly prepared Co_3O_4 has already been shown to be an effective catalyst of Tishchenko coupling [69]. This suggests that redox catalyst can indeed be effective for this reaction. It is likely that the redox behavior is not directly involved in the reaction mechanism but provides, by modification of the catalyst in the reaction medium, the correct type of oxygen vacancies to promote the critical step of Tishchenko coupling, indicated by Tanabe and Saito [64] as the disproportionation between two adsorbed aldehydes to crate the surface alcoxide active.

The formation of monoolefin, whose selectivitites are reported in Fig. 5.12, follows different trends on the three catalysts. While, as already observed, ethylene selectivities follow the order 1Al>0.25Co>0.25Ga, the selectivities of propylene and butene follow the order 0.25Co>1Al>0.25Ga. The selectivities of propylene and butene on 0.25Co increase with contact time at 350 °C and stall, in the case of propylene, or decrease, in the case of butene, when the temperature is raised to 400 °C. On 1Al and 0.25Ga, the selectivities of propylene and butene are extremely low at 350 °C and become significant only when the temperature of reaction is increased.

The three catalysts are differently ranked in the formation of ethylene and higher olefins. This suggests possible different mechanisms of formation. Ethylene is clearly produced via dehydration of ethanol over acid sites of catalysts, either directly (monomolecular reaction) or through etherification to diethyl ether (bi-molecular path), which is dehydrated to ethylene [70]. Trace amounts of ethylene have also been observed when ethyl acetate is fed to the reactor instead of ethanol (Tab. 5.7). Also in this case, it is likely that ethylene is formed by dehydration of the ethanol issued from the decomposition of the ethylacetate

intermediate. The observation of some propylene when ethyl acetate is fed is particularly relevant, as it shows that propylene can be formed by hydrogenation of acetone by hydrogen exchange and dehydration of the isopropanol formed. The formation route of propene from ethanol via acetone as an intermediate is widely reported. Commonly, propene is formed by the following sequence: ethanol → acetaldehyde → acetone → propanol → propene. A similar route was reported for In_2O_3-zeolite [7] and Sr modified In_2O_3 [71]. The authors indicated that the conversion of intermediate acetone to propene is promoted with the acidity of zeolite [7]. Moreover, this conversion can be catalyzed by Brønsted acid site of HZSM-5 in other research [72,73]. Among the catalysts, Co-substituted perovskite exhibits the highest yield of acetone, nearly 40 % at complete conversion of ethanol, and the quantity of propene is slightly higher than other samples.

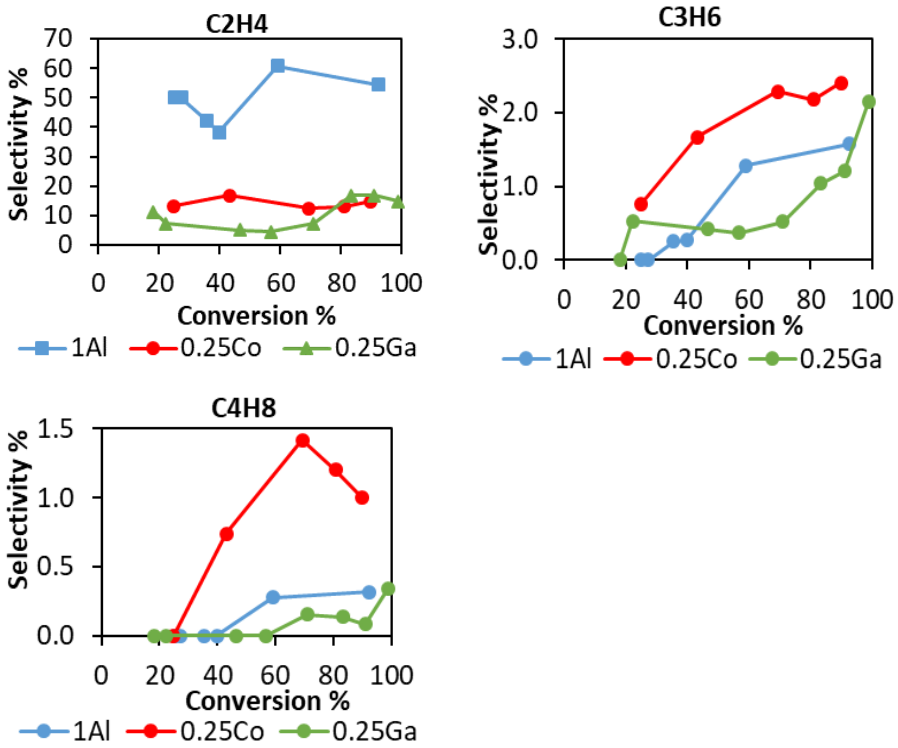

Figure 5.12 - Selectivities of ethylene, propylene and butene vs. ethanol conversion on the three catalysts.

An alternative route of formation of propylene would be through oligomerisation and metathesis of ethylene. This route normally requires the presence of bifunctional metal-acid catalysts. The possibility of this route on our catalysts has been tested by feeding ethylene instead of ethanol to the reactor in the same reaction conditions. The conversion of ethylene was lower than 1% on all catalysts in the first three hours of reaction. Olefins with 6 or more carbon atoms represented nearly the totality of products, the carbon balance

being better than 99%. Only in the case of 0.25Ga, the conversion rose to 3 % after 3 hours of reaction, the carbon balance decreasing to 97%. These results seem to show that our perovskites can weakly catalyze oligomerisation-metathesis reactions but strongly favour the formation of relatively heavy olefins. This effect could also be related to the direct feeding of ethylene, as, when ethanol is fed, water from ethanol dehydration is present on the surface and can favour the desorption of small olefins. The more likely way of formation of propylene from ethanol seems indeed from acetone by a hydrogenation-dehydration mechanism. The way of formation of relatively high amounts of butane from ethanol on 0.25Co is more problematic and possibly related to the dehydration of a butanol intermediate.

No alkanes were detected in the conversion products of ethanol, despite reports on the hydrogenating activity of $LaAlO_3$ [74] and $LaCoO_3$ [75] and on disproportionation of ethanol to acetaldehyde and ethane on several oxides [76].

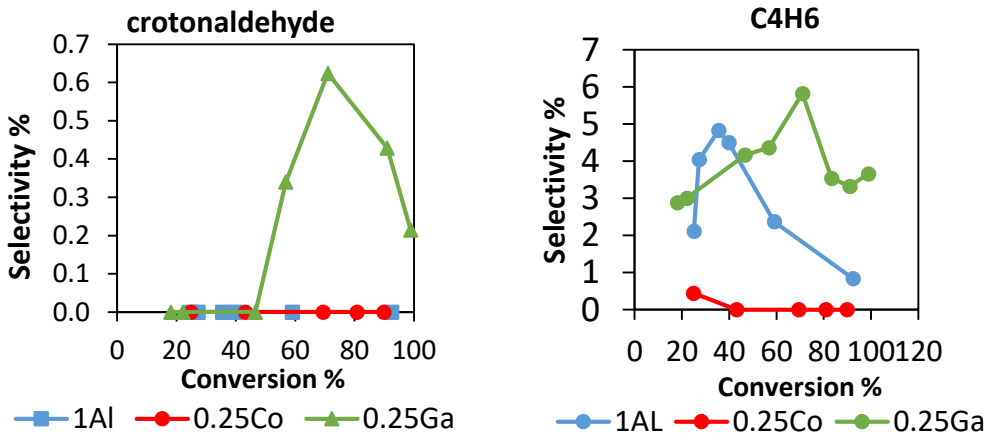

Figure 5.13 - Selectivity of products from aldol coupling of acetaldehyde vs. conversion of ethanol.

An industrially relevant route of synthesis of butadiene passes through the dimerisation of acetaldehyde to form acetaldol (3-hydroxy-butanal) [77]. This intermediate is dehydrated to form crotonaldehyde (2-butenal), which undergoes a Meerwein–Ponndorf–Verley reduction by ethanol to form crotylalcohol (2-butenol), which can be dehydrated to butadiene-1,3 or hydrogenated to butanol. On our catalysts, the main products related to this reaction pathway are crotonaldehyde and butadiene, whose selectivity is reported in Fig. 5.13 as a function of the ethanol conversion. The selectivity of butadiene reaches maxima at 5% on 1Al at 35% conversion and 6 % on 0.25Ga at 70 % conversion. On

0.25Co, only traces of butadiene are observed at low conversions. Crotonaldehyde, the main intermediate in the formation of butadiene, is only observed on 0.25 Ga at high conversion of ethanol. The small amount observed suggests than crotonaldehyde is a fast-reacting precursor of butadiene.

The comparison between the three catalysts in the route from acetaldehyde to butadiene has to take into account the competition with different reaction pathways. The poor activity of 0.25Co in the formation of butadiene has to be related to the consumption of acetaldehyde in the acetaldehyde-to-acetone route, largely more favoured on this catalyst. The role of gallium doping in promoting the activity of the Lebedev catalysts for the formation of butadiene from ethanol has already been addressed [13]. Gallium is expected to introduce Lewis acid sites in along the basic sites of the $MgO\text{-}SiO_2$ catalysts, providing acid-base pairs. The concentration of gallium sites has been considered critical, the catalytic results presenting a volcano shape with the amount of gallium. In the case of Ga-containing perovskite, we observed that the selectivity to butadiene is similar on 0.25Ga and 1Al at low conversion but severely decreases on 1Al at high conversion. It is possible that the higher acidity of 1Al favours consecutive reactions which decrease the yield of butadiene. This suggests again that the relative strength of the acid and basic functions is critical and has to be finely tuned. We can only regret that the presence of a significant amount of amorphous basic carbonates in 1Al and 0.25Ga severely perturbs the results of surface characterization of these materials.

5. 3 CONCLUSIONS

All the catalysts were prepared by sol-gel route exhibiting perovskite as the only crystalline phase, and Ga and Co are well introduced into the perovskite structure upon calcination at 700 °C. Among the catalysts, $LaAlO_3$ has the strongest acidity and thus yielding the higher quantity of olefins than that over $LaAl_{0.75}Co_{0.25}O_3$ and $LaAl_{0.75}Ga_{0.25}O_3$. Basic sites dominate on the catalysts, whereas substitutions lead to a decrease in acidity. On the reducible catalyst $LaAl_{0.75}Co_{0.25}O_3$, acetaldehyde is majorly converted to acetone. This is attributed to the partial reduction of the catalyst, forming oxygen vacancies which constitute the proper acid-base pairs for the formation of the active species of Tishchenko coupling. Acetaldehyde not converted to acetone underwent aldol coupling and forms crotonaldehyde and butadiene. Acid-base sites are also critical for this reaction pathways and Ga-substituted perovskite provides a more stable production of butadiene than the

more acidic $LaAlO_3$. The study highlights the tunability to acid-base properties of the perovskite catalysts by substitution, controlling the reaction pathways to different products.

5.4 REFERENCES

1 Y. Sun and J. Cheng, *Bioresour. Technol.*, 2002, **83**, 1–11.
2 J. Goldemberg, *Science (80-.).*, 2007, **315**, 808 LP – 810.
3 Global Ethanol Production, https://afdc.energy.gov/data/10331.
4 Z. Sun, G. Bottari, M. C. A. Stuart, G. Bonura, C. Cannilla, F. Frusteri, K. Barta, C. N. Giordano, V. S. Lucia and S. Contesse, *ACS Sustain. Chem. Eng.*, 2017, **5**, 1738–1746.
5 J. Sun and Y. Wang, *ACS Catal.*, 2014, **4**, 1078–1090.
6 V. L. Sushkevich, I. I. Ivanova, V. V. Ordomsky and E. Taarning, *ChemSusChem*, 2014, **7**, 2527–2536.
7 F. Xue, C. Miao, Y. Yue, W. Hua and Z. Gao, *Green Chem.*, 2017, **19**, 5582–5590.
8 M. Iwamoto, *Catal. Today*, 2015, **242**, 243–248.
9 R. A. L. Baylon, J. Sun and Y. Wang, *Catal. Today*, 2016, **259**, 446–452.
10 R. S. Murthy, P. Patnaik, P. Sidheswaran and M. Jayamani, *J. Catal.*, 1988, **109**, 298–302.
11 D. He, Y. Ding, W. Chen, Y. Lu and H. Luo, *J. Mol. Catal. A Chem.*, 2005, **226**, 89–92.
12 T. Takei, N. Iguchi and M. Haruta, *Catal. Surv. from Asia*, 2011, **15**, 80–88.
13 J. V. Ochoa, A. Malmusi, C. Recchi and F. Cavani, *ChemCatChem*, 2017, **9**, 2128–2135.
14 J. V. Ochoa, C. Bandinelli, O. Vozniuk, A. Chieregato, A. Malmusi, C. Recchi and F. Cavani, *Green Chem.*, 2016, **18**, 1653–1663.
15 M. D. Jones, C. Keir, C. Di Iulio, R. A. M. Robertson, C. V Williams and D. C. Apperley, *Catal. Sci. Technol.*, 2011, **1**, 267–272.
16 M. A. Pena and J. L. G. Fierro, *Chem. Rev.*, 2001, **101**, 1981–2017.
17 J. Zhu, H. Li, L. Zhong, P. Xiao, X. Xu, X. Yang, Z. Zhao and J. Li, *ACS Catal.*, 2014, **4**, 2917–2940.
18 U. Oemar, P. S. Ang, K. Hidajat and S. Kawi, *Int. J. Hydrogen Energy*, 2013, **38**, 5525–5534.
19 C. P. B. Quitete, R. L. Manfro and M. M. V. M. Souza, *Int. J. Hydrogen Energy*, 2017, **42**, 9873–9880.
20 Yasushi, D. Mukai, Y. Murai, S. Tochiya, Y. Izutsu, K. Sekiguchi, N. Hosomura, H. Arai, E. Kikuchi and Y. Sugiura, *Appl. Catal. A Gen.*, 2013, **451**, 160–167.
21 K. H. Lin, C. Bin Wang and S. H. Chien, *Int. J. Hydrogen Energy*, 2013, **38**, 3226–3232.
22 Q. Zhang, L. Li, B. Jiang, K. Wang, D. Tang and B. Dou, *Int. J. Hydrogen Energy*, 2017, **42**, 17102–17111.
23 K. Zhao, F. He, Z. Huang, G. Wei, A. Zheng, H. Li and Z. Zhao, *Appl. Energy*, 2016, **168**, 193–203.
24 L. D. Vella, J. A. Villoria, S. Specchia, N. Mota, J. L. G. Fierro and V. Specchia, *Catal. Today*, 2011, **171**, 84–96.
25 T. H. Nguyen, A. Łamacz, P. Beaunier, S. Czajkowska, M. Domański, A. Krztoń, T. Van Le and G. Djéga-Mariadassou, *Appl. Catal. B Environ.*, 2014, **152**–**153**, 360–369.
26 S. Ramesh and N. J. Venkatesha, *ACS Sustanaible Chem. Eng.*, 2017, **5**, 1339–

1346.
27 J. Yao, J. Liu, H. Hofbauer, G. Chen, B. Yan, R. Shan and W. Li, *Energy Convers. Manag.*, 2016, **117**, 343–350.
28 G. Chen, J. Yao, J. Liu, B. Yan, R. Shan and W. Li, *Bioresour. Technol.*, 2015, **198**, 108–114.
29 G. Chen, J. Yao, J. Liu, B. Yan and R. Shan, *Renew. Energy*, 2016, **91**, 315–322.
30 K. A. Resende, C. N. Vila-Neto, R. C. Rabelo-Neto, F. B. Noronha and C. E. Hori, *Catal. Today*, 2015, **242**, 71–79.
31 X. Yang, L. Yang, W. Fan and H. Lin, *Catal. Today*, 2016, **269**, 56–64.
32 M.-Y. Chen, C.-B. Chen, B. Zada, Y. Fu, M. H. Qiao, K. N. Fan, X. X. Zhang, B. N. Zong, A. Sarkar, M. K. Nazeeruddin, M. Grätzel and S. I. Seok, *Green Chem.*, 2016, **18**, 3858–3866.
33 H. Deng, L. Lin, Y. Sun, C. Pang, J. Zhuang, P. Ouyang, Z. Li and S. Liu, *Catal. Letters*, 2008, **126**, 106–111.
34 H. Deng, L. Lin, Y. Sun, C. Pang, J. Zhuang, P. Ouyang, J. Li and S. Liu, *Energy & Fuels*, 2009, **23**, 19–24.
35 J. Hwang, R. R. Rao, L. Giordano, Y. Katayama, Y. Yu and Y. Shao-Horn, *Science*, 2017, **358**, 751–756.
36 J. A. Onrubia and J. R. González-velasco, *Appl. Catal. B, Environ.*, 2017, **213**, 198–210.
37 X. Yang, L. Luo and H. Zhong, *Catal. Commun.*, 2005, **6**, 13–17.
38 A. K. Ladavos and P. J. Pomonis, *Appl. Catal. A Gen.*, 1997, **165**, 73–85.
39 N. Russo, S. Furfori, D. Fino, G. Saracco and V. Specchia, *Appl. Catal. B Environ.*, 2008, **83**, 85–95.
40 S. Irusta, M. P. Pina and M. Men, *J. Catal.*, 1998, **412**, 400–412.
41 M. S. Batista, M. Wallau, E. A. Sanches and Y. P. Mascarenhas, *Appl. Catal. B Environ.*, 2009, **90**, 441–450.
42 Y. Wang, J. Ren, Y. Wang, F. Zhang, X. Liu, Y. Guo and G. Lu, *J. Phys. Chem. C*, 2008, **112**, 15293–15298.
43 T. Valdes-Solıs, G. Marban and A. B. Fuertes, *Chem. Mater.*, 2005, **17**, 2003–2006.
44 Y. Wang, H. Arandiyan, H. A. Tahini, J. Scott, X. Tan, H. Dai, J. D. Gale, A. L. Rohl, S. C. Smith and R. Amal, *Nat. Commun.*, 2017, **8**, 1–7.
45 G. Tesquet, J. Faye, F. Hosoglu, A.-S. Mamede, F. Dumeignil and M. Capron, *Appl. Catal. A Gen.*, 2016, **511**, 141–148.
46 R.-K. Chen, T.-F. Yu, M.-X. Wu, T.-W. Tzeng, P.-W. Chung and Y.-C. Lin, *ACS Sustain. Chem. Eng.*, 2018, **6**, 11949–11958.
47 T.-F. Yu, C.-W. Chang, P.-W. Chung and Y.-C. Lin, *Fuel Process. Technol.*, 2019, **194**, 106117.
48 R. D. Shannon, *Acta Cryst.*, 1976, 751.
49 X. Zhu, X. Tu, M. Chen, Y. Yang, C. Zheng, J. Zhou and X. Gao, *Catal. Commun.*, 2017, **92**, 35–39.
50 N. A. Merino, B. P. Barbero, P. Ruiz and L. E. Cadús, *J. Catal.*, 2006, **240**, 245–257.
51 J. Zhang, X. Weng, Z. Wu, Y. Liu and H. Wang, *Appl. Catal. B Environ.*, 2012, **126**, 231–238.
52 S. Ivanova, A. Senyshyn, E. Zhecheva, K. Tenchev, V. Nikolov, R. Stoyanova and H. Fuess, *J. Alloys Compd.*, 2009, **480**, 279–285.
53 N. A. Merino, B. P. Barbero, P. Grange and L. E. Cadús, *J. Catal.*, 2005, **231**, 232–244.
54 B. Białobok, J. Trawczyński, W. Miśta and M. Zawadzki, *Appl. Catal. B Environ.*, 2007, **72**, 395–403.

55 L. B. Sis, G. P. Wirtz and S. C. Sorenson, *J. Appl. Phys.*, 1973, **44**, 5553.
56 G. Fierro, M. Lo Jacono, M. Inversi, R. Dragone and P. Porta, *Top. Catal.*, 2000, **10**, 39–48.
57 A. Gervasini and A. Auroux, *J. Catal.*, 1991, **131**, 190–198.
58 M. A. Aramendía, V. Borau, C. Jiménez, J. M. Marinas, A. Porras and F. J. Urbano, *J. Catal.*, 1996, **161**, 829–838.
59 F. Polo-Garzon and Z. Wu, *J. Mater. Chem. A*, 2018, **6**, 2877–2894.
60 G. S. Foo, F. Polo-Garzon, V. Fung, D. Jiang, S. H. Overbury and Z. Wu, *ACS Catal.*, 2017, **7**, 4423–4434.
61 S. Sugunan and V. Meera, *React. Kinet. Catal. Lett.*, 1997, **62**, 327–332.
62 H. Hattori, *Chem. Rev.*, 1995, **95**, 537–558.
63 Y. Ogata and A. Kawasaki, *Tetrahedron*, 1969, **25**, 929–935.
64 K. Tanabe and K. Saito, *J. Catal.*, 1974, **35**, 247–255.
65 T. Seki, T. Nakajo and M. Onaka, *Chem. Lett.*, 2006, **35**, 824–829.
66 S. W. Colley, J. Tabatabaei, K. C. Waugh and M. A. Wood, *J. Catal.*, 2005, **236**, 21–33.
67 E. Santacesaria, G. Carotenuto, R. Tesser and M. Di Serio, *Chem. Eng. J.*, 2012, **179**, 209–220.
68 S. Tosoni and G. Pacchioni, *J. Catal.*, 2016, **344**, 465–473.
69 R. V Jagadeesh, H. Junge, M.-M. Pohl, J. Radnik, A. Brückner and M. Beller, *J. Am. Chem. Soc.*, 2013, **135**, 10776–10782.
70 I. Rossetti, M. Compagnoni, E. Finocchio, G. Ramis, A. Di Michele, Y. Millot and S. Dzwigaj, *Appl. Catal. B Environ.*, 2017, **210**, 407–420.
71 S. Mizuno, M. Kurosawa, M. Tanaka and M. Iwamoto, *Chem. Lett.*, 2012, **41**, 892–894.
72 Z. Dolejšek, J. Nováková, V. Bosáček and L. Kubelková, *Zeolites*, 1991, **11**, 244–247.
73 Z. Song, A. Takahashi, N. Mimura and T. Fujitani, *Catal. Letters*, 2009, **131**, 364–369.
74 J. O. Petunchi, M. A. Ulla, J. A. Marcos and E. A. Lombardo, *J. Catal.*, 1981, **70**, 356–363.
75 K. Ichimura, Y. Inoue and I. Yasumori, *Prop. Appl. perovskite-Type oxides*, 1993, 235–271.
76 A. Malmusi, J. Velasquez Ochoa, T. Tabanelli, F. Basile, C. Lucarelli, S. Agnoli, F. Carraro, G. Granozzi and F. Cavani, *Appl. Catal. A Gen.*, 2019, **570**, 139–147.
77 A. Chieregato, J. V. Ochoa, C. Bandinelli, G. Fornasari, F. Cavani and M. Mella, *ChemSusChem*, 2015, **8**, 377–388.

ABSTRACT. Development of active and stable noble metal-free catalysts is more and more required for environmental applications and valorization of renewable resources. Easy tuning of the reactivity of mixed oxide perovskites by cation and anion substitutions renders them a promising field of catalyst innovation. In the thesis, two classes of perovskite materials have been synthesized, characterized and tested in catalysis. Cation substitution of Co and Ga for Al in $LaAlO_3$ has allowed to modify both redox and acid-base properties, whereas partial hydride substitutions for oxygen in $LaSrCoO_4$ has provided a test-bed of hydrogenation activity.

Tailoring the redox properties of the $LaAlO_3$ mixed oxide by Co substitution has allowed to develop a multifunctional catalysts dealing with NO_x and soot decontamination of diesel exhausts. NO_x-assisted soot oxidation involves NO to NO_2 conversion and subsequent soot oxidation by the formed NO_2 at relatively low temperature. $LaAlO_3$ materials with different degrees of Co substitution for Al were prepared by sol-gel method and their catalytic activity was correlated with crystallinity, redox properties and mobility of lattice oxygen. Among the studied samples $LaAl_{1-x}Co_xO_3$ with x 0.75 exhibits superior catalytic activity for both NO to NO_2 oxidation and NO_x-assisted soot oxidation. The excellent performance is attributed to the synergetic interaction between Al-Co in B-site of the structure and may be linked to the high lattice surface oxygen supported by a well-crystallized perovskite structure.

The production of bio-ethanol is one of the staples of the replacement of fossil fuels with renewable biomass-derived resources. Valorisation of bio-ethanol for the production of chemicals requires a fine control of the acid-base properties of catalysts. While most of the research on perovskite catalysts has focused on their redox properties, studies on their acid-base properties have been much less developed. Partial substitution of Co and Ga for Al in $LaAlO_3$ has allowed to tune the acidity and basicity of the material and to control the relative activity of dehydration and dehydrogenation of ethanol, controlling the ratio between ethylene and acetaldehyde. The nature of the introduced cation allowed to form different Lewis acid-base pairs, orienting the reactivity of the acetaldehyde intermediates towards Tishchenko or aldol coupling, allowing to direct the reaction cascade towards the formation of butadiene or acetone and odd-C oxygenates.

While most of the literature on perovskite reactivity has focused on their structure/properties modifications by cation substitutions, there is a limited number of works on substitutions in the anion sites. Oxyhydride perovskites, $ABO_{3-x}H_x$, where hydride anions H^- can substitute O^{2-} in any sites of the BO_6 octahedron, have been reported presenting important hydride mobility, suggesting potential applications in hydrogenation catalysis. Oxyhydrides $LaSrCoO_3H_{0.7}$ and $BaTiO_{3-x}H_x$ have been prepared, characterized and tested in a model hydrogenation reaction. The reactivity of hydride species has been tested using chemical titration of toluene at temperatures at which hydrides are expected to be mobile. The results show that $LaSrCoO_{4-x}H_y$ exhibited a much higher activity than $BaTiO_{3-x}H_x$, due to the metallic sites formed by partial reduction of $LaSrCoO_{4-x}H_y$, indicating a possible use of perovskites as support for hydrogenation catalysts.

RÉSUMÉ. Le développement de catalyseurs actifs et stables exempts de métaux nobles est de plus en plus requis pour les applications environnementales et la valorisation des ressources renouvelables. Le réglage aisé de la réactivité des oxydes mixtes à structure pérovskite par des substitutions de cations et d'anions en fait un domaine prometteur d'innovation des catalyseurs. Dans cette thèse, deux classes de matériaux à base de pérovskite ont été synthétisées, caractérisées et testées en catalyse. La substitution de Al par des cations Co et Ga dans $LaAlO_3$ a permis de modifier les propriétés rédox et acide-base, alors que les substitutions partielles de l'oxygène par l'hydrure dans $LaSrCoO_4$ ont permis de nouveaux essais d'activité d'hydrogénation.

La maîtrise des propriétés redox de l'oxyde mixte $LaAlO_3$ par substitution de Co a permis de développer un catalyseur multifonctionnel actif dans la décontamination des NO_x et de la suie des gaz d'échappement de moteurs diesel. L'oxydation des suies assistée par NO_x implique une conversion de NO en NO_2 et une oxydation ultérieure des suies par le NO_2 formé à une température relativement basse. Des matériaux $LaAlO_3$ avec différents degrés de substitution de Co pour Al ont été préparés par la méthode sol-gel et leur activité catalytique a été corrélée à la cristallinité, aux propriétés redox et à la mobilité de l'oxygène de réseau. Parmi les échantillons étudiés, $LaAl_{1-x}Co_xO_3$ avec x 0,75 présente une activité catalytique supérieure pour l'oxydation du NO en NO_2 et l'oxydation de la suie assistée par le NO_x. L'excellente performance est attribuée à l'interaction synergique entre Al-Co dans le site B de la structure et peut être liée à l' élevé oxygène de surface supporté par une structure de pérovskite bien cristallisée.

La production de bioéthanol est l'un des éléments essentiels du remplacement des combustibles fossiles par des ressources renouvelables issues de la biomasse. La valorisation du bioéthanol pour la production de produits chimiques nécessite un contrôle minutieux des propriétés acido-basiques des catalyseurs. Alors que la plupart des recherches sur les catalyseurs pérovskites ont porté sur leurs propriétés rédox, les études sur leurs propriétés acide-base ont été beaucoup moins développées. La substitution partielle de Al par Co et Ga dans $LaAlO_3$ a permis d'ajuster l'acidité et la basicité du matériau et de contrôler l'activité relative de déshydratation et de déshydrogénation de l'éthanol, en contrôlant le rapport entre éthylène et acétaldéhyde formés. La nature du cation introduit a permis de former différentes paires base-acide de Lewis, orientant la réactivité de l'intermédiaire acétaldéhyde vers le couplage de Tishchenko ou le couplage aldolique, permettant ainsi d'orienter la cascade réactionnelle vers la formation de butadiène ou d'acétone et oxygénés a nombre de carbones impair.

Alors que la plupart de la littérature sur la réactivité des pérovskites est centrée sur leurs modifications de structure et propriétés par substitution de cations, il existe un nombre limité de travaux sur les substitutions dans les sites anioniques. Les pérovskites oxyhydrures, $ABO_{3-x}H_x$, où les anions hydrure H^- peuvent remplacer O^{2-} à n'importe quel site de l'octaèdre BO_6, ont présenté une mobilité d'hydrures importante, suggérant des applications potentielles en catalyse d'hydrogénation. Les oxyhydrures $LaSrCoO_3H_{0.7}$ et $BaTiO_{3-x}H_x$ ont été préparés, caractérisés et testés dans une réaction d'hydrogénation modèle. La réactivité des espèces hydrures a été testée par titrage chimique du toluène à des températures auxquelles les hydrures devraient être mobiles. Les résultats montrent que $LaSrCoO_{4-x}H_y$ présente une activité nettement supérieure au $BaTiO_{3-x}H_x$, activité qui doit être attribuée aux sites métalliques formés par réduction partielle de $LaSrCoO_{4-x}H_y$, indiquant une utilisation possible des pérovskites comme support pour les catalyseurs d'hydrogénation.